MRI contrast agents for iron probing

A thesis submitted for the degree of

Doctor of Philosophy in Inorganic Chemistry



Zepeng Cao

St John's College

University of Oxford

Hilary Term 2026

Abstract

Iron is indispensable in biology, yet the functionally relevant, weakly bound labile iron pool (LIP) remains difficult to interrogate non-invasively in living systems. Magnetic resonance imaging offers deep tissue penetration and whole-organ coverage, but the development of small-molecule MRI contrast agents that respond directly to LIP remains limited. This thesis examines whether gadolinium-based molecular probes bearing appended iron-binding groups can convert probe–iron association into a measurable change in longitudinal relaxation.

Two probe families were developed from a Gd–DO3A platform incorporating either a salicylate-derived arm (SCA) or a catechol-derived arm (Cat). Their behaviour was examined through a staged workflow comprising synthesis, aqueous relaxometry, UV–Vis spectroscopy, in vitro evaluation for toxicity, and sensitivity to LIP, and exploratory in vivo MRI. To interpret the relaxometry data, a species-based framework was used to distinguish simple additive contributions from relaxation changes arising from associated Gd–Fe species.

In aqueous solution, the two probe families showed clearly different iron-dependent behaviour. The SCA system, especially in the presence of Fe^{3+}, gave a reproducible deviation from additive relaxation behaviour, consistent with formation of an associated species with enhanced relaxivity. This dataset could be described using a minimal 1:1 association model, although the derived binding parameters should be treated as semi-quantitative because of model correlation and experimental limitation. In contrast, the Cat system showed weaker iron-dependent effects and

did not support equally robust mechanistic interpretation. UV–Vis measurements were consistent with differential metal interactions across the two ligand platforms.

Biological evaluation demonstrated that GdSCA functions as a conventional small-molecule gadolinium contrast agent, producing reproducible T_1-weighted liver enhancement in vivo. When systemic iron handling was experimentally perturbed, measurable differences in the magnitude and temporal profile of liver signal enhancement were observed; however, these changes could not be unambiguously attributed to a specific response to labile iron.

Taken together, this work establishes the chemical feasibility of iron-responsive relaxivity modulation in Gd-based molecular probes, identifies the SCA scaffold as the more promising platform, and provides a basis for further development of MRI agents for iron-related biology.

Acknowledgement

These four years at the University of Oxford mark not only the completion of my DPhil and the close of nine years of study in the United Kingdom, but also a major milestone in my life. This thesis represents the end of my formal student years and the beginning of a new chapter of contributing more directly to society. Whatever merit this work may have belongs only partly to me and very largely to those who have supported me, both within and beyond the laboratory.

I am deeply indebted to my supervisors, Professor Stephen Faulkner and Professor Samira Lakhal-Littleton.

Professor Faulkner, as the Head of Chemistry, carries many responsibilities, yet he has always put his students first. His scientific insight, patient guidance, and constant humour have shaped both this project and my way of thinking as a researcher. He has consistently created spaces for individual support, from subgroup discussions to one-to-one meetings, and he has cared just as much about our wellbeing as about our data. At some of the most difficult moments in my personal life, including bereavement, he offered not only advice but simple, human presence. If my Oxford years were a crown of jewels, Steve would be the largest and brightest stone in it.

Professor Lakhal-Littleton, in DPAG, is an outstanding scientist and an inspiring role model. She combines intellectual rigour, hard work, and integrity with deep care for those around her, as a professor and as a mother. I have been extremely fortunate to be one of her DPhil students. Her example has given me constant motivation to push towards being a better researcher. I have often felt that I fell short of her expectations, yet her trust and support never wavered. This thesis is, in many ways, my attempt to justify that trust and to make her proud.

I am very grateful to the members of the Faulkner and Lakhal-Littleton groups, past and present, for creating such a stimulating and supportive environment. To colleagues in the chemistry including Deborah, Dani, Mathew, Antoine, Carlson, Kezi, Xuejian, Adam, Daohe, Cameron, Agnes, Xiaofan, Charlotte, Qidian, Ceri, Rong, Euan; and DPAG labs, Goran, Mayra, Nashita, Dillon, thank you for your ideas, your help at the bench, and your patience in answering countless questions. Working alongside such talented and generous scientists has been a privilege.

Beyond my immediate research groups, I would like to thank Gregory Rees, Zongyao Zhang, and Chris Ball, and the many members of the chemistry and DPAG technical and administrative staff. Their expertise in maintaining instruments, providing

technical advice, and handling everyday logistics has quietly underpinned almost every piece of data in this thesis. Much of their work is invisible in the final document, but it has never gone unnoticed by me.

Outside the laboratory, I owe more than I can say to my family. To my wife, Shuhan Li, thank you for your unwavering love, patience, and belief in me. You have stood beside me through long nights, failed experiments, and rare moments of success, always offering warmth, honesty, and stability. Your support has turned difficult years into a journey we shared together.

To our son Jincheng Cao (Born in March 2026), you have already brought a profound sense of purpose and perspective into my life. Even before your arrival, you reminded me that there is something greater than any experiment or thesis. I hope that, in time, this work may stand as a small reflection of perseverance and responsibility as I begin my role as your father. (The footprint belongs my son)

To my parents, I owe the foundations of everything I have done. Your sacrifices, encouragement, and unconditional support have shaped my values and carried me through every stage of my education. You taught me to work hard, remain curious, and act with integrity. This thesis is only a small return for the faith you have always placed in me. I am also grateful to my grandparents and wider family for their constant encouragement and for reminding me of the importance of family, tradition, and staying true to one's roots.

For day to day life, St John's College and the University of Oxford have provided an intellectually rich environment and a place that has felt like home throughout my DPhil. For friendship, I am thankful to my friends, especially Shaohong, Zongyao, Yishun, Qihao, and Leike. For networks, opportunities, I also wish to acknowledge the support from CSSAUK and other societies and communities. For my previous education, Durham University, especially Professor Andrew Beeby, laid the academic foundations and first awakened my interest in research. I am deeply grateful for all these experiences and the people behind them.

Finally, to those who take the time to read this thesis, thank you for engaging with my work. Research can at times feel solitary, yet it gains meaning when it becomes part of a wider conversation. I hope that the results and ideas presented here will make a useful contribution to the field and perhaps serve as a small step towards further progress. This journey has been challenging and demanding, but also profoundly rewarding. It has only been possible because of the kindness, encouragement, and support of the individuals and organisations acknowledged here, to whom I offer my sincere and lasting thanks.

Abbreviations & terminologies

Abbreviation	Definition
a.u.	Arbitrary units
Ac	Actinide elements (Z = 89-103)
ANOVA	Analysis of variance (statistical method used to compare means across multiple groups)
BIL	Bilirubin (a parameter for urinalysis)
BLO	Blood (a parameter for urinalysis)
BSA	Bovine serum albumin (protein stabiliser in biological media)
CAT	Catechol-derived arm (iron-binding motif in probe design)
CSAP	Capped square antiprism geometry
CT	Computed tomography
DCM	Dichloromethane
Dcytb	Duodenal cytochrome b (membrane ferrireductase enabling $Fe^{3+} \rightarrow Fe^{2+}$ reduction for absorption)
dia	Diamagnetic
DMEM	Dulbecco's Modified Eagle Medium (nutrient-rich cell culture medium supporting mammalian cell growth)
DMSO	Dimethyl sulfoxide
DMT1	Divalent metal transporter 1 (transmembrane protein importing Fe^{2+} into cells/endosomes)
DNA	Deoxyribonucleic acid
DO3A	1,4,7,10-tetraazacyclododecane-1,4,7-triacetic acid
DO3A-CAT	DO3A-derived catechol ligand
DO3A-SCA	DO3A-derived salicylate ligand
DOTA	1,4,7,10-tetraazacyclododecane-1,4,7,10-tetraacetic acid
DTPA	Diethylenetriaminepentaacetic acid
ECG	Electrocardiogram
EDTA	Ethylenediaminetetraacetic acid
Et_2O	Diethyl ether
EtOAc	Ethyl acetate
EuSCA	Europium complex of SCA ligand
FBS	Fetal bovine serum (cell culture supplement providing growth factors)
FCM	Ferric carboxymaltose
FDA	Food and Drug Administration
FPN	Ferroportin (cellular iron exporter controlling iron efflux)

GBCA	Gadolinium-based contrast agent
Gd	Gadolinium
GdCat	Gadolinium-catechol probe
GdSCA	Gadolinium-salicylate probe
GLU	Glucose (a parameter for urinalysis)
HBSS	Hanks' balanced salt solution
HepG2	Human hepatocellular carcinoma cell line
Hg	Haemoglobin
HH	Hereditary haemochromatosis
HOMO	Highest occupied molecular orbital
HPLC	High-performance liquid chromatography
ICP-MS	Inductively coupled plasma mass spectrometry
IDA	Iron deficiency anaemia
ILCT	Intraligand charge transfer
IMAIOS	A website that probvided a CT scan model of mouse
IPCA	Iron-probing contrast agent
IS	Inner-sphere
IV	Intravenous
KET	Ketone (a parameter for urinalysis)
LC-MS	Liquid chromatography-mass spectrometry
LDH	Lactate dehydrogenase (enzyme released upon cell membrane damage; cytotoxicity marker, or it may refer to LDH cytotoxicity)
LEU	Leukocytes (a parameter for urinalysis)
LIP	Labile iron pool (bioavailable, weakly bound intracellular iron fraction)
LMCT	Ligand-to-metal charge transfer
Ln	Lanthanide
LUMO	Lowest unoccupied molecular orbital
MeCN	Acetonitrile
MRI	Magnetic resonance imaging
NIT	Nitrite (a parameter for urinalysis)
NMR	Nuclear magnetic resonance
NTBI	Non-transferrin-bound iron (circulating redox-active iron species)
obs	Observed
OD	Optical density
OS	Outer-sphere
OTf	Triflate

P/S	Penicillin-streptomycin
para	Paramagnetic
PBS	Phosphate-buffered saline
PET	Photoinduced electron transfer
PFD	Perfluorodecalin
PRO	Protein (a parameter for urinalysis)
q	Hydration number (number of coordinated water molecules to metal centre)
R_1	Longitudinal relaxation rate
r_1	Longitudinal relaxivity
R_2	Transverse relaxation rate
r_2	Transverse relaxivity
RBC	Red blood cell
ROI	Region of interest
ROS	Reactive oxygen species
SAP	Square antiprism
SBM	Solomon-Bloembergen-Morgan theory
SCA	Salicylate-derived arm (iron-binding motif in probe design)
sd	Standard deviation
SG	Specific gravity (a parameter for urinalysis)
T_1	Longitudinal relaxation time
T_2	Transverse relaxation time
TCSPC	Time-correlated single-photon counting
TFA	Trifluoroacetic acid
TfR1	Transferrin receptor 1 (mediates cellular iron uptake)
TfR2	Transferrin receptor 2
TLC	Thin-layer chromatography
TSAT	Transferrin saturation
TTP	Tricapped trigonal prism
URO	Urobilinogen (a parameter for urinalysis)
UV-Vis	Ultraviolet-visible spectroscopy
WHO	World health organization
λ	Wavelength
τR	Rotational correlation time (molecular tumbling timescale influencing relaxivity)

Contents

Abstract i
Acknowledgement iii
Abbreviations & terminologies iii
Contents viii
1. Introduction 1
1.1. Physiology 1
1.1.1. Iron distribution and dietary supply 1
1.1.2. The form of physiological iron 5
1.1.3. Iron homeostasis 8
1.1.4. Labile iron 19
1.1.5. Iron-related diseases 21
1.1.6. Iron assessment 26
1.2. Chemistry 33
1.2.1. The history of lanthanide chemistry 33
1.2.2. Lanthanide coordination and periodicity 34
1.2.3. Lanthanide photophysics 36
1.2.4. Paramagnetism 39
1.2.5. Solomon-Bloembergen-Morgan Theory for Gd complexes 41
1.2.6. Iron coordination 45
1.2.7. Iron-binding chelators 50
1.3. NMR & MRI 54
1.3.1. History and Nobel prizes 54
1.3.2. Mechanisms 55
1.3.3. Parameters and calculations 60
1.3.4. Type of Images 66
1.3.5. Contrast agent chemistry and exploitation 70
1.3.6. Clinical MRI 78
1.3.7. Studies on probing MRI contrast agents 82
2. Concept of an iron-specific contrast agent 86
2.1. Design rationale for iron-responsive Gd complexes 86
2.2. Selection of Iron-Binding Motifs 88
2.3. A Species-Resolved Relaxation Model for Gd–Fe Systems 92

2.3.1. Definition of Contributing Species 92
2.3.2. Dynamic Equilibrium Between Species 93
2.3.3. Fe–Probe Exchange Kinetics 95
2.3.4. Limiting Conditions and Model Assumptions 98
2.3.5. Potential interference of other species 100
2.4. SBM Extension to Gd–Fe Systems 102
2.5. Feasibility and Experimental Framework 105
2.5.1. Overall Experimental 105
2.5.2. Multi-Level Experimental Systems 107
2.5.3. Evaluation Criteria: Sensitivity, Selectivity, and Safety 108
3. Gd contrast agents in aqueous solution 110
3.1. Experimental Scope and Analytical Strategy 110
3.2. T1 relaxation measurements in aqueous solution 111
3.2.1. Analytical basis for T1 relaxation measurements 111
3.2.2. Method of T1 measurement and data analysis 112
3.2.3. Baseline relaxation behaviour of the probe and free iron systems in water 114
3.2.4. Iron-dependent modulation of R1 in probe-containing systems 121
3.2.5. Comparative interpretation in the context of the Gd–Fe interaction model 127
3.3. UV-Vis absorption 132
3.3.1. Research Objective of UV-Vis absorption 132
3.3.2. UV–Vis Rationale 133
3.3.3. Method of UV–Vis 135
3.3.4. Intrinsic UV–Vis absorption of probes and metal Ions in aqueous Solution 136
3.3.5. UV–Vis Titration of EuSCA with Metal 141
3.3.6. UV–Vis Titration of TbCat with Metal Ions 144
3.3.7. Electronic Interpretation and Comparative UV–Vis Analysis . 147
3.4. Binding simulations using DynaFit 152
3.4.1. Rationale for DynaFit analysis 152
3.4.2. DynaFit models and fitted parameters 154
3.4.3. DynaFit analysis of T1 relaxation data 157
3.4.4. DynaFit analysis of UV–Vis data 162

3.4.5. Result dissection of binding model and constant 167
3.4.6. Limitations of DynaFit fitting 171
3.4.7. Summary of DynaFit analysis 175
3.5. Summary and limitations of Chapter 3 176
4. Testing contrast agents in vitro 181
4.1. General concept and cellular model 181
4.2. Cytotoxicity 183
4.2.1. Rationale of contrast agent toxicity in vitro 183
4.2.2. Method of LDH cytotoxicity 185
4.2.3. Method development and validation of the LDH assay 186
4.2.1. LDH Cytotoxicity evaluation of GdSCA and GdCat 190
4.3. MRI in vitro 192
4.3.1. Aim and concept 192
4.3.2. Method of MRI in vitro 194
4.3.3. Setup design and development 196
4.3.4. Iron-dependent MRI signal modulation 198
4.3.5. Analysis and conclusion 203
4.4. Summary and limitations of Chapter 4 205
5. Gd contrast agents in vivo 209
5.1. General concept for in vivo experiment 209
5.1.1. Ethical declaration 209
5.1.2. Rationale for Animal Studies 209
5.2. Toxicity in vivo 210
5.2.1. Assessment method and strategy 210
5.2.2. Urine-based assessment 212
5.2.3. Body-weight and clinical health assessment 220
5.2.4. Summary and limitations of in vivo toxicity assessment 223
5.3. In vivo MRI 224
5.3.1. Objective of In vivo MRI 224
5.3.2. Basic experimental design for in vivo MRI 226
5.3.3. Contrast performance of GdSCA for in vivo MRI 240
5.3.4. In vivo MRI with GdSCA under altered iron handling with FCM 252
5.4. Summary and limitations of Chapter 5 267

6. Conclusion 270
7. Experimental procedure 278
7.1. General Concept and Synthetic Plan 278
7.2. General methods 280
7.3. Purity control 281
7.3.1. Purification of ligand precursors 283
7.3.2. Purification and Assessment of Complexes 285
7.4. Chemical Synthetics 286
7.4.1. Triester synthesis 286
7.4.2. BrSCA synthesis (bromination) 287
7.4.3. Triester-SCA synthesis (TriSCA; alkylation) 288
7.4.4. DO3A-SCA by deprotection 289
7.4.5. LnSCA complexation 289
7.4.6. TriCat by SN2 290
7.4.7. DO3A-CAT by deprotection 291
7.4.8. LnCAT complexation 292
8. Appendix 293
8.1. Declaration of the use of AI 293
8.2. PIL licence 294
8.3. Experimental Protocols 296
8.3.1. DynaFit script template example 296
8.3.2. DynaFit results Table 298
8.3.3. Final protocol for LDH assay 300
8.3.4. Protocol of MRI in Vitro 303
8.3.5. Urine analysis protocol 304
8.3.6. Protocol of MRI In vivo 305

Introduction

1.1. Physiology

Iron has long been associated with human health, with iron-containing materials used empirically in several ancient medical traditions to treat conditions resembling anaemia. A mechanistic understanding emerged much later, alongside the development of modern chemistry and the recognition of iron as a constituent of blood and haemoglobin. Subsequent discoveries established its roles in cellular respiration, storage, transport, and systemic regulation.[1] Iron is therefore now understood not simply as a dietary nutrient, but as a tightly regulated biological element whose physiological importance depends on its distribution, chemical form, and accessibility. These features provide the basis for the discussion of iron distribution and physiological handling that follows. [2]

1.1.1. Iron distribution and dietary supply

Iron is a trace metal in the human body, yet it is indispensable for oxygen transport, energy metabolism, and a wide range of enzymatic processes. In healthy adults, total body iron is typically in the range of approximately 3 to 5 g, although this varies with sex, age, body size, and physiological state. Despite this modest absolute quantity, iron is distributed across highly specialised compartments and is subject to exceptionally tight regulation, reflecting the need to maintain functional availability while preventing toxicity from unshielded redox-active iron. [3-5]

A large proportion of body iron is incorporated into haemoglobin within circulating erythrocytes, making the erythroid compartment the dominant iron pool in humans. Smaller but still physiologically important fractions are found in myoglobin within muscle and in a wide variety of enzymes and cofactors involved in respiration, DNA synthesis, and intermediary metabolism. [5] The remainder is stored predominantly in hepatocytes and cells of the mononuclear phagocyte system, especially macrophages in the liver, spleen, and bone marrow, where iron can be retained and subsequently mobilised according to systemic demand. [3, 5, 6]

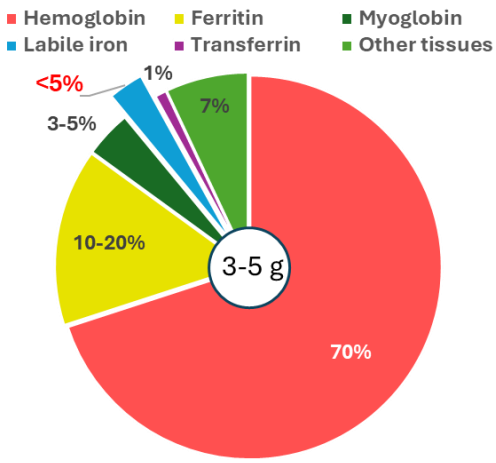


Figure 1 - Schematic distribution of total body iron among major compartments[7]

This compartmentalisation is central to iron physiology. Functionally, body iron may be viewed as existing in two broad and interdependent pools: a functional pool, in which iron is directly engaged in oxygen transport, oxygen storage, and catalytic activity, and a storage pool, in which iron is retained in a chemically buffered form that can be mobilised when required. These pools are not static. Rather, they are linked through continuous turnover, particularly through erythrocyte production and recycling. [5, 8] Consequently, total body iron content alone provides only a partial

description of physiological iron status; the biological significance of iron depends equally on its localisation, chemical form, and accessibility.[6]

A defining feature of iron biology is that iron is rarely permitted to exist in an unbound state. Because ferrous and ferric iron can participate in redox chemistry and catalyse the generation of reactive oxygen species, most physiological iron is coordinated within proteins or other molecular frameworks.[5, 6] Systemic iron transport is mediated principally by transferrin, intracellular storage is dominated by ferritin, and utilisation is channelled into highly specific biochemical contexts such as haem and iron–sulfur cluster biosynthesis. [8] This extensive sequestration is essential for preventing indiscriminate iron reactivity, but it also means that the biologically relevant iron available for exchange or sensing represents only a small fraction of total body iron. [5]

Iron balance differs from that of many other nutrients because there is no regulated excretory pathway for iron in humans. Daily iron loss is relatively small and occurs mainly through epithelial shedding, minor bleeding, and, in premenopausal women, menstruation. Systemic iron balance therefore depends predominantly on matching physiological need through intestinal absorption and long-term conservation, rather than through active elimination of excess iron. This feature makes dietary supply a central determinant of iron homeostasis over time. [3, 9, 10]

Dietary iron occurs in two principal forms: haem iron and non-haem iron. Haem iron is found in animal-derived foods and is generally more efficiently absorbed, whereas non-haem iron is present in plant-based foods and fortified products and is more

strongly influenced by luminal chemistry and dietary composition.[9] In practical terms, this means that total iron intake is not equivalent to effective iron acquisition. Iron bioavailability depends on both the source of iron and the surrounding nutritional context. [10]

The absorption of non-haem iron is particularly sensitive to enhancers and inhibitors. Ascorbic acid can promote absorption by improving solubility and supporting reduction to the ferrous state, whereas phytates, polyphenols, and calcium can reduce iron uptake under certain dietary conditions. [10] These interactions are important when considering nutritional iron sufficiency at the population level, but they also illustrate a broader principle relevant to this thesis: iron physiology cannot be inferred solely from total iron quantity. Chemical speciation and molecular environment strongly influence whether iron is biologically available. [9]

Iron requirements vary across the lifespan and between physiological states. Growth, menstruation, pregnancy, and other conditions associated with altered erythropoietic demand or blood loss substantially influence iron requirement. For this reason, dietary reference values differ according to sex and life stage. At the population level, such guidance is essential for nutritional policy and clinical risk stratification. However, these reference values describe expected intake requirements in healthy populations; they do not directly report how iron is partitioned between storage, transport, utilisation, and chemically accessible pools in vivo. [9, 11]

These distinctions are especially important when interpreting iron status in complex

biological settings. An individual may have apparently adequate total body iron yet limited functionally accessible iron or conversely may accumulate excess iron in storage compartments without this being reflected uniformly across all tissues or subcellular environments.[8] Thus, while dietary supply and whole-body distribution provide the basis of iron homeostasis, they do not fully resolve the question most relevant to the present thesis: which forms of iron are available, under physiological conditions, to participate in local molecular interactions that might influence probe behaviour. This question motivates the more detailed consideration of iron trafficking, regulation, and labile iron in the following sections. [5, 6]

1.1.2. The form of physiological iron

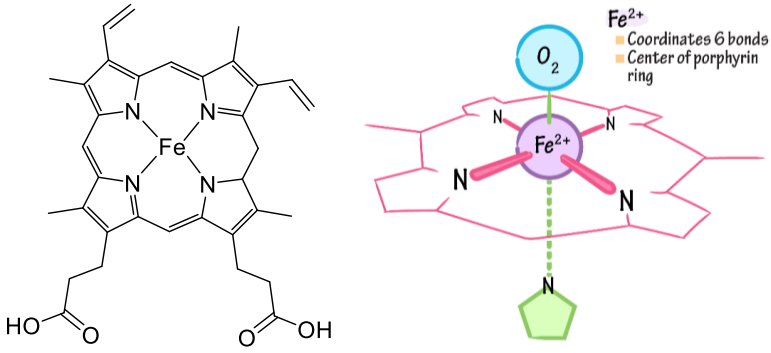


Figure 2 – haem group structure and oxygen binding illustration[12]

Iron in biological systems exists in a series of structurally and functionally distinct forms, reflecting its diverse roles in oxygen transport, metabolism, and cellular regulation. A defining feature of physiological iron is that it is rarely present as a free ion; instead, it is tightly coordinated within proteins or organised molecular assemblies.[1] This extensive coordination is necessary both to enable specific

biochemical functions and to limit the potential toxicity associated with redox-active iron. Consequently, the biological behaviour of iron is determined not only by its quantity, but by its oxidation state, ligand environment, and degree of accessibility.

The largest fraction of iron in the human body is found in haemoglobin, the principal oxygen transport protein, accounting for approximately 70–80% of total body iron. Haemoglobin is synthesised during erythropoiesis in the bone marrow and retained within mature erythrocytes, which are highly specialised for gas transport. Structurally, haemoglobin is a tetramer composed of two α- and two β-globin subunits, each containing a haem prosthetic group. [1] Within each haem unit, ferrous iron (Fe^{2+}) is coordinated in a porphyrin macrocycle by four nitrogen atoms in a square planar arrangement, with an additional axial ligand provided by a histidine residue. The sixth coordination site is reversibly occupied by molecular oxygen, enabling oxygen binding and release.[13] Maintenance of the iron in the Fe^{2+} state is essential for function, while oxidation to Fe^{3+} produces methaemoglobin, which is incapable of oxygen transport. This strict dependence on coordination environment and redox state illustrates the tight control required for functional iron chemistry in vivo. [1]

In contrast to haemoglobin, myoglobin represents a smaller haem-based iron pool localised mainly in cardiac and oxidative skeletal muscle. [14] It is a monomeric protein containing a single haem group and functions primarily in intracellular oxygen storage and delivery to mitochondria. Its haem iron is maintained in the Fe^{2+} state, while oxidation to Fe^{3+} compromises oxygen-binding function. Under pathological

conditions, the redox-active iron centre may also contribute to oxidative processes.[15]

Systemic iron transport is mediated primarily by transferrin, the principal iron-binding protein in extracellular fluids.[16] Each transferrin molecule can bind two Fe^{3+} ions with high affinity and delivers them to cells through transferrin receptor-mediated uptake. Iron binding is pH-dependent, allowing tight association in plasma and release within acidified endosomes. Because transferrin is normally only partially saturated, it also provides an important buffering capacity that limits the accumulation of non-transferrin-bound iron.[1]

Ferritin is the principal intracellular iron-storage protein and is particularly abundant in hepatocytes and macrophages. It forms a 24-subunit protein shell that stores iron within a ferric mineral core, thereby maintaining iron in a relatively non-reactive but mobilisable form.[17, 18] Ferritin therefore acts as an important intracellular buffer against fluctuations in iron availability. Under iron-overload conditions, excess stored iron may accumulate as haemosiderin, while circulating ferritin is also widely used as a clinical marker of iron stores.[19]

Taken together, these physiological forms of iron illustrate a common principle: iron is functionally partitioned into tightly regulated pools that differ in coordination, reactivity, and biological role. Haem proteins provide specialised functional environments for oxygen binding, transferrin ensures safe systemic transport, and ferritin acts as a buffered storage reservoir.[20, 21] Across all these systems, iron is largely sequestered within stable coordination environments, minimising the presence of free or weakly bound species. However, this organisation also implies

that only a small fraction of total iron is chemically accessible at any given time. This distinction is particularly important in the context of molecular interrogation, where the interaction of small-molecule probes depends not on total iron content, but on the subset of iron that is available for exchange or reaction. This accessible fraction, often referred to as labile iron, is considered in the following section.

1.1.3. Iron homeostasis

1.1.3.1. Iron absorption

Iron absorption happened in the epithelium cells in the enterocytes of the small intestine as illustrated in Figure 3.

Dietary iron, predominantly existing in its oxidised ferric form (Fe^{3+}), is initially released as labile iron species within the intestinal lumen following digestion. Prior to uptake by enterocytes, this ferric iron requires enzymatic reduction to ferrous iron (Fe^{2+}), a reaction catalysed by duodenal cytochrome B (Dcytb), a membrane-associated ferrireductase whose activity is potentiated by ascorbic acid. The resulting ferrous iron, in the presence of a proton gradient, is subsequently transported into the enterocyte cytoplasm through the apically localised divalent metal transporter 1 (DMT1). [22, 23]

Upon intracellular entry, the absorbed ferrous iron contributes directly to the labile iron pool (LIP), a transient, metabolically reactive reservoir of cytosolic iron. [24] Within this intracellular compartment, a fraction of ferrous iron reversibly associates with apoferritin, thereby forming ferritin complexes that serve as an intracellular

buffering system, dynamically regulating free cytoplasmic iron levels.

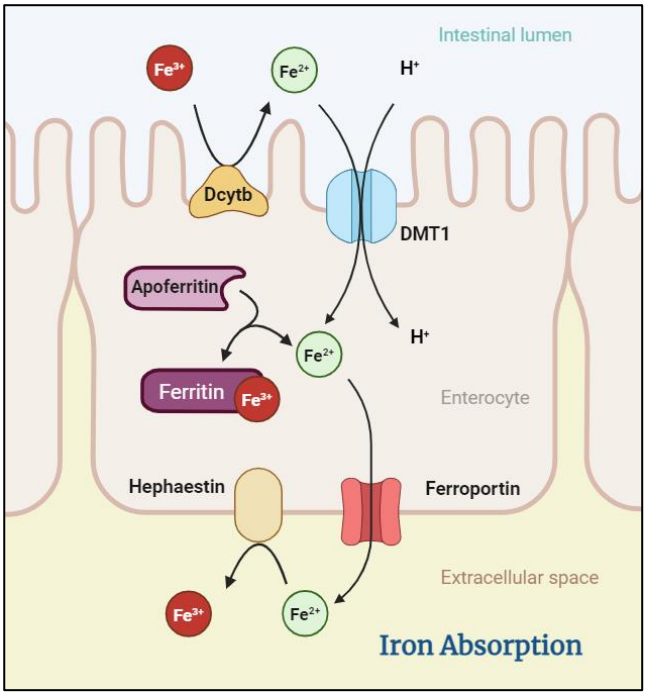


Figure 3 – Iron Absorption process in the enterocytes (plotted by Biorender)

Concurrently, iron not sequestered by ferritin is translocated across the basolateral membrane into the extracellular compartment through ferroportin (FPN), currently recognised as the sole cellular iron efflux transporter. This exported ferrous iron undergoes immediate oxidation back to ferric iron via hephaestin, a copper-dependent ferroxidase intimately associated with ferroportin at the basolateral membrane, thereby concluding the absorptive process within enterocytes.[25]

1.1.3.2. Iron transportation

In the human circulatory system, iron is transported predominantly in a protein-bound form to maintain solubility, minimise redox activity and enable targeted tissue delivery. Nearly all plasma iron is associated with transferrin, which binds ferric iron

and facilitates its uptake by iron-dependent cells. Under physiological conditions, the total serum iron concentration ranges between 10 and 30 micromoles per litre, with transferrin typically one-third saturated. This leaves a substantial reserve of unoccupied binding sites, ensuring a buffer against dietary fluctuations and transient changes in iron availability.[26]

A small fraction of circulating iron exists outside the transferrin-bound pool as labile plasma iron. This component consists of weakly chelated, low-molecular-weight iron species that are redox-active and capable of catalysing the formation of reactive oxygen species. In healthy individuals, labile plasma iron is tightly restricted to sub-micromolar levels or remains undetectable. However, in pathological conditions such as hereditary haemochromatosis, transfusional iron overload or ineffective erythropoiesis, transferrin may become saturated and labile iron accumulates, contributing to cellular toxicity and tissue injury.[27, 28]

Once loaded with iron, transferrin circulates to sites of demand, where it binds to cell surface transferrin receptors and is internalised through clathrin-mediated endocytosis.[5] Iron is released within the endosomal compartment and enters the cytoplasm, while the apotransferrin–receptor complex is recycled to the cell surface. At physiological pH, apotransferrin dissociates and re-enters the plasma to initiate a new transport cycle. This highly efficient recycling process allows a single transferrin molecule to undergo repeated rounds of iron delivery without degradation. Clinically, serum iron status is assessed using parameters such as serum iron concentration, transferrin saturation and total iron-binding capacity. These measures provide

insight into the functional state of iron distribution in circulation and are routinely used in the diagnosis and management of iron-related disorders.[1]

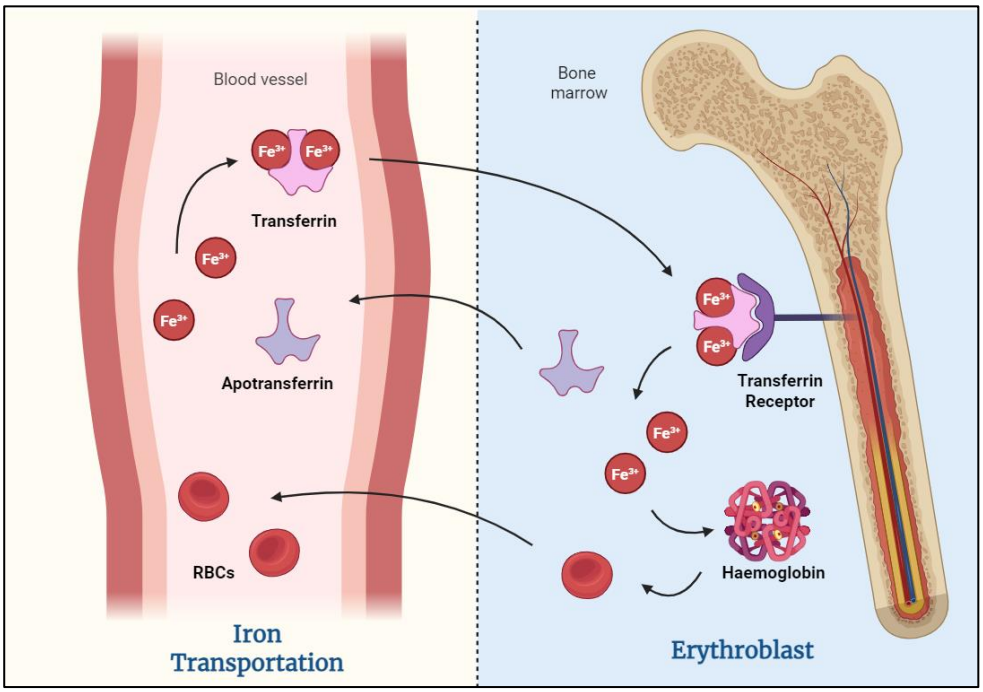


Figure 4 – Iron transportation process in blood vessels and erythroblast process in bone marrow (plotted by Biorender)

1.1.3.3. Erythropoiesis

Erythropoiesis is the process by which erythrocytes are generated from haematopoietic stem cells through a series of lineage-committed intermediates. It occurs primarily in the bone marrow under physiological conditions and is tightly regulated by both systemic signals and the local bone marrow microenvironment. The earliest morphologically recognisable erythroid precursor is the proerythroblast, which arises from common myeloid progenitors and initiates a cascade of differentiation marked by progressive nuclear condensation, haemoglobin accumulation and organelle clearance. [5, 29]

The proerythroblast is a large, basophilic cell characterised by a prominent nucleolus and a high nuclear-to-cytoplasmic ratio. As it matures through the basophilic, polychromatic and orthochromatic erythroblast stages, the cell volume decreases, chromatin becomes increasingly condensed and the cytoplasm acquires eosinophilic staining due to the accumulation of haemoglobin. Mitochondria and ribosomes, essential for early haem synthesis and globin translation, are abundant during the initial stages but are systematically degraded through mitophagy and ribophagy as differentiation proceeds. In the final stages of terminal differentiation, the orthochromatic erythroblast undergoes enucleation, yielding a reticulocyte that is subsequently released into the bloodstream. The reticulocyte continues to remodel its membrane and complete organelle clearance before maturing into a fully functional erythrocyte.

Iron metabolism is integral to erythroblast development, as haem biosynthesis requires a continuous supply of ferrous iron to mitochondria. Transferrin-bound iron is delivered to erythroblasts via high levels of transferrin receptor 1, which is abundantly expressed during all nucleated stages. Once internalised, iron is released in the endosome, transported to the cytosol and routed to the mitochondria for incorporation into haem. Excess intracellular iron is transiently stored in ferritin, although ferritin expression decreases sharply in the late stages of erythropoiesis to minimise oxidative stress and avoid iron retention in mature erythrocytes.[29, 30]

The rate of erythropoiesis is primarily regulated by erythropoietin, a renal hormone that responds to tissue hypoxia. Iron availability also exerts a critical influence, as

iron-restricted conditions impair erythroid proliferation and terminal differentiation, leading to the formation of hypochromic erythrocytes and anaemia. Erythroblasts are particularly vulnerable to perturbations in iron homeostasis, and their iron-handling machinery must be tightly coordinated to balance iron acquisition, utilisation and detoxification throughout differentiation.[31]

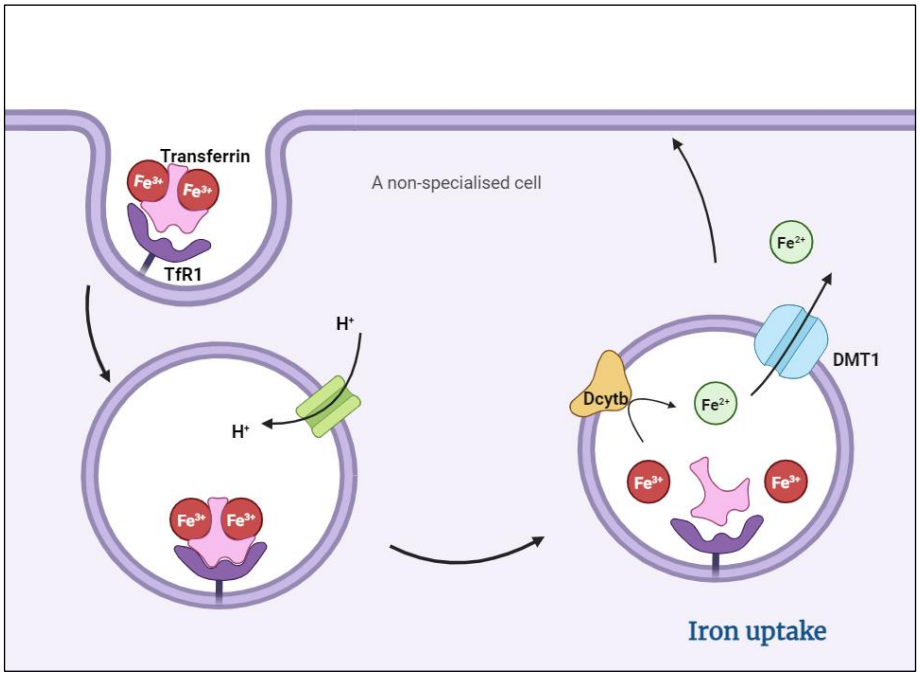


Figure 5 - Iron uptake process in a non-specialised cell (plotted by Biorender)

1.1.3.4. Endocytosis-mediated iron uptake

Cellular uptake of iron in most human cell types is primarily mediated through receptor-dependent endocytosis of transferrin-bound iron. Under physiological conditions, iron circulates in the plasma complexed to transferrin in its ferric form. Cells requiring iron express transferrin receptor 1 (TfR1) on their surface, which binds di-ferric transferrin with high affinity. The transferrin–TfR1 complex is then internalised via clathrin-mediated endocytosis into early endosomes, a process that

is rapid, selective and tightly regulated. [32]

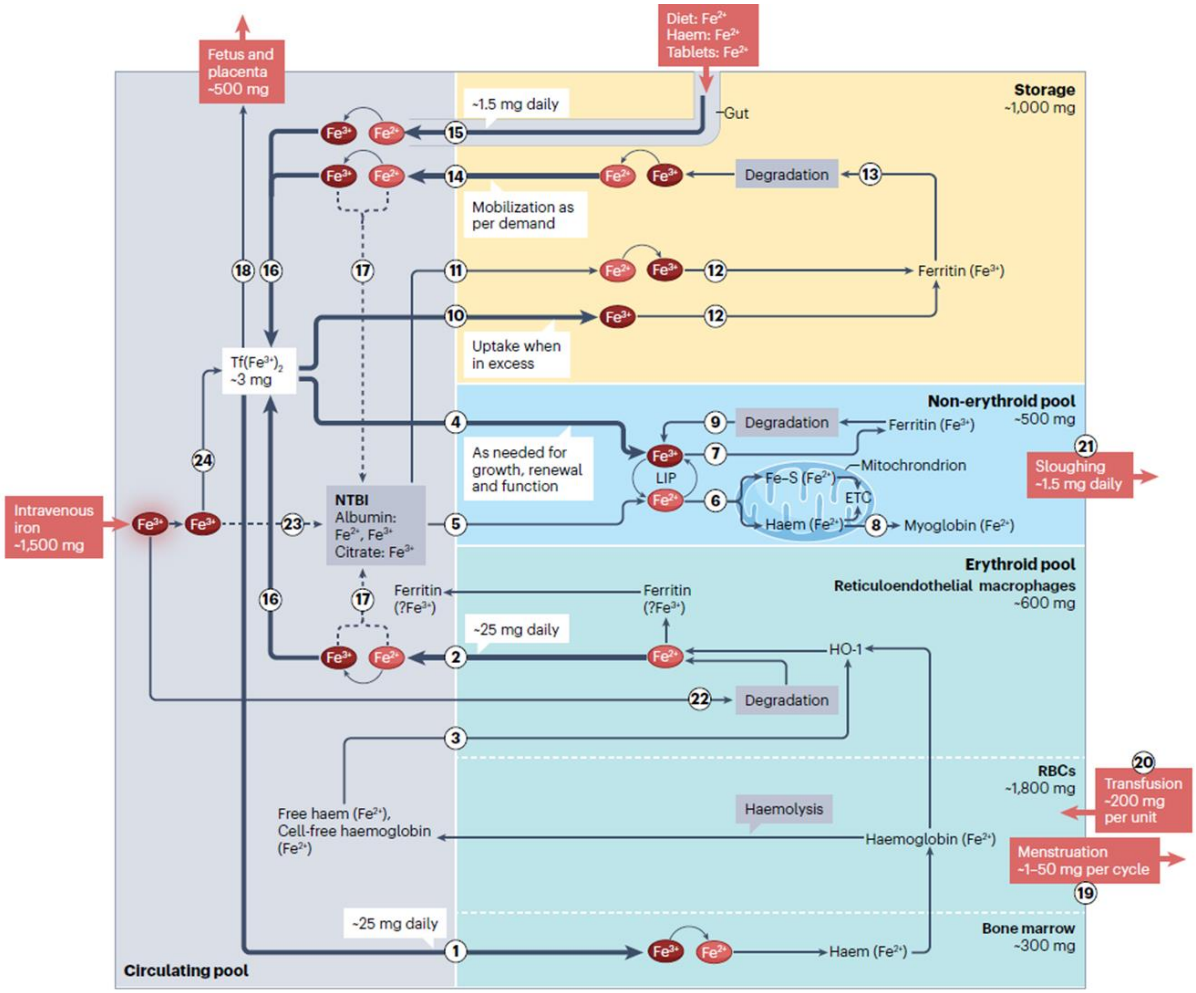


Figure 6 - The oxidative states, binding ligands and functional pools of iron in the body[2]

Within the endosomal compartment, the luminal pH decreases to approximately 5.5, facilitating conformational changes in transferrin and weakening its iron-binding affinity.[33, 34] Under these acidic conditions, ferric iron is released from transferrin while the apotransferrin remains bound to the receptor. The liberated Fe^{3+} is subsequently reduced to Fe^{2+} by endosomal ferrireductases such as six-transmembrane epithelial antigen of the prostate 3 (STEAP3), a reaction essential for enabling transmembrane transport of iron into the cytosol. This transport step is mediated by DMT1, which is localised on the endosomal membrane and selectively

imports ferrous iron into the cytoplasm.[23]

Once in the cytosol, Fe^{2+} enters the labile iron pool, a kinetically accessible reservoir that supplies iron to various intracellular destinations including mitochondria, the site of haem and iron–sulphur cluster biosynthesis. Excess iron may be transiently stored in cytosolic ferritin to avoid redox-mediated toxicity.[27] Meanwhile, the apotransferrin–TfR1 complex is recycled back to the cell surface via recycling endosomes. At physiological pH, apotransferrin dissociates from the receptor and re-enters the plasma, completing the iron delivery cycle. This highly efficient recycling system allows transferrin to participate in multiple iron transport rounds without degradation, while maintaining tight control over iron flux.[35]

This endocytic iron uptake pathway is particularly active in cells with high iron demand, such as erythroblasts, hepatocytes and proliferating cells. Its efficiency and specificity are essential for meeting metabolic requirements while preventing the accumulation of unbound iron species capable of catalysing oxidative damage.

1.1.3.5. Iron Storage

Iron storage is a critical component of cellular iron homeostasis, allowing cells to sequester excess iron in a chemically inert form while maintaining a readily accessible reserve for metabolic use. In most nucleated cells, excess iron that is not immediately utilised is directed into storage to minimise the risk of oxidative damage arising from unbound ferrous iron. This process is essential because the labile iron pool, although necessary for biosynthesis, is redox-active and can catalyse the

formation of reactive oxygen species through Fenton-type reactions if left unregulated.[27, 36, 37]

Stored iron originates primarily from transferrin-mediated uptake, following its release from endosomes into the cytosol. Once in the cytoplasm, iron destined for storage is transiently associated with the labile iron pool before being incorporated into long-term storage compartments. The decision to store iron is influenced by the intracellular iron load, as well as by external factors such as hypoxia, oxidative stress and inflammation. In iron-replete states, iron storage increases to protect cellular integrity, whereas in iron-deficient conditions, storage is minimised to prioritise delivery to essential biosynthetic pathways such as haem and Fe–S cluster synthesis.[6, 36]

At the molecular level, iron storage is tightly controlled via post-transcriptional regulation. Iron-responsive elements in the untranslated regions of relevant mRNAs serve as binding sites for iron regulatory proteins, which modulate translation in response to labile iron levels. When cytosolic iron is limited, the translation of storage-related proteins is repressed to conserve iron for essential processes. Conversely, in iron-rich conditions, this repression is lifted to facilitate safe iron sequestration. [32]

In pathological states involving chronic iron overload, such as hereditary haemochromatosis or transfusion-dependent anaemias, iron storage mechanisms may become saturated. When this occurs, excess iron accumulates in the form of haemosiderin, an insoluble and less bioavailable complex derived from partially

degraded storage proteins. Haemosiderin is typically found in macrophages of the liver, spleen and bone marrow, and its presence is often regarded as a histological marker of iron loading. However, unlike regulated storage forms, haemosiderin lacks efficient mobilisation mechanisms and may contribute to long-term tissue injury due to its persistence and potential for redox activity.

Together, these systems establish a flexible and responsive framework for iron storage, balancing the dual requirement of protection from iron toxicity with the metabolic necessity of iron availability.

1.1.3.6. Iron recycling

Macrophages play a central role in systemic iron recycling, particularly through the phagocytic clearance of senescent or damaged erythrocytes. This function is primarily localised to specialised macrophage populations within the reticuloendothelial system, including Kupffer cells in the liver, splenic red pulp macrophages and bone marrow-derived macrophages. These cells are responsible for recovering iron from aged erythrocytes, which have a lifespan of approximately 120 days in humans, thereby maintaining a continuous internal supply of bioavailable iron.[32]

The process begins with erythrophagocytosis, during which macrophages engulf senescent erythrocytes and degrade them within phagolysosomes. Haemoglobin is released and rapidly catabolised by haem oxygenase 1, which cleaves the haem moiety to yield biliverdin, carbon monoxide and ferrous iron. The liberated iron is

then transported to the cytosol, where it transiently enters the labile iron pool. Depending on cellular and systemic needs, this iron may be either stored intracellularly or exported into the circulation.[22, 38]

Iron export from macrophages is mediated by ferroportin, the only known iron exporter in humans. Once transported across the plasma membrane, ferrous iron is oxidised to the ferric form by multicopper ferroxidases such as ceruloplasmin in plasma or hephaestin in tissue interfaces, enabling its loading onto transferrin.[39] This recycling process accounts for the majority of daily iron turnover in adults, far exceeding intestinal absorption. Accordingly, iron handling in macrophages is tightly coupled to erythropoietic activity and regulated by systemic iron signals, particularly hepcidin. Hepcidin binds to ferroportin and induces its internalisation and degradation, thereby limiting iron efflux during conditions of iron overload or inflammation.[40]

Macrophages also contribute to iron buffering under pathophysiological conditions, including infection, haemolysis and tissue injury. In inflammatory settings, iron may be retained within macrophages to restrict its availability to invading pathogens, a process often referred to as nutritional immunity. Conversely, in conditions of iron overload, macrophages may accumulate excess iron in the form of ferritin or haemosiderin, contributing to tissue iron deposition and potential oxidative damage.[40, 41]

Together, macrophages serve as both custodians and gatekeepers of systemic iron availability, linking erythrocyte turnover with transferrin-mediated iron transport

and maintaining iron equilibrium across physiological and pathological states.

1.1.4. Labile iron

Labile iron, also referred to as the chelatable or redox-active iron pool, represents a small but critically important fraction of total biological iron. It is present both intracellularly and in plasma, existing in a loosely bound state that permits dynamic exchange with surrounding molecules.[22, 42] In contrast to iron tightly sequestered within proteins such as transferrin, ferritin or haem-containing enzymes, labile iron is only transiently associated with low molecular weight ligands, allowing it to participate in metal-dependent catalysis, transport, and cofactor assembly. However, this chemical accessibility also renders it capable of promoting oxidative damage via reactive oxygen species (ROS) generation, particularly under conditions of iron overload or regulatory failure.[2]

Within the circulation, labile plasma iron constitutes a minor component of non-transferrin-bound iron (NTBI), and is typically undetectable under physiological conditions. It emerges primarily when transferrin saturation exceeds 60 to 70 percent, such as in hereditary haemochromatosis or transfusion-associated iron overload. In this context, ferric iron (Fe^{3+}) may circulate loosely bound to organic acids, amino acids or small peptides, contributing to a redox-active pool that bypasses the transferrin–receptor regulatory axis.[28] Although the absolute concentration is low, often in the sub-micromolar range, even minimal increases in labile plasma iron are clinically significant due to their capacity to catalyse Fenton-

type reactions and initiate lipid peroxidation, endothelial injury and systemic oxidative stress.[43]

Intracellularly, labile iron exists predominantly in the cytosol and mitochondrial matrix, where it forms part of the labile iron pool (LIP). [7] The LIP is maintained in the low micromolar range and functions as the primary readily exchangeable source of iron for essential processes such as haem synthesis, iron–sulphur cluster biogenesis and DNA synthesis. This pool contains both ferrous (Fe^{2+}) and ferric (Fe^{3+}) species, with the relative distribution governed by compartment-specific pH and redox environment. At physiological pH, ferric iron is favoured; however, for membrane transport and cofactor insertion, iron must often be reduced to the more soluble ferrous form by intracellular ferrireductases. Once imported via DMT1 or released from endosomes, labile ferrous iron is directed either towards biosynthetic pathways, transient storage, or targeted efflux, depending on cellular demand and systemic signals. [2]

Despite its functional necessity, labile iron poses a significant threat to cellular integrity if not tightly regulated. [27, 44]The redox-active nature of Fe^{2+} allows it to participate in the Fenton reaction, whereby hydrogen peroxide is converted into hydroxyl radicals (HO·), one of the most reactive and damaging species in biological systems:[27, 37]

$$Fe^{2+} + H_2O_2 \rightarrow Fe^{3+} + HO^{\cdot} + OH^{-}$$
$$Fe^{3+} + H_2O_2 \rightarrow Fe^{2+} + HOO^{\cdot} + H^{+}$$

Reaction 1 – Fenton reaction for free radical generation[27, 44]

These ROS can non-specifically damage lipids, proteins and nucleic acids, leading to oxidative stress, cell death and tissue injury. [45]Accordingly, the size and reactivity of the labile iron pool must be tightly buffered by iron-binding proteins and intracellular antioxidant systems. Disruption of this balance is a key feature of many iron-related pathologies and represents a central challenge in the development of iron-based diagnostics and therapeutics.[46]

1.1.5. Iron-related diseases

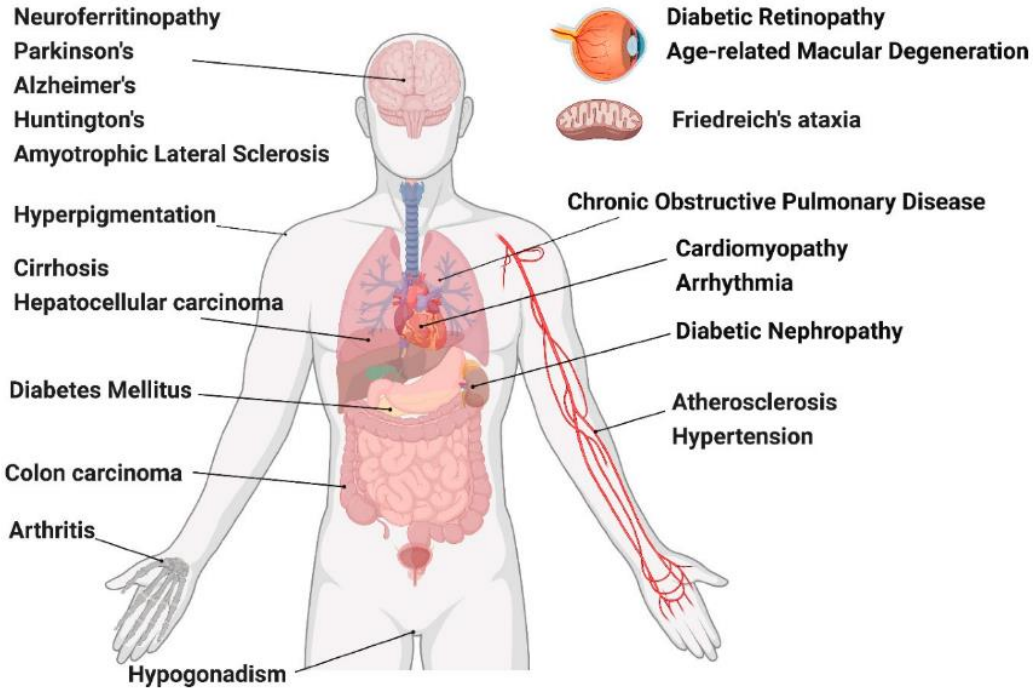


Figure 7 - Iron overload and Associated Diseases[47]

Iron homeostasis is tightly regulated under physiological conditions, yet its disruption is implicated in a wide spectrum of human diseases. These disorders range from iron deficiency, which impairs essential biochemical processes, to iron overload, which induces oxidative injury in multiple organs.[48] In many cases, pathological

changes are driven not only by alterations in total body iron but also by dysregulation of the labile iron pool, a readily exchangeable and redox-active fraction of iron that exerts disproportionate biological effects.[49] The following section summarises the major categories of iron-related diseases, outlines their principal causes and mechanisms, and highlights their relationship to labile iron where relevant, together with an overview of current clinical diagnostic approaches.[46, 50]

1.1.5.1. Iron Deficiency Anaemia

Iron deficiency anaemia (IDA) is the most prevalent nutritional disorder worldwide, affecting over a third of women and children based on WHO's report.[51] It arises when iron availability is insufficient to sustain effective erythropoiesis, most commonly due to chronic blood loss, inadequate dietary intake, or impaired intestinal absorption. Although IDA is classically defined by reduced haemoglobin levels, it reflects a broader deficiency in systemic iron availability.[51, 52]

Clinically, IDA presents with non-specific symptoms including fatigue, pallor, reduced exercise tolerance, and impaired concentration. In more prolonged or severe cases, features such as brittle nails, hair loss, or developmental delay in children may be observed. Diagnosis relies primarily on haematological and biochemical indices, including decreased haemoglobin, reduced mean corpuscular volume (MCV), low serum ferritin, and reduced transferrin saturation (TSAT), with ferritin typically declining at earlier stages of depletion.[53]

At the mechanistic level, the functional consequences of IDA are driven by depletion of the labile iron pool, the fraction of iron that is readily available for cellular

processes. This reduction limits iron supply to mitochondria and other intracellular sites, impairing haem synthesis, oxidative metabolism, and iron–sulphur cluster formation. As a result, cellular dysfunction arises not only from reduced haemoglobin production but also from compromised iron-dependent biochemical pathways, highlighting that the impact of IDA extends beyond oxygen transport to fundamental metabolic processes. [54, 55]

From a clinical perspective, iron deficiency anaemia is primarily managed through iron repletion. Oral iron supplementation remains the first-line treatment, although its effectiveness may be limited by poor absorption and gastrointestinal side effects. In more severe cases or where oral therapy is ineffective, intravenous iron is used to achieve more rapid correction. Blood transfusion is reserved for acute or life-threatening anaemia. [51]

1.1.5.2. Non-anaemic iron deficiency

Non-anaemic iron deficiency (NAID) refers to a state in which total body iron stores are preserved or even elevated, yet the availability of iron to support physiological processes is insufficient. [2] This condition is commonly observed in chronic inflammatory states, including heart failure, chronic kidney disease, and other systemic disorders, where iron demand is unmet despite apparently adequate iron levels. [40]

The pathophysiology of non-anaemic iron deficiency is driven by inflammation-induced disruption of systemic iron flux. Under physiological conditions, iron is continuously exported from enterocytes, macrophages, and hepatocytes via

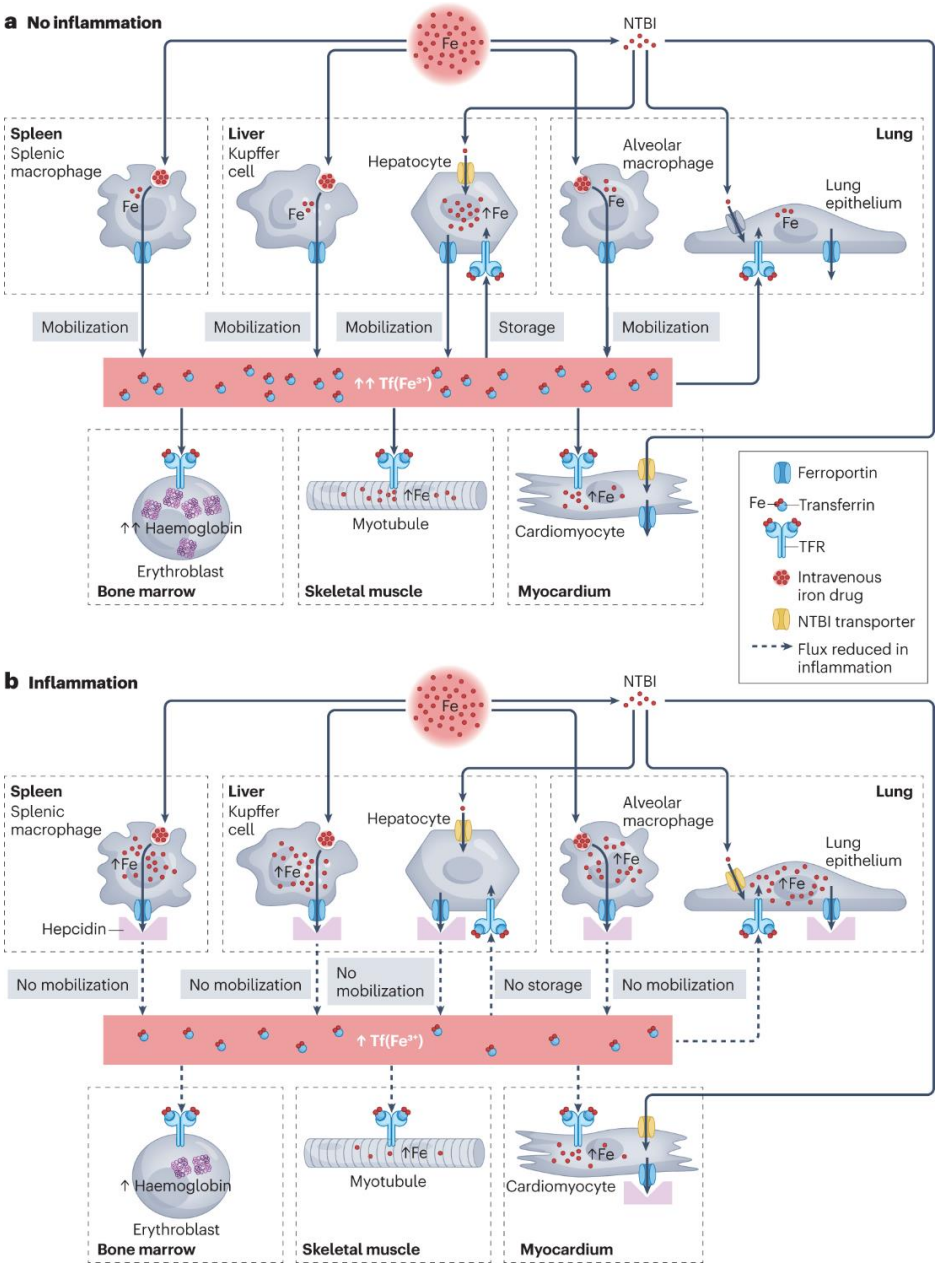


Figure 8 - Scheme of inflammation-induced NAID. Inflammatory signalling increases hepcidin expression, which inhibits ferroportin-mediated iron export from enterocytes and macrophages. This results in reduced circulating transferrin-bound iron and sequestration of iron within storage compartments, despite preserved total body iron.[2]

ferroportin, maintaining circulating transferrin-bound iron for tissue uptake.[56] In inflammatory states, increased hepcidin expression suppresses ferroportin activity across these compartments, reducing both intestinal iron absorption and the

mobilisation of stored iron. As a result, iron becomes sequestered within storage sites while the supply of transferrin-bound iron to the circulation declines.

Consequently, tissues experience restricted iron availability despite preserved or elevated total body iron, reflecting a fundamental dissociation between iron stores and functional accessibility.[2]

From a functional perspective, this imbalance reflects a reduction in the labile iron pool available to cells. [2] Although total iron is not depleted, the restriction of iron flux limits its incorporation into haem, iron–sulphur clusters, and other iron-dependent systems. Thus, NAID represents a state in which iron is present but not accessible, highlighting a fundamental dissociation between iron storage and biological availability.

1.1.5.3. Iron overload

Iron overload refers to a pathological state in which total body iron exceeds the buffering capacity of physiological storage and transport systems, leading to progressive accumulation of iron in tissues.[57] Clinically, early manifestations are often non-specific, including fatigue and arthralgia, whereas sustained iron deposition can result in organ dysfunction, particularly in the liver, heart, and endocrine tissues. These effects reflect the cumulative burden of excess iron within parenchymal cells rather than a single acute process.[57, 58]

At the mechanistic level, iron overload is characterised by saturation of transferrin and the subsequent emergence of non-transferrin-bound iron (NTBI) in the

circulation. [57] Under physiological conditions, circulating iron is tightly bound to transferrin; however, once this capacity is exceeded, excess iron appears as poorly regulated NTBI species, which are readily taken up by tissues. This uptake leads to expansion of the intracellular labile iron pool, a redox-active fraction capable of participating in catalytic reactions.[58] Elevated labile iron promotes the generation of reactive oxygen species through Fenton-type chemistry, resulting in oxidative damage to lipids, proteins, and nucleic acids. [50]

From a functional perspective, the toxicity associated with iron overload arises not solely from the quantity of accumulated iron but from the presence of chemically reactive and weakly controlled iron species.[59] The expansion of the labile iron pool therefore represents a critical determinant of tissue injury, highlighting the importance of iron speciation and accessibility in addition to total iron levels. [50]

1.1.6. Iron assessment

The accurate assessment of iron status is essential both in clinical medicine and biomedical research, given the central role of iron in oxygen transport, mitochondrial respiration, and cellular proliferation. Disorders of iron homeostasis—ranging from iron deficiency anaemia to systemic iron overload—are implicated in a wide spectrum of pathological conditions including chronic inflammation, infection, malignancy, and genetic disorders.[60, 61] Consequently, the ability to evaluate iron levels at the systemic, tissue, and cellular level has become fundamental not only for diagnosis and monitoring, but also for the design of therapeutic interventions and

experimental models.

Despite its physiological importance, iron presents unique challenges to measurement. Its distribution across multiple compartments—circulating, stored, and functional—and its tight regulation via protein binding and redox control mean that no single parameter can fully capture an individual's iron status. In both clinical and experimental settings, a combination of biochemical, histological, and imaging-based techniques is typically employed to derive a composite picture of iron availability and distribution. These tools differ widely in terms of invasiveness, specificity, spatial resolution, and sensitivity to confounding factors such as inflammation, making methodological selection highly context-dependent. The sections that follow will outline the key approaches currently used to assess iron, focusing on their respective utilities and limitations.

1.1.6.1. Clinical assessment of iron

In clinical practice, the initial evaluation of iron status typically begins with haematological indices derived from a complete blood count. Parameters such as haemoglobin (Hb), mean corpuscular volume (MCV), and mean corpuscular haemoglobin (MCH) provide indirect insight into iron availability, particularly in the context of erythropoiesis.[5, 31] A decrease in Hb, often accompanied by microcytosis and hypochromia, is characteristic of iron deficiency anaemia. However, these changes represent relatively late manifestations of deficiency and may be influenced by a variety of non-iron-related conditions, including chronic disease, haemoglobinopathies, and bone marrow disorders.[1] As such, they are useful as

screening tools but lack sensitivity and specificity for early-stage iron imbalance.

To complement these findings, a suite of serum-based biochemical markers is routinely employed to evaluate iron supply, storage, and transport.[62, 63] Serum iron reflects the circulating iron bound to transferrin but is highly variable and susceptible to diurnal fluctuation. Total iron-binding capacity (TIBC) and transferrin saturation (TSAT) offer a more stable assessment of transferrin function, although they too are influenced by nutritional and inflammatory status. Serum ferritin is widely regarded as the most reliable indicator of body iron stores under physiological conditions, yet its role as an acute-phase reactant limits its interpretability in the presence of systemic inflammation or infection. More recently, soluble transferrin receptor (sTfR) has gained prominence as a marker of cellular iron demand, being less affected by inflammatory stimuli and useful in distinguishing functional iron deficiency from true storage depletion. Nevertheless, each of these markers provides only a partial view, and their diagnostic value is maximised when interpreted in combination.[40, 43]

To overcome these limitations, non-invasive imaging techniques have been developed to estimate iron distribution at the organ level. Among these, T2*-weighted magnetic resonance imaging (MRI) has emerged as a robust and reproducible modality for quantifying iron accumulation in the liver, heart, and pancreas.[64, 65] This technique exploits the paramagnetic properties of iron to influence local magnetic field inhomogeneity and is particularly valuable in the longitudinal monitoring of transfusion-dependent patients. However, MRI-based assessments predominantly reflect bulk iron accumulation and remain insensitive to

dynamic changes in functional or intracellular iron pools. Furthermore, they lack the resolution to discriminate between chemically distinct forms of iron.[66]

Taken together, current approaches to iron assessment provide complementary but indirect information, reflecting different aspects of iron storage, transport, and distribution. As a result, measurable parameters do not necessarily correspond to the biologically available fraction of iron, highlighting a fundamental limitation in linking clinical measurements to functional iron status.

1.1.6.2. Experimental assessment of iron

In preclinical and in vitro research, a variety of analytical techniques have been developed to interrogate iron content, localisation, and functional availability across cellular and molecular scales. Colorimetric assays, based on chromogenic chelators such as Ferene S and bathophenanthroline sulphonate (BPS), are frequently employed to quantify total iron concentration in biological samples including culture media, serum, or tissue homogenates [57, 67]. These methods rely on the reduction of ferric to ferrous iron and subsequent complex formation, producing a measurable colour change proportional to iron content. While relatively simple and cost-effective, such assays typically require sample digestion and provide no spatial or compartment-specific information, limiting their utility in mechanistic studies.

To address these limitations, researchers have turned to fluorescent and absorbance-based probes capable of detecting labile iron pools in live cells or fixed specimens.[68] These probes—such as calcein-AM or phen green derivatives—offer semi-quantitative insights into readily exchangeable iron fractions, which are

thought to reflect short-term bioavailability and redox activity. In parallel, histological methods including DAB-enhanced Perl's staining and Turnbull's blue have been adapted for use in animal tissues and cell cultures, enabling the visualisation of iron accumulation at subcellular resolution.[60, 69] At the molecular level, the expression of iron-handling proteins such as transferrin receptor 1, ferritin, and divalent metal transporter 1 is frequently assessed via Western blotting, immunofluorescence, or quantitative PCR as an indirect readout of cellular iron status. For more precise quantification, techniques such as atomic absorption spectroscopy (AAS) or inductively coupled plasma mass spectrometry (ICP-MS) are employed to measure total iron content in biological specimens with high sensitivity and specificity. These complementary approaches together provide a toolkit for dissecting iron homeostasis under controlled experimental conditions.[26, 70]

Table 1 Comparison of experimental methods for iron assessment[42]

Method	**Target**	**Strength**	**Limitations**
Colourimetry assays (e.g. Ferene-S, BPS)	Total Fe concentration	Simple, quantitative	No spatial or speciation information
ICP-MS / AAS	Total elemental Fe	High sensitivity and accuracy	Destructive, no localisation or speciation
Fluorescent probes (e.g. calcein-AM)	LIP (relative)	Dynamic, live-cell compatible	Semi-quantitative, limited specificity
Histological staining (Perl's / Turnbull's)	Fe deposition (Fe3+ / Fe2+)	Provides spatial information	Qualitative, limited chemical resolution
Protein expression (TfR1, ferritin, DMT1)	Cellular Fe response	Provides mechanistic insight	Indirect measurement
MRI	Tissue Fe burden	Non-invasive, in vivo applicable	Reflects bulk Fe only, no speciation

1.1.7. Limitation of iron assessment

Despite the diversity of available methods, the comprehensive assessment of iron status remains inherently challenging due to the compartmentalised, dynamic, and context-sensitive nature of iron physiology. Many conventional biomarkers, particularly those used in clinical settings, are highly susceptible to confounding factors such as inflammation, infection, or comorbid metabolic.[63] Acute-phase responses can obscure ferritin levels, while systemic iron concentrations may fluctuate independently of tissue or cellular iron availability. Similarly, although MRI techniques offer valuable non-invasive insights into gross iron overload, they are largely insensitive to subtle changes in functional iron pools or transient perturbations at the cellular level.[71] The lack of spatial specificity in most biochemical assays further complicates efforts to delineate organ- or cell-type-specific patterns of iron handling, which are increasingly recognised as clinically and experimentally relevant.

From a research perspective, current methodologies often involve a trade-off between precision and invasiveness, or between molecular resolution and physiological relevance. For example, while in vitro fluorescent probes and transcriptomic markers can reveal mechanistic trends under controlled conditions, they rarely translate directly to in vivo or whole-organism contexts.[72, 73] Conversely, systemic measurements provide only indirect approximations of intracellular events and are typically blind to the labile iron pools that play critical roles in oxidative stress, signalling, and cell fate decisions.[45, 70] These limitations highlight a growing need for

tools capable of resolving iron distribution and flux in situ, with high spatial and temporal resolution, and under physiologically relevant conditions. In this context, molecular imaging approaches—including the development of iron-sensitive contrast agents for magnetic resonance imaging—offer a promising avenue for bridging the gap between biochemical quantification and functional visualisation.[70]

1.2. Chemistry

1.2.1. The history of lanthanide chemistry

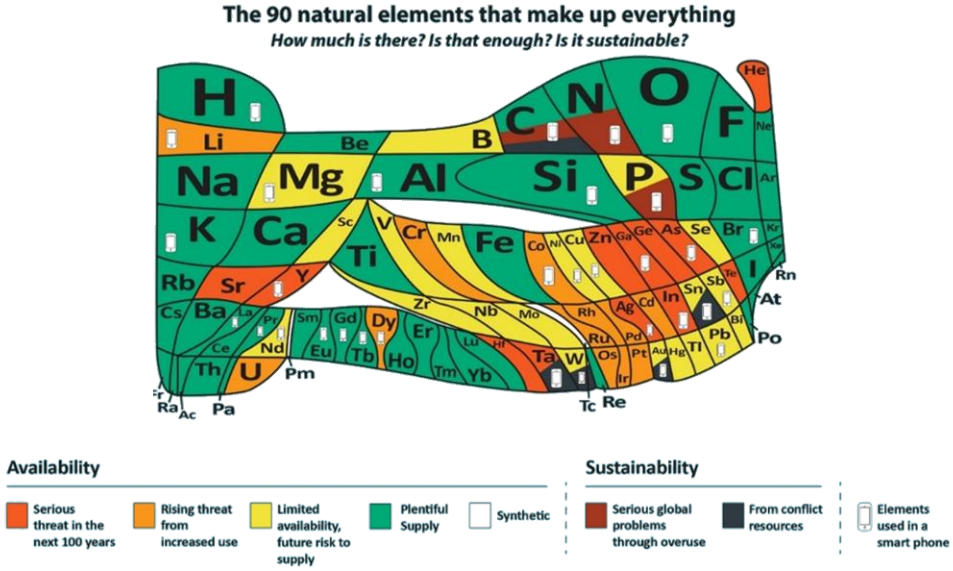


Figure 9 – The most abundant 90 natural elements[74]

The lanthanides comprise the 4f-block elements from La to Lu and were historically difficult to identify and separate because of their closely related chemical behaviour.[75] Their chemistry became substantially clearer with the development of modern atomic theory, which established the characteristic role of the shielded 4f orbitals. This electronic structure accounts for many of the distinctive magnetic and optical properties that have made lanthanides important in modern inorganic chemistry. Although often termed “rare earths”, their practical challenge lies more in separation than in absolute abundance.[74] These shared electronic and chemical features provide the basis for the coordination chemistry, photophysics, and magnetic behaviour discussed below.[76]

1.2.2. Lanthanide coordination and periodicity

The coordination chemistry of the lanthanide series is governed by the characteristic electronic structure of the 4f orbitals. As discussed in Section 1.2.1, the 4f electrons are effectively shielded by the filled 5s and 5p orbitals, resulting in minimal direct participation in bonding. Consequently, lanthanide–ligand interactions are predominantly electrostatic in nature, with limited covalent character. This leads to a high degree of chemical similarity across the series, distinguishing lanthanides from transition metals, where ligand field effects play a more dominant role in determining structure and reactivity.[77, 78]

Under most chemical, aqueous, and biological conditions, lanthanides are predominantly encountered in the +3 oxidation state.[79] Within this framework, several common coordination features emerge. Owing to their relatively large ionic radii and the absence of strong directional bonding, lanthanide ions typically exhibit high and variable coordination numbers, most commonly in the range of 7–10. Coordination geometries are correspondingly flexible and are largely determined by steric and electrostatic factors rather than ligand field stabilisation.[80] As a result, lanthanide complexes frequently adopt irregular polyhedral structures rather than well-defined geometries characteristic of transition metal complexes.[81, 82]

A further important feature of lanthanide coordination chemistry is the kinetic lability of their complexes in aqueous solution. Because metal–ligand interactions are largely ionic, ligand exchange processes are generally rapid. While this lability

can facilitate dynamic processes such as exchange-based sensing, it also necessitates the use of multidentate ligands to achieve sufficient thermodynamic stability and kinetic inertness, particularly in biological environments. Macrocyclic chelators such as DOTA and its derivatives are therefore widely employed to stabilise lanthanide ions, including Gd^{3+}, in functional systems.[83, 84]

Table 2 - Electronic Configurations, Common Oxidation States, and Ionic Electronic Configurations of Eu, Gd, and Tb[77]

Element		Atomic Number	Elemental e- Config.	Oxidation States	Ionic e- Config.
Europium	Eu	63	[Xe] $4f^7$ $6s^2$	+2	[Xe] $4f^7$
				+3	[Xe] $4f^6$
Gadolinium	Gd	64	[Xe] $4f^7$ $5d^1$ $6s^2$	+3	[Xe] $4f^7$
Terbium	Tb	65	[Xe] $4f^9$ $6s^2$	+3	[Xe] $4f^8$
				+4	[Xe] $4f^7$

Although lanthanides exhibit broad chemical similarity, systematic variations arise across the series, primarily as a result of the lanthanide contraction. The progressive decrease in ionic radius from La^{3+} to Lu^{3+} reflects the inefficient shielding of nuclear charge by 4f electrons, leading to an increase in effective nuclear charge. This contraction results in shorter metal–ligand bond distances and a tendency towards more compact coordination environments for the later lanthanides. [76]In coordination chemistry, these size-dependent effects can influence ligand binding affinity, preferred coordination number, and complex stability.[85]

Within this common structural framework, the coordination environment plays a critical role in determining the physicochemical properties of lanthanide complexes. Parameters such as hydration number, ligand donor set, and overall geometry

directly influence dynamic processes including water exchange and molecular tumbling.[86, 87] These factors are particularly important for paramagnetic lanthanide ions such as Gd^{3+}, where small changes in coordination sphere can significantly alter magnetic relaxation behaviour.[88]

It is therefore important to recognise that, while lanthanide ions are often treated as chemically similar, their behaviour is not identical. Broad similarities in trivalent coordination chemistry coexist with systematic variations arising from ionic size and electronic configuration. This combination allows chemically related lanthanide ions to be employed in different experimental roles within a common ligand framework, while still reflecting underlying coordination chemistry.[89] These principles form the basis for understanding the behaviour of gadolinium complexes in magnetic resonance imaging, and for interpreting the use of alternative lanthanide ions in complementary spectroscopic studies.[78, 90]

1.2.3. Lanthanide photophysics

The photophysical behaviour of lanthanide ions arises primarily from electronic transitions within the 4f orbitals, which are effectively shielded by the filled 5s and 5p shells. As a result, these transitions are only weakly influenced by the surrounding coordination environment, giving rise to narrow, line-like emission bands and long excited-state lifetimes.[91] This behaviour distinguishes lanthanides from transition metal complexes, where d-orbital interactions with ligands strongly perturb electronic structure and optical spectra.[92]

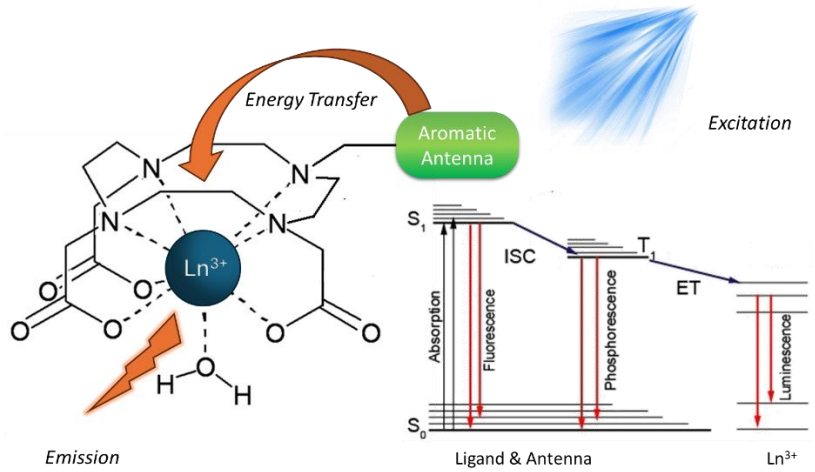


Figure 10 – Model of antenna effect and its energy level diagram

A defining consequence of this electronic structure is that f–f transitions are formally Laporte-forbidden, resulting in very low molar absorption coefficients.[93] Direct excitation of lanthanide ions is therefore inefficient, and their optical behaviour cannot be effectively accessed through metal-centred absorption alone. Instead, most practical lanthanide photophysical systems rely on indirect excitation pathways, in which light absorption is mediated by the surrounding ligand framework rather than the metal centre itself.[92, 94]

This limitation is overcome through the incorporation of sensitising ligands, commonly referred to as antennae.[78] In this process, an organic chromophore absorbs incident light and is promoted to a singlet excited state, followed by intersystem crossing to a triplet state.[92] Energy is then transferred from this ligand-centred triplet state to the lanthanide ion, populating the metal-centred excited states from which characteristic emission occurs. The antenna effect therefore decouples light absorption from emission and allows photophysical behaviour to be tuned through ligand design.[95]

The efficiency of this energy transfer process is critically dependent on the relative energy levels of the ligand and the lanthanide ion.[96] In particular, the triplet state of the antenna must lie sufficiently above the accepting excited state of the lanthanide to enable efficient forward transfer while suppressing back-transfer and non-radiative decay.[92] This requirement leads to pronounced element-specific behaviour across the lanthanide series, such that a given chromophore may sensitise some lanthanide ions effectively but not others. In addition, although 4f orbitals are largely shielded, subtle variations in coordination environment and symmetry can influence transition probabilities and emission intensity, particularly in systems where ligand perturbation modifies the electronic structure of the chromophore.[78, 90]

Lanthanide emission is also highly sensitive to non-radiative quenching processes, particularly those associated with high-energy vibrational oscillators such as O–H bonds.[36] Coordination of water molecules in the inner sphere provides an efficient pathway for vibrational energy transfer, significantly reducing luminescence intensity and lifetime. Consequently, ligand design often aims to minimise direct solvent coordination by increasing denticity or steric shielding.[97] This requirement introduces an important distinction between luminescent and magnetic resonance systems: while suppression of inner-sphere water coordination is beneficial for luminescence, controlled water access is essential for efficient proton relaxation in MRI contrast agents.[98]

Europium(III) and terbium(III) possess energy level structures that are well matched to common antenna chromophores and are therefore widely used as luminescent

probes.[99] In contrast, gadolinium(III), despite sharing similar coordination chemistry, does not typically provide useful optical emission as a consequence of having a high energy first excited state and is instead exploited for its paramagnetic properties in magnetic resonance imaging.[76, 100] This distinction allows chemically related lanthanide complexes to be employed in complementary roles: luminescent lanthanides may be used to probe ligand-centred or coordination-dependent electronic behaviour, while corresponding gadolinium complexes are used to evaluate magnetic relaxation properties.[92]

1.2.4. Paramagnetism

Paramagnetism is a fundamental magnetic phenomenon arising from the presence of unpaired electrons in a chemical species.[101] When exposed to an external magnetic field, paramagnetic substances experience a net attraction due to the alignment of their magnetic moments with the applied field. In contrast, diamagnetism describes the behaviour of materials in which all electrons are paired; such systems generate only a weak, opposing magnetic field and are therefore repelled by an external field. While diamagnetism is a universal property of all matter, it is typically overshadowed in species that contain unpaired electrons, where paramagnetic effects dominate.[102]

At the electronic level, paramagnetism originates from both spin and orbital angular momentum associated with unpaired electrons. The magnitude of the magnetic moment depends on the number of unpaired electrons as well as their electronic

configuration. In many transition metal systems, orbital contributions are partially quenched by ligand field effects, and magnetic behaviour can often be approximated using spin-only models.[103] However, this simplification does not universally apply, particularly in systems where orbital contributions remain significant.

Within this broader framework, both lanthanide ions and biologically relevant transition metals such as iron represent important classes of paramagnetic species, albeit with distinct underlying mechanisms and consequences.

In the case of the lanthanide series, paramagnetism is governed by electrons in the 4f orbitals. These orbitals are effectively shielded from the surrounding ligand environment by filled outer shells, resulting in minimal ligand field perturbation.[82] Consequently, both spin and orbital angular momentum contribute significantly to the overall magnetic moment, and the total angular momentum quantum number J provides a more appropriate description of their magnetic properties. This leads to relatively large magnetic moments and pronounced anisotropy across much of the series. [104] Notably, Gd^{3+}, with its half-filled $4f^7$ configuration, represents a special case in which orbital contributions are minimised, yielding a large and nearly isotropic magnetic moment. [105-107]

In contrast, paramagnetism in iron arises from its partially filled 3d orbitals, which are far more exposed to the ligand field. As a result, the magnetic properties of iron are highly sensitive to its chemical environment, oxidation state, and coordination geometry. For example, Fe^{2+} and Fe^{3+} may adopt either high-spin or low-spin configurations depending on ligand field strength, leading to substantial variation in

the number of unpaired electrons and, consequently, in magnetic moment. This tunability is central to the diverse biological roles of iron, where changes in coordination environment can directly modulate electronic structure and reactivity.[108]

From a functional perspective, the contrast between lanthanide and iron paramagnetism is particularly instructive. Lanthanides typically exhibit predictable and relatively environment-insensitive magnetic behaviour, whereas iron displays a high degree of responsiveness to local chemical conditions. This distinction is highly relevant in the context of probe design. Lanthanide-based systems, such as Gd^{3+} complexes, are often employed to provide consistent and strong magnetic effects, while iron, especially in its labile or loosely bound forms, may serve as a dynamic target whose magnetic properties reflect underlying biological processes. [36]

Taken together, paramagnetism provides a unifying framework for understanding the magnetic behaviour of both lanthanides and transition metals. By linking electronic structure to observable magnetic effects, it offers critical insight into the design of functional systems, particularly in biomedical imaging, where subtle variations in magnetic properties can be harnessed to generate meaningful contrast.[101]

1.2.5. Solomon-Bloembergen-Morgan Theory for Gd complexes

The contrast enhancement observed in T_1-weighted MRI arises from modulation of the longitudinal relaxation rate of water protons. In the presence of paramagnetic

species such as Gd^{3+}, this relaxation is accelerated through dipolar interactions between unpaired electron spins and nearby nuclear spins. These processes are described by the Solomon–Bloembergen–Morgan (SBM) framework,[109-111] which provides a quantitative basis for relating molecular structure and dynamics to relaxivity.[83]

In this framework, the observed relaxation rate is expressed as the sum of diamagnetic and paramagnetic contributions:

$$(1/\mathrm{T_1})_{\mathrm{obs}} = \mathrm{R_{obs}} = (1/\mathrm{T_1})_{\mathrm{d}} + (1/\mathrm{T_1})_{\mathrm{p}} = (1/\mathrm{T_1})_{\mathrm{d}} + \sum \mathrm{r_1[para]}$$

Equation 1 – R_1 is the sum of the diamagnetic and paramagnetic contributions[112]

where $(1/T_1)_{\mathrm{obs}}$ is the measured longitudinal relaxation rate, $(1/T_1)_d$ is the background relaxation rate in the absence of paramagnetic species, r_1 is the longitudinal relaxivity, and $[\mathrm{Gd}]$ is the concentration of the paramagnetic complex. This expression forms the basis for experimental determination of relaxivity.

Within the SBM formalism, the paramagnetic contribution to relaxation is further decomposed into two principal components:

$$(1/\mathrm{T_1})_{\mathrm{p}} = (1/\mathrm{T_1})_{\mathrm{IS}} + (1/\mathrm{T_1})_{\mathrm{OS}}$$

Equation 2 – Gd complex's paramagnetic relaxation is the sum of inner and outer spheres[83]

where the inner-sphere term $(1/T_1)_{\mathrm{IS}}$ arises from water molecules directly coordinated to the Gd^{3+} centre, and the outer-sphere term $(1/T_1)_{\mathrm{OS}}$ arises from diffusional interactions with surrounding water molecules. In this context, second-

sphere water molecules, which are hydrogen-bonded or transiently associated with the complex, are generally treated as part of the outer-sphere contribution rather than as a separate term.[113]

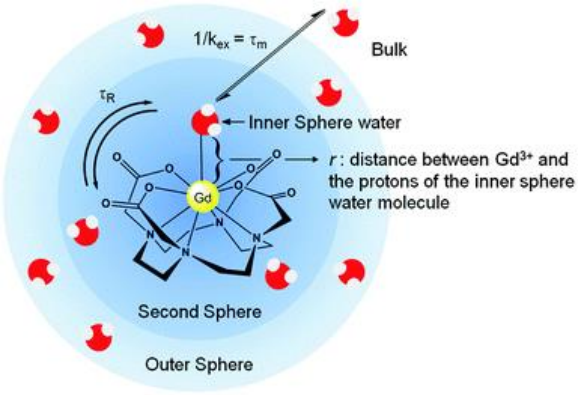


Figure 11 - illustration of inner-sphere and outer-sphere relaxation processes[114]

The inner-sphere contribution, which typically dominates relaxivity, depends on both structural and dynamic parameters and may be expressed in simplified form as:

$$\frac{1}{T_1^{IS}} = \frac{qP_m}{T_{1m} + \tau_m}$$

Equation 3 – Inner sphere contributions to relaxivity[83]

where q is the hydration number (the number of water molecules directly coordinated to the paramagnetic centre), P_m is the mole fraction of coordinated water, T_{1m} is the longitudinal relaxation time of the bound water molecule, and τ_m is the residence lifetime of water in the coordination sphere (i.e., the inverse of the water exchange rate). This expression reflects the fact that relaxation enhancement depends both on how efficiently a bound water molecule is relaxed and on how long it remains in the coordination environment before exchanging with

bulk solvent.[86]

The microscopic origin of relaxation is described by dipole–dipole interactions between electron and nuclear spins. In the SBM framework, the corresponding relaxation rate may be written as:

$$\frac{1}{T_1} \propto \frac{1}{r^6} \cdot J(\omega)$$

Equation 4 – Relaxativity correlation with distance of paramagnetic centre and the nuclear spin and spectral density

where r is the distance between the paramagnetic centre and the nuclear spin, and $J(\omega)$ is the spectral density function describing the frequency dependence of magnetic field fluctuations. The r^{-6}dependence highlights the strong sensitivity of relaxivity to spatial proximity, such that even small changes in distance can lead to substantial variations in relaxation efficiency. [112]

The spectral density function is commonly expressed as:

$$J(\omega) = \frac{\tau_c}{1 + \omega^2 \tau_c^2}$$

Equation 5 – Function of spectral density

where ω is the Larmor frequency of the nuclear spin, and τ_c is the effective correlation time governing the fluctuation of local magnetic fields. The correlation time incorporates multiple dynamic processes and may be written as:

$$\tau_c^{-1} = \tau_R^{-1} + \tau_m^{-1} + \tau_S^{-1}$$

Equation 6 – Expression of effective correlation time

where τ_R is the rotational correlation time of the complex, τ_m is the water residence lifetime, and τ_S is the electronic relaxation time of the paramagnetic centre. This relation reflects the fact that molecular tumbling, water exchange, and electronic spin relaxation all contribute to the temporal modulation of dipolar interactions.

The functional form of $J(\omega)$ implies that relaxivity depends critically on the relationship between the fluctuation timescale (τ_c) and the observation frequency. In particular, efficient relaxation occurs when these timescales are matched, giving rise to an optimal dynamic regime. Consequently, both excessively rapid and excessively slow dynamics may reduce relaxivity. [112]

Taken together, the SBM framework establishes that relaxivity is governed by a combination of structural factors, including hydration number and metal–proton distance, and dynamic factors, including molecular rotation, water exchange, and electronic relaxation. These dependencies demonstrate that relaxivity is not an intrinsic constant of a contrast agent, but is highly sensitive to its local molecular environment.[115, 116]

1.2.6. Iron coordination

Iron exhibits rich and versatile coordination chemistry, primarily due to its ability to access multiple oxidation states, most notably Fe^{2+} and Fe^{3+}. These two forms dominate under physiological and most experimental conditions and display distinct electronic structures, coordination preferences, and reactivity profiles. As a consequence, iron coordination chemistry is highly sensitive to its chemical

environment, in contrast to the more predictable behaviour observed in the lanthanide series.[26]

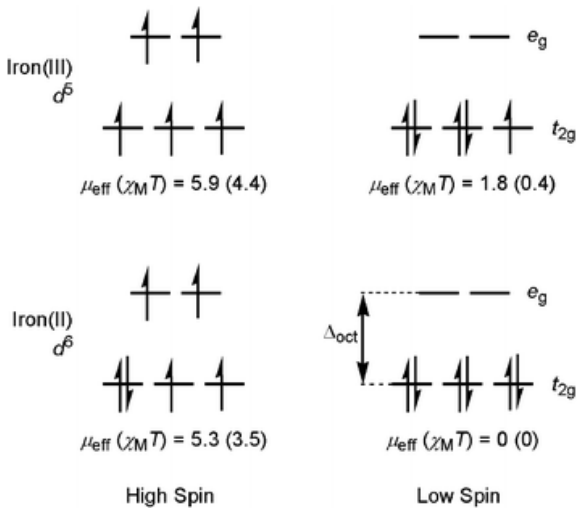


Figure 12 – Field of d-orbital occupancies of ferric and ferrous ion in high/low spin states and their corresponding effective magnetic moments[108]

At the electronic level, Fe^{2+} possesses a $3d^6$ configuration, whereas Fe^{3+} adopts a $3d^5$ configuration as shown in Figure 12. The distribution of these d-electrons within ligand field-split orbitals gives rise to either high-spin or low-spin states, depending on the strength of the coordinating ligands. In weak ligand fields, such as those provided by water or oxygen donors, both Fe^{2+} and Fe^{3+} typically exist in high-spin configurations, maximising the number of unpaired electrons. In contrast, strong-field ligands, such as cyanide or certain nitrogen donors, can induce low-spin states, particularly for Fe^{2+}, leading to significant changes in magnetic properties and reactivity. [81, 106]

Fe^{3+}, with its higher positive charge and smaller ionic radius, generally forms more stable and kinetically inert complexes compared to Fe^{2+}. It exhibits a strong

preference for hard donor atoms, particularly oxygen-based ligands, and is commonly found in octahedral coordination environments. In biological systems, Fe^{3+} is often tightly bound within proteins or stored in mineralised forms to minimise its participation in uncontrolled redox reactions. In contrast, Fe^{2+} is more labile, with faster ligand exchange kinetics and a greater tendency to participate in redox processes. This increased reactivity is central to its functional roles but also underlies its potential toxicity.[36, 117]

A defining feature of iron coordination chemistry is its redox flexibility. The Fe^{2+}/Fe^{3+} redox couple is readily accessible under physiological conditions, allowing iron to cycle between these states in response to environmental cues.[118]

For the aqueous Fe^{3+}/Fe^{2+} couple under standard acidic conditions, the standard reduction potential is approximately +0.77 V versus the standard hydrogen electrode. This positive potential reflects the ability of Fe^{3+} to accept an electron and undergo reduction to Fe^{2+}, although the relative thermodynamic stability of the two oxidation states depends strongly on the surrounding redox and coordination environment. Ligand coordination can shift the Fe^{3+}/Fe^{2+} reduction potential by preferentially stabilising one oxidation state; in particular, the greater charge density and harder Lewis acidity of Fe^{3+} favour strong interactions with hard oxygen-donor ligands.

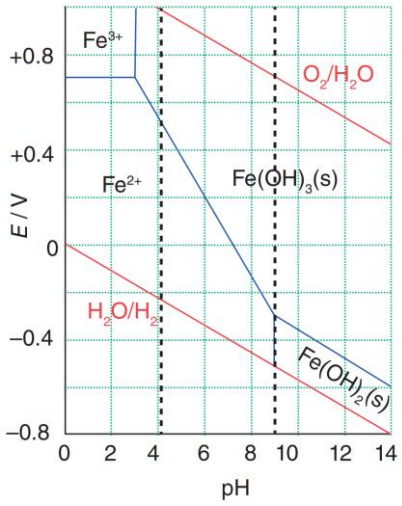


Figure 13 – Pourbaix diagram of iron in water[119]

In aqueous solution, however, redox potential alone does not fully describe iron speciation, since proton activity and hydrolysis must also be considered. This relationship is illustrated by the Pourbaix diagram in Figure 13, which maps the thermodynamically favoured forms of iron as a function of electrode potential and pH. Under reducing conditions, soluble Fe^{2+} is favoured over a comparatively broad pH range, whereas increasing potential favours Fe^{3+}; however, as the pH increases, free aqueous Fe^{3+} becomes progressively less favourable relative to hydrolysed and condensed Fe(III) species, including poorly soluble iron(III) oxides and hydroxides. The diagram therefore emphasises that the terms Fe^{2+} and Fe^{3+} describe oxidation states rather than unique aqueous species, and that both redox potential and pH must be considered when discussing their stability and solution behaviour.

This redox activity is fundamental to a wide range of biological processes, including oxygen transport, electron transfer, and catalytic transformations. However, it also introduces complexity in coordination behaviour, as ligand binding can both

influence and be influenced by the oxidation state of the metal centre. [2, 28, 43]

Coordination geometry in iron complexes is most commonly octahedral, although deviations can occur depending on ligand constraints and electronic configuration. For instance, low-spin Fe^{2+} complexes often adopt more rigid and symmetric geometries, while high-spin species may display greater structural flexibility. Furthermore, changes in coordination number and geometry can accompany redox transitions, adding an additional layer of dynamic behaviour to iron-containing systems. [13]

From a kinetic perspective, Fe^{2+} complexes are generally more labile than their Fe^{3+} counterparts, undergoing rapid ligand exchange in aqueous environments. This lability is particularly relevant in the context of labile iron pools, where loosely coordinated Fe^{2+} species can interact transiently with a variety of biomolecules.[2] In contrast, Fe^{3+} complexes often exhibit greater kinetic stability, especially when incorporated into multidentate ligand frameworks or protein active sites.[81]

The interplay between oxidation state, ligand environment, and coordination dynamics is especially significant in the context of paramagnetism and imaging applications. Both Fe^{2+} and Fe^{3+} are typically paramagnetic in their high-spin forms, contributing to local magnetic field perturbations. However, their magnetic properties are highly context-dependent, varying with spin state and coordination environment.[82, 88] This variability presents both a challenge and an opportunity: while it complicates direct interpretation, it also enables the development of responsive systems that reflect underlying biochemical conditions.

Taken together, iron coordination chemistry is characterised by a high degree of adaptability, arising from its accessible redox states, variable spin configurations, and flexible coordination environments. A detailed understanding of these factors is essential for interpreting iron behaviour in biological systems and for designing probes capable of selectively interacting with specific iron species, particularly in the context of detecting labile or transient forms of iron in vivo.[120]

1.2.7. Iron-binding chelators

Building on the coordination preferences of iron described above, chelating ligands provide a means of stabilising iron through simultaneous coordination by two or more donor atoms. For Fe^{3+}, established chelating groups are dominated by oxygen-containing donors, including catecholates, hydroxamates, hydroxypyridinones and aminocarboxylates. Catecholates, for example, provide two adjacent oxygen donors with high electron density and can form stable bidentate complexes with ferric iron. Hydroxamates and hydroxypyridinones similarly provide O,O-donor environments and are widely represented among synthetic chelators and naturally occurring siderophores. These examples demonstrate that appropriately arranged oxygen-donor groups provide an important structural basis for Fe^{3+} coordination.[121]

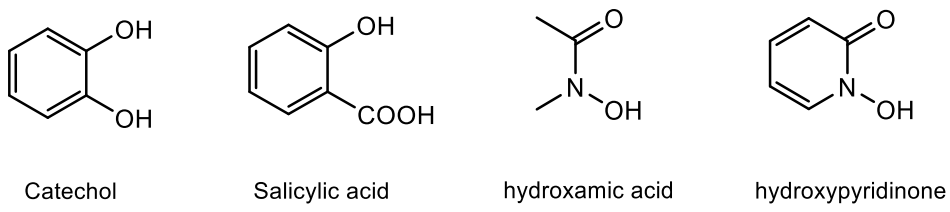
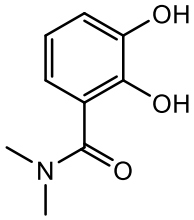
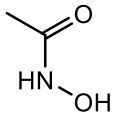
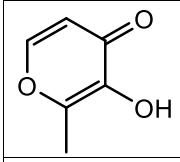
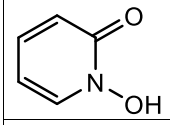
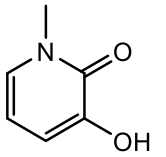
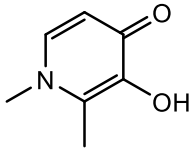
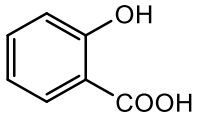


Figure 14 – Some representative Iron-binding motifs

Table 3 – Literature pKa and affinity values of iron binding motif[121]. The literature pFe was defined as the -log[Fe^{3+}], where $[Fe^{3+}]_{total}$ = 1 μM; $[ligand]_{total}$ = 10 μM

Structure	Name	pKa_1	pKa_2	$log\beta_3$	pFe^{3+}
	N,N-Dimethyl-2,3-dihydroxybenzamide	8.4	12.1	40.2	15
	Acetohydroxamic acid	-	9.4	28.3	13
	Maltol	-	8.7	28.5	15
	1-Hydroxypyridin-2-one	-	5.8	27	16
	1-Methyl-3-hydroxy-pyridin-2-one	0.2	8.6	32	16
	deferiprone	3.6	9.9	37.2	20
	Salicylic acid	3.0	13.6	-	-

$$\beta_3 = \frac{[\mathrm{FeL_3}]}{[\mathrm{Fe^{3+}}][L]^3}$$

The effectiveness of an iron-binding ligand, however, depends on more than donor identity alone. Ligand denticity and the number of chelate rings formed can substantially influence thermodynamic stability. For six-coordinate Fe^{3+}, several bidentate ligands may satisfy the coordination sphere independently, whereas incorporation of multiple donor atoms within a single multidentate framework can

increase complex stability through the chelate effect. In ferric chelator systems, a general stability trend of hexadentate > tridentate > bidentate has been reported, with five- and six-membered chelate rings being particularly favourable. [121] The spatial organisation of these donor groups is also important. Studies of tris-catecholamide ligands have shown that changes in ligand architecture can substantially alter Fe^{3+} binding even when the nature of the donor groups is retained. Preorganisation and geometric complementarity can therefore favour binding by positioning the donor atoms close to the arrangement required by the metal centre and reducing the structural reorganisation associated with complex formation. [122] Protonation provides an additional consideration, particularly for phenolic oxygen donors: increased donor basicity may favour Fe^{3+} coordination but also increases competition from H^+. Consequently, iron-binding affinity is inherently dependent on solution conditions such as pH and cannot be assessed solely from the identity of the coordinating group. [121]

A distinction must also be made between affinity and selectivity. A ligand may form a highly stable Fe^{3+} complex without being selective for iron if similarly favourable complexes are formed with competing metal ions; aminocarboxylate chelators provide an example of strong Fe^{3+} binding accompanied by relatively poor metal selectivity. [121] Thus, selectivity depends on the relative compatibility of the ligand with different metal ions, incorporating donor preference together with factors such as geometry and ligand architecture. Oxidation state introduces a further distinction. Fe^{2+} has a lower charge density than Fe^{3+} and therefore shows less pronounced

preference for hard oxygen donors, allowing softer donor environments to become more competitive. Ward and co-workers demonstrated this directly using a ligand containing both salicylamide O,O- and bipyridine N,N-donor sites: Fe^{3+} preferentially occupied the harder salicylamide environment, whereas Fe^{2+} favoured the softer bipyridine site. [123]

Catecholate and salicylate systems provide particularly well-established examples of ferric O,O-donor chemistry. Catechol-derived ligands coordinate Fe^{3+} through adjacent phenolic oxygen atoms and can form highly stable ferric complexes; this coordination motif is also widely employed by natural siderophores for iron acquisition.[124, 125] Salicylate and salicylamide groups provide a related O,O-donor arrangement, and ferric coordination by these motifs has been demonstrated both through equilibrium studies of salicylic acid derivatives and through structural characterisation of multidentate tris-salicylate systems.[126, 127] Together with hydroxamates, hydroxypyridinones and related donor groups, these studies illustrate how donor identity, denticity, preorganisation and protonation collectively determine the ability of a ligand to bind iron, while metal selectivity must ultimately be considered relative to competing ions and the oxidation state of the metal.

1.3. NMR & MRI

1.3.1. History and Nobel prizes

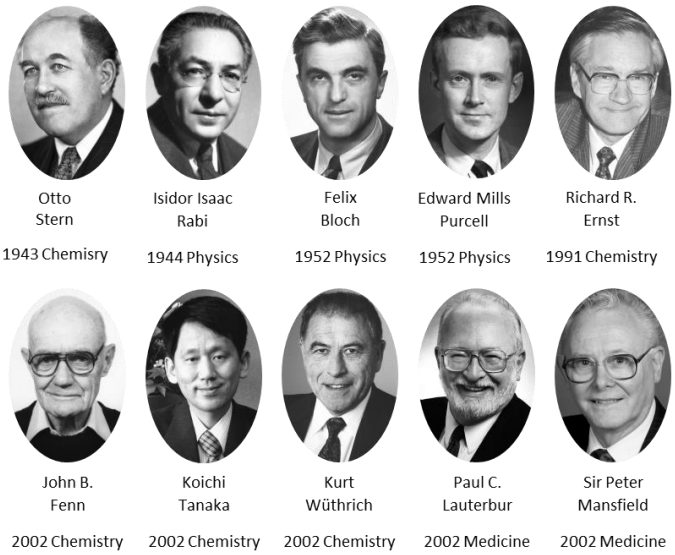


Figure 15 – Nobel Prize winners related to NMR and MRI

Nuclear magnetic resonance developed during the mid-20th century from early demonstrations of nuclear resonance to the practical observation of NMR in condensed matter by Bloch and Purcell. Subsequent developments, including Fourier-transform methods, established NMR as a major analytical technique for molecular structure determination. The later introduction of magnetic-field gradients enabled spatial encoding of the NMR signal, extending the same physical principles to magnetic resonance imaging. Central to both techniques is the behaviour of nuclear magnetisation following radiofrequency excitation, particularly the processes of longitudinal and transverse relaxation. These principles form the basis of MRI signal generation and contrast and are considered in the following sections.[103, 128]

1.3.2. Mechanisms

At its simplest, nuclear magnetic resonance (NMR) and magnetic resonance imaging (MRI) can be understood by picturing nuclei as tiny bar magnets. When these nuclei are placed in a strong external magnetic field, the majority orient in line with the field, while a smaller fraction point in the opposite direction. The difference between these two populations is extraordinarily small—only a few spins per million—but when multiplied across the vast number of nuclei in biological tissue, it produces a detectable bulk magnetisation.[129, 130] This simple imbalance, created by the magnetic field and sustained by thermal energy, is the origin of measurable NMR and MRI signals. By applying brief pulses of radiofrequency (RF) energy, this equilibrium can be perturbed, and the subsequent evolution of the nuclear magnetisation generates signals that can be detected and analysed. In spectroscopy, these signals contain molecular-level structural information, while in imaging, additional spatial encoding allows them to be transformed into spatially resolved maps of tissue contrast. [128, 130]

The simple picture of "nuclear magnets aligning with the field" can be described more formally in terms of nuclear spin and magnetic moment. For nuclei with non-zero spin, application of an external magnetic field, B_0, results in Zeeman splitting into discrete energy states. For a spin-1/2 nucleus such as the proton, two states exist and, at thermal equilibrium, are populated according to the Boltzmann distribution, yielding a slight excess of spins in the lower-energy state. Although this population difference is small, its collective effect produces a macroscopic equilibrium magnetisation vector, M_0, aligned along the applied field. [129-131]

The magnetisation precesses around the axis of the magnetic field at the Larmor frequency:

$$\omega_0 = \gamma B_0$$

Equation 7 –Larmor precession frequency of nuclear spins

where γ is the gyromagnetic ratio, a characteristic constant of the nucleus. This direct relationship between magnetic field and precession frequency is fundamental to both NMR and MRI. [128, 130]

The ability to manipulate and detect this magnetisation depends on the application of radiofrequency fields. An RF pulse applied at the Larmor frequency delivers energy to the spin system, tipping the magnetisation vector away from its equilibrium alignment. The resulting transverse magnetisation precesses about B_0 and induces a voltage in the receiver coil, producing the detectable MR signal. Following excitation, the disturbed magnetisation gradually returns towards equilibrium through two simultaneous but distinct processes: longitudinal and transverse relaxation. Longitudinal relaxation, characterised by the time constant T_1, describes recovery of the longitudinal component of magnetisation towards M_0 ; and Transverse relaxation is characterised by T_2 and describes the progressive loss of phase coherence among spins in the transverse plane:

$$M_z(t) = M_0\left(1 - e^{-t/T_1}\right)$$
$$M_{xy}(t) = M_{xy}(0)\, e^{-t/T_2}$$

Equation 8 – Longitudinal (T_1) and transverse (T_2) relaxation decay[129]

Although both processes occur simultaneously, they arise from different physical

mechanisms, and their relative magnitudes vary between tissues and molecular environments. In practice, the rates $R_1 = 1/T_1$ and $R_2 = 1/T_2$ are frequently employed, as independent contributions to relaxation rates can often be treated additively. The evolution of the magnetisation under the influence of applied magnetic fields and relaxation is described more generally by the Bloch equations; however, for the present work, the experimentally relevant quantities are principally T_1, T_2 and their corresponding relaxation rates. [129]

Whereas these principles describe the generation and relaxation of an MR signal, formation of an image additionally requires the spatial origin of that signal to be encoded. If all nuclei experienced an identical B_0, equivalent protons at different positions would precess at the same Larmor frequency and could not be spatially distinguished. MRI overcomes this limitation by applying linear magnetic-field gradients along three orthogonal spatial directions, conventionally denoted x, y, and z. These gradients introduce small, controlled variations in magnetic field strength with position. For example, for a gradient G_x applied alo*ng the x-direction,*

$$B(x) = B_0 + G_x\, x$$

$$\omega(x) = \gamma(B_0 + G_x x)$$

Equation 10 – Position-dependent magnetic field and Larmor frequency during spatial encoding.[132]

Thus, nuclei at different positions experience slightly different magnetic fields and consequently acquire position-dependent frequencies or phases. This provides the physical basis for spatial localisation in MRI.

For conventional two-dimensional imaging, the three spatial dimensions can be considered separately. The z-direction is commonly used for slice selection, determining which plane of the sample is imaged. A magnetic-field gradient G_z is applied simultaneously with an RF pulse, causing the Larmor frequency to vary with position along z. The RF pulse excites only the range of frequencies within its defined bandwidth and therefore only the corresponding range of z-positions, producing a slice of finite thickness. The centre frequency of the RF pulse determines the position of the slice, while its bandwidth together with the gradient strength determines the slice thickness.

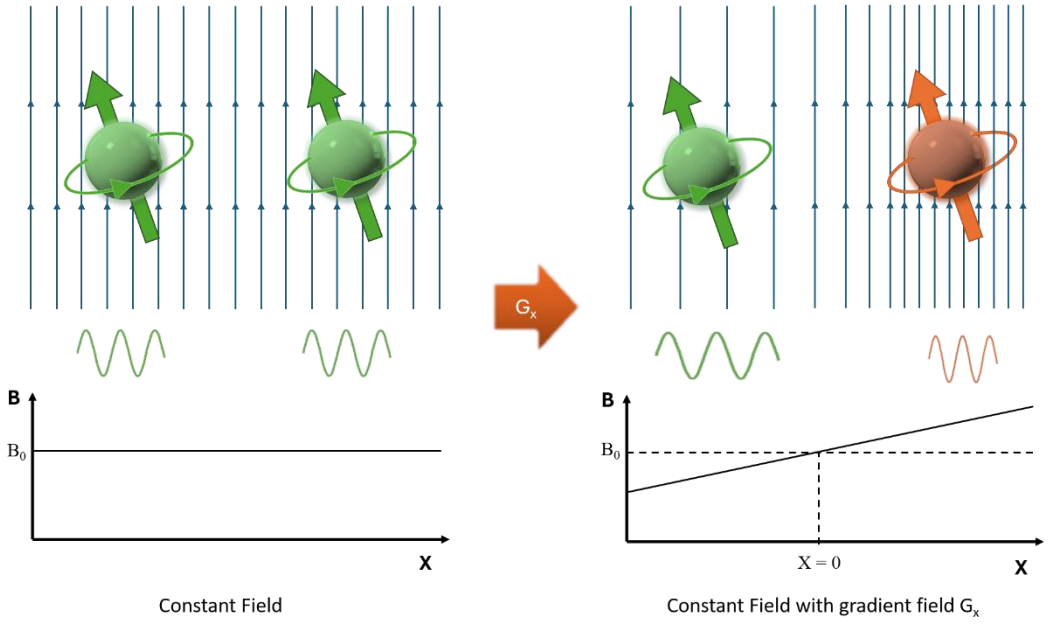


Figure 16 – Frequency encoding along the x-direction with an applied gradient field G_x. [132]

Within this selected xy-plane, the remaining two dimensions are spatially encoded independently. The x-direction is commonly assigned as the frequency-encoding, or readout, direction. Application of G_x during signal acquisition causes nuclei at different x-positions to precess at different frequencies; the frequency content of

the detected signal therefore provides positional information along this axis. The y-direction is commonly assigned as the phase-encoding direction. A gradient G_y is applied for a finite period before signal acquisition, during which nuclei at different y-positions precess at different instantaneous frequencies and consequently accumulate different phase shifts. After G_y is removed their frequencies return to their previous values, but the position-dependent phase differences remain. Repeating the measurement with systematically varied G_y strengths provides sufficient phase information to distinguish positions along the y-axis. The assignments of x, y, and z to frequency encoding, phase encoding, and slice selection are interchangeable in practice; they are used here simply to illustrate the three orthogonal components of spatial encoding.

Importantly, the scanner does not acquire an anatomical image directly. Instead, the frequency- and phase-encoded signals are sampled into k-space, a spatial-frequency representation of the imaged object. Individual points in k-space do not correspond directly to individual pixels in the final image; rather, each contains spatial-frequency information contributing to the reconstructed image as a whole. Once sufficient k-space data have been acquired, Fourier transformation converts this encoded information into spatial coordinates, producing an image composed of volume elements, or voxels. The signal intensity assigned to each voxel depends on the local proton signal and is influenced by proton density, T_1, T_2, and the parameters of the pulse sequence.[132]

1.3.3. Parameters and calculations

The concept of nuclear relaxation arises directly from the Bloch equations, which describe the time-dependent behaviour of the nuclear magnetisation vector under the influence of an external magnetic field. When an ensemble of nuclear spins is placed in a uniform magnetic field B_0, the spins tend to align with the field to form a bulk magnetisation M. After a perturbation, such as a radiofrequency pulse, this magnetisation does not instantaneously return to equilibrium but instead evolves gradually through characteristic exponential processes. [129, 130]

Longitudinal relaxation, characterised by T_1, describes the recovery of the z-component of magnetisation along the direction of the static magnetic field. It is often referred to as spin–lattice relaxation because it involves an exchange of energy between the nuclear spins and their surrounding molecular environment, or lattice. The recovery follows an exponential approach to equilibrium, expressed as

$$M_Z(t) = M_0(1 - e^{-\frac{t}{T_1}})$$

Equation 9 – Exponential recovery of longitudinal magnetisation $M_z(t)$ towards equilibrium M_0, governed by the relaxation time T_1 [129]

This equation defines T_1 as the time required for M_z to recover to approximately 63% of its equilibrium value after excitation. Physically, shorter T_1 values correspond to more efficient energy exchange between nuclear spins and their environment.

In contrast, transverse relaxation, characterised by T_2, describes the loss of phase coherence among spins precessing in the transverse plane. Although the magnitude

of the transverse magnetisation decays exponentially as

$$M_{xy}(t) = M_{xy}(0)e^{-\frac{t}{T_2}}$$

Equation 10 – Exponential decay of transverse magnetisation $M_{xy}(t)$ due to loss of phase coherence, characterised by the relaxation time T_2. [129]

this process does not involve net energy exchange with the lattice. Instead, it reflects stochastic variations in local magnetic fields that cause spins to precess at slightly different rates, leading to progressive dephasing. The transverse relaxation time $\boldsymbol{T_2}$ is therefore always shorter than or equal to $\boldsymbol{T_1}$, and the two together provide a complete description of the temporal evolution of magnetisation in the simplest case.

It is often convenient to describe relaxation in terms of rates rather than times, by defining the relaxation rates R_i as the reciprocals of the corresponding relaxation times.

This notation provides a linear measure of the efficiency of relaxation processes and simplifies the representation of multiple contributions, which can be considered additive. The observed relaxation rate thus quantifies how quickly magnetisation returns to equilibrium after perturbation. This linear formulation will later prove essential for expressing how the presence of paramagnetic species enhances relaxation and for deriving the concentration-dependent relationships used to define relaxivity.[115, 133]

In real systems, the observed relaxation of nuclear spins rarely arises solely from diamagnetic interactions. When unpaired electrons are present, as in the case of

paramagnetic ions or complexes, their strong magnetic moments create fluctuating local magnetic fields that couple efficiently with nearby nuclear spins. These interactions provide additional pathways for energy exchange and phase randomisation, thereby accelerating both longitudinal and transverse relaxation processes. The overall relaxation rate measured experimentally therefore contains contributions from both diamagnetic and paramagnetic mechanisms, and can be expressed as:

$$R_i^{obs} = R_i^{dia} + R_i^{para}$$

Equation 11 –Observed relaxation rate R_i^{obs} expressed as the sum of diamagnetic and paramagnetic contributions.[130]

where R_i^{obs} is the total measured relaxation rate, R_i^{dia} the intrinsic diamagnetic background, and R_i^{para} the additional contribution induced by the paramagnetic species. This additive formulation reflects the independence of different microscopic relaxation pathways and holds accurately under dilute conditions where mutual interactions between paramagnetic centres are negligible.

In dilute solutions, the paramagnetic contribution to the relaxation rate scales linearly with the concentration of the paramagnetic centres, giving

$$\mathrm{R_i^{para}} = \mathrm{r_i C}$$

Equation 12 – Paramagnetic relaxation rate R_i^{para} proportional to relaxivity r_i and contrast agent concentration C

where r_i is the relaxivity and C the molar concentration of the paramagnetic species. Relaxivity quantifies the efficiency with which a paramagnetic centre

enhances the relaxation of surrounding nuclei, typically water protons in the case of MRI contrast agents. Its units are $mM^{-1}\cdot s^{-1}$, corresponding to the increase in relaxation rate per millimolar concentration of the agent. The physical interpretation is straightforward: a higher r_i indicates that each paramagnetic ion perturbs the nearby nuclear magnetic environment more effectively, producing faster relaxation.[130]

By combining the diamagnetic and paramagnetic terms, the observed relaxation rate can be written as

$$\mathrm{R_i^{obs}} = \mathrm{R_i^{dia}} + \mathrm{r_i C}$$

Equation 13 - Observed relaxation rate R_i^{obs} increases linearly with contrast agent concentration, with slope r_i and intercept R_i^{dia}.

This simple yet powerful relation forms the empirical foundation for evaluating MRI contrast agents. It implies that, when other experimental parameters are held constant, plotting the measured relaxation rate against concentration yields a straight line whose slope corresponds to the relaxivity. This linear dependence not only provides a convenient means of characterising contrast efficiency but also offers insight into the molecular and electronic factors governing magnetic relaxation. [130]

The expression above serves as the practical form of the broader physical principle that underlies paramagnetic relaxation enhancement. Its validity stems from the fact that each paramagnetic centre acts as an independent relaxation sink for the surrounding nuclear spins, and their collective influence adds linearly in the low-concentration regime. At higher concentrations, where dipole–dipole interactions

among paramagnetic centres or cross-relaxation between sites become significant, deviations from linearity can occur. However, within the concentration range relevant to diagnostic and mechanistic studies, the linear approximation remains remarkably robust.[134]

The empirical form of Equation 13 - Observed relaxation rate R_i^{obs}increases linearly with contrast agent concentration, with slope $r_i$and intercept R_i^{dia}., thus bridges the microscopic dynamics described by relaxation theory and the macroscopic measurements obtained in NMR or MRI experiments. The next step in this framework is to examine the theoretical origins of this proportionality, which are captured by the Solomon–Bloembergen–Morgan (SBM) theory. This model provides a quantitative description of how the fluctuating magnetic fields associated with unpaired electron spins couple to nuclear spins through dipolar and contact interactions, establishing the physical basis for the observed concentration dependence of relaxation rates. [130]

The linear relationship between the observed relaxation rate and the concentration of paramagnetic species arises from the classical Solomon–Bloembergen–Morgan (SBM) theory, which provides a microscopic description of how unpaired electron spins accelerate nuclear relaxation. In this framework, the unpaired electrons of a paramagnetic ion create local magnetic fields that fluctuate in time due to molecular motion and electronic relaxation. These field fluctuations modulate the energy levels of nearby nuclei and provide efficient relaxation pathways through dipolar coupling between the electronic and nuclear magnetic moments.

According to the SBM model, the longitudinal and transverse relaxation rates are governed by the spectral density of these magnetic field fluctuations and depend on several key molecular parameters: the distance between the metal centre and the interacting nucleus, the rotational correlation time of the complex, and the electronic relaxation time of the unpaired electrons. Although the full mathematical expressions are lengthy, the essential outcome is that both $1/T_1$ and $1/T_2$ are directly proportional to the concentration of paramagnetic centres, the square of the magnetic moment, and the inverse sixth power of the metal–proton distance. The correlation time τ_c, which encompasses rotational motion and electron spin relaxation, determines the field dependence of relaxivity and explains why relaxation rates vary with magnetic field strength and temperature.

This model also distinguishes two mechanistic regimes of relaxation enhancement: the *inner-sphere* contribution, in which water molecules are directly coordinated to the metal centre, and the *outer-sphere* contribution, arising from water molecules that diffuse near but are not chemically bound to the complex. Both mechanisms contribute additively to the overall paramagnetic relaxation rate, reinforcing the empirical linear form $R_i^{para} = r_i C$. The relative magnitudes of these contributions depend on molecular structure, hydration number, and the dynamics of water exchange between bound and bulk states, which together define the effective relaxivity observed in solution.

In essence, the SBM framework provides the theoretical justification for the concentration dependence expressed in the previous section. It links measurable

parameters such as r_i to molecular and electronic properties of the contrast agent, bridging the gap between physical theory and experimental observation. The simplified linear expression therefore represents not a purely empirical relationship but a low-concentration limit of the more general SBM model, which remains the foundation for modern analyses of paramagnetic relaxation and contrast agent design.

Taken together, these theoretical principles define the physical origin of nuclear relaxation and its modulation by paramagnetic species. The Bloch equations provide a phenomenological description of how magnetisation returns to equilibrium, while the Solomon–Bloembergen–Morgan model supplies the microscopic interpretation that relates molecular motion and electronic properties to observable relaxation rates. The resulting linear relationship between relaxation rate and concentration offers a practical bridge between experiment and theory, allowing relaxivity to serve as a quantitative descriptor of contrast efficiency. In subsequent sections, this conceptual foundation will be applied to interpret the relaxation behaviour of the complexes investigated in this work.

1.3.4. Type of Images

Having established the theoretical framework of relaxation and its quantitative relationships, it is now necessary to distinguish between the different relaxation constants that govern the decay and recovery of magnetisation in magnetic resonance imaging. Although the Bloch equations describe relaxation

phenomenologically, the physical meaning and practical implications of each relaxation time, T_1, T_2, and T_2*, are distinct and deserve independent consideration. Understanding these differences is fundamental for interpreting MRI signal formation, image contrast, and sequence design.

In essence, T_1 and T_2 characterise two complementary processes by which the disturbed magnetisation returns to equilibrium. T_1, or longitudinal relaxation time, reflects the rate at which the z-component of magnetisation recovers along the direction of the main magnetic field through energy exchange with the surrounding lattice. T_2, or transverse relaxation time, represents the loss of phase coherence among spins precessing in the transverse plane, driven by microscopic fluctuations in local magnetic fields. T_2*, the apparent transverse relaxation time, further incorporates dephasing caused by macroscopic magnetic field inhomogeneity and susceptibility variations, which are not refocused by simple gradient-echo sequences.[135]

These relaxation constants not only determine how the nuclear magnetisation evolves over time but also dictate the brightness and contrast observed in MRI images. The degree to which a particular relaxation process influences the final image depends on the timing parameters of the pulse sequence—primarily the repetition time (TR) and the echo time (TE)—which selectively weight the contribution of T_1 and T_2 relaxation to the observed signal. Consequently, understanding the physical distinction between relaxation mechanisms and their imaging manifestations is essential for linking the underlying spin dynamics to the

macroscopic information conveyed by MRI.[136]

The process of longitudinal relaxation, described by the time constant T_1, reflects how the z-component of magnetisation recovers towards its equilibrium value following excitation. During an RF pulse, part of the bulk magnetisation is tipped away from alignment with the main magnetic field B_0. Once the pulse is turned off, the spins gradually release the absorbed energy to their molecular surroundings—a process often termed *spin–lattice relaxation*. This energy transfer allows the longitudinal magnetisation (M_z) to regrow exponentially according to $M_z(t) = M_0(1 - e^{-t/T_1})$. The efficiency of this relaxation depends strongly on the correlation between the frequency of molecular motion and the Larmor frequency: relaxation is most efficient when these frequencies are comparable, a condition typically met in liquids and soft tissues. Therefore, T_1 values vary across materials and magnetic field strengths, reflecting differences in molecular mobility and local magnetic environments.[129, 137]

In contrast, transverse relaxation, characterised by T_2, describes the progressive loss of phase coherence among spins precessing in the transverse plane. After excitation, all spins start in phase, producing a coherent transverse magnetisation that induces a detectable signal. However, local fluctuations in magnetic fields—arising from molecular interactions, dipole–dipole coupling, and diffusion through inhomogeneous regions—cause spins to precess at slightly different frequencies. As these phase differences accumulate, the transverse magnetisation decays exponentially as $M_{xy}(t) = M_{xy}(0)e^{-t/T_2}$. Unlike T_1 relaxation, this process does not

involve net energy exchange with the lattice but instead reflects a loss of coherence within the spin system itself. Because any mechanism that drives T_1 relaxation also introduces dephasing, T_2 is always shorter than or equal to T_1 for a given sample. [129, 137]

In practice, the measured transverse decay in an MRI experiment is often faster than that predicted by T_2 alone. This accelerated decay arises from larger-scale magnetic field variations across the sample, including those caused by imperfect shimming, tissue interfaces, or intrinsic magnetic susceptibility differences between materials. The combined effect of these microscopic and macroscopic sources of dephasing is expressed by the apparent transverse relaxation time, T_2^*, defined by the relation

$$\frac{1}{\mathrm{T}_2^*} = \frac{1}{\mathrm{T}_2} + \frac{1}{\mathrm{T}_{\mathrm{inh}}}$$

Equation 14 – Relationship between transverse relaxation components, where T_2^* reflects both intrinsic decay (T_2) and additional dephasing from magnetic field inhomogeneity.[138]

where T_{inh} represents the contribution from field inhomogeneity. Since this component is not refocused in gradient-echo sequences, T_2^* is always shorter than T_2. The presence of strong susceptibility gradients—such as those near air–tissue boundaries or metallic interfaces—can markedly accelerate signal loss, making T_2^* a sensitive indicator of magnetic field perturbations and tissue microstructure.

Together, these three relaxation constants describe complementary aspects of the same physical system: T_1 quantifies the recovery of longitudinal magnetisation through energy exchange, T_2 characterises the intrinsic loss of transverse coherence,

and T_2* incorporates additional dephasing from external field variations. Their interplay defines the temporal evolution of the MR signal, providing the physical basis for the various contrast mechanisms explored in MRI imaging.[128]

In practice, the relaxation times that determine image contrast can also be measured quantitatively. T_1 values are typically obtained using inversion recovery or variable flip angle methods, while T_2 and T_2* are derived from multi-echo spin-echo and gradient-echo acquisitions, respectively.[139] Fitting the signal evolution across multiple TR or TE values yields the corresponding relaxation curves, from which quantitative maps of T_1, T_2, or T_2* can be generated. These measurements convert qualitative image contrast into numerical parameters that reflect the intrinsic biophysical properties of tissues or materials.[66]

In summary, T_1, T_2, and T_2* describe complementary aspects of the magnetisation recovery and decay processes, and their influence on MRI signal intensity underlies all image contrast mechanisms. Understanding their distinct physical origins and imaging manifestations provides the necessary foundation for the quantitative evaluation of relaxation behaviour and, ultimately, for the interpretation of MRI-based measurements in experimental and clinical contexts.[139, 140]

1.3.5. Contrast agent chemistry and exploitation

The image contrast in magnetic resonance imaging arises primarily from the intrinsic differences in T_1 and T_2 relaxation times among tissues. These variations reflect underlying differences in water content, molecular composition, and local magnetic

environments. However, in many clinical and research settings, the natural range of relaxation times is insufficient to delineate fine structural details or to detect subtle pathological changes. The signal intensities of neighbouring tissues may overlap, resulting in poor diagnostic discrimination. Consequently, external contrast agents are employed to amplify these differences by locally modifying the relaxation rates of surrounding water protons.[87]

Contrast agents function by introducing local magnetic field perturbations that enhance the efficiency of nuclear spin relaxation. Through their strong magnetic moments, these agents accelerate the exchange of energy between nuclear spins and their environment, thereby shortening the relaxation times of nearby water molecules. This effect is particularly pronounced for T_1 relaxation, where an increase in the longitudinal relaxation rate ($R_1 = 1/T_1$) leads to a corresponding increase in signal intensity on T_1-weighted images. The resulting bright enhancement allows regions of agent accumulation — such as blood vessels, perfused tissues, or pathological lesions—to be visualised with greater clarity and sensitivity.

Two principal categories of contrast agents are recognised in MRI: T_1-type or *positive* agents, which shorten T_1 and increase signal brightness, and T_2-type or *negative* agents, which shorten T_2 and T_2*, causing local signal attenuation.[141] Among these, T_1 agents have achieved the widest clinical adoption due to their predictable and linear relaxivity behaviour, as well as their ability to enhance anatomical and vascular contrast without introducing image distortion. T_2 agents, often based on iron oxide nanoparticles, have been developed for specialised applications such as liver imaging

and cell tracking but are less commonly used in routine diagnostics.[71]

The following sections focus on the fundamental principles and chemical design of T_1 contrast agents, which remain the cornerstone of MRI enhancement. Their mechanism of action, molecular architecture, and industrial development exemplify how coordination chemistry, magnetic properties, and biomedical engineering converge to extend the capabilities of magnetic resonance imaging beyond the limits of intrinsic tissue contrast.[142]

The design of an effective T_1 contrast agent requires a delicate balance between magnetic efficiency, chemical stability, and biological safety. The majority of clinically approved agents are based on Gd^{3+}, whose seven unpaired electrons (S = 7/2) provide a strong magnetic moment and exceptionally high paramagnetic relaxation efficiency. Gadolinium is particularly well suited for this purpose because its electronic relaxation time is compatible with the Larmor frequency of water protons under clinical magnetic field strengths, enabling efficient dipolar coupling. However, the free Gd^{3+} ion is highly toxic owing to its strong affinity for biological anions such as phosphate and carbonate, which can lead to displacement of essential metal ions in vivo.[114] Consequently, all Gd-based agents must employ thermodynamically and kinetically stable chelating ligands that prevent metal release while maintaining access of water molecules to the coordination sphere.[83]

Two principal classes of Gd^{3+} chelates have been developed: linear and macrocyclic complexes. Linear ligands, such as diethylenetriaminepentaacetic acid (DTPA), form open-chain structures that wrap around the metal ion but offer limited rigidity.

Although their relaxivity is typically high due to favourable water exchange kinetics, the relatively lower kinetic stability of linear chelates increases the risk of trans-metalation and gadolinium release.[143] Macrocyclic ligands, exemplified by 1,4,7,10-tetraazacyclododecane derivatives such as DOTA and DO3A, encapsulate the Gd^{3+} ion within a pre-organised cyclic cavity.[144] This architecture confers superior thermodynamic stability and kinetic inertness, substantially reducing the potential for dissociation under physiological conditions. The trade-off is often a slower rate of inner-sphere water exchange, which can modestly reduce relaxivity. Modern agent design therefore seeks to fine-tune these opposing factors by introducing pendant arms or modifying donor groups to accelerate exchange without compromising complex stability. [143]

Several molecular parameters determine the overall relaxivity of a chelated complex. The number of coordinated water molecules (q) in the inner sphere directly influences the magnitude of relaxation enhancement, while the residence time of these water molecules (τ_m) and the rotational correlation time (τ_r) control the efficiency of magnetic field modulation. Strategies to increase relaxivity include the incorporation of bulky substituents or macromolecular attachments—such as albumin-binding groups or polymer conjugation—to slow molecular tumbling and thus extend τ_r. Alternatively, design modifications that slightly weaken the metal–water bond can accelerate water exchange, optimising τ_m towards the SBM ideal where ω_Hτ_c ≈ 1.[101] In practice, high-performance agents achieve relaxivity values (r_1) in the range of 4–6 $mM^{-1}{\cdot}s^{-1}$ at 1.5 T, though newer macrocyclic and protein-

targeted systems can exceed 10 $mM^{-1} \cdot s^{-1}$.[98, 144]

Manganese(II) (Mn^{2+}) complexes have been explored as alternative T_1 agents due to manganese's essential biological role and strong paramagnetic character (S = 5/2). While their inherent relaxivity can rival that of gadolinium, Mn-based agents often suffer from limited chemical stability and variable oxidation states, complicating formulation and safety control. To mitigate these issues, macrocyclic ligands similar to those used for gadolinium have been adapted to stabilise Mn^{2+}, producing compounds such as Mn-DPDP (mangafodipir), which was previously approved for liver imaging. Although its clinical use has declined, manganese-based chemistry continues to inspire the development of biodegradable or responsive agents aimed at reducing the reliance on gadolinium.[114, 133]

Beyond these conventional small-molecule chelates, current research explores innovative architectures to further improve relaxivity and functionality. Examples include multimeric complexes, dendrimer conjugates, and nanoparticle hybrids that slow molecular motion through increased molecular weight, as well as responsive systems that alter their magnetic properties in response to local biochemical stimuli such as pH, enzymatic activity, or redox state. These approaches exemplify how molecular engineering can extend the capabilities of classical T_1 agents, linking coordination chemistry to the broader goals of precision imaging and targeted diagnostics.

Since their introduction in the late 1980s, gadolinium-based T_1 contrast agents have become indispensable tools in clinical MRI, accounting for the overwhelming

majority of all contrast-enhanced scans worldwide. Their success stems from the reproducible linear relationship between relaxivity and concentration, the high magnetic efficiency of Gd^{3+}, and the ability of well-designed chelating ligands to ensure both stability and biological tolerance.[145] The first generation of commercial agents, such as gadopentetate dimeglumine (Magnevist, Bayer) and gadoterate meglumine (Dotarem, Guerbet), established the clinical utility of contrast enhancement in neuroimaging, angiography, and oncological diagnostics.[144] These early agents were largely based on linear or macrocyclic polyaminocarboxylate ligands, designed to balance rapid renal clearance with adequate in vivo stability.[72]

Over time, safety considerations have reshaped the landscape of MRI contrast agent development. Reports of nephrogenic systemic fibrosis (NSF) in patients with severe renal impairment and growing evidence of long-term gadolinium deposition in tissues prompted a regulatory shift towards more stable macrocyclic complexes. These agents—such as gadobutrol (Gadovist, Bayer), gadoterate (Dotarem, Guerbet), and gadoteridol (ProHance, Bracco)—exhibit superior kinetic inertness, minimal transmetallation risk, and consistent relaxivity across a broad range of physiological conditions. As a result, macrocyclic formulations have become the global standard of care and are recommended by both the U.S. Food and Drug Administration (FDA) and the European Medicines Agency (EMA) as the preferred class for routine use.[144]

Beyond the classical Gd chelates, efforts to develop alternative and next-generation T_1 agents continue to expand. Manganese-based agents, exemplified by Mangafodipir (Teslascan), demonstrated the potential of biologically essential

metals but were discontinued due to formulation challenges and limited market demand. Nonetheless, manganese chemistry remains an active area of research, particularly for biodegradable or activatable probes.[146] More recently, high-relaxivity macrocyclic agents such as gadopiclenol have entered clinical evaluation, representing an evolutionary step towards higher contrast efficiency at lower administered doses. Concurrently, targeted and responsive contrast agents are being investigated for molecular imaging applications, enabling detection of specific biochemical processes rather than purely anatomical features.[147]

By comparison, T_2 and T_2*-type agents—most notably superparamagnetic iron oxide nanoparticles (SPIONs)—have achieved only niche clinical use. Their strong magnetic susceptibility produces pronounced negative contrast, making them useful for liver imaging and macrophage tracking but less versatile for general diagnostic imaging. Commercial products such as Feridex (Berlex Imaging) and Resovist (Bayer) have since been withdrawn from the market, although research continues into new formulations for cell labelling and theranostic applications.[148]

Today, the MRI contrast agent industry is dominated by a small number of multinational pharmaceutical companies, with Bayer, Guerbet, and Bracco as leading suppliers. The global market continues to evolve towards safer, more efficient, and more specialised agents. Current development trends include increasing relaxivity through molecular or macromolecular design, reducing gadolinium dosage without compromising image quality, and exploring responsive or multimodal systems that integrate MRI with complementary imaging techniques such as positron emission

tomography (PET) or optical fluorescence.[78] These innovations reflect a broader shift in MRI contrast research—from generic enhancement towards functional and molecular specificity—while retaining the fundamental T_1 relaxation mechanism as the cornerstone of image contrast modulation.[149]

Contrast agents extend the capabilities of magnetic resonance imaging beyond the intrinsic limitations of tissue relaxation differences, providing a powerful means to amplify signal intensity and enhance diagnostic precision. Among them, gadolinium-based T_1 agents remain the cornerstone of clinical MRI due to their strong paramagnetic properties, predictable relaxivity, and well-established safety profiles when stabilised within macrocyclic chelates.[88, 144] Their design embodies the convergence of coordination chemistry, molecular dynamics, and biocompatibility, translating the principles of nuclear spin relaxation into tangible clinical utility.[65, 150]

Over three decades of industrial and clinical development have refined these agents from the early linear chelates to the highly stable macrocyclic formulations that now dominate the market. This evolution reflects a continual balancing of competing priorities: maximising relaxivity while minimising toxicity, improving molecular efficiency while ensuring rapid elimination, and enhancing image quality while adhering to stringent safety regulations. The current generation of T_1 agents represents the outcome of these design optimisations, offering consistent performance across a wide range of diagnostic applications.

Looking forward, the field is shifting towards contrast agents that deliver more than simple anatomical enhancement. New strategies aim to integrate responsiveness,

targeting, and multimodality into contrast design, enabling the detection of specific molecular events and physiological states. The pursuit of higher relaxivity at lower doses, together with increasing interest in biocompatible metal centres such as manganese, underscores the ongoing drive to improve both efficacy and safety. Ultimately, the next generation of MRI contrast agents will build upon the same physical principles of spin relaxation that underpin current practice, but with the added sophistication of chemical and biological selectivity.[151, 152]

1.3.6. Clinical MRI

Magnetic resonance imaging (MRI) has evolved into a central tool in both clinical diagnostics and biomedical research, yet the operational context, experimental constraints, and achievable performance differ substantially between human imaging and preclinical systems. In clinical practice, MRI is typically performed at magnetic field strengths of 1.5 T or 3 T, with 7 T systems increasingly emerging in specialised centres. These field strengths represent a balance between signal-to-noise ratio, acquisition time, hardware limitations, and, critically, patient safety and regulatory constraints.[140, 148] By contrast, preclinical MRI systems used in research settings, particularly for small animal imaging such as mice, commonly operate at significantly higher magnetic fields, typically in the range of 7–14 T or above.[72] The use of higher fields in preclinical systems enables increased sensitivity and spatial resolution, which are essential for imaging small anatomical structures and detecting subtle contrast changes in limited sample volumes.

Despite these differences, the fundamental physical principles governing MRI remain consistent across clinical and research environments. Signal generation arises from nuclear spin relaxation, and contrast is primarily modulated through differences in longitudinal (T_1) and transverse (T_2) relaxation properties of tissues. However, the translation between clinical and preclinical MRI is non-trivial.[153] Higher magnetic field strengths in preclinical systems lead to altered relaxation behaviour, changes in relaxivity profiles of contrast agents, and increased susceptibility effects, meaning that quantitative results obtained in animal models cannot be directly extrapolated to clinical settings without careful consideration.[83] Furthermore, experimental design differs significantly: clinical MRI prioritises robustness, reproducibility, and patient throughput, whereas research MRI allows greater flexibility in acquisition parameters, sequence optimisation, and experimental manipulation, including the use of custom pulse sequences and non-standard imaging protocols.[154]

The current state-of-the-art in MRI continues to push both spatial and functional boundaries. Clinically, ultra-high-field MRI at 7 T enables sub-millimetre spatial resolution and improved contrast in neurological imaging, while advanced techniques such as quantitative mapping, diffusion imaging, and functional MRI provide increasingly rich physiological information. In research settings, even higher field strengths, combined with specialised coils and optimised sequences, allow imaging at near cellular or microstructural resolution in small animal models. These advances are accompanied by increasingly sophisticated data analysis frameworks, including parametric mapping and dynamic imaging, which enable temporal and

functional characterisation of biological systems. [72]

The role of contrast agents further highlights the divergence and overlap between clinical and research MRI. In clinical practice, gadolinium-based contrast agents (GBCAs) are administered under strict regulatory control, with dosing typically standardised on a body-weight basis (commonly around 0.1 mmol kg^{-1} for most extracellular agents).[155] These agents are required to meet stringent criteria, including high thermodynamic stability, kinetic inertness, rapid clearance, and minimal toxicity. Their clinical utility lies primarily in enhancing lesion visibility through non-specific mechanisms related to perfusion, vascular permeability, and extracellular distribution.[83] In contrast, research applications frequently employ a broader range of contrast strategies, including higher local concentrations, modified dosing regimens, and experimental agents that may not yet meet clinical safety requirements. In small animal studies, doses are often adjusted not only for body weight but also for experimental sensitivity, and higher effective concentrations are commonly used to ensure detectable signal changes within limited voxel sizes.[153]

Importantly, the behaviour of contrast agents is strongly dependent on both the magnetic field strength and the biological environment. Relaxivity, which defines the efficiency of a contrast agent in modulating proton relaxation, is not an intrinsic constant but varies with field strength, molecular dynamics, and water exchange kinetics. As a result, contrast agents optimised for clinical field strengths may exhibit different performance profiles in preclinical systems, and vice versa.[152] This discrepancy is particularly relevant for the development of novel molecular probes,

where proof-of-concept studies are typically conducted in high-field preclinical systems before translation to lower-field clinical environments.[92]

In addition to differences in performance, safety considerations impose a fundamental distinction between clinical and research contrast agent use. Clinically approved GBCAs must demonstrate minimal toxicity and negligible metal release under physiological conditions.[154] Nevertheless, concerns regarding gadolinium retention in tissues and the risk of nephrogenic systemic fibrosis (NSF) in patients with impaired renal function have prompted ongoing reassessment of their safety profile.[156, 157] In contrast, research studies can explore a wider chemical space, including systems with altered coordination environments, responsive functionalities, or multi-metal architectures, which may not yet satisfy clinical safety requirements but provide valuable insight into mechanistic behaviour.[141, 158]

Taken together, clinical and research MRI share a common physical foundation but differ substantially in operational constraints, achievable resolution, and contrast agent design.[148] Clinical MRI prioritises safety, reproducibility, and translational robustness, whereas research MRI emphasises sensitivity, flexibility, and mechanistic exploration. Bridging these two domains is essential for the development of next-generation MRI contrast agents, particularly those designed to report on specific biochemical processes. In this context, understanding how contrast behaviour varies with field strength, dosing, and biological environment is critical for translating molecular imaging strategies from preclinical models to clinical application.

1.3.7. Studies on probing MRI contrast agents

Magnetic resonance imaging, despite its clinical success, remains fundamentally limited in its ability to report directly on specific molecular or biochemical processes. This limitation has motivated the development of so-called “probing” or responsive MRI contrast agents, which are designed to translate defined chemical interactions into measurable changes in relaxivity, thereby enabling functional or molecular-level imaging. In contrast to conventional gadolinium-based contrast agents, whose signal enhancement arises from passive distribution and non-specific physiological effects, probing agents rely on modulation of key physicochemical parameters such as coordination environment, hydration number (q), water exchange kinetics, or molecular tumbling, in response to a specific stimulus.[65, 69]

Over the past two decades, a range of responsive MRI probes has been reported, targeting diverse analytes including metal ions, pH, enzymatic activity, redox state, and metabolites. Early work in this area demonstrated that ligand design could be used to control access of water molecules to the inner coordination sphere of a Gd^{3+} centre, thereby modulating relaxivity upon analyte binding. For example, systems incorporating pendant binding groups have been developed to respond to biologically relevant metal ions such as Ca^{2+}, Zn^{2+}, and Cu^{2+}, where metal coordination induces structural or dynamic changes that alter proton relaxation efficiency.[152, 159]

Among these systems, Ca^{2+}-responsive agents represent one of the earliest and most

extensively studied classes. These probes typically combine a Gd^{3+} chelate with a calcium-binding moiety such as BAPTA, where Ca^{2+} binding alters the coordination environment of the gadolinium centre, often by displacing donor atoms and increasing water accessibility, resulting in an increase in relaxivity. Similarly, Zn^{2+}-responsive probes have been developed to monitor zinc secretion in biological systems, including pancreatic β-cells, where binding-induced changes in hydration or protein association lead to measurable MRI contrast changes.[160] These examples demonstrate that, in principle, MRI can be extended beyond anatomical imaging to report on specific chemical events.[92]

In addition to metal ion sensing, enzyme-responsive MRI contrast agents have been explored as a means of detecting biological activity. In such systems, enzymatic cleavage of a masking group can trigger a change in molecular structure, often leading to altered water accessibility or increased molecular size, thereby enhancing relaxivity. Redox-responsive agents have also been developed, where changes in oxidation state influence either the coordination chemistry of the paramagnetic centre or the accessibility of water molecules, enabling detection of oxidative stress or hypoxic environments.[161] However, while these systems are conceptually powerful, their translation to in vivo applications remains challenging due to issues of sensitivity, specificity, and competing background effects.[160]

Despite these advances, the majority of reported probing MRI contrast agents remain at the proof-of-concept stage, with relatively few systems achieving robust performance in complex biological environments. One of the central challenges lies

in the inherently low sensitivity of MRI compared to optical or nuclear imaging techniques.[92] As a result, the signal change associated with a specific molecular interaction must be sufficiently large to be distinguished from background variation in tissue relaxation properties. This requirement places stringent constraints on probe design, particularly in terms of achieving significant relaxivity modulation upon analyte binding.[162, 163]

Another key limitation is the difficulty of achieving true chemical specificity in vivo. Many responsive systems rely on changes in coordination chemistry that may be influenced by multiple competing species in biological environments, including endogenous metal ions, proteins, and small molecules.[66, 164] Consequently, observed signal changes may not be uniquely attributable to the target analyte, complicating interpretation. These challenges are particularly pronounced for transition metal ions, where complex speciation and redox behaviour further limit the selectivity of probe–analyte interactions.

In this context, iron represents a particularly important yet underdeveloped target for probing MRI. Iron is central to numerous physiological processes, including oxygen transport, mitochondrial respiration, and redox regulation, and its dysregulation is implicated in a wide range of diseases. However, the biologically relevant fraction of iron, often referred to as the labile iron pool, is chemically heterogeneous, dynamically regulated, and present at relatively low concentrations. To date, there is no clinically established small-molecule MRI contrast agent capable of directly detecting this pool with specificity.

Several studies have attempted to address this challenge by incorporating iron-binding motifs into gadolinium-based probes, with the aim of converting probe–iron association into a measurable change in relaxivity. In such systems, iron binding may influence relaxivity through multiple mechanisms, including direct paramagnetic coupling, changes in molecular tumbling, or alteration of water exchange dynamics. However, distinguishing these effects from simple additive relaxation contributions remains non-trivial, and robust mechanistic interpretation is often lacking.[165, 166]

Taken together, while significant progress has been made in the design of responsive MRI contrast agents, the field remains limited by challenges in sensitivity, specificity, and mechanistic clarity. In particular, the development of probes capable of selectively detecting iron in biologically relevant contexts remains an open problem. Addressing this challenge requires not only advances in ligand design, but also a framework for interpreting relaxometry behaviour in systems where multiple species and interactions contribute to the observed signal. The work presented in this thesis aims to contribute to this area by developing and analysing gadolinium-based probes that respond to iron through interaction-dependent relaxivity changes.[163, 167]

2. Concept of an iron-specific contrast agent

2.1. Design rationale for iron-responsive Gd complexes

Iron is indispensable for cellular metabolism, oxygen transport, and mitochondrial respiration. However, dysregulation of iron homeostasis underlies a wide spectrum of pathological conditions, including neurodegeneration, cardiomyopathy, anaemia of chronic disease, infection, and cancer. In particular, the intracellular labile iron pool represents a dynamic and redox-active fraction of iron that participates directly in Fenton chemistry and oxidative signalling.[27, 28]

Despite its biological importance, the labile iron pool remains difficult to quantify non-invasively. Existing clinical imaging modalities primarily detect iron indirectly, most commonly through T_2 or T_2* signal attenuation caused by magnetic susceptibility effects of iron deposits. While such approaches are valuable for assessing bulk iron overload, they lack molecular specificity and are insensitive to transient or compartmentalised iron fluctuations.[107]

Moreover, susceptibility-based methods predominantly report on aggregated or mineralised iron species rather than the bioavailable and kinetically labile fraction that is most closely linked to cellular dysfunction. Consequently, there remains an unmet need for imaging strategies capable of reporting dynamic, bioactive iron in vivo.[39, 168]

Gadolinium-based contrast agents are widely used in clinical MRI owing to their

strong T_1 shortening capability and favourable safety profile when chelated appropriately. Their relaxivity arises from well-established paramagnetic mechanisms that are sensitive to molecular environment, rotational dynamics, and electronic relaxation processes. Importantly, relaxivity is not a fixed property, but may be modulated by changes in coordination, proximity effects, or molecular assembly. [87]

Given that iron ions possess unpaired electrons and exhibit distinct magnetic and electronic characteristics, it is theoretically plausible that controlled interaction between a Gd-based complex and labile iron could alter relaxivity through changes in rotational dynamics and additional relaxation contributions associated with the proximal paramagnetic centre. Such a system would convert fluctuations in bioavailable iron into measurable T_1 contrast enhancement.[83, 169]

Therefore, guided by the biological importance of iron dysregulation and the paramagnetic tunability of Gd-based contrast agents, the present project adopts a rational modification strategy built upon the clinically established Dotarem® framework. GdDO3A-based derivatives are extensively commercialised owing to their high thermodynamic stability, kinetic inertness, and well-characterised relaxometry behaviour. These attributes provide a secure and translationally relevant platform for functional adaptation without compromising metal chelate integrity.[144]

Crucially, the design strategy was constrained by established determinants of relaxivity. The inner-sphere hydration number (q), water exchange kinetics (τM), and

rotational correlation time (τR) are known to govern longitudinal relaxivity. In the present design, structural modification was therefore intended to preserve the essential Gd^{3+} coordination environment and water accessibility, rather than generate responsiveness through deliberate alteration of the hydration state. For this reason, only a single pendant acetate arm of the DOTA macrocycle was replaced with an iron-binding functionality, while retaining the remaining coordination environment necessary for stable Gd^{3+} chelation and inner-sphere water access.

This asymmetric substitution introduces a secondary metal-binding site in defined spatial proximity to the paramagnetic centre, without fundamentally perturbing the Gd coordination core. If coordination of labile Fe^{2+} or Fe^{3+}, the resulting Gd–Fe assembly is hypothesised to alter rotational dynamics and local magnetic field fluctuations, thereby modulating relaxivity beyond that of the parent complex. Importantly, this approach seeks not to increase intrinsic relaxivity through increased hydration number, but to generate an emergent relaxation contribution arising from controlled paramagnetic proximity. [71]

2.2. Selection of Iron-Binding Motifs

In this project, SCA- and Cat- derived groups were selected as the pendant iron-recognition sites on the basis of their established O,O-donor coordination chemistry as discussed in Section 1.2.7. Both motifs were intended primarily to target Fe^{3+}, whose high charge density and hard Lewis acidity favour coordination by anionic oxygen donors. Cat- groups are well-established ferric-binding units in siderophore

chemistry, while SCA-derived ligands also display extensive Fe^{3+} coordination chemistry.[121]

Although SCA and Cat are both bidentate O,O-donor motifs, the chemical nature and protonation state of their donor atoms are substantially different. Catechol coordinates Fe^{3+} through two adjacent phenolate donors, forming a five-membered catecholate chelate. Both donor groups originate from phenolic OH groups; free catechol has reported values of approximately 9.2 and 13, such that both sites are predominantly protonated at physiological pH and ferric binding is strongly coupled to deprotonation.[121] In contrast, salicylate provides a mixed phenolate–carboxylate donor set. The carboxylic acid group of salicylic acid is substantially more acidic, whereas the phenolic group has a much higher of approximately 13–14; consequently, the carboxylate donor is already deprotonated at physiological pH while phenolate coordination remains coupled to proton loss.[126] Catecholate therefore provides two strongly basic phenolate donors once fully deprotonated, whereas SCA combines one strongly donating phenolate with a less basic but constitutively ionised carboxylate donor. These differences are expected to produce distinct pH-dependent and conditional Fe^{3+}-binding behaviour, without implying a priori that either complete probe has the higher affinity.

Importantly, the objective was not to maximise Fe^{3+} affinity. High-affinity multidentate chelators are deliberately used therapeutically to sequester and remove iron, whereas an imaging probe should ideally detect the labile iron pool without substantially perturbing it. Excessively strong binding could, in principle,

retain iron during probe clearance and result in unwanted iron removal. The desired recognition site should therefore bind sufficiently strongly to generate a measurable response, but retain the potential for reversible iron exchange. The use of individual bidentate pendant motifs was consistent with this requirement and avoided deliberately constructing a high-denticity iron-sequestering chelator.[2, 121]

A particularly relevant precedent was reported by Aime and co-workers using a Gd–DTPA derivative bearing peripheral salicylamide groups. In this system, Gd^{3+} remained bound within the central chelating framework while Fe^{3+} coordinated at the external salicylate-derived sites to form heterobimetallic species, which were characterised in part through water-proton relaxation measurements. This demonstrated that peripheral ferric coordination could be incorporated alongside a Gd-based relaxation centre and provided a direct conceptual precedent for the present probe architecture.[170]

Although Fe^{3+} was the principal coordination target, Fe^{2+} was also considered because both oxidation states contribute to biologically labile iron and O,O coordination of Fe^{2+} remains chemically possible. The lower charge density of Fe^{2+}, however, reduces the strong preference for hard oxygen donors observed for Fe^{3+}; oxidation-state-dependent donor preference has been demonstrated experimentally, with Fe^{3+} favouring salicylamide O,O sites while Fe^{2+} favoured softer bipyridine N,N donors. Fe^{2+} was therefore included as an experimentally relevant comparison rather than assumed to interact identically with the two recognition motifs. Likewise, affinity for Fe^{3+} was not taken to imply absolute metal selectivity,

which required subsequent experimental assessment against competing ions.

The GdSCA and GdCat complexes shown in Figure 17 were synthesised from a common DO3A-based scaffold through stepwise functionalisation with the corresponding SCA-/Cat-derived pendant group. The three acetate arms of DO3A were retained as ^{t}Bu-esters during this functionalisation, and the resulting protected ligands were treated as the principal purification checkpoint because their lower polarity allowed effective purification by repeated silica column chromatography. Purity at this stage was assessed primarily by ^{1}H NMR spectroscopy: the major resonances were required to be assignable to the proposed structure with appropriate relative integrations, with particular attention paid to the three diagnostic aromatic proton environments and the absence of significant unexplained peaks or shoulders. Following removal of the ^{t}Bu-ester protecting groups, the resulting DO3A-SCA and DO3A-Cat ligands were reassessed by NMR spectroscopy before complexation with Gd^{3+}. The final lanthanide complexes were purified by dialysis in earlier preparations and, subsequently, by semi-preparative HPLC, with analytical HPLC of the latter preparations showing a single detectable chromatographic peak under the conditions employed; mass spectrometry provided complementary confirmation of molecular identity. These sequential purification and analytical checks provided reasonable evidence that the compounds used in the subsequent binding and relaxometry studies were of sufficient purity for their interpretation. Full synthetic procedures, characterisation data, and a detailed discussion of the purification and purity-control strategy are provided in Chapter 7.

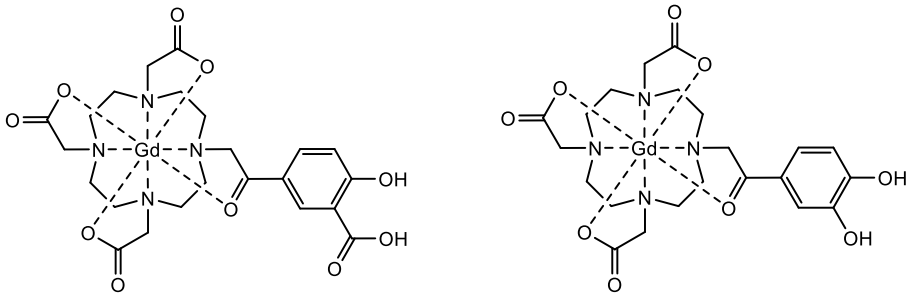


Figure 17 – Structure of GdSCA (left) and GdCat (right)

2.3. A Species-Resolved Relaxation Model for Gd–Fe Systems

2.3.1. Definition of Contributing Species

NB *in this Chapter, Gd may refer to Gd contrast agent rather than the element*

To analyse relaxivity modulation in an iron–contrast agent system, it is first necessary to define the molecular species present in solution. In an aqueous system containing a Gd-based contrast agent and labile iron, four principal species contribute to the observed longitudinal relaxation rate:

- bulk water molecules (diamagnetic background),
- the free Gd complex,
- free labile iron ions,
- the coordinated Gd–Fe adduct.

The experimentally observed longitudinal relaxation rate may therefore be expressed as the sum of these individual contributions: [116]

$$R_{1,obs} = R_{1,water} + R_{1,Gd} + R_{1,Fe} + R_{1,Gd-Fe}$$

$$R_{1,obs} = R_{1,water} + R_{1,Gd} + R_{1,Fe} + R_{1,Gd-Fe}$$

$R_{1,obs}$ Calculated longitudinal relaxation rate from the measured T1,
$R_{1,water}$ Relaxation rate from diamagnetic background contribution from bulk solvent,
$R_{1,Gd}$ Relaxation rate from the free Gd contrast agent,
$R_{1,Fe}$ Relaxation rate from free labile iron,
$R_{1,Gd-Fe}$ Relaxation rate from the coordinated Gd-complex–Fe species.

Equation 15 – Decomposition of the observed longitudinal relaxation rate into contributions from solvent background, free Gd contrast agent, free iron, and the associated Gd–Fe species.

Under dilute conditions typical for relaxometry measurements, each paramagnetic contribution can be expressed as the product of relaxivity and concentration: $R_{1,i} = r_{1,i}[i]$. Then, substitution into the expression above yields:

$$R_{1,obs} = R_{1,water} + r_{1,Gd}[Gd] + r_{1,Fe}[Fe] + r_{1,GdFe}[GdFe]$$

Equation 16 – Observed longitudinal relaxation rate $R_{1,obs}$ expressed as the sum of water baseline and contributions from Gd contrast agent, Fe, and Gd-Fe species.

This formulation provides a species-resolved description of the relaxation behaviour of the system.

2.3.2. Dynamic Equilibrium Between Species

In practice, the concentrations of these species are not independent but are governed by chemical equilibrium. Assume a ratio of 1:1 binding of the Fe ions and the Gd contrast agents, the coordination of iron to the contrast agent may be described by the reversible binding process:

$$\mathrm{Gd} + \mathrm{Fe} \rightleftharpoons \mathrm{GdFe}$$

where Gd denotes the Gd contrast agents and Fe denotes the Fe ions,

The equilibrium constant is given by

$$\mathrm{K_{eq}} = \frac{[\mathrm{GdFe}]}{[\mathrm{Gd}][\mathrm{Fe}]}$$

Equation 17 – Equilibrium association constant K_{eq} describing formation of the Gd–Fe complex from free Gd and Fe species.

Because binding occurs dynamically, the concentrations appearing in the relaxation equation correspond to equilibrium concentrations rather than initial analytical concentrations.

Mass balance relationships may therefore be written as

$$[\mathrm{Gd}]_{\mathrm{tot}} = [\mathrm{Gd}] + [\mathrm{GdFe}]$$

$$[\mathrm{Fe}]_{\mathrm{tot}} = [\mathrm{Fe}] + [\mathrm{GdFe}]$$

Equation 18 – Mass balance relationships for Gd and Fe, expressing total concentrations as the sum of free and associated (Gd–Fe) species.

Substitution into the relaxation expression yields:

$$R_{1,obs} = R_{1,water} + r_{1,Gd}([Gd]_{tot} - [GdFe]) + r_{1,Fe}([Fe]_{tot} - [GdFe]) + r_{1,GdFe}[GdFe]$$

$$= R_{1,water} + r_{1,Gd}[Gd]_{tot} + r_{1,Fe}[Fe]_{tot} + (r_{1,GdFe} - r_{1,Gd} - r_{1,Fe})[GdFe]$$

Equation 19 – Expanded expression for $R_{1,\mathrm{obs}}$ incorporating total concentrations and the Gd–Fe association term, highlighting the non-additive relaxivity contribution from the bound species.

This expression highlights the central role of the coordinated species in determining whether relaxivity deviates from simple additive behaviour.

It is convenient to define the additional relaxation contribution arising from coordination between the contrast agent and iron as

$$\Delta R_1 = \left(r_{1,GdFe} - r_{1,Gd} - r_{1,Fe}\right)[GdFe]$$

Equation 20 – Incremental relaxation term ΔR_1 proportional to the concentration of the Gd–Fe species, defined by the excess relaxivity of the bound complex over the sum of free Gd and Fe contributions.

The observed relaxation rate can therefore be written in a compact form as

$$R_{1,obs} = R_{1,water} + r_{1,Gd}[Gd]_{tot} + r_{1,Fe}[Fe]_{tot} + \Delta R_1$$

Equation 21 – Observed longitudinal relaxation rate expressed as the sum of baseline, additive relaxivity contributions, and the interaction term ΔR_1 arising from Gd–Fe association.

where ΔR_1 represents the additional relaxation contribution arising from interaction between the Gd contrast agent and iron.

This formulation highlights that the observable MRI response is governed not only by the intrinsic relaxivities of the isolated species, but also by the interaction term associated with formation of the coordinated assembly.

2.3.3. Fe–Probe Exchange Kinetics

The equilibrium treatment introduced above describes the distribution of free and iron-associated probe species, but does not describe the rate at which this distribution is established or maintained. For a reversible association process,

$$Gd - complex + Fe \underset{k_{off}}{\overset{k_{on}}{\rightleftharpoons}} Gd - complex - -Fe$$

the equilibrium association constant is related to the forward and reverse rate

constants by

$$K_{\mathrm{eq}} = \frac{k_{\mathrm{on}}}{k_{\mathrm{off}}}$$

where k_{on} and k_{off} describe the association and dissociation processes, respectively. Thus, the equilibrium constant defines the relative populations of the free and associated species, whereas the individual rate constants determine the timescale over which those populations are established and interconverted.

Formation of Fe(III) complexes with oxygen-donor ligands can occur on experimentally accessible kinetic timescales. For example, stopped-flow studies of Fe(III)–catechol complexation have reported a formation rate constant of approximately $3.1 \times 10^{3}\ \mathrm{M}^{-1}\,\mathrm{s}^{-1}$, while studies of Fe(III)–salicylate have likewise demonstrated measurable reversible complex formation and dissociation.[125] These values cannot be transferred quantitatively to the present GdSCA–Fe or GdCat–Fe systems because the ligand architecture, protonation state, iron speciation and experimental conditions differ. Nevertheless, they indicate that Fe–O-donor association and dissociation can occur on timescales considerably longer than the rapid exchange processes associated with small-molecule coordination chemistry.

An important consequence is that the establishment of thermodynamic equilibrium and the subsequent dynamic exchange of iron are distinct considerations. If the association and dissociation processes are sufficiently rapid relative to the experimental preparation period, the equilibrium concentrations used in the relaxation model are expected to be established before measurement. In the present

experiments, samples were not measured immediately following the addition of iron; sample preparation, instrument setup, background measurements and sequential acquisition resulted in a minimum pre-measurement interval of approximately 15 min. Although the time required for the specific GdSCA–Fe and GdCat–Fe systems to reach equilibrium was not independently determined, this interval provides a substantial period for equilibration relative to the timescales reported for related Fe(III)–O-donor complexes.[171]

Once equilibrium has been established, however, Fe association and dissociation may continue during the relaxation experiment. The relevance of this exchange depends on its timescale relative to longitudinal relaxation. Defining an overall exchange rate approximately as

$$k_{\mathrm{ex,Fe}} \approx k_{\mathrm{on}}[\mathrm{Fe}] + k_{\mathrm{off}}$$

a regime in which $k_{\mathrm{ex,Fe}} \gg R_1$ corresponds to rapid interconversion of free and associated probe states during relaxation, whereas $k_{\mathrm{ex,Fe}} \ll R_1$ corresponds to comparatively static chemical populations during an individual relaxation event. When $k_{\mathrm{ex,Fe}}$ becomes comparable to R_1, chemical exchange and magnetisation recovery may become kinetically coupled, and a simple equilibrium population-weighted treatment may no longer provide a complete description of the relaxation behaviour. [125]

The present model does not determine k_{on} or k_{off}, and therefore does not assign the Gd–Fe systems to a specific fast-, slow- or intermediate-exchange regime. Instead, it assumes that equilibrium speciation is established before measurement

and uses the resulting species populations to describe the observed relaxation response. The fitted K_{eq}should therefore be interpreted as an equilibrium-model parameter rather than as a direct measure of Fe-binding kinetics. This distinction is particularly important because the final pH of the Fe-containing relaxometry solutions was not independently controlled, whereas the probes themselves had been prepared under pH 7 conditions. Since Fe(III) hydrolysis and ligand protonation can affect both speciation and complexation kinetics, literature rate constants are used here only to provide kinetic context rather than quantitative estimates for the present systems.

2.3.4. Limiting Conditions and Model Assumptions

The species-resolved formulation derived above allows the behaviour of the system to be analysed under several limiting conditions.

First, if the binding affinity between the Gd contrast agent and iron is negligible, the concentration of the coordinated species approaches zero: $[\mathrm{GdFe}] \approx 0$. Under this condition, the contribution of the coordinated species to longitudinal relaxation becomes insignificant and the observed relaxation rate reduces to the linear superposition of the independent components:

$$R_{1,obs} \approx R_{1,water} + r_{1,Gd}[Gd]_{tot} + r_{1,Fe}[Fe]_{tot}$$

Equation 22 – Approximate expression for $R_{1,\mathrm{obs}}$assuming additive contributions from contrast agent and iron, neglecting interaction effects.

In this regime, the presence of iron does not produce any additional contrast

mechanism beyond the intrinsic relaxivity of the isolated species.

Second, even if coordination between the contrast agent and iron occurs, no enhancement in relaxivity will arise if the coordinated assembly does not introduce a new relaxation pathway. Mathematically, this corresponds to the condition:

$$r_{1,GdFe} \approx r_{1,Gd} + r_{1,Fe}$$

Equation 23 – Additive approximation of relaxivity, where the relaxivity of the Gd–Fe species is assumed to equal the sum of the individual contributions from free Gd and Fe.

In this situation, the relaxation behaviour remains strictly additive, and the formation of the coordinated species does not generate a detectable deviation from the baseline relaxation rate.

Together, these two limiting conditions define the baseline behaviour expected for a system in which the Gd contrast agent and iron act as independent paramagnetic centres.

The theoretical framework developed above further assumes that the relaxation behaviour of the system is dominated by the interaction between the Gd contrast agent and labile iron. In practical biological environments, however, additional metal ions and biomolecules may compete for coordination or influence the relaxation properties of the probe. To establish the fundamental relaxation mechanism, the initial theoretical analysis therefore considers an idealised system in which interference from other metal ions, proteins, or small biomolecules is minimal.

Such conditions are most closely approximated in simplified aqueous systems, where

only water, the Gd contrast agent, and iron are present. Under these circumstances, the contribution of the coordinated Gd–Fe species can be examined in isolation, providing a clear framework for understanding how iron binding may influence relaxivity. Subsequent experimental sections extend this analysis to increasingly complex environments, including cellular systems and in vivo models.

The species-resolved framework developed in this section establishes the quantitative conditions under which coordination between the contrast agent and iron can produce an observable change in longitudinal relaxation. In particular, the model highlights that a measurable signal enhancement requires both appreciable formation of the coordinated species and a relaxivity contribution that exceeds the linear combination of the isolated components.

While the equations above describe the macroscopic behaviour of the system, the physical origin of the enhanced relaxivity remains to be considered. In particular, the question arises as to why the coordinated Gd–Fe assembly may exhibit relaxivity greater than that of the independent paramagnetic species.

The following section therefore examines the molecular mechanisms that may give rise to such relaxivity modulation, with particular emphasis on rotational dynamics, electronic relaxation, and distance-dependent magnetic interactions.

2.3.5. Potential interference of other species

In addition to iron, other paramagnetic metal ions present in biological systems may,

in principle, contribute to longitudinal relaxation. However, their influence is expected to be negligible under physiological conditions.

Ions that are paramagnetic:

Element	Medium amount	Ion forms in physiology
Ca	1000 g	Ca^{2+}
K	140 g	K^{+}
Na	100 g	Na^{+}
Mg	19 g	Mg^{2+}
Fe	4.2 g	Fe^{2+}, Fe^{3+}
Zn	2.3 g	Zn^{2+}
Ga	0.7 g	Ga^{3+}
Rb	0.68 g	Rb^{+}
Sr	0.32 g	Sr^{2+}
Pb	0.12 g	Pb^{2+}
Cu	0.072 g	Cu^{+}, Cu^{2+}
Al	0.06 g	Al^{3+}
Cd	0.05 g	Cd^{2+}

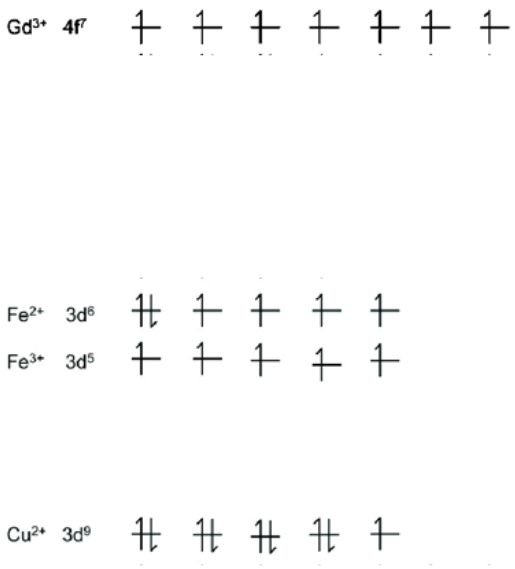


Figure 18 - comparison of physiological metal abundance and electronic configurations[172]

Manganese, for example, exists predominantly as Mn^{2+}, which is strongly paramagnetic due to the presence of five unpaired electrons. Despite this, the total body content of manganese is extremely low, typically on the order of 10–20 mg in adults, and its concentration in blood and intracellular environments is tightly regulated. As a result, the probability of significant interaction between Mn^{2+} and the contrast agent is limited, and its contribution to overall relaxivity is expected to be minimal.[146]

Similarly, copper is present in biological systems at relatively low concentrations compared to iron. While Cu^{2+} is paramagnetic, it contains only a single unpaired

electron and is typically tightly bound within proteins, further limiting its availability for interaction with molecular probes.[173]

In contrast, iron is both highly abundant, with total body levels on the order of several grams, and present in redox-active forms (Fe^{2+} and Fe^{3+}) capable of participating in dynamic coordination processes. This combination of high abundance, paramagnetism, and partial chemical accessibility distinguishes iron as the dominant contributor to any observable changes in relaxivity.

Taken together, these considerations indicate that, among biologically relevant metal ions, iron is uniquely positioned to generate a measurable and physiologically relevant MRI response, while contributions from other paramagnetic species are expected to be negligible.

2.4. SBM Extension to Gd–Fe Systems

As established in Section 2.3, the observed enhancement in longitudinal relaxation arises from the formation of a coordinated Gd–Fe species, which introduces a positive deviation from linear additivity. However, this formulation does not account for the physical origin of the increased relaxivity. To address this, the Solomon–Bloembergen–Morgan (SBM) framework introduced in Chapter Section 1.2.5 is applied here to analyse how coordination of iron perturbs the parameters governing paramagnetic relaxation.[83]

Within the SBM formalism, longitudinal relaxation is determined by dipolar

interactions between electron spins and nearby nuclear spins, with the inner-sphere contribution described by:

$$\frac{1}{T_1^{IS}} \propto \frac{q}{r^6} \cdot J(\omega)$$

Equation 24 – Inner-sphere relaxation contribution proportional to hydration number q, inverse sixth power of distance r^{-6}, and the spectral density function $J(\omega)$

where q is the hydration number, r is the distance between the paramagnetic centre and the nuclear spin, and $J(\omega)$ is the spectral density function. The latter depends on the effective correlation time τ_c, which incorporates molecular rotation, water exchange, and electronic relaxation processes:

$$\tau_c^{-1} = \tau_R^{-1} + \tau_m^{-1} + \tau_S^{-1}$$

Equation 25 – Effective correlation time τ_c defined by contributions from rotational motion, water exchange, and electron spin relaxation

From this formulation, any increase in relaxivity must arise from perturbations to one or more of these parameters.

In the present system, coordination of iron introduces a secondary metal centre in close proximity to Gd^{3+}, which is expected to influence relaxivity primarily through three mechanisms within the SBM framework.

First, the presence of iron is expected to perturb the organisation and dynamics of water molecules in the vicinity of the Gd centre. While the inner-sphere hydration number (q) is preserved by design, the local hydrogen-bonding network may be altered through coordination or electrostatic interactions involving Fe^{2+} or Fe^{3+}. This

may increase the residence time and effective contribution of second-sphere water molecules, thereby enhancing the overall relaxation efficiency. Within the SBM framework, such effects can be interpreted as an increase in the effective correlation time associated with water-mediated interactions.

Second, coordination of iron modifies the dynamic terms contributing to the effective correlation time. In particular, the introduction of an additional paramagnetic centre is expected to influence the local magnetic fluctuation environment, thereby altering the effective electronic relaxation term (τ_S). Unlike the case of a single paramagnetic centre, the Gd–Fe assembly constitutes a coupled system in which magnetic field fluctuations arise from the combined influence of both metal ions. This leads to a modified spectral density function $J(\omega)$, reflecting changes in the frequency distribution of magnetic fluctuations experienced by nearby protons.

Third, the spatial proximity between Gd and Fe introduces additional dipolar interaction pathways. Given the strong r^{-6}dependence of paramagnetic relaxation, even small changes in effective distances between paramagnetic centres and surrounding water protons can produce significant changes in relaxivity. In this context, the appended iron-binding arm serves to position the secondary metal centre within a defined distance range, enabling efficient coupling without disrupting the primary coordination environment of Gd^{3+}.

Notably, in contrast to macromolecular contrast agents, the overall molecular size of the system is not expected to change substantially upon iron binding. As such,

variations in rotational correlation time (τ_R) are unlikely to dominate the observed relaxivity enhancement. Instead, the dominant contributions arise from local structural and magnetic perturbations, including altered water organisation, modified electronic relaxation behaviour, and distance-dependent dipolar coupling.

Taken together, these effects provide a mechanistic basis for the condition:

$$r_{1,\mathrm{GdFe}} > r_{1,\mathrm{Gd}} + r_{1,\mathrm{Fe}}$$

Equation 26 – Non-additive relaxivity behaviour where the Gd–Fe complex exhibits higher relaxivity than the sum of the individual Gd and Fe contributions.

as defined in Section 2.2. Within the SBM framework, this inequality reflects the emergence of additional relaxation pathways that are not present in the isolated components, but arise from the coupled paramagnetic environment of the Gd–Fe assembly.

This analysis demonstrates that relaxivity enhancement in the present system can be understood as a direct consequence of perturbations to SBM parameters induced by controlled metal–metal proximity, providing a theoretical foundation for the molecular design strategy described in the following section.

2.5. Feasibility and Experimental Framework

2.5.1. Overall Experimental

The development and evaluation of the proposed iron-responsive contrast agents follow a staged workflow, progressing from molecular design to in vivo validation.

This workflow is summarised schematically in Figure 19

The initial stage involves the rational design of candidate complexes based on literature precedents and refinement of prior work. Particular emphasis is placed on balancing iron-binding capability with preservation of the Gd coordination environment, as discussed in previous sections.

Following design, the target complexes are synthesised using established coordination chemistry strategies. This stage provides structurally defined compounds incorporating both the Gd-chelating scaffold and the iron-binding moieties.

Subsequent characterisation is carried out in aqueous solution. T_1 relaxometry titration is employed to quantify changes in longitudinal relaxation in response to iron concentration, while UV–Vis titration provides complementary information on metal–ligand binding. In particular, spectral changes associated with the aromatic iron-binding groups enable estimation of binding affinity and stoichiometry through curve fitting.

Cytotoxicity studies are conducted to determine the maximum tolerated concentration of the complexes in biological systems. These experiments establish safe working concentrations for subsequent functional studies.

Functional evaluation is then performed in cell-based systems, where in vitro MRI measurements are carried out under controlled conditions representing physiologically relevant variations in iron levels, including normal and iron-

overloaded states. [174]

Finally, in vivo studies are conducted in animal models. Following administration of the contrast agents, MRI measurements are performed to assess contrast enhancement. Post-imaging analysis, including tissue dissection, enables further evaluation of distribution and biological response.[174]

This staged workflow enables systematic evaluation of the proposed system across increasing levels of complexity, from controlled chemical environments to whole-organism studies.

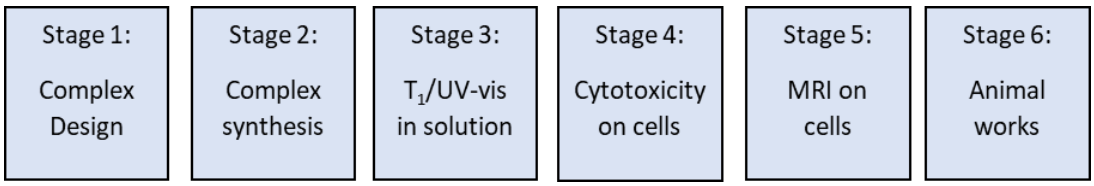


Figure 19 - Stages of MRI contrast agent development during this research

2.5.2. Multi-Level Experimental Systems

The experimental design is structured across three levels of increasing biological complexity: 1) aqueous (chemical system); 2) in vitro (cellular system); 3) in vivo (animal model).

The aqueous system provides a controlled environment for isolating the interaction between the Gd contrast agent and iron. In this context, relaxometry and spectroscopic measurements enable direct evaluation of binding behaviour and its effect on longitudinal relaxation.

The cellular system introduces biological complexity, including intracellular compartmentalisation and physiological regulation of iron. Experiments at this level assess whether the contrast agents remain responsive under biologically relevant conditions.

The in vivo system further incorporates systemic factors such as distribution, metabolism, and clearance. MRI measurements in animal models provide an assessment of the practical imaging performance of the probes under physiological conditions.

This hierarchical approach allows mechanistic insights obtained in simple systems to be tested and validated in increasingly complex environments.

2.5.3. Evaluation Criteria: Sensitivity, Selectivity, and Safety

The performance of the proposed contrast agents is evaluated according to three key criteria: sensitivity, selectivity, and safety.

Sensitivity refers to the ability of the system to generate measurable changes in longitudinal relaxation in response to iron. This is assessed primarily through T_1 titration experiments in aqueous solution, as well as MRI measurements in cellular and in vivo systems.

Selectivity describes the specificity of the response toward iron in the presence of competing metal ions. This is evaluated by examining relaxivity changes under conditions where other biologically relevant ions are present, thereby assessing the

extent to which the observed signal arises specifically from iron coordination.

Safety is assessed through cytotoxicity studies and in vivo tolerance. In vitro toxicity measurements establish acceptable concentration ranges for cellular experiments, while in vivo studies provide an indication of systemic safety and biological compatibility.

Together, these criteria provide a comprehensive framework for evaluating the performance of the contrast agents, linking molecular design to functional imaging outcomes.

3. Gd contrast agents in aqueous solution

3.1. Experimental Scope and Analytical Strategy

This chapter builds on the framework established in Chapter 2, where the potential of Gd–Fe interactions to modulate longitudinal relaxation was defined. The focus here is to translate this concept into experimentally measurable behaviour in aqueous solution.

Aqueous systems provide a controlled environment in which probe structure, iron speciation, and concentration can be systematically varied. Within this context, T_1 relaxation measurements are used as the primary readout, as changes in R_1 reflect the influence of paramagnetic centres on surrounding water protons.[83] Particular attention is given to deviations from additive behaviour, which may indicate the formation of probe–iron associated species.

To support interpretation, DynaFit modelling is applied to analyse relaxation data within an equilibrium framework, while UV–Vis absorption spectroscopy provides complementary evidence for metal–ligand interactions.[175] Together, these approaches enable a consistent evaluation of iron-dependent behaviour in solution.

Synthetic procedures and detailed characterisation are described in Chapter 7. This chapter therefore focuses on functional behaviour in solution, establishing the experimental basis for subsequent in vitro and in vivo studies.

3.2. T1 relaxation measurements in aqueous solution

3.2.1. Analytical basis for T1 relaxation measurements

Longitudinal relaxation measurements were used in this chapter to examine how the aqueous relaxation behaviour of the probe systems varies as a function of composition. The primary experimentally determined quantity was the longitudinal relaxation time (T_1), which was converted to the relaxation rate according to $R_1 = 1/T_1$. This transformation provides a direct and concentration-independent basis for comparison between samples, and forms the foundation for the determination of longitudinal relaxivity (r_1).

As outlined in Chapter 1 and developed further in Chapter 2, the observed relaxation rate in systems containing both Gd-based contrast agents and iron can be interpreted as arising from multiple contributing species. In the absence of interaction, the overall behaviour is expected to follow a linear superposition of independent paramagnetic contributions. The central objective of the present measurements is therefore to establish the baseline relaxation behaviour of the individual components, and to determine whether systems containing both probe and iron exhibit deviations from this additive behaviour.

$$R_{1,obs} = R_{1,water} + r_{1,Gd}[Gd] + r_{1,Fe}[Fe] + r_{1,GdFe}[GdFe]$$

(Equation 16 on Page 93)

In practice, a linear dependence of R_1 on solute concentration permits assignment of a longitudinal relaxivity r_1, which serves as a convenient descriptor of baseline

behaviour for isolated species. However, not all systems investigated in this work exhibited such linearity across the full concentration range. Where the dependence of R_1 on concentration was non-linear, or where the slope varied systematically with composition, the data were instead interpreted in terms of concentration-dependent response profiles. In particular, for experiments in which iron was introduced into solutions containing a fixed concentration of probe, the resulting variation in R_1 reflects the combined contributions of free iron and any probe-associated species. Under these conditions, the extracted slopes do not represent intrinsic relaxivities of the probe, but instead provide an empirical measure of iron-dependent modulation of longitudinal relaxation.

3.2.2. Method of T1 measurement and data analysis

Longitudinal relaxation measurements were performed to obtain concentration-dependent T_1 data for the probe systems and iron-containing solutions investigated in this chapter. All measurements were carried out on a Bruker AVIII HD 500 MHz NMR spectrometer equipped with a 5 mm z-gradient broadband X–^{19}F/^{1}H BBFO SMART probe and controlled using TopSpin software (version 3, Bruker BioSpin). Experiments were conducted under ambient temperature and atmospheric pressure. Prior to acquisition, probe tuning and matching, magnetic field shimming, and receiver gain optimisation were performed for each sample to ensure consistent measurement conditions.

Aqueous solutions of defined composition were prepared from concentrated stock

solutions by parallel dilution. For each experimental series, samples spanning the desired concentration range were prepared with typical volumes sufficient to fill the sensitive region of the NMR probe. Samples were introduced into melting-point tubes and placed within standard 5 mm NMR tubes to ensure reproducible positioning during measurement while minimising sample consumption.

Two types of measurements were performed. First, concentration-dependent datasets were acquired for GdSCA and GdCat in water to establish their intrinsic aqueous relaxation behaviour. Corresponding measurements were also performed for Fe^{2+} and Fe^{3+} in water to define the baseline relaxation characteristics of the free iron species. Secondly, titration experiments were conducted in which Fe^{2+} or Fe^{3+} was incrementally added to solutions containing a fixed concentration of probe (typically 1 mM). These experiments were designed to probe iron-dependent modulation of relaxation behaviour under a defined chemical background.

For each sample, the ^{1}H resonance from the milli-q water solvent was used for analysis. T_1 values were determined using a series of relaxation delays spanning at least five times the expected T_1, with typically 16–32 delay points acquired per dataset. Following acquisition, spectra were Fourier transformed, phase-corrected, and baseline-corrected prior to integration of the signal intensity. The resulting signal intensities were fitted as a function of delay time using a mono-exponential recovery model to obtain T_1 values.

The measured T_1 values were converted to longitudinal relaxation rates according to $R_1 = 1/T_1$. Linear regression and graphical analysis were performed using GraphPad

Prism. Where appropriate, DynaFit was used as a complementary tool to explore alternative empirical descriptions of the concentration-dependent behaviour. These analyses were used in a descriptive manner to support interpretation of the data trends.

To improve robustness, measurements were performed using independently prepared solutions across multiple experimental runs wherever possible. Residual uncertainty may arise from solution preparation, volumetric handling, temperature variation during acquisition, signal integration, and model selection during fitting. Accordingly, the resulting values are interpreted primarily as a basis for comparison between systems rather than as over-precise absolute descriptors.

3.2.3. Baseline relaxation behaviour of the probe and free iron systems in water

The aqueous relaxation behaviour of the individual components was first examined in order to establish the reference against which iron-dependent modulation could be evaluated. In the absence of interaction between components, the longitudinal relaxation rate is expected to follow an approximately additive relationship, in which the contributions from the Gd contrast agent and any paramagnetic ions can be described independently. Establishing this baseline is therefore essential for identifying deviations from additive behaviour in the probe–iron systems.

For GdSCA in water, a clear linear dependence of R_1 on concentration was observed across three independent measurement series in Figure 20. Linear fitting yielded an

apparent intrinsic relaxivity of approximately 4.67 mM^{-1} s^{-1} under the present conditions. The reproducibility and linearity of the dataset indicate that the SCA-based complex behaves as a well-defined T_1-shortening species in aqueous solution, and that its relaxation behaviour can be described using a single concentration-independent parameter over the range studied.

A similar linear dependence of R_1 on concentration was observed for GdCat in Figure 21, although with a consistently lower slope, corresponding to an intrinsic relaxivity of approximately 2.94 mM^{-1} s^{-1}. Under otherwise comparable conditions, the Cat-based system therefore exhibits a weaker baseline longitudinal relaxation effect than the SCA analogue.

Despite sharing the same Gd–DO3A coordination core, GdSCA and GdCat exhibited different intrinsic relaxivities. This difference may arise from the distinct chemical environments introduced by the pendant groups. In particular, the additional ionisable carboxylate in SCA changes the overall charge and local hydration environment, which could influence the accessibility and exchange of water around the Gd centre. The two pendant groups may also impose different conformational and local motional behaviour, potentially affecting the effective rotational correlation time, which is an important determinant of Gd(III) relaxivity. Differences in second-sphere hydration may provide a further contribution. These effects are plausible consequences of the different ligand environments, although the present data do not distinguish whether hydration, water exchange, rotational dynamics, or a combination of these factors is responsible. [83]

This difference establishes that the two probe platforms do not share an identical relaxometry baseline, and that any subsequent differences in iron-dependent response must be interpreted in the context of these distinct intrinsic properties.

When Fe^{2+} was examined in water in the absence of probe, the dependence of R_1 on concentration was also approximately linear with background noise as Figure 22. The apparent longitudinal relaxation effect of free Fe^{2+} was approximately 0.30 $mM^{-1}\,s^{-1}$, indicating that ferrous ion alone provides only a weak contribution to T_1 shortening under these conditions. This observation is significant for subsequent interpretation, as it implies that large increases in R_1 observed in probe-containing systems cannot be attributed solely to the independent contribution of Fe^{2+}.

In contrast, Fe^{3+} in water exhibited a distinctly non-linear dependence of R_1 on concentration in Figure 23. The data were more appropriately described by quadratic fitting, and a single concentration-independent relaxivity could not be assigned across the full concentration range.

This difference between Fe^{2+} and Fe^{3+} can be rationalised by their different aqueous speciation. Under the present conditions, Fe^{2+} can reasonably be approximated as a predominantly hydrated ferrous species, such that its contribution to longitudinal relaxation remains approximately proportional to the total iron concentration. Consistent with this interpretation, previous measurements of paramagnetic ions in aqueous solution have shown that, when the contributing species and hydration environment remain effectively constant, the relaxation rate varies linearly with paramagnetic ion concentration.[176] Fe^{3+}, in contrast, has a substantially higher

charge density and is considerably more susceptible to hydrolysis, giving rise to equilibria between hydrated, hydroxo, and higher-order ferric species. Studies of Fe^{3+} relaxometry have therefore deliberately employed strongly acidic conditions to suppress hydrolysis when characterising the ferric aqua ion, while more general Fe(III) coordination systems show clear pH-dependent changes in speciation and relaxivity.[177]

Accordingly, the non-linear dependence observed for Fe^{3+} in the present aqueous measurements may reflect a concentration-dependent change in the distribution of ferric species, such that the effective relaxation contribution per mole of total iron is not constant across the concentration range. Changes in hydration and water exchange, together with differences in the electronic relaxation properties of the contributing species, could consequently alter the apparent relaxivity as the Fe^{3+} concentration increases.[178] The present measurements do not directly resolve the individual ferric species, and therefore do not establish which hydrolysed or higher-order species are responsible for the observed curvature. The quadratic fit should consequently be regarded as an empirical description of the concentration dependence rather than as a mechanistic model of ferric relaxation. This distinction is important for subsequent analysis, where the aqueous Fe^{3+} response is treated as a concentration-dependent baseline rather than a single intrinsic relaxivity.[179]

Over the range from 0 to 1 mM, the apparent response lay broadly in the region of 1.0–1.1 mM^{-1} s^{-1}, but this value should be regarded as a local descriptive measure rather than an intrinsic r_1 in the same sense as that obtained for the Gd contrast

agents. The non-linearity of the ferric dataset indicates that the behaviour of free Fe^{3+} in aqueous solution is itself concentration-dependent under the present conditions, and therefore does not constitute a simple linear reference system.[176, 177]

Taken together, these baseline measurements define the reference behaviour expected in the absence of probe–iron interaction. Both GdSCA and GdCat exhibit well-defined intrinsic relaxivities in water, while free Fe^{2+} contributes only weakly and approximately linearly to longitudinal relaxation. Free Fe^{3+}, however, displays non-linear behaviour, indicating that its contribution cannot be fully captured by a single constant parameter. These observations establish the limits of an additive description and provide the necessary framework for identifying deviations arising in probe-containing systems, as discussed in the following section.

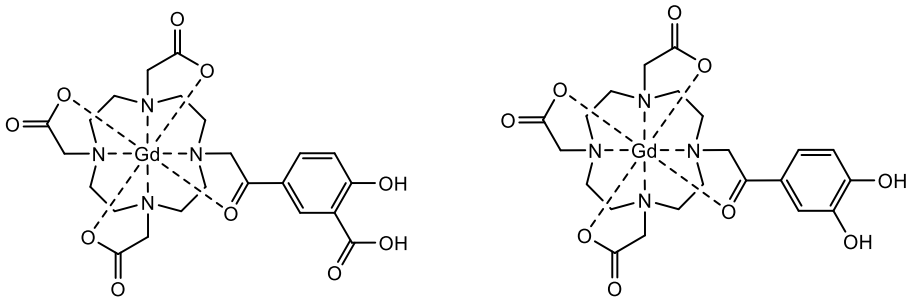


Figure 17 – Structure of GdSCA (left) and GdCat (right) (From Page 92)

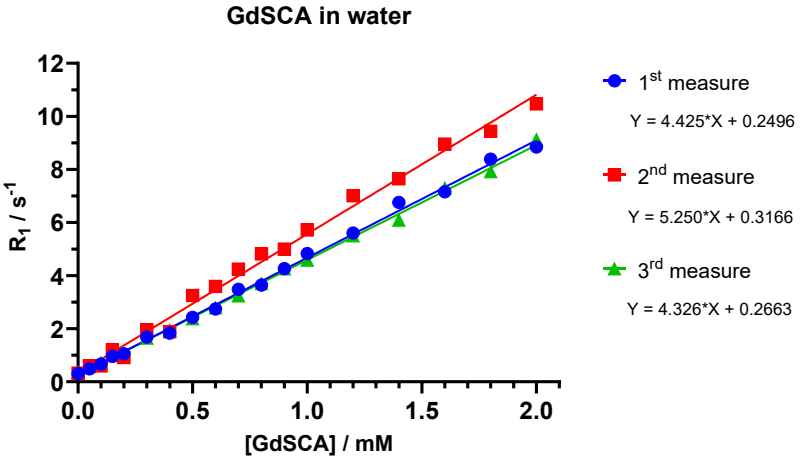


Figure 20 – Concentration dependence of R_1 of GdSCA in water at room temperature. R_1 values were measured in three independent measurement series. The solid lines represent linear least-squares fits, and the gradients represent the intrinsic relaxivity, r_1 of GdSCA, of around 4.67 $mM^{-1}\ s^{-1}$.

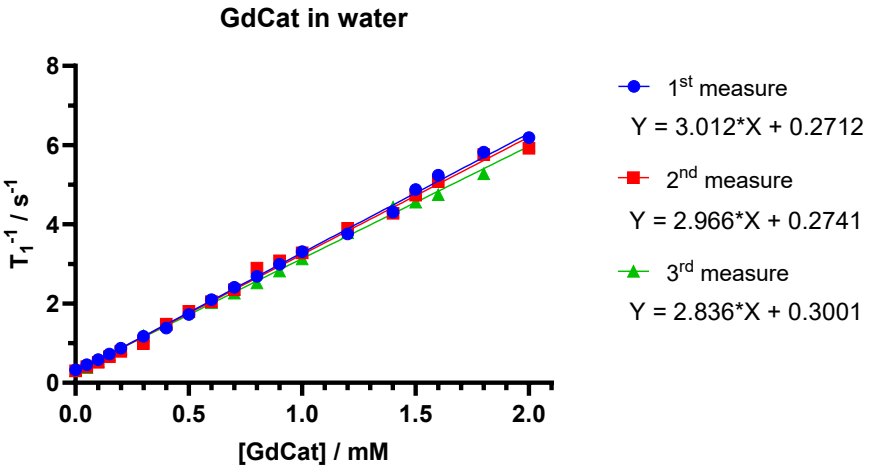


Figure 21 – Concentration dependence of R_1 of GdCat in water at room temperature. R_1 values were measured in three independent measurement series. The solid lines represent linear least-squares fits, and the gradients represent the intrinsic relaxivity, r_1 of GdCat, of around 2.94 $mM^{-1}\ s^{-1}$.

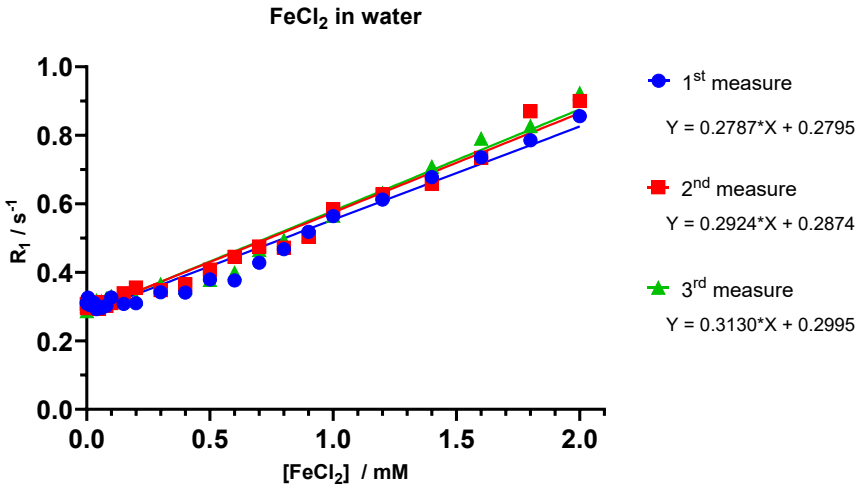


Figure 22 – Concentration dependence of R_1 of Fe^{2+} in water at room temperature. R_1 values were measured in three independent measurement series. The solid lines represent linear least-squares fits, and the gradients represent the apparent longitudinal relaxation effect of Fe^{2+}, of around 0.30 $mM^{-1}\ s^{-1}$.

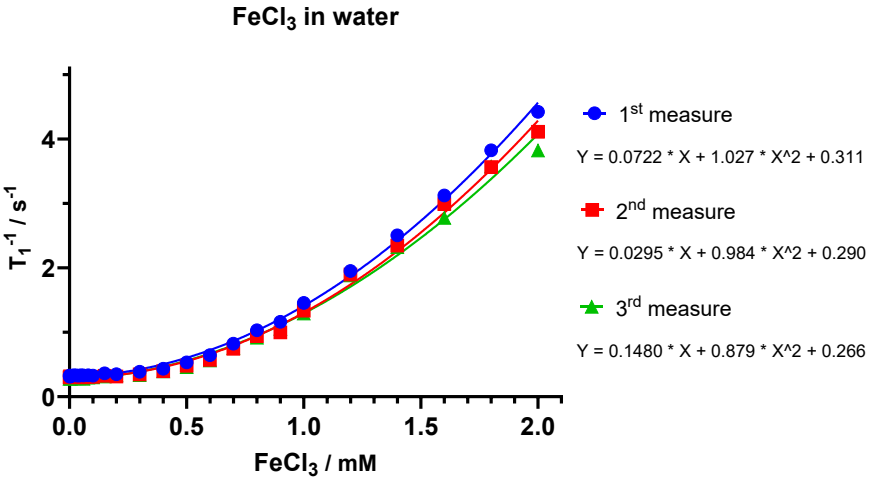


Figure 23 - Concentration dependence of R_1 of Fe^{3+} in water at room temperature. R_1 values were measured in three independent measurement series. The data could not be adequately described by a single linear fit over the full concentration range and were instead fitted using quadratic functions. Over the 0–1 mM range, the apparent response was in the region of 1.01–1.10 $mM^{-1}\ s^{-1}$.

3.2.4. Iron-dependent modulation of R1 in probe-containing systems

3.2.4.1. Iron titration in the SCA system

The effect of iron on longitudinal relaxation was first examined in the presence of a fixed concentration of GdSCA (1 mM), in order to assess whether the observed behaviour could be described by additive contributions from the probe and free iron, or whether deviations indicative of interaction-dependent effects were present.

Upon addition of Fe^{3+} to the SCA-containing solution, a pronounced increase in R_1 was observed in Figure 25. The dependence of R_1 on Fe^{3+} concentration was not adequately described by a single linear fit across the full concentration range. Instead, two concentration regimes could be identified, with a markedly steeper response at low Fe^{3+} concentrations and a substantially reduced slope at higher concentrations. In the low-concentration regime, the apparent response significantly exceeded that expected from simple superposition of the intrinsic relaxivities of GdSCA and free Fe^{3+}. This behaviour is consistent with the presence of an additional relaxation contribution that cannot be accounted for by independent paramagnetic effects alone.

At higher Fe^{3+} concentrations, the increase in R_1 became more gradual, and the apparent slope approached values closer to those expected for additive behaviour. This transition suggests that the magnitude of the additional relaxation contribution is concentration-dependent, and that the conditions required for maximal deviation

from additivity are most effectively realised at lower Fe^{3+} concentrations under the present experimental conditions.

In the case of Fe^{2+} as Figure 24, addition to the SCA-containing solution also resulted in an increase in R_1, although the magnitude of the effect was smaller than that observed for Fe^{3+}. As with Fe^{3+}, the response could be described in terms of two concentration regimes, with a more pronounced increase at lower concentrations and a reduced slope at higher concentrations. However, the overall enhancement was more modest, and the deviation from behaviour expected on the basis of independent contributions was correspondingly less pronounced.

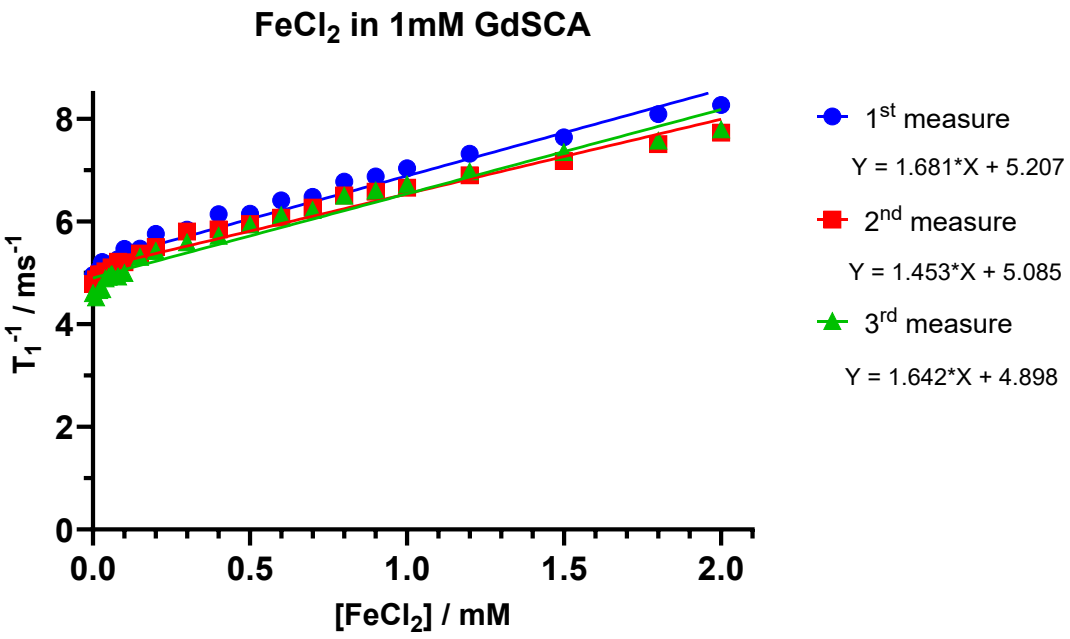


Figure 24 – Concentration dependence of R_1 of Fe^{2+} in the presence of 1 mM GdSCA at room temperature. R_1 values were measured in three independent measurement series. The data were fitted in two concentration regimes. In the low-concentration region, the apparent response slope was around 4.56 $mM^{-1}\ s^{-1}$, whereas in the higher-concentration region it was around 1.37 $mM^{-1}\ s^{-1}$.

Taken together, these observations indicate that the SCA system exhibits a clear iron-dependent modulation of longitudinal relaxation, with the magnitude of the effect strongly dependent on the oxidation state of iron. In particular, the Fe^{3+}-containing system displays a pronounced deviation from additive behaviour at low concentrations, consistent with the emergence of an additional relaxation contribution associated with interaction between the probe and iron, as described in Section 3.2.1

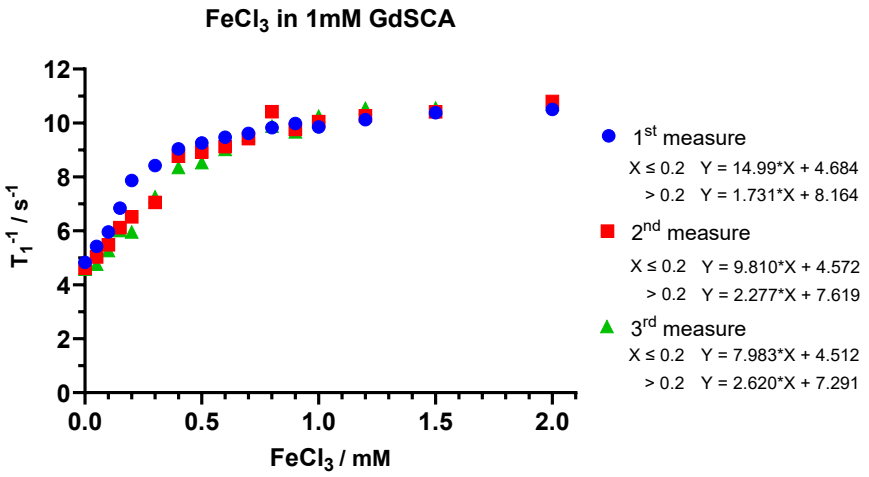


Figure 25 – Concentration dependence of R_1 of Fe^{3+} in the presence of 1 mM GdSCA at room temperature. R_1 values were measured in three independent measurement series. The data were fitted in two concentration regimes. In the low-concentration region, the apparent response slope was around 10.9 $mM^{-1}\ s^{-1}$, whereas in the higher-concentration region it was around 2.21 $mM^{-1}\ s^{-1}$.

3.2.4.2. Iron titration in the Cat system

An analogous series of experiments was carried out in the presence of 1 mM GdCat, in order to assess whether similar iron-dependent modulation of relaxation behaviour was observed for the catechol-based system.

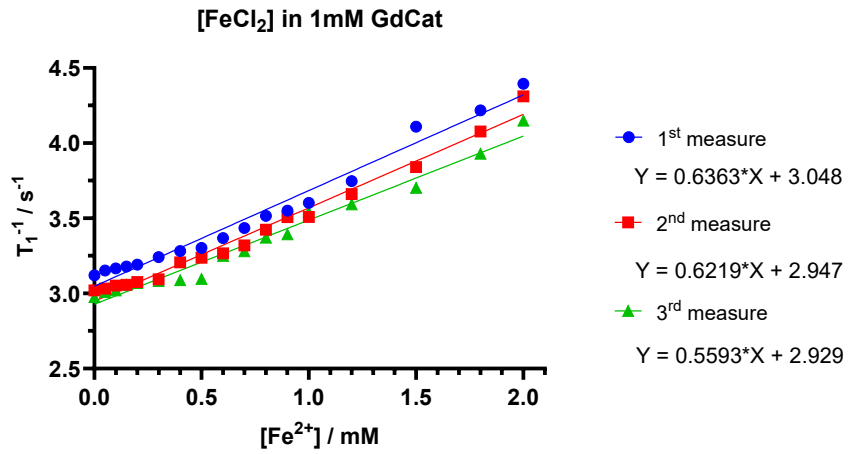


Figure 26– Concentration dependence of R_1 of Fe^{2+} in the presence of 1 mM GdCat at room temperature. R_1 values were measured in three independent measurement series. The solid lines represent linear least-squares fits, and the gradients represent the apparent iron-dependent response in the presence of 1 mM GdCat, of around 0.61 $mM^{-1}\,s^{-1}$.

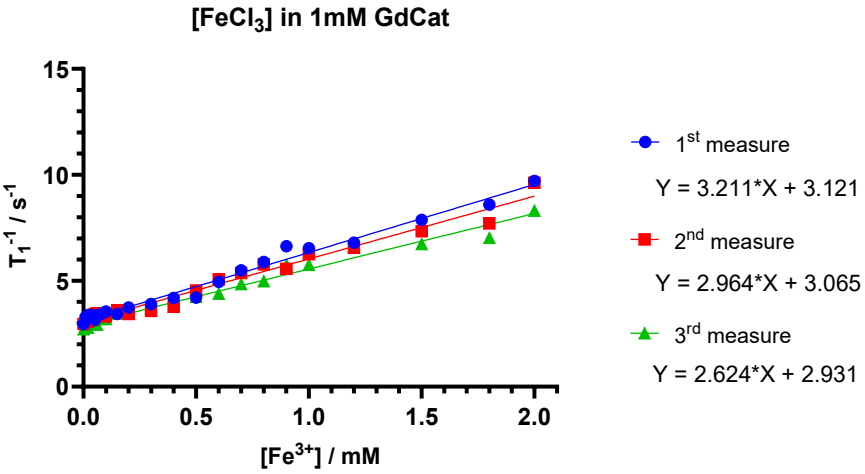


Figure 27– Concentration dependence of R_1 of Fe^{3+} in the presence of 1 mM GdCat at room temperature. R_1 values were measured in three independent measurement series. The solid lines represent linear least-squares fits, and the gradients represent the apparent iron-dependent response in the presence of 1 mM GdCat, of around 2.93 $mM^{-1}\,s^{-1}$.

Addition of Fe^{3+} to the Cat-containing solution resulted in an increase in R_1 that was approximately linear over the concentration range examined in Figure 27. The

magnitude of the response was greater than that observed for Fe^{2+}, indicating a degree of ferric preference similar to that observed in the SCA system. However, in contrast to the SCA case, the overall dependence of R_1 on Fe^{3+} concentration remained closer to linear behaviour, and no strongly enhanced low-concentration regime was observed. The apparent response could therefore be described to a reasonable approximation in terms of additive contributions, with only limited evidence for substantial deviation.

For Fe^{2+}, addition to the Cat-containing solution produced a comparatively small increase in R_1, again with an approximately linear dependence on concentration in Figure 26. The magnitude of the response was weak relative to that observed for Fe^{3+}, and the data did not indicate any pronounced deviation from behaviour expected for independent contributions.

These results suggest that, while the Cat system is capable of responding to the presence of iron, the extent of iron-dependent modulation of relaxation behaviour is substantially smaller than that observed for the SCA system. In particular, the absence of a strongly enhanced low-concentration response and the near-linear dependence of R_1 on iron concentration indicate that any additional relaxation contribution associated with probe–iron interaction is limited in magnitude under the present conditions.

3.2.4.3. Control experiments and assessment of ion selectivity

To assess whether the observed iron-dependent modulation of longitudinal relaxation could be attributed to specific probe–iron interactions rather than more

general ionic or electrostatic effects, control experiments were performed using Ca^{2+} and Zn^{2+} under analogous conditions.

Solutions containing 1 mM GdSCA or GdCat were prepared in the presence or absence of 1 mM Ca^{2+} or Zn^{2+}, and the corresponding R_1 values were compared in Figure 28. Under these conditions, no significant increase in R_1 was observed for either Ca^{2+} or Zn^{2+} relative to the corresponding probe-only solutions. The relaxation behaviour remained comparable to that of the baseline aqueous systems, with no evidence of enhanced T_1 shortening by running one-way-Anova test.

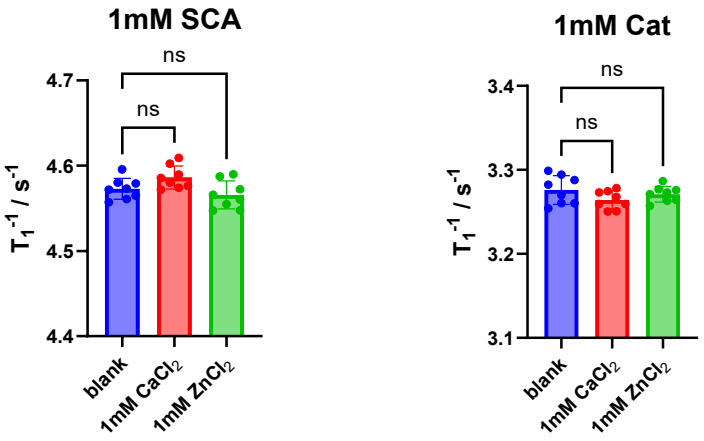


Figure 28 – Disturbance of Ca^{2+} and Zn^{2+} on GdSCA and Cat by measurement of observed T_1 of system of 1mM of GdSCA or GdCat with water / $CaCl_2$(1mM) / $ZnCl_2$(1mM)

This observation indicates that the presence of an additional divalent metal ion is not sufficient to produce a measurable increase in longitudinal relaxation under the conditions employed. In particular, the absence of a detectable response in the presence of Ca^{2+} suggests that non-specific ionic strength effects or general electrostatic interactions do not account for the enhanced R_1 values observed in the iron-containing systems. Similarly, the lack of response for Zn^{2+} indicates that the

effect is not a generic feature of transition metal ions, but is instead dependent on the specific chemical properties of iron.

When considered alongside the results presented previously in Section 3.2.4, these control experiments support the interpretation that the observed enhancement in R_1 arises from interaction between the probe and iron, rather than from non-specific physicochemical effects. In particular, the selective response to iron, combined with the absence of comparable effects for Ca^{2+} and Zn^{2+}, is consistent with the presence of an additional relaxation contribution associated with probe–iron interaction, as described by the analytical framework introduced in Section 3.2.1.

These findings therefore provide an important constraint on the interpretation of the aqueous relaxation data. While the measurements do not in themselves establish the detailed nature of the interaction between the probe and iron, they indicate that the observed relaxivity modulation is not a general property of ionic solutions, but is associated with specific chemical interactions involving iron under the conditions studied.[65, 83]

3.2.5. Comparative interpretation in the context of the Gd–Fe interaction model

The aqueous relaxation data can be interpreted within the species-resolved framework introduced in Section 2.3, in which the observed R_1 is described by the contributions of free complex, free iron, and a potential interaction term associated with Complex–iron association. The central observation is that the magnitude of this

interaction-dependent contribution differs substantially between the two ligand platforms and between the two oxidation states of iron. GdSCA showed the clearest deviation from additive relaxation behaviour, particularly with Fe^{3+}. For GdSCA, the Fe^{3+} response was particularly sensitive at low iron concentrations (biological concentration), where the apparent slope exceeded that expected from simple superposition of the intrinsic probe and free-iron contributions. Fe^{2+} also produced a measurable enhancement, but this was substantially smaller. GdCat also showed similar trend but weaker than GdSCA.

The marked difference between the SCA and Cat systems can first be considered in terms of their coordination chemistry. Under a simplified 1:1 description (which will be explained in Section 3.4), both ligands provide bidentate O,O coordination to Fe^{3+}, but the donor sets are not equivalent. The SCA arm presents a phenolate–carboxylate environment, whereas Cat provides two adjacent phenolate donors. The corresponding chelates also differ in ring size after binding an iron: salicylate-type coordination forms a six-membered metallocycle, whereas catecholate coordination forms a five-membered ring. These differences alter the bite geometry and conformational constraints imposed on the Fe centre. Structural studies of ferric catecholate complexes show that the narrow bite of the five-membered catecholate chelate is accommodated within a distorted octahedral environment, while salicylate-type complexes adopt a different O,O coordination geometry and can accommodate substantial variation in chelate-ring conformation.[122, 123] In addition, the different donor basicities and protonation equilibria of phenolate and

carboxylate groups can influence the conditional stability of the Fe-bound species. Salicylate–Fe^{3+} systems are also known to support multiple coordination stoichiometries, demonstrating that apparently simple O,O binding can generate chemically different associated species.[126] These differences provide a plausible coordination-chemical basis for the substantially different apparent responses of GdSCA and GdCat, without requiring the SCA response to be interpreted simply as evidence of a higher intrinsic Fe^{3+} affinity.

The strong dependence on iron oxidation state can likewise be considered at both the coordination and relaxation levels. Fe^{3+} has a higher charge density than Fe^{2+} and therefore has a stronger preference for hard O-donor environments. This oxidation-state-dependent donor preference has been demonstrated experimentally in systems containing competing salicylamide O,O and bipyridine N,N binding sites, where Fe^{3+} preferentially occupies the O,O environment while Fe^{2+} favours the softer N-donor site.[123] Thus, even when the same SCA or Cat pendant group is present, Fe^{2+} and Fe^{3+} cannot be assumed to generate identical coordination geometries or hydration environments. Computational studies of hydrated iron ions further show shorter Fe–O distances for Fe^{3+} than Fe^{2+}, consistent with the greater electrostatic interaction associated with the higher ferric charge.[180] These coordination differences are relevant to relaxation because the magnetic contribution of an iron centre depends not simply on the number of unpaired electrons, but on the electronic relaxation behaviour, metal–proton distance, hydration and molecular dynamics of the species through which the paramagnetic interaction is transmitted.

Studies of Fe^{3+} complexes have shown that T_{1e}, water exchange and Fe–H distance can all contribute significantly to proton relaxivity.[179] The weaker Fe^{2+}-dependent response observed here can therefore plausibly reflect differences in both the coordination environment and the relaxation properties of the resulting Fe-containing species, rather than oxidation state alone acting as a measure of magnetic strength.

The ligand dependence of the relaxation response provides a further distinction between binding and signal generation. Within the SBM framework, the relaxivity of a Gd^{3+} complex depends on parameters including hydration number, rotational correlation time, water exchange and electronic relaxation, while second-sphere water can provide an additional contribution. The present probes were designed to retain the established Gd coordination environment, so a major change in inner-sphere hydration is not necessarily required to explain an iron-dependent response. Instead, association of Fe could alter the local hydration environment, constrain or modify molecular motion, or change the spatial arrangement of the two paramagnetic centres. The latter may be particularly important because paramagnetic dipolar interactions depend strongly on distance; Caravan and co-workers noted that even small changes in the metal–proton distance can produce substantial changes in relaxation. Accordingly, the same degree of iron association need not generate the same ΔR_1 for SCA and Cat if the resulting Gd–Fe species differ in geometry, water accessibility or dynamics. Aime and co-workers provide a relevant precedent for this interpretation, having demonstrated Fe^{3+} binding to

peripheral salicylate-derived groups within a Gd-containing complex and observed relaxation behaviour associated with the resulting heterobimetallic species.

This distinction is important when interpreting the fitted association parameters. The relaxometry observable reports the combined effects of species population and species-specific relaxivity; consequently, a larger apparent binding response does not necessarily correspond directly to a proportionally larger intrinsic Fe-binding constant. This is particularly evident in the present DynaFit analysis, where the relaxation response coefficient for GdSCA–Fe^{3+} was better constrained than the associated equilibrium constant, while the latter showed substantial parameter correlation. The Cat datasets, by comparison, did not contain sufficient deviation from additive behaviour to resolve the interaction parameters reliably. The apparent superiority of SCA should therefore be understood primarily as a more effective conversion of iron association into a measurable relaxation perturbation under the present conditions, rather than as definitive evidence that SCA intrinsically binds Fe more strongly than Cat.

Finally, the Ca^{2+} and Zn^{2+} controls provide an important constraint on these interpretations. Their lack of a comparable enhancement indicates that the observed positive deviation cannot readily be attributed to ionic strength or to a generic response to added metal ions. Instead, the effect is associated with chemical interactions that are substantially more pronounced for iron under the conditions investigated. This does not by itself establish a unique molecular structure for the Gd–Fe species, but, when considered together with the oxidation-state and ligand-

dependent trends, it supports the interpretation that the additional relaxation pathway arises from specific probe–iron coordination chemistry.

Taken together, the aqueous T_1 measurements indicate that iron-dependent relaxivity is governed by more than the extent of metal binding alone. The SCA and Cat ligands present different O,O coordination environments to iron, while Fe^{2+} and Fe^{3+} can generate different coordination and electronic environments within the same ligand framework. These factors can in turn influence the geometry and dynamics of the associated Gd–Fe species and the efficiency with which paramagnetic interactions are transmitted to surrounding water. The pronounced SCA–Fe^{3+} response therefore represents not simply strong iron binding, but the more effective coupling of probe–iron association to an additional relaxation pathway. The detailed identity of this pathway cannot be established from the present measurements alone, but the results demonstrate that its magnitude is strongly dependent on both ligand structure and iron oxidation state.

3.3. UV-Vis absorption

3.3.1. Research Objective of UV-Vis absorption

The objective of this UV–Vis study is to examine the concentration-dependent electronic response of EuSCA and TbCat upon interaction with Fe^{2+} and Fe^{3+} in aqueous solution. As the chromophore arms of these complexes serve both as antennae and as potential Fe-binding sites, changes in the absorption profile provide a direct spectroscopic readout of coordination-induced electronic perturbation.

Eu^{3+} and Tb^{3+} analogues were employed for these measurements due to their improved spectroscopic sensitivity compared to the corresponding Gd^{3+} complexes, which require substantially higher concentrations to achieve comparable signal intensity. Given the structural similarity across the lanthanide series, the Eu and Tb systems are considered suitable spectroscopic surrogates for the Gd-based probes investigated in subsequent relaxometry studies.

This section therefore focuses on assessing iron selectivity, oxidation-state dependence, and saturation behaviour through controlled titration experiments.

3.3.2. UV–Vis Rationale

The spectroscopic sensitivity of EuSCA and TbCat arises from the incorporation of aromatic chromophore arms within the lanthanide–DO3A framework. Although lanthanide ions such as Eu^{3+} and Tb^{3+} exhibit intrinsic f–f transitions, these are Laporte-forbidden and characterised by low molar absorptivity. In contrast, the salicylate unit in EuSCA and the catechol moiety in TbCat contain conjugated π systems that dominate the UV–Vis absorption profile of the complexes.

These aromatic groups function as antennae, harvesting incident light and enabling efficient sensitisation of the lanthanide centre as the antenna effect discussed in Section1.2.3. Importantly, the oxygen donor atoms embedded within these chromophores also constitute potential coordination sites for secondary metal ions. EuSCA presents an ortho-phenolate and carboxylate donor environment, whereas TbCat features a catechol motif comprising two adjacent phenolic oxygen atoms.

Both represent O,O donor sets capable of chelation and are structurally positioned on a single pendant arm of the DO3A scaffold.[169]

Given that the chromophore and the prospective metal-binding site are structurally coincident, coordination of an external metal ion is expected to directly perturb the electronic structure of the π system. Such perturbation may be reflected in intensity variation, wavelength shifts, band merging, or the emergence of additional absorption features. UV–Vis spectroscopy therefore provides a direct means of monitoring coordination-induced electronic modulation in these systems.

From a biological perspective, iron was selected as the primary target metal owing to its central role in cellular redox processes and iron homeostasis.[2] Notably, iron exists in both Fe^{2+} and Fe^{3+} oxidation states under physiological conditions, and the labile iron pool comprises contributions from both forms. Investigating both oxidation states is therefore essential to evaluate potential redox-state-dependent behaviour. Calcium and zinc were included as comparison ions: Ca^{2+} is highly abundant in biological environments and represents a hard divalent cation, while Zn^{2+} is a biologically relevant transition metal frequently encountered in metalloproteins. Inclusion of these ions enables assessment of iron selectivity in the presence of competing physiological metals.[181]

Based on the ligand architecture, each probe contains a single O,O donor set located on one pendant arm, suggesting the possibility of a 1:1 probe–metal binding interaction. Examination of the concentration-dependent spectral response up to two equivalents of metal therefore allows evaluation of saturation behaviour

consistent with such stoichiometry.

3.3.3. Method of UV–Vis

3.3.3.1. Instrumentation and Data Acquisition

UV–Vis absorption spectra were recorded using a Jasco V-770 UV–Visible/NIR spectrophotometer operated under the Spectra Manager™ software suite. Spectra were acquired in continuous scan mode at a rate of 400 nm min^{-1} with a spectral bandwidth of 1 nm. Data points were collected at 0.1 nm intervals with a response time of 0.06 s. Measurements were performed in 1 cm quartz cuvettes at room temperature.

All spectra had their auto-zero corrected prior to acquisition, and baseline correction was carried out using the corresponding solvent as blank under identical experimental conditions. Each reported spectrum represents the average of three independent scans.

3.3.3.2. Rationale for Cation Selection

Iron was selected as the primary target cation owing to its central role in cellular iron homeostasis and redox chemistry.[169, 182] Importantly, iron exists in both Fe^{2+} and Fe^{3+} oxidation states under physiological conditions, and both forms contribute to the labile iron pool. Investigation of both oxidation states therefore enables assessment of potential redox-state-dependent interactions.

Calcium and zinc were included as comparison ions to evaluate selectivity under biologically relevant conditions. Ca^{2+} is a highly abundant divalent cation in

extracellular and intracellular environments and represents a hard metal centre with strong hydration. Zn^{2+}, in contrast, is a biologically essential transition metal frequently encountered in metalloproteins. Comparison among Fe^{2+}, Fe^{3+}, Ca^{2+} and Zn^{2+} thus permits evaluation of iron specificity in the presence of physiologically relevant competing ions.

3.3.3.3. Sample Preparation and Concentration Strategy

Probe working solutions were prepared in aqueous media at fixed concentrations (EuSCA, 20 µM; TbCat, 40 µM). To ensure that spectral changes arise exclusively from metal coordination rather than dilution effects, metal stock solutions were prepared in the corresponding probe solution. This approach maintains constant probe concentration throughout the titration.

Metal ions were added incrementally to achieve concentrations ranging from 0 to 2 molar equivalents relative to the probe (or 1.8 equivalents for selected TbCat experiments). This range was selected to evaluate concentration-dependent spectral evolution and to assess potential saturation behaviour consistent with a 1:1 binding model based on the single O,O donor arm present in each ligand architecture.

Metal-only control experiments were performed across comparable concentration ranges to verify linear Beer–Lambert behaviour and to exclude intrinsic metal absorption as the primary source of spectral change.

3.3.4. Intrinsic UV–Vis absorption of probes and metal Ions in

aqueous Solution

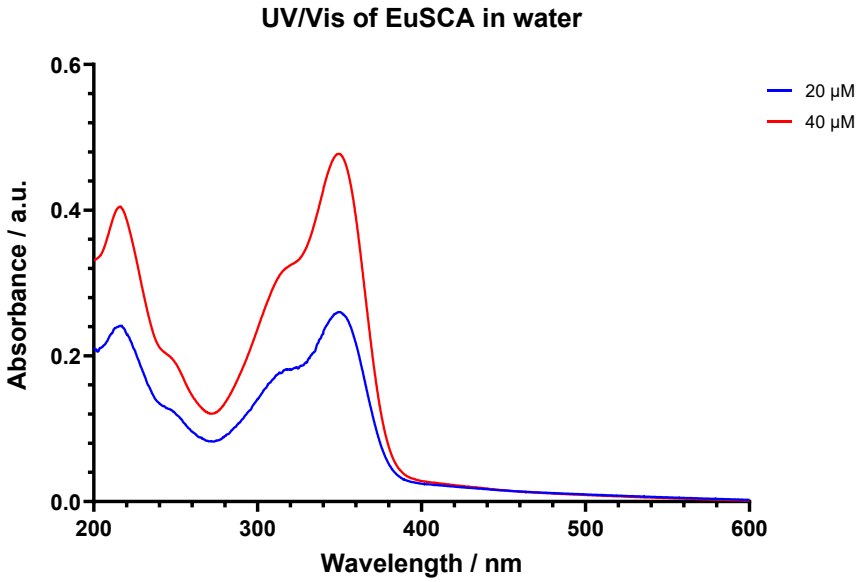


Figure 29 - UV–Vis absorption spectra of EuSCA (20 µM and 40 µM) in aqueous solution at room temperature. Three well-defined absorption maxima are observed at 216.6, 318.7 (approximate), and 350.1 nm.

The intrinsic UV–Vis absorption behaviour of the individual components was first examined in aqueous solution to establish reference spectra prior to metal titration studies.

EuSCA (20 µM) exhibits three principal absorption features at 216.6 nm, approximately 318.7 nm, and 350.1 nm. The absorbance values of these bands were maintained below 0.30 in order to ensure operation within the linear range of the instrument and to provide sufficient dynamic headroom for subsequent titration-induced increases without approaching detector saturation. In addition to measurements at 20 µM, EuSCA was also examined at 40 µM to confirm proportional absorbance scaling and to assess concentration-dependent stability of peak

positions.

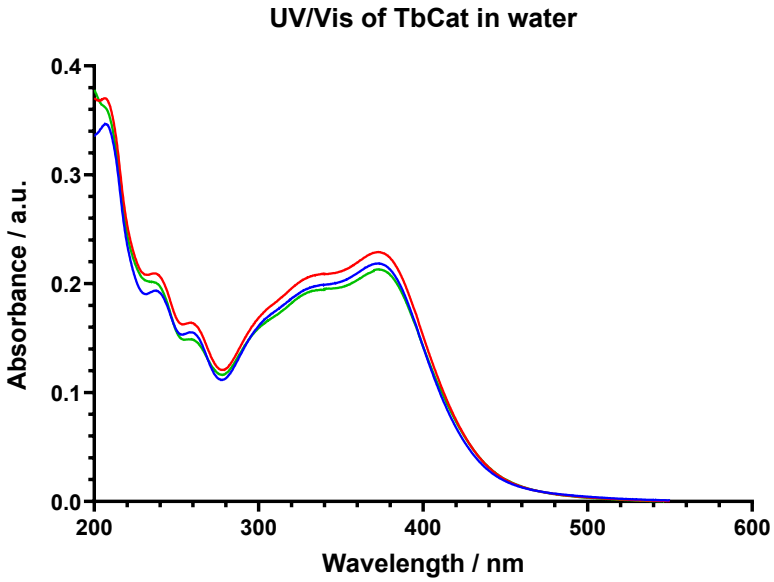


Figure 30 - UV–Vis absorption spectra of TbCat (40 µM) in aqueous solution at room temperature with measurements of three repeats. Absorption maxima are observed at 206.6, 237.4, 259.4, and 372.6 nm. In addition, two weak shoulder features are present at approximately 300 nm and approximately 330 nm.

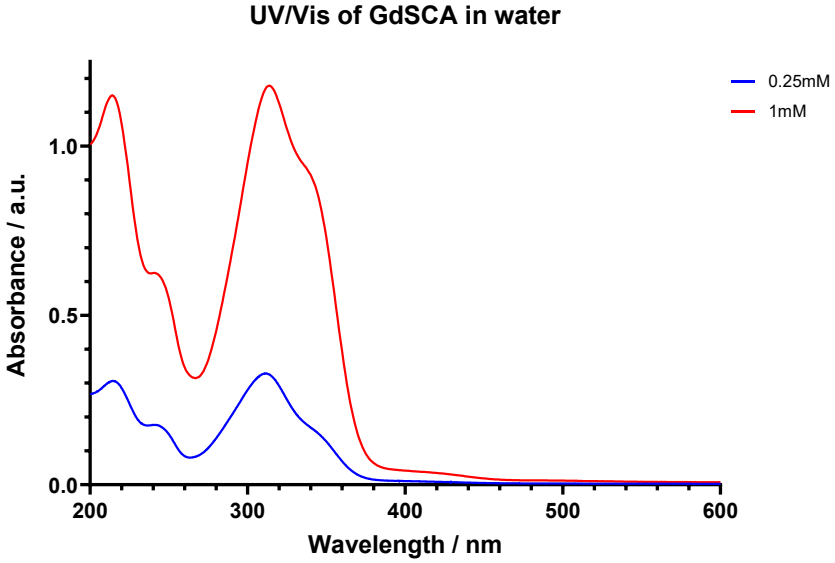


Figure 31- UV–Vis absorption spectra of GdSCA (1mM and 0.25mM) in aqueous solution at room temperature, recorded from three independent measurements. Absorption maxima are observed at 214.8, 243.4, and 309.6 nm. In addition, one weak shoulder feature is present at approximately 380 nm.

TbCat (40 µM) displays well-defined absorption maxima at 206.6, 237.4, 259.4, and 372.6 nm. Two very weak shoulder features are discernible at approximately 300 nm and approximately 330 nm. Unlike EuSCA, TbCat spectra were collected as three independent measurements without averaging, in order to evaluate the extent of experimental fluctuation. While absorbance intensity varied by up to approximately 10% between measurements, peak positions remained consistent, indicating that wavelength reproducibility was robust under the experimental conditions.

For comparison, GdSCA was examined at a higher concentration (0.25 mM) owing to its reduced spectroscopic sensitivity. At this concentration, absorption features were observed at 215 nm (A = 0.306), 311.6 nm (A = 0.329), and an estimated band near 348.2 nm (A ≈ 0.13). The requirement for significantly higher concentration to obtain comparable signal intensity supports the use of Eu^{3+} and Tb^{3+} analogues as spectroscopic surrogates for mechanistic UV–Vis investigations.

The intrinsic absorption behaviour of iron salts was also examined independently. Aqueous Fe^{3+} solutions exhibit broad absorption features centred at approximately 220 nm and 300 nm, whereas Fe^{2+} displays features at approximately 205 nm and 290 nm. Across the concentration range of 4–40 µM, the overall absorbance of both species increases proportionally with concentration across the spectral window, consistent with Beer–Lambert behaviour. These measurements confirm that iron absorption alone produces linear scaling without abrupt band restructuring under the conditions employed.

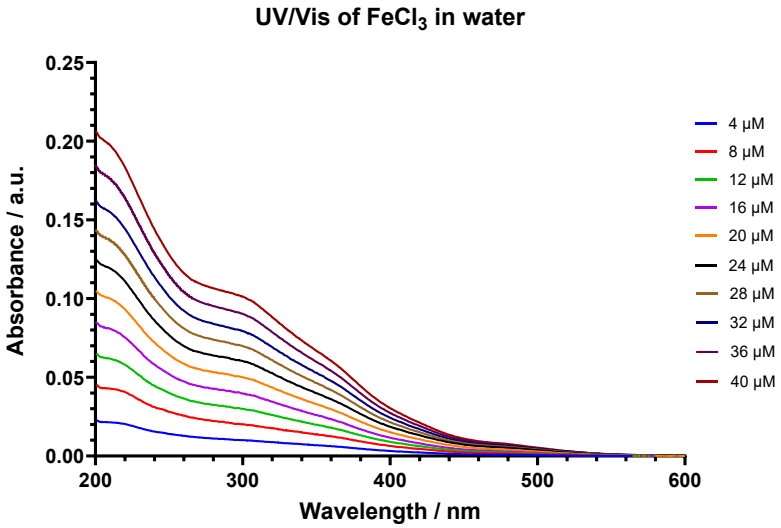


Figure 32 - UV–Vis absorption spectra of Fe^{3+} (4–40 µM) in aqueous solution at room temperature. Two broad absorption features are observed at approximately 220 nm and 300 nm.

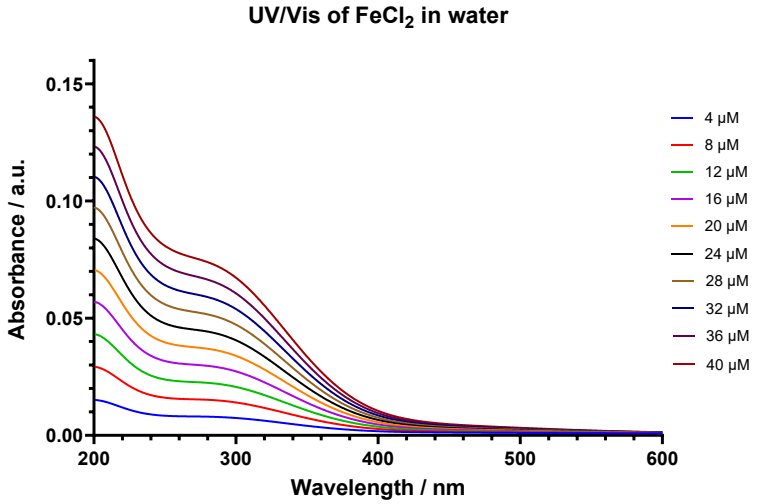


Figure 33 - UV–Vis absorption spectra of Fe^{2+} (4–40 µM) in aqueous solution at room temperature. Two absorption features are detected at approximately 205 nm and 290 nm.

Taken together, these baseline spectra establish distinct and well-defined chromophore features for EuSCA and TbCat, a comparatively weaker response for GdSCA, and linear concentration dependence for iron salts. This framework enables differentiation between intrinsic metal absorption and coordination-induced

spectral perturbation in subsequent titration experiments.

3.3.5. UV–Vis Titration of EuSCA with Metal

The UV–Vis response of EuSCA (20 µM) was investigated upon titration with Fe^{3+}, Fe^{2+}, Zn^{2+}, and Ca^{2+} in aqueous solution up to two equivalents of metal.

Addition of 1 equivalent of Fe^{3+} (20 µM) induces pronounced spectral changes. The band at 216.6 nm increases by approximately 8%, while the 318.7 nm band increases by 18% and undergoes a hypsochromic shift to 305.7 nm. In contrast, the 350.1 nm band decreases substantially by approximately 46% and shifts to 347.2 nm.

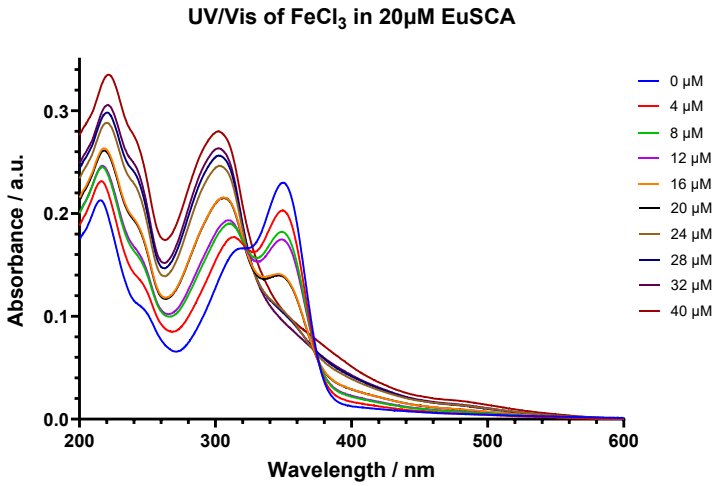


Figure 34 - UV–Vis absorption spectra of EuSCA (20 µM) during titration with $FeCl_3$ (0–40 µM, 0–2 equivalents) in aqueous solution at room temperature. At 1 equivalent, the 216.6 nm band increases by 8%, the 318.7 nm band increases by 18% and undergoes a 13.0 nm hypsochromic shift to 305.7 nm, while the 350.1 nm band decreases by 46% and shifts to 347.2 nm. At 2 equivalents, the increases at 216.6 nm and 318.7 nm reach 39% and 54%, respectively, with the latter further shifting to 302.3 nm; concurrently, the 350.1 nm band decreases by 60% and is nearly completely suppressed.

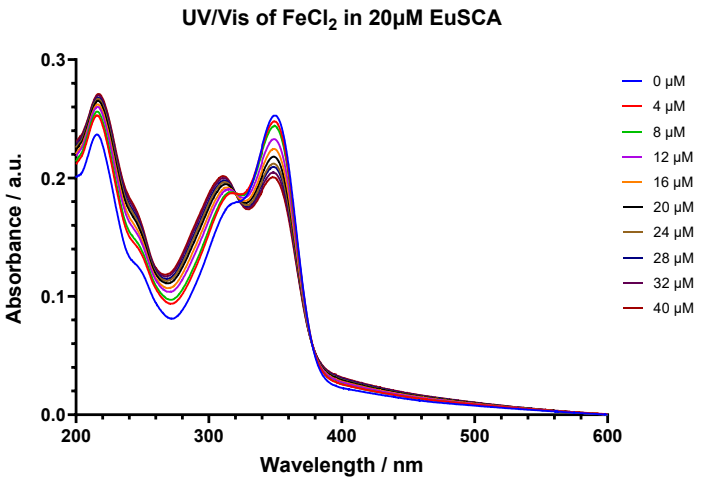


Figure 35 - UV–Vis absorption spectra of EuSCA (20 µM) during titration with $FeCl_2$ (0–40 µM, 0–2 equivalents) in aqueous solution at room temperature. The free probe exhibits absorption maxima at 216.6, 318.7, and 350.1 nm. At 1 equivalent, the 216.6 and 318.7 nm bands increase by approximately 10% and 7%, respectively, while the 350.1 nm band decreases by 16%. At 2 equivalents, the increases reach 12% and 11%, respectively, and the 318.7 nm band undergoes a 7.8 nm hypsochromic shift; the 350.1 nm band decreases by 23% and shifts to 347.7 nm.

Upon increasing the Fe^{3+} concentration to 2 equivalents (40 µM), these effects intensify. The 216.6 nm and 318.7 nm bands increase by 39% and 54%, respectively, with the latter shifting further to 302.3 nm. Concurrently, the 350.1 nm band decreases by approximately 60% and becomes nearly completely suppressed.

In comparison, Fe^{2+} produces more moderate spectral perturbation. At 1 equivalent, the 216.6 nm and 318.7 nm bands increase by approximately 10% and 7%, respectively, while the 350.1 nm band decreases by 16% with a minor hypsochromic shift. At 2 equivalents, the increases reach 12% and 11%, respectively, and the 350.1 nm band decreases by approximately 23%, accompanied by a slight wavelength shift to 347.7 nm.

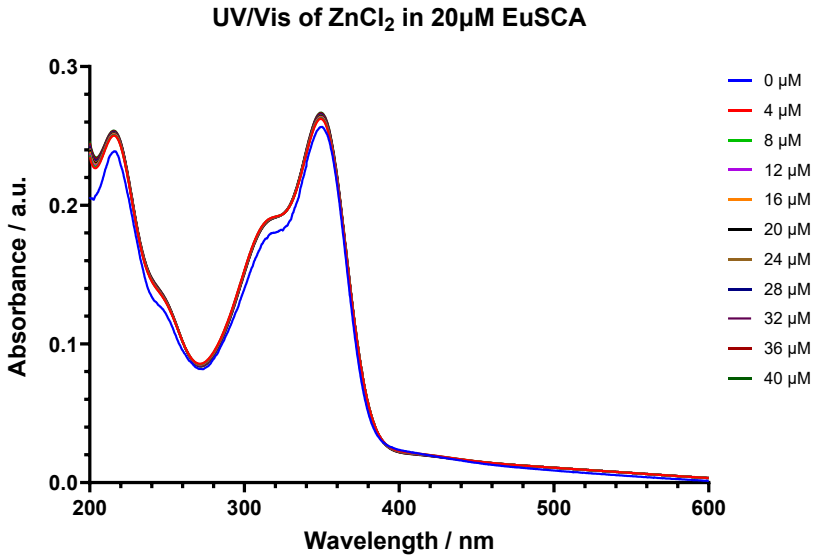


Figure 36 - UV–Vis absorption spectra of EuSCA (20 µM) during titration with ZnCl2 (0–40 µM, 0–2 equivalents) in aqueous solution at room temperature. At 1 equivalent, minimal spectral variation is observed, with the 350.1 nm band remaining essentially unchanged. At 2 equivalents, the 216.6 nm and 318.7 nm bands increase slightly by approximately 5–6%, while the 350.1 nm band shows a marginal increase without significant wavelength shift.

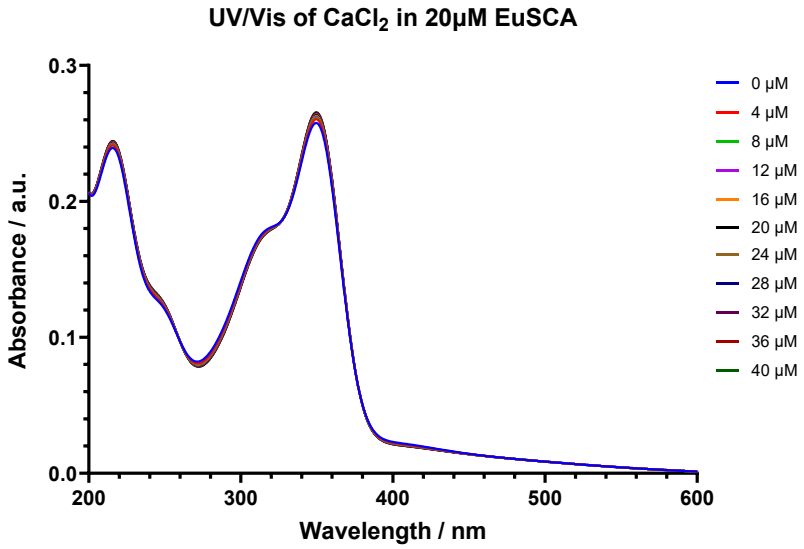


Figure 37 - UV–Vis absorption spectra of EuSCA (20 µM) during titration with CaCl2 (0–40 µM, 0–2 equivalents) in aqueous solution at room temperature. No significant spectral changes are observed at either 1 or 2 equivalents. The absorption bands remain effectively unchanged in both intensity and wavelength position throughout the titration.

Titration with Zn^{2+} results in only minimal spectral variation. At 2 equivalents, small

increases of approximately 5–6% are observed for the higher-energy bands, while the 350.1 nm band remains largely unchanged. Ca^{2+} induces negligible spectral change across the examined concentration range, with both band intensities and positions remaining effectively constant.

Overall, EuSCA exhibits a markedly stronger spectral response to Fe^{3+} than to Fe^{2+}, whereas Zn^{2+} and Ca^{2+} produce minimal perturbation under identical conditions.

3.3.6. UV–Vis Titration of TbCat with Metal Ions

The UV–Vis response of TbCat (40 µM) was examined upon titration with Fe^{3+}, Fe^{2+}, Zn^{2+}, and Ca^{2+} in aqueous solution up to 1.8 equivalents of metal.

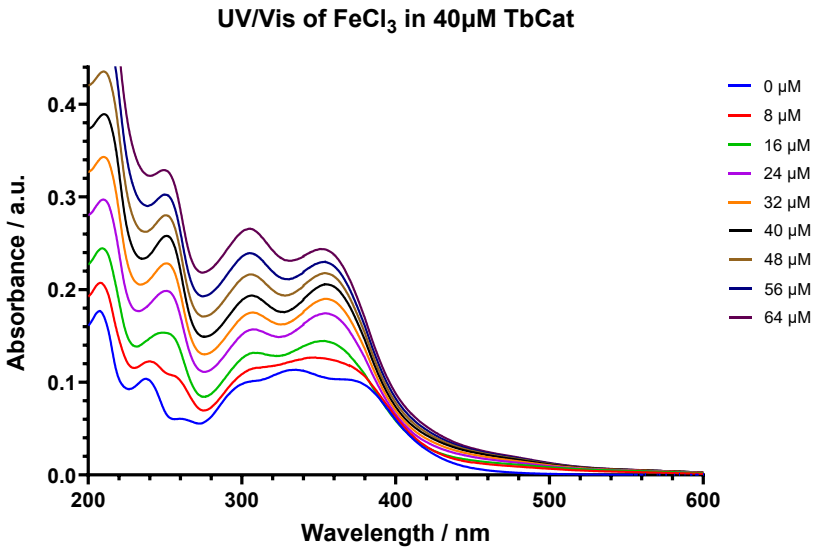


Figure 38 - UV–Vis absorption spectra of TbCat (40 µM) during titration with $FeCl_3$ (0–64 µM, 0–1.6 equivalents) in aqueous solution at room temperature. At 1 equivalent (40 µM), substantial spectral reorganisation is observed: the bands at 237.4 and 259.4 nm merge into a single feature centred at 246.8 nm, a new band appears at 307.4 nm, and the principal 372.6 nm band shifts to 352.4 nm. At 1.6 equivalents (72 µM), the hyperchromic effect intensifies, with further enhancement of the 250–310 nm region and continued suppression of the original 372 nm

band.

Addition of 1 equivalent of Fe^{3+} (40 µM) produces substantial spectral reorganisation. The previously distinct bands at 237.4 and 259.4 nm merge into a single feature centred at 246.8 nm. A new band emerges at 307.4 nm, and the principal band at 372.6 nm shifts to 352.4 nm with increased intensity in the 250–310 nm region.

Upon further increase to 1.8 equivalents (72 µM), these changes intensify. The 250–310 nm region exhibits continued hyperchromic growth, the shoulder near 330 nm becomes indistinguishable, and the 372 nm band remains displaced relative to the metal-free spectrum.

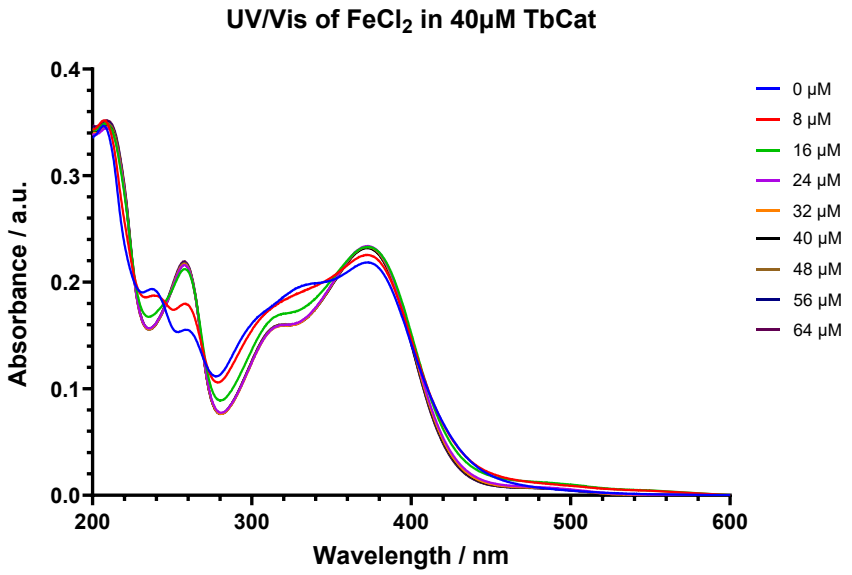


Figure 39 - UV–Vis absorption spectra of TbCat (40 µM) during titration with $FeCl_2$ (0–64 µM, 0–1.8 equivalents) in aqueous solution at room temperature. At 1 equivalent, the 237.4 nm band disappears, the 259.4 nm band increases in intensity, and the shoulder features near 300 and 330 nm merge into a single band centred at 319 nm; the 372.6 nm band increases modestly without significant wavelength shift. At 1.8 equivalents, these trends persist, with further enhancement of the high-energy bands and continued growth of the 372 nm feature.

In contrast, Fe^{2+} induces a different pattern of spectral change. At 1 equivalent, the 237.4 nm band disappears, while the 259.4 nm band increases in intensity. The shoulder features near 300 and 330 nm merge into a single band centred at approximately 319 nm. The principal 372.6 nm band increases modestly without substantial wavelength displacement.

At 1.8 equivalents, these trends persist, with incremental enhancement of the high-energy bands and continued growth of the 372 nm feature.

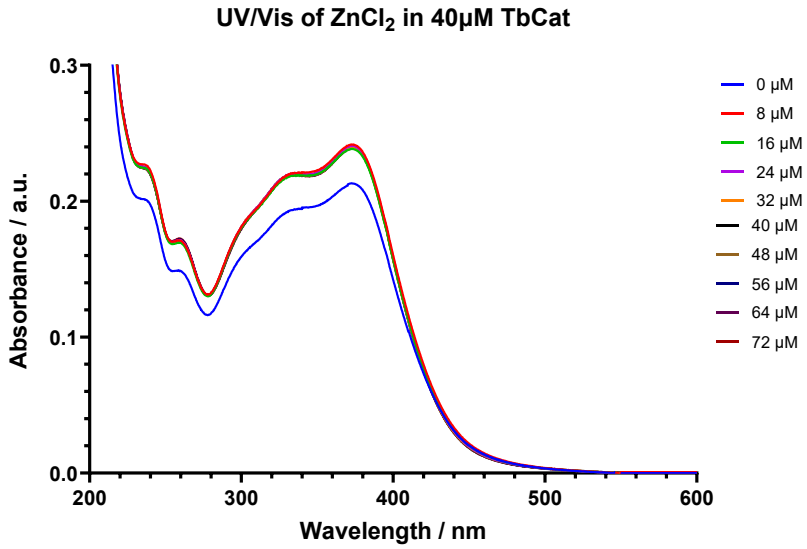


Figure 40 - UV–Vis absorption spectra of TbCat (40 µM) during titration with Zn Cl_2 (0–72 µM, 0–1.8 equivalents) in aqueous solution at room temperature. Only minor spectral changes are observed. The principal 372.6 nm band increases slightly in intensity without appreciable wavelength shift, and no significant reorganisation of the higher-energy bands is detected.

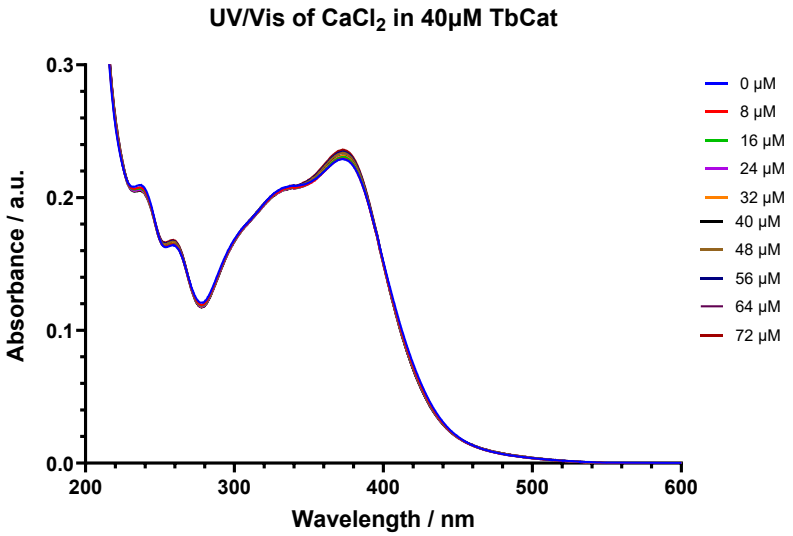


Figure 41 - UV–Vis absorption spectra of TbCat (40 µM) during titration with $CaCl_2$ (0–72 µM, 0–1.8 equivalents) in aqueous solution at room temperature. The absorption profile remains largely unchanged throughout the titration, with only a slight increase in the 372.6 nm band and no discernible spectral reorganisation.

Titration with Zn^{2+} results in only minor spectral variation, primarily a slight increase in the 372.6 nm band without significant band restructuring. Ca^{2+} produces negligible changes across the examined concentration range, with the overall spectral profile remaining essentially unchanged.

Collectively, TbCat exhibits pronounced spectral reorganisation upon interaction with Fe^{3+}, a distinct but more moderate response to Fe^{2+}, and minimal perturbation in the presence of Zn^{2+} or Ca^{2+}.

3.3.7. Electronic Interpretation and Comparative UV–Vis Analysis

The absorption spectra of EuSCA and TbCat can be interpreted primarily in terms of ligand-centred electronic transitions associated with the salicylate- and catechol-derived chromophores. This distinction is important because the intense absorption

bands observed here are unlikely to arise directly from the lanthanide ions, for which 4f–4f absorption transitions are characteristically weak. Literature calculations on salicylic acid identify several allowed transitions within the aromatic π system, including lower-energy HOMO→LUMO and higher-energy HOMO−1→LUMO+1 excitations with predominantly π→π* character.[183] Consistent with this assignment, the structurally related GdSCA complex has previously been reported to exhibit a strong absorption at approximately 309 nm that was assigned to a ligand-centred π→π* transition.[184] The absorption features of EuSCA can therefore be considered within the same manifold of salicylate-derived π→π* states, although direct assignment of individual EuSCA molecular orbitals would require calculation of the complete complex.

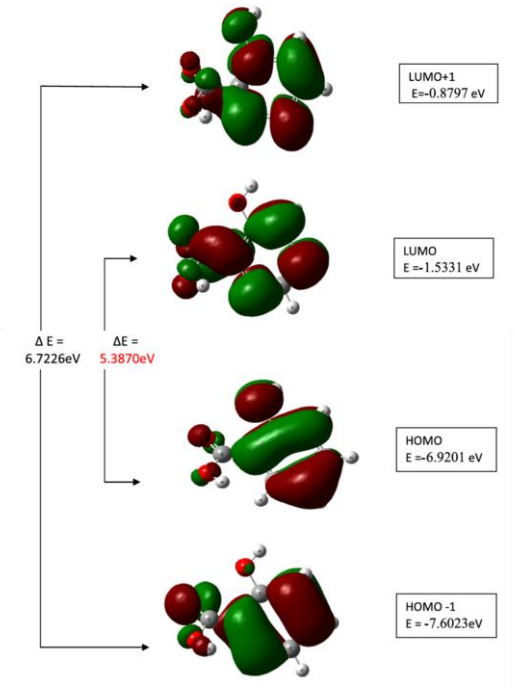


Figure 42 – DFT calculation of LUMO+1 / LUMO / HOMO / HOME-1 of salicylic acid[183]

This framework provides a possible explanation for the reciprocal spectral changes observed upon iron coordination to EuSCA. The free complex contains a shoulder at approximately 319 nm together with a prominent lower-energy feature at 350 nm. Addition of Fe^{3+} strongly attenuates the 350 nm band, which decreases by approximately 60% at two equivalents of Fe^{3+}, while the higher-energy feature increases substantially and shifts from approximately 319 to 302 nm. Fe^{2+} produces changes in the same general direction but of considerably smaller magnitude: the 350 nm feature remains clearly observable, while the higher-energy band increases only modestly. Rather than representing simple additive absorption from iron, this reciprocal behaviour is consistent with redistribution of oscillator strength between ligand-centred electronic states as coordination perturbs the electronic structure of the SCA chromophore. In this interpretation, interaction of iron with the phenolate–carboxylate O,O donor site modifies the energies, mixing and transition probabilities of the π and π* orbitals involved in the absorption process. The substantially greater effect of Fe^{3+} is consistent with its stronger interaction with hard oxygen donors and with computational studies showing oxidation-state-dependent electronic structures for Fe^{2+}- and Fe^{3+}-salicylate complexes.[183] Importantly, the assignment of the 350 nm feature to a specific HOMO→LUMO transition remains tentative; the literature calculations on the parent salicylate provide an electronic model rather than a direct calculation of EuSCA.

The catechol-containing system requires a somewhat different interpretation. Calculations on free catechol similarly identify several ligand-centred π →π* excited

states involving different combinations of occupied and unoccupied π orbitals.[185] Thus, the multiple bands observed for TbCat should not be regarded as arising from a single π→π* excitation. Upon Fe^{3+} addition, the 237 and 259 nm features merge, a feature near 307 nm becomes apparent, and the lower-energy band initially centred at 372.6 nm is displaced to approximately 352 nm. Fe^{2+} again produces a distinct and less extensive reorganisation. These observations are consistent with substantial modification of the catechol π-electronic system upon Fe coordination, but catechol differs from salicylate in an important respect: its coordination chemistry with Fe^{3+} can be coupled to ligand-to-metal charge transfer and redox chemistry. Classical studies of Fe^{3+}–catechol systems show that initial catecholate coordination can be followed by reduction of Fe^{3+} and oxidation of the catechol ligand.[185] Consequently, the electronic structure of an Fe-bound catechol unit may contain contributions beyond those of an unperturbed ligand-centred π→π* system.

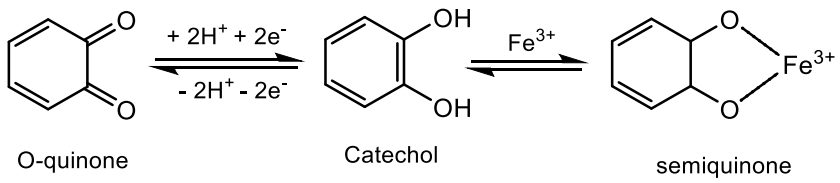


Figure 43 – Scheme of semiquinone formation

This possibility is illustrated by considering catechol and o-quinone as limiting oxidation states of the same aromatic framework. Calculations reported for the catechol/o-quinone redox couple show that oxidation substantially reorganises the frontier orbitals and introduces lower-energy excited states into the near-UV/visible region; in the calculated o-quinone spectrum, states with both n→π* and π→π*

character occur at considerably lower energies than the principal catechol absorption.[185] Fe^{3+} binding to TbCat could therefore perturb the absorption spectrum through a combination of conventional coordination-induced changes to ligand-centred π→π* transitions, ligand-to-metal charge-transfer character, and increased quinonoid character within the coordinated catechol unit. A limiting electronic description involving Fe^{3+}–catecholate and Fe^{2+}–semiquinone character is chemically plausible, although the present UV–Vis measurements do not establish the formation of semiquinone or o-quinone species.[186] The longer-wavelength changes observed for TbCat should therefore be interpreted as evidence of substantial electronic reorganisation rather than assigned uniquely to a particular redox intermediate.

This electronic interpretation also helps distinguish what is measured by UV–Vis spectroscopy from the relaxometric response discussed earlier in this chapter. A large spectral perturbation indicates that metal association substantially modifies the electronic structure of the chromophore, but it does not necessarily imply either stronger binding or a larger change in relaxivity. The latter additionally depends on the identity and population of the associated species, water accessibility and exchange, molecular reorientation and the electronic relaxation properties of the paramagnetic centres. This distinction is consistent with the observation that TbCat undergoes substantial spectral reorganisation in the presence of Fe^{3+}, whereas the SCA system provides the clearer evidence for an associated species with enhanced relaxivity. Thus, UV–Vis spectroscopy provides complementary evidence for Fe-

dependent interaction rather than a direct predictor of the magnitude of the MRI response. This also agrees with the broader conclusion of the preceding relaxometry analysis that coordination alone is insufficient; the associated species must possess relaxation properties distinct from those of its individual components.

Finally, although the aromatic groups incorporated into EuSCA and TbCat may function as sensitising antennae in luminescent lanthanide complexes, the present experiments measure absorption rather than the subsequent photophysical processes responsible for lanthanide sensitisation. The antenna effect conventionally describes absorption by the chromophore followed by processes such as intersystem crossing and energy transfer to a lanthanide excited state. Since neither ligand-to-lanthanide energy transfer nor lanthanide-centred emission is interrogated in these UV–Vis measurements, the SCA and Cat groups are more appropriately described here simply as chromophores.

3.4. Binding simulations using DynaFit

3.4.1. Rationale for DynaFit analysis

DynaFit (version 4.08.067, BioKin Ltd., Petr Kuzmič) was used to analyse the concentration-dependent titration data obtained from the T_1 relaxometry and UV–Vis measurements. DynaFit is a numerical fitting program that allows experimental data to be analysed according to user-defined chemical equilibrium models. Rather than fitting the data to an empirical mathematical function, the reaction scheme, equilibrium constants, component concentrations and response parameters are

defined explicitly, and the program calculates the corresponding equilibrium distribution of species. The model parameters are then iteratively adjusted to minimise the difference between the calculated and experimentally observed responses.

For the experiments described in this chapter, the concentration of the lanthanide complex was kept nominally constant while the concentration of the added metal ion was varied. The experimental input therefore consisted of the metal concentration at each titration point together with the corresponding measured observable, either the longitudinal relaxation rate, R_1, or the absorbance at a selected UV–Vis wavelength. The probe concentration and species-specific response coefficients were included as model parameters, while initial estimates were supplied for the equilibrium constants before optimisation. DynaFit then calculated the concentrations of the species predicted by the proposed equilibrium and used their associated response coefficients to reproduce the experimental titration curve.

The same general modelling framework was applied to both datasets, although the experimentally measured response differed between the two techniques. In the relaxometry analysis, the fitted response described the contribution of the species present in solution to the observed R_1, whereas in the UV–Vis analysis the response corresponded to the absorbance of the relevant species at the selected wavelength. In both cases, the objective was to determine whether the concentration-dependent experimental behaviour could be described by a defined probe–metal association model and to obtain the corresponding fitted equilibrium parameters.

3.4.2. DynaFit models and fitted parameters

A series of candidate equilibrium models was evaluated in DynaFit in order to compare different possible probe-to-metal binding stoichiometries. In the following expressions, Ln denotes the lanthanide complex and M denotes the added metal ion. The models considered included a 1:1 association, sequential formation of 2:1 and 3:1 Ln:M species, and an alternative one-step 2:1 association:

1 : 1	$\mathrm{M} + \mathrm{Ln} \rightleftharpoons \mathrm{LnM}$	$\mathrm{K}_{1,\ \mathrm{binding}} = \frac{[\mathrm{LnM}]}{[\mathrm{Ln}][\mathrm{M}]}$
2 : 1	$\mathrm{LnM} + \mathrm{Ln} \rightleftharpoons \mathrm{Ln_2M}$	$\mathrm{K}_{2,\ \mathrm{binding}} = \frac{[\mathrm{Ln_2M}]}{[\mathrm{LnM}][\mathrm{Ln}]}$
3 : 1	$\mathrm{Ln_2M} + \mathrm{Ln} \rightleftharpoons \mathrm{Ln_3M}$	$\mathrm{K}_{3,\ \mathrm{binding}} = \frac{[\mathrm{Ln_3M}]}{[\mathrm{Ln_2M}][\mathrm{Ln}]}$
2* : 1	$\mathrm{M} + \mathrm{Ln} + \mathrm{Ln} \rightleftharpoons \mathrm{Ln_2M}$	$\mathrm{K}^{*}_{1,\ \mathrm{binding}} = \frac{[\mathrm{Ln_2M}]}{[\mathrm{Ln}]^2[\mathrm{M}]}$

Equation 27 - candidate binding models with their bind constant expression

The first three equilibria represent sequential binding steps, whereas $\mathrm{K}^{*}_{1,\mathrm{binding}}$ describes direct overall formation of the 2:1 Ln:M species. The latter therefore has different dimensionality from the stepwise association constants and should not be compared numerically with $K_{1,\mathrm{binding}}$ or $K_{2,\mathrm{binding}}$ as though they represented the same equilibrium quantity.

For each model, initial estimates were supplied for the equilibrium constant(s), probe concentration and species-specific response coefficients. The response

coefficient defines how strongly a particular calculated species contributes to the experimentally measured signal. Its physical meaning therefore depends on the technique being modelled: in the relaxometry analysis it describes the contribution of a species to the observed R_1, whereas in the UV–Vis analysis it describes the contribution of that species to the absorbance measured at the selected wavelength. The exact response treatment used for the two datasets is described separately in Sections 3.4.3 and 3.4.4.

Because several fitted quantities were not known precisely before analysis, the fitting procedure used an iterative confidence-refinement approach. In the DynaFit script, a numerical value entered without a question mark was treated as fixed, a value followed by *?* represented an adjustable parameter with a reasonably informed initial estimate, and a value followed by *??* represented an adjustable parameter for which the initial estimate was less well constrained. The equilibrium constant remained adjustable throughout the final fitting stage because its determination was the principal objective of the analysis.

Value	Value?	Value??
Fixed parameter	Adjustable, reasonable estimate	adjustable, poor-confidence estimate

For each candidate binding model, DynaFit was used to optimise the adjustable parameters against the experimental titration data. The fitted values were then

inspected manually and compared with the current estimates. Where substantial disagreement remained, the estimate was revised and the fitting procedure repeated. Where repeated fitting returned a value consistent with the estimate, the assigned confidence was increased progressively. This cycle was continued until the non-equilibrium parameters, principally the probe concentration and response coefficients, were sufficiently stable to be fixed, while the equilibrium constant remained adjustable.

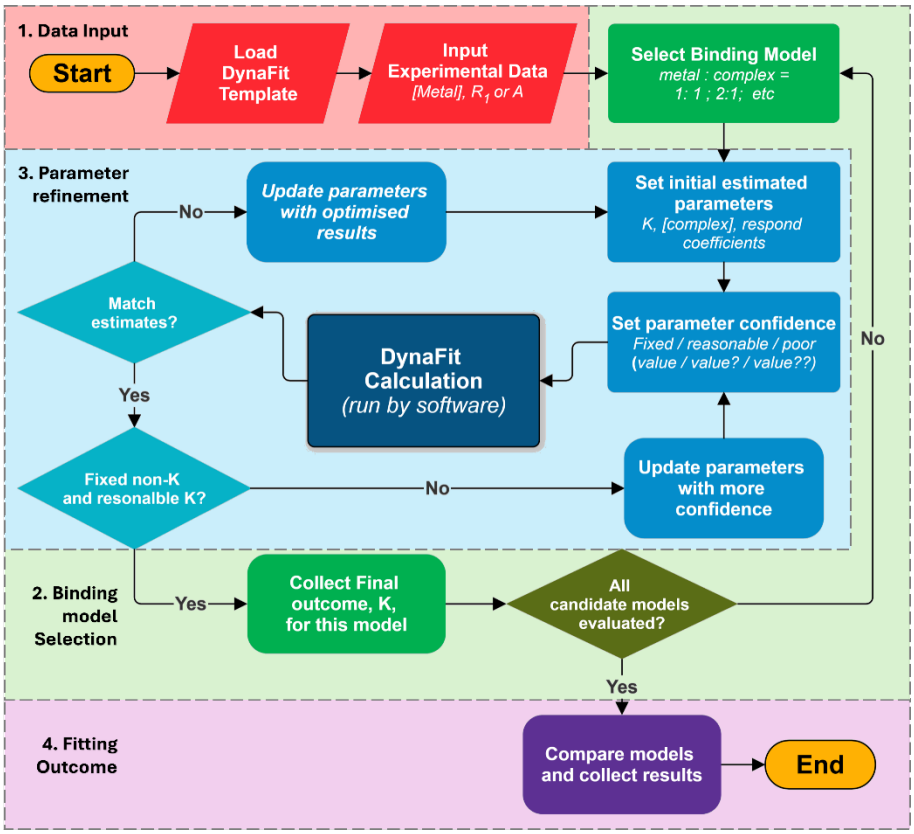


Figure 44 - Iterative DynaFit fitting and model-comparison workflow

The same refinement procedure was applied independently to each candidate binding model. A final fitted equilibrium constant and associated statistical parameters were therefore obtained for each model, allowing the different

stoichiometric descriptions to be compared subsequently on the basis of parameter stability, uncertainty and their ability to reproduce the experimental titration behaviour.

3.4.3. DynaFit analysis of T1 relaxation data

The DynaFit procedure described above was applied to the T_1 relaxometry datasets obtained for the GdSCA and GdCat systems in the presence of Fe^{3+} and Fe^{2+}. In these experiments, the Gd complex concentration was nominally fixed at 1 mM, while the concentration of added iron was varied over the titration range. The experimental input consisted of the iron concentration at each titration point and the corresponding measured longitudinal relaxation rate, R_1.

For the relaxometry analysis, the calculated DynaFit response was generated from the equilibrium concentrations of the species defined by each binding model together with their corresponding response coefficients. In general terms, the calculated relaxation response can be represented as discussed in Equation 1 and Equation 15

For clarity, only representative fitted binding isotherms are shown in the main text. The complete set of fitted isotherms for the alternative binding models and replicate datasets is provided in Appendix 0. Quantitative comparison of the fitted equilibrium constants and the relative performance of the alternative models is discussed separately in Section 3.4.5.

3.4.3.1. GdSCA system

The GdSCA relaxometry datasets showed the clearest concentration-dependent deviation from simple additive relaxation behaviour, particularly in the presence of Fe^{3+}. As described in Section 3.2, the Fe^{3+} titration produced a pronounced increase in R_1 at relatively low iron concentration, followed by a smaller incremental increase at higher concentrations. This non-linear response provided the strongest basis for testing whether the data could be represented by an equilibrium association model.

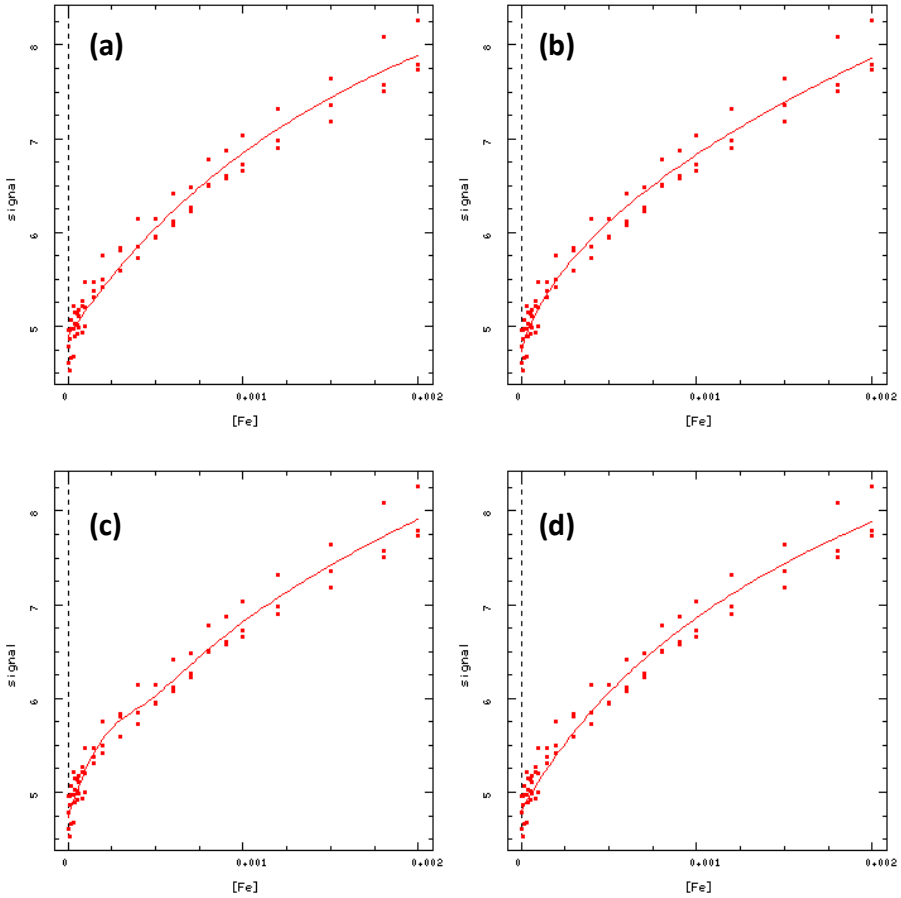


Figure 45 – Binding isotherms for the binding models of T1 relaxmetry data of $FeCl_2$ in 1mM of GdSCA (data from Figure 24) where (a-d) represent the fitting model of GdSCA vs Fe^{2+} (a) 1:1 binding; (b) 2:1 binding (2-step); (c) 3:1 binding (3-step); (d) 2*:1 binding (1-step)

DynaFit fitting of the GdSCA–Fe^{3+} data produced binding isotherms that reproduced

the overall concentration-dependent form of the experimental response. The fitted curve captures both the initially steep increase in R_1 and the subsequent reduction in slope at higher iron concentrations. This behaviour is consistent with a concentration-dependent redistribution between free and associated species, although the fitted isotherm itself does not uniquely establish the underlying binding stoichiometry.

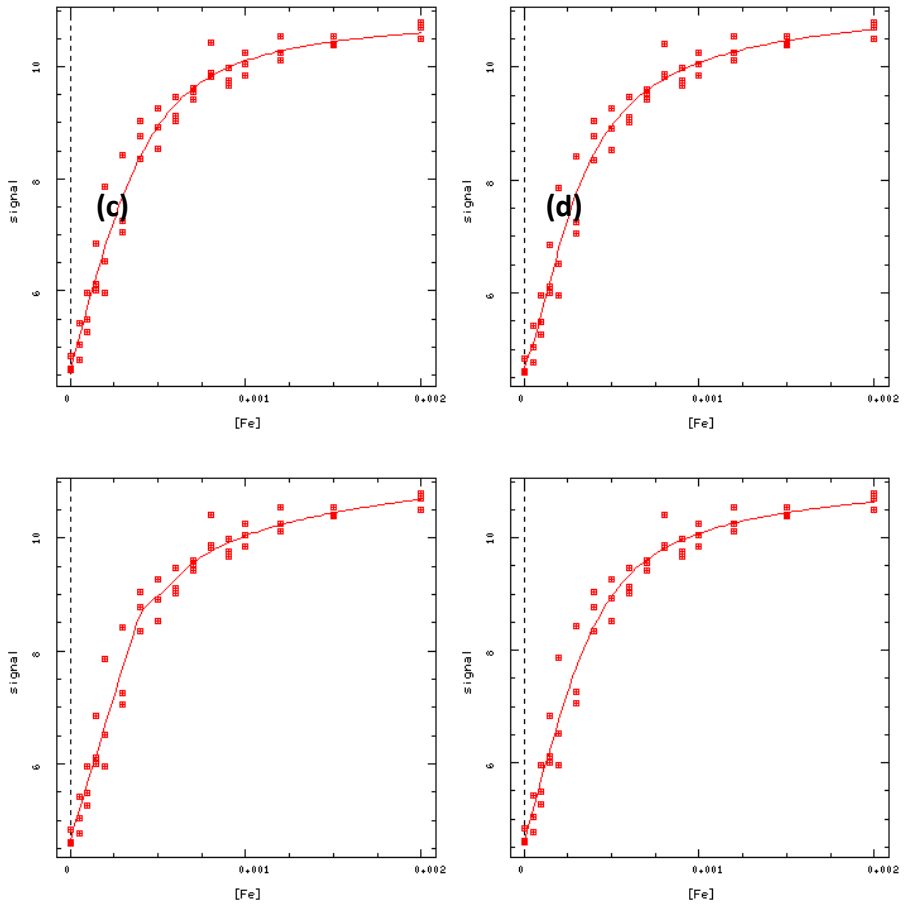


Figure 46 – Binding isotherms for the binding models of T1 relaxmetry data of $FeCl_3$ in 1mM of GdSCA (data from Figure 25) where (a-d) represent the fitting model of GdSCA vs Fe^{3+}. (a) 1:1 binding; (b) 2:1 binding (2-step); (c) 3:1 binding (3-step); (d) 2*:1 binding (1-step)

The GdSCA–Fe^{2+} dataset also showed a concentration-dependent increase in R_1, but the magnitude of the deviation was smaller than for Fe^{3+}. DynaFit was therefore

able to reproduce the general titration behaviour, although the distinction between alternative binding models was less pronounced from the fitted isotherms alone.

Taken together, the GdSCA datasets provided the most informative relaxometric basis for equilibrium modelling, with the Fe^{3+} system showing the strongest interaction-dependent relaxation response. The numerical fitted parameters and comparison between the tested binding models are considered in Section 3.4.5.

3.4.3.2. GdCat system

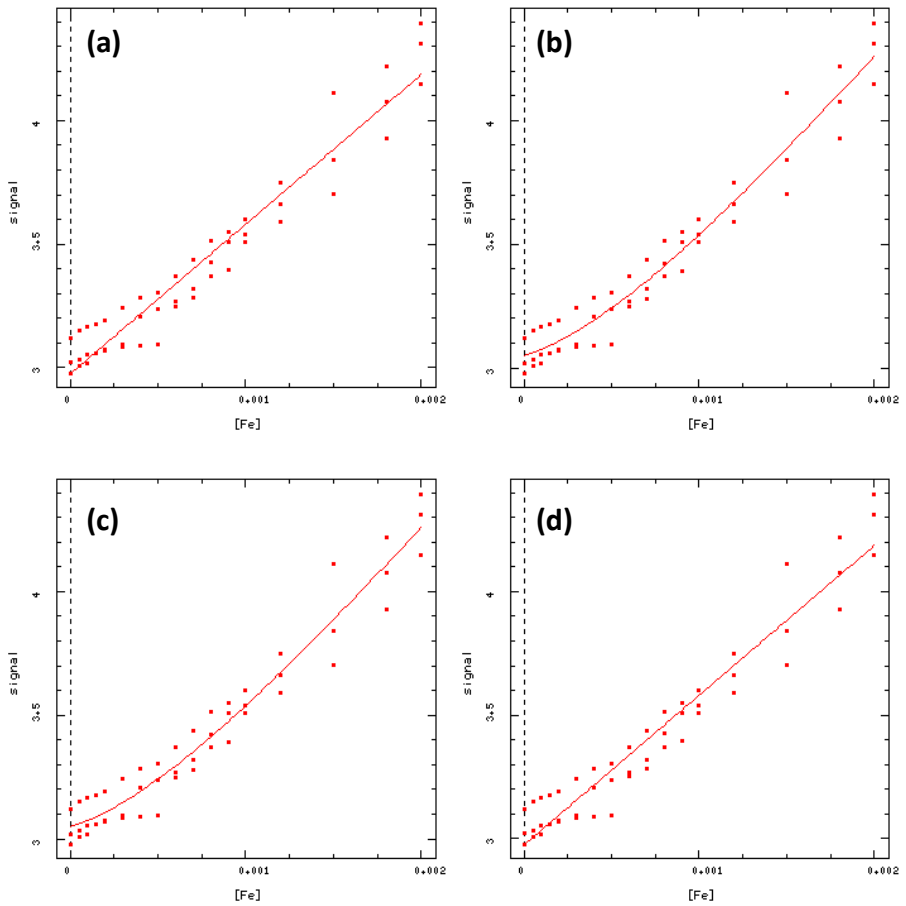


Figure 47 – Binding isotherms for the binding models of T1 relaxmetry data of $FeCl_2$ in 1mM of GdCat (data from Figure 26) where (a-d) represent the fitting model of GdCat vs Fe^{2+}. (a) 1:1 binding; (b) 1:2 binding (2-step); (c) 1:3 binding (3-step); (d) 1:2 binding (1-step)

The GdCat relaxometry datasets showed substantially weaker modulation by added iron than the corresponding GdSCA systems. The experimental responses remained closer to the behaviour expected from the individual components, particularly for Fe^{2+}, and therefore contained less information with which to distinguish between competing association models.

For GdCat with Fe^{3+}, DynaFit fitting generated isotherms that reproduced the overall concentration-dependent response, but the fitted curves were less strongly differentiated than for the GdSCA–Fe^{3+} system. This reflects the smaller experimental deviation from additive relaxation behaviour and the correspondingly weaker sensitivity of the dataset to the details of the assumed equilibrium model.

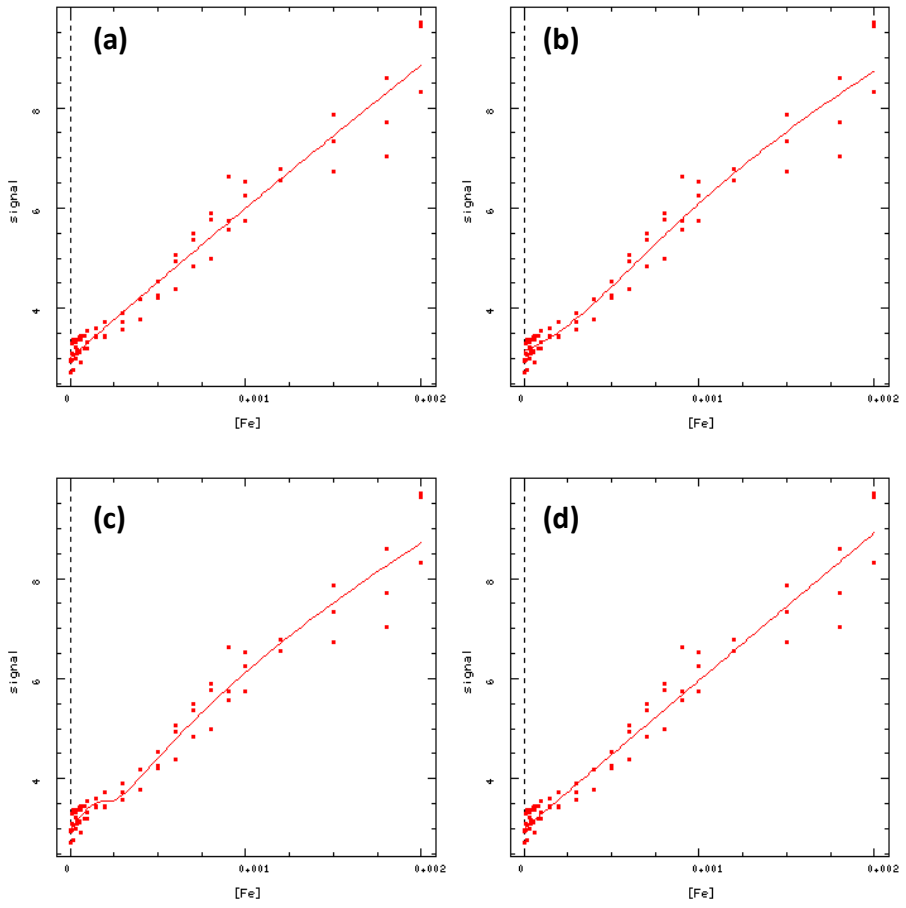


Figure 48 – Binding isotherms for the binding models of T1 relaxmetry data of $FeCl_3$ in 1mM of GdCat (data from Figure 27) where (a-d) represent the fitting model of GdCat vs Fe^{3+}. (a) 1:1 binding; (b) 1:2 binding (2-step); (c) 1:3 binding (3-step); (d) 1:2 binding (1-step)

The GdCat–Fe^{2+} dataset showed the weakest interaction-dependent relaxation response of the four systems examined. Although numerical fitting could still be performed, the resulting isotherms provided limited evidence for a well-resolved association process on the basis of relaxometry alone.

Overall, the GdCat datasets were less informative for quantitative equilibrium modelling than the GdSCA datasets. The significance of the fitted constants, the comparison between candidate binding models, and the extent to which the Cat parameters could be reliably constrained are discussed in Sections 3.4.5 and 3.4.6.

3.4.4. DynaFit analysis of UV–Vis data

The DynaFit procedure was subsequently applied to the UV–Vis titration datasets obtained for EuSCA and TbCat in the presence of Fe^{3+}, Fe^{2+} and the control metal ions. In these experiments, the concentration of the lanthanide complex was maintained at a nominally fixed value, while the concentration of added metal ion was varied over the titration range. EuSCA was measured at 20 µM and TbCat at 40 µM. For the DynaFit analysis, the experimental input consisted of the metal concentration at each titration point and the corresponding absorbance measured at a selected representative wavelength.

A single wavelength was used for each fitting dataset rather than the complete absorption spectrum. The selected wavelength corresponded to a characteristic

absorption feature that remained sufficiently well defined during the titration and showed minimal displacement in wavelength, allowing the change in absorbance to be followed consistently as the metal concentration increased. The fitted response was therefore based on the concentration-dependent absorbance at this selected wavelength.

For the UV–Vis analysis, the calculated response may be represented generally by:

$$A_{\lambda,\mathrm{calc}} = l \sum_{i} \varepsilon_{i,\lambda} [i]$$

Equation 28 – Applied Beer-Lambert Law for absorption and concentration of species

where $l$is the optical path length, $\varepsilon_{i,\lambda}$is the response coefficient of species $i$at the selected wavelength, and $[i]$is the equilibrium concentration calculated by DynaFit. The same candidate binding models described in Section 3.4.2 were examined using this spectroscopic response.

For clarity, only representative fitted binding isotherms are shown in the main text. The complete set of fitted isotherms and alternative model outputs is provided in Appendix 0. Quantitative comparison of the fitted equilibrium constants and the relative behaviour of the candidate models is presented in Section 3.4.5.

3.4.4.1. EuSCA system

The EuSCA titrations showed the clearest spectroscopic response in the presence of Fe^{3+}, consistent with the substantial perturbation of the SCA-centred absorption bands described in Section 3.3. The Fe^{3+} dataset therefore provided the most

informative UV–Vis basis for equilibrium modelling within the SCA series.

DynaFit fitting reproduced the concentration-dependent change in absorbance observed during the EuSCA–Fe^{3+} titration. The resulting binding isotherm describes the progressive spectral response over the measured metal concentration range and provides a model-based representation of the underlying change in species population.

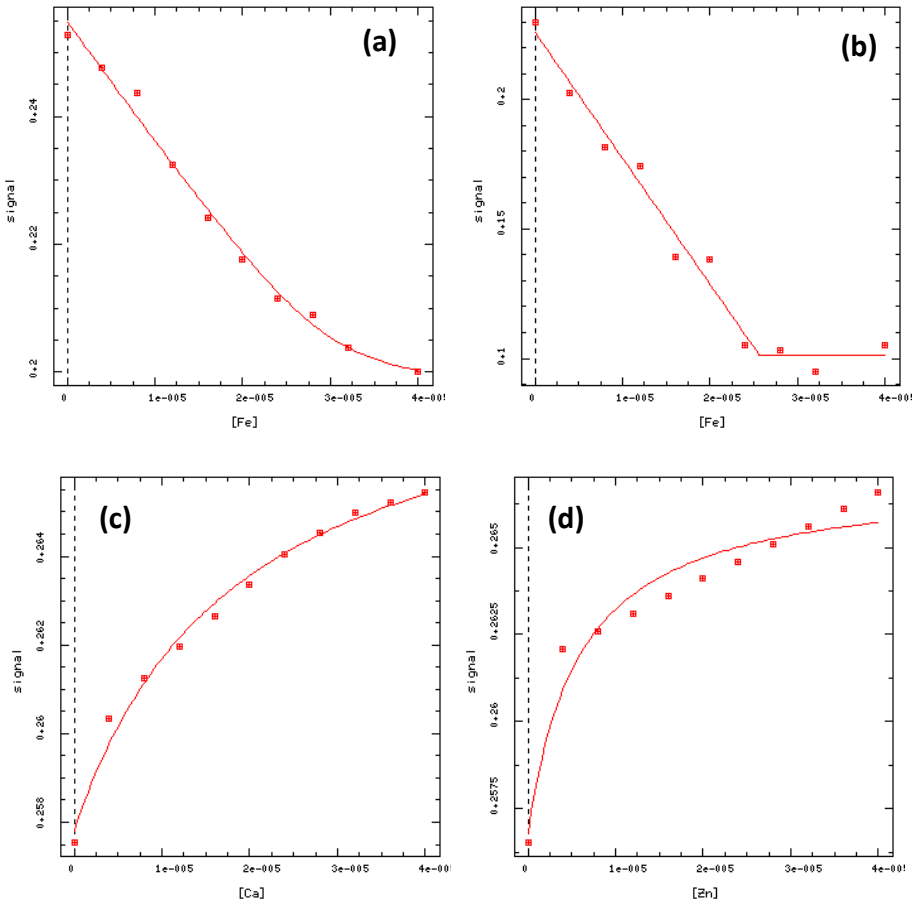


Figure 49 – The 1:1 binding isotherms for the binding models of UV-Vis data in 20 µM EuSCA at 350.0 nm (data from Figure 34-Figure 37) where (a-d) represent the guest cation. (a) $FeCl_2$; (b) $FeCl_3$; (c) $CaCl_2$; (d) $ZnCl_2$

The EuSCA–Fe^{2+} titration also produced a measurable absorbance response,

although the magnitude of the spectral perturbation was smaller than that observed for Fe^{3+}. Correspondingly, the fitted isotherms showed a less pronounced change across the titration range.

By comparison, Zn^{2+} and Ca^{2+} produced only small or negligible changes in the EuSCA absorption spectrum. These datasets therefore provided substantially less information for quantitative equilibrium fitting. Their role in the present analysis was primarily as comparative controls for metal-dependent spectral response rather than as strongly constrained sources of association constants.

Overall, the EuSCA UV–Vis datasets reinforce the preferential response of the SCA platform towards iron, particularly Fe^{3+}. The fitted equilibrium constants and their relationship to the relaxometry-derived parameters are considered in Section 3.4.5.

3.4.4.2. TbCat system

The TbCat titrations also showed clear metal-dependent spectral perturbation, particularly in the presence of Fe^{3+}. As described in Section 3.3, Fe^{3+} produced substantial reorganisation of the catechol-centred absorption features, indicating a marked change in the electronic environment of the Cat chromophore.

DynaFit fitting of the TbCat–Fe^{3+} dataset generated binding isotherms that reproduced the concentration-dependent absorbance response over the measured range. The corresponding Fe^{2+} titration produced a weaker spectroscopic response and consequently a less pronounced fitted isotherm.

The Zn^{2+} and Ca^{2+} control titrations again produced only limited spectral changes

relative to the iron systems and therefore offered less strongly constrained equilibrium information. The complete fitted outputs for these control datasets are provided in Appendix 0.

Taken together, the UV–Vis data show that both SCA- and Cat-based probes undergo detectable electronic perturbation in the presence of iron, with Fe^{3+} producing the strongest response. This contrasts with the relaxometry results, where the SCA system exhibited substantially stronger iron-dependent modulation than the Cat system. The implications of this difference, together with comparison of the fitted binding models and equilibrium constants, are discussed in Section 3.4.5.

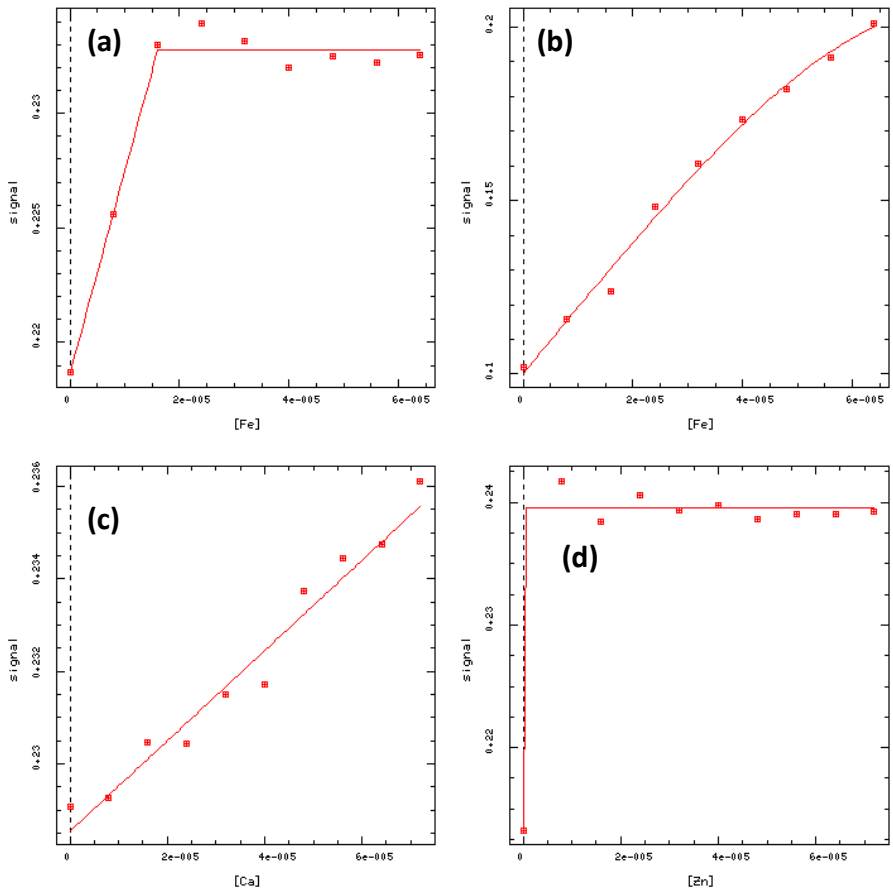


Figure 50 – 1: 1 binding isotherms for the binding models of UV-Vis data in 40 µM TbCat at 372.6 nm (data from Figure 38-Figure 41) where (a-d) represent the guest cation. (a) $FeCl_2$; (b) $FeCl_3$;

(c) $CaCl_2$; (d) $ZnCl_2$

3.4.5. Result dissection of binding model and constant

The DynaFit results were interpreted by considering both the numerical fitting outputs and the broader experimental behaviour of the probe–metal systems. Because several variables influence the fitted equilibrium parameters, the discussion was divided into four complementary comparisons. First, the relative performance of the candidate binding models was assessed to determine which stoichiometric description provided the most interpretable and sufficiently constrained parameterisation. The resulting trends were then considered in terms of differences between the SCA- and Cat-based probes, differences between the metal ions investigated, and finally differences between the relaxometry and UV–Vis datasets. This structure allows the equilibrium modelling to be interpreted in the context of both probe design and the physical observable used for fitting.

3.4.5.1. Comparison of binding models

Table 4 – Representative comparison of binding models for GdSCA–Fe^{3+} relaxometry

Model	Par#Set	Binding Constant	Std. Error	CV / %	Fitting
1:1	K_1	10030	770	7.7	Good
2:1	K_1	13800	2500	17.8	Medium
	K_2	1660	400	24.1	
3:1	K_1	1.50×10^8	3.30×10^8	218.4	Poor
	K_2	1.00×10^8	2.00×10^8	222.2	
	K_3	3.10×10^5	1.40×10^6	440.9	

Alternative binding models were compared on the basis of parameter stability, uncertainty and chemical interpretability, rather than solely on the numerical quality of the fit. In general, increasing model complexity introduced additional equilibrium

constants that were less well constrained and, in several cases, produced strongly divergent parameter values. This behaviour was most clearly observed for the GdSCA–Fe^{3+} relaxometry dataset as a representative data set (Table 4), for which the 1:1 model produced a well-defined (7.7% error) association constant, whereas sequential 2:1 (~20% error)and 3:1 models (~200% error) introduced progressively larger uncertainties, where the one-step 2:1 has K in a different unit (M^{-2}), which was not compared with other models.

Similar behaviour was observed across the other relaxometry datasets, where higher-order models frequently produced poorly balanced sequential constants or large uncertainties. These results indicate that the available titration data generally do not justify the additional complexity of the higher-order models. The 1:1 association model was therefore taken as the principal model for subsequent comparison of probe and metal-ion behaviour, while the complete higher-order fitting results are provided in Appendix 8.3.2.

3.4.5.2. Comparison of SCA and Cat systems

The fitted parameters showed a clear difference between the SCA- and Cat-based probes, particularly in the relaxometry datasets. For Fe^{3+}, the 1:1 model gave an association constant of approximately $1.0 \times 10^4\ \mathrm{M}^{-1}$ for GdSCA, compared with approximately $2.6 \times 10^1\ \mathrm{M}^{-1}$ for GdCat. The corresponding T_1 data also showed a substantially larger concentration-dependent response for GdSCA, consistent with the stronger deviation from additive relaxation described in Section 3.2. These results indicate that formation of an Fe^{3+}-associated species produces a much

greater relaxation response for the SCA probe than for the Cat analogue.

A similar difference was observed for Fe^{2+}. The GdSCA 1:1 model gave an apparent association constant in the $10^2\ M^{-1}$range, whereas the GdCat–Fe^{2+} fit approached the no-association limit. Thus, across both iron oxidation states, the SCA platform gave a more clearly resolved relaxometric response than the Cat platform.

This difference was not reproduced simply by considering the UV–Vis response. Both SCA and Cat showed measurable spectral perturbation following addition of Fe, particularly Fe^{3+}, demonstrating that the Cat ligand is also capable of responding to metal coordination. From the experimental result, metal binding to SCA still produced a much larger change in Gd-centred relaxation than metal binding to Cat, which is consistent with the relaxometry. Based on the fitting results, SCA provided the more effective conversion of metal association into a measurable Gd-centred relaxation response.

Table 5 - Comparison of 1:1 fitted parameters for SCA and Cat

Complex	Cation	Binding Constant	Std. Error	CV / %	Response
GdSCA	Fe^{3+}	10030	770	7.7	Strong
	Fe^{2+}	443	10	2.3	Moderate
GdCat	Fe^{3+}	25.56	0.5	2	Weak
	Fe^{2+}	6.27×10^{-11}	1.40×10^{-12}	2.3	Not Resolved

Overall, the DynaFit analysis therefore supports GdSCA as the more promising platform for iron-responsive MRI, because its metal-dependent interaction is accompanied by a substantially larger and more readily modelled relaxation response.

3.4.5.3. Comparison of metal-ion responses

The DynaFit analysis was also used to compare the fitted binding parameters obtained with different metal ions. However, the quality of the resulting parameterisation differed substantially between the iron and non-iron datasets. For the SCA-based system as an example in Table 6, the Fe^{3+} and Fe^{2+} datasets both allowed the fitting procedure to return finite association constants, with the fitted value for Fe^{3+} being substantially greater than that obtained for Fe^{2+}. This provided a consistent model-based difference between the two oxidation states.

Table 6 - Comparison of UV–Vis responses of EuSCA towards different metal ions

Cation	Binding Constant	Std. Error	CV / %	[EuSCA] / µM	Fitting Response
Fe^{3+}	1.68×10^{17}	1.4×10^{-16}	8.5	25.6	Strong
Fe^{2+}	1.23×10^{6}	2.7×10^{6}	22.0	30.1	Moderate
Ca^{2+}	7.1×10^{13}	4.1×10^{12}	5.7	8.9×10^{9}	Unreliable
Zn^{2+}	7.2×10^{13}	6.8×10^{12}	9.4	8.9×10^{9}	Unreliable

By contrast, the Ca^{2+} and Zn^{2+} datasets did not provide sufficient information for a meaningful determination of the corresponding association constants. During fitting, DynaFit was able to reduce the numerical fitting error by substantially altering the estimated EuSCA concentration from its experimentally expected value. Though the parameters were more informative rather than quantitative and accurate, for the iron-containing datasets, the fitted probe concentration was reasonably close to the experimentally prepared concentration of 20 µM. In comparison, the corresponding fits for Ca^{2+} and Zn^{2+} drove the fitted EuSCA concentration to approximately 9000 M. Such a large deviation from the experimental concentration indicates that the optimisation was exploiting poorly constrained parameters to reproduce the measured response, rather than providing a physically meaningful equilibrium

description.

These results indicate that the DynaFit analysis could provide a useful quantitative description of the iron-containing datasets, whereas the Ca^{2+} and Zn^{2+} datasets did not contain sufficient information to determine meaningful binding constants. The fitted values obtained for the latter should therefore not be interpreted as evidence for, or against, a particular metal-binding affinity. Instead, they demonstrate that the model could reduce the fitting residual only by allowing parameters that were not well constrained by the experimental data to move away from their physically expected values.

The fitted Fe^{3+} and Fe^{2+} results were subsequently compared with the corresponding relaxometry and UV–Vis observations. More detailed consideration of parameter uncertainty, the deviation of fitted parameters from their experimental estimates, and the implications of these differences for the reliability of the fitted association constants is provided in Section 3.4.6.

3.4.6. Limitations of DynaFit fitting

The DynaFit analysis provided a useful framework for examining whether the experimental data could be described by probe–metal association models, but the resulting parameters should not be regarded as equally well determined across all datasets. The reliability of a fitted equilibrium constant depends not only on the numerical convergence of the optimisation, but also on the amount of information contained in the experimental response and on how independently the parameters

contributing to that response can be constrained. Several factors therefore need to be considered when interpreting the fitted association constants obtained in this study, including parameter correlation, the iterative treatment of auxiliary parameters, the different concentration ranges and observables used for T_1 and UV–Vis measurements, and potential contributions from sample impurities or other species.

Parameter identifiability: The first limitation concerns parameter identifiability. In both the relaxometry and UV–Vis models, the observed response depends on both the equilibrium distribution of species and the response coefficient assigned to each species. Consequently, different combinations of an association constant and a bound-species response coefficient can produce similar calculated responses. This is particularly relevant to the relaxometry data, where K_1 and the response coefficient of the associated Gd–Fe species were found to be correlated. The DynaFit optimisation may therefore determine the overall fitted response more strongly than it determines each individual parameter. In addition, the iterative procedure used in this study progressively fixed auxiliary parameters such as the probe concentration and response coefficients once the fitted values were consistent with their estimates. This improved numerical stability, but means that the uncertainty reported for the final K_1 does not fully incorporate uncertainty in parameters that had already been fixed. The fitted association constants should therefore be interpreted as apparent values whose precision depends on the constraints imposed by the individual dataset.

Model complexity: The second limitation concerns the flexibility of the fitting procedure. DynaFit optimises the numerical agreement between the calculated and experimental responses and does not, by itself, determine whether every fitted parameter remains consistent with the experimental preparation. This was particularly evident when higher-order models or weak-response datasets were considered. Additional binding steps introduced extra equilibrium constants and response coefficients, allowing the calculated response to be adjusted more flexibly, but in several cases this was accompanied by strongly divergent or physically unrealistic fitted parameters. A similar effect was observed for the fitted probe concentration in some UV–Vis datasets. Although the optimisation could reduce the fitting error, the fitted concentration could become substantially different from the experimentally prepared concentration. Such behaviour indicates that the additional degrees of freedom were being used to reproduce the measured response rather than providing independent evidence for the proposed binding process. Consequently, a lower fitting error was not taken as sufficient justification for a more complex model or a fitted parameter that was inconsistent with the experimental system.

Fitting for UV-Vis vs Relaxometry: The third limitation arises from the different concentration ranges sampled by the two techniques. The T_1 measurements covered a substantially wider Fe concentration range, approximately 0–2 mM, whereas the UV–Vis experiments were performed over a lower concentration range of approximately 0–100 µM. These datasets therefore did not sample the same region

of the binding response to the same extent. The wider relaxometry range included both the low-metal region and the higher-concentration regime in which the observed R_1 response became increasingly non-linear, whereas the UV–Vis measurements principally sampled the lower concentration region. In particular, the non-linear relaxation behaviour of free Fe^{3+} means that its contribution cannot necessarily be represented by a single concentration-independent response coefficient across the complete relaxometry range.

This difference means that the association constants obtained from T_1 and UV–Vis data should not be expected to agree exactly even when both datasets are described using the same underlying 1:1 equilibrium model. Agreement in binding stoichiometry and in the qualitative direction of the fitted response is therefore more informative than exact numerical agreement between $K_{\mathrm{T1}}$and $K_{\mathrm{UV-vis}}$.

Purity: The fourth limitation relates to the different susceptibility of the two experimental observables to contributions from species other than the intended probe–metal complex. The UV–Vis response is sensitive to any absorbing species present in the sample, meaning that impurities or products arising from incomplete purification may potentially contribute to the measured absorbance or produce small changes in the observed spectral feature. This is particularly relevant because the DynaFit UV–Vis analysis used the absorbance at a fixed representative wavelength rather than tracking the instantaneous maximum of the absorption band. Consequently, a small displacement of an absorption band, or a change in the spectrum arising from another absorbing component, could appear as a change in

the fitted observable even if it did not directly originate from the proposed probe–metal association.

In comparison, the T_1 response is less susceptible to contributions from diamagnetic organic impurities because a significant change in R_1 requires a paramagnetic contribution or a change in the relaxation environment. This does not eliminate interference from impurities or other species, but it provides a different sensitivity profile from UV–Vis spectroscopy. Thus, the UV–Vis and relaxometry datasets provide complementary rather than interchangeable evidence for the proposed binding process.

3.4.7. Summary of DynaFit analysis

DynaFit provided a common equilibrium-based framework for analysing the concentration-dependent T_1 relaxometry and UV–Vis responses of the lanthanide probes. Candidate binding models were evaluated by fitting the experimental data to the corresponding equilibrium schemes, with the fitted equilibrium constants and species-specific response coefficients used to describe the observed titration behaviour. Among the models examined, the 1:1 association model generally provided the most parsimonious and interpretable description of the informative datasets, while higher-order models introduced additional parameters that were less consistently constrained.

The fitted results further indicated differences between the two probe platforms and between the two iron oxidation states. The SCA-based system gave the most clearly

resolved relaxometric binding behaviour, particularly for Fe^{3+}, for which the fitted association constant was substantially greater than that obtained for Fe^{2+}. The Cat system produced weaker and less consistently constrained relaxometry-derived association parameters. In the UV–Vis analysis, Fe-dependent responses could also be fitted using the proposed equilibrium models, although several weak-response datasets did not provide sufficiently constrained finite association constants. The DynaFit results therefore support the SCA platform as the more clearly resolved system for quantitative analysis of iron-associated changes in the present study.

Overall, the DynaFit analysis supports a 1:1 probe–metal association as the principal model for the most informative datasets and provides apparent association constants for comparison of the systems studied. The T_1 and UV–Vis analyses should, however, be regarded as complementary applications of the same equilibrium framework rather than interchangeable measurements, because they probe different physical responses over different concentration ranges. The fitted constants therefore provide quantitative or semi-quantitative measures of the proposed association under the experimental conditions, rather than definitive intrinsic thermodynamic binding constants.

3.5. Summary and limitations of Chapter 3

This chapter has examined the behaviour of the GdSCA and GdCAT systems in aqueous solution, with the aim of determining whether iron–probe interactions can give rise to measurable modulation of longitudinal relaxation and thereby provide a chemical basis for iron-responsive MRI contrast.

T_1 relaxometry measurements established the baseline behaviour of both probe systems in the absence of iron, demonstrating concentration-dependent relaxation consistent with conventional gadolinium-based contrast agents. Upon the introduction of iron, distinct differences between the two ligand platforms were observed. The SCA-based system, particularly in the presence of Fe^{3+}, showed reproducible deviations from simple additive relaxation behaviour, indicating the formation of an associated species that contributes disproportionately to the observed R_1. In contrast, the CAT-based system exhibited weaker and less consistent responses, limiting mechanistic interpretation under the same framework.

Complementary UV–Vis spectroscopy provided independent support for differential metal interaction across the ligand platforms. The SCA-derived complexes showed clear spectral perturbations upon Fe^{3+} addition, consistent with coordination-driven electronic changes, whereas the CAT system exhibited less distinct and less reproducible responses. These observations reinforce the relaxometry findings and indicate that the SCA scaffold provides a more robust and experimentally tractable platform for iron interaction in aqueous solution.

Taken together, the DynaFit analysis provided an equilibrium-based approach for interpreting the concentration-dependent T_1 and UV–Vis responses of the lanthanide

probes. The candidate binding models were compared using their fitted parameters and the stability of the resulting parameter sets, with the 1:1 probe–metal association generally providing the most interpretable description of the informative datasets. The analysis therefore provided estimates of the apparent association constants and supported the use of a simple 1:1 binding model for the most clearly resolved probe–iron systems.

This chapter also used DynaFit to examine the aqueous behaviour of the GdSCA and GdCat probe systems using T_1 relaxometry, UV–Vis spectroscopy and equilibrium-based analysis. T_1 measurements established the baseline relaxation properties of the two probes and showed distinct iron-dependent responses, with the clearest deviation from additive relaxation observed for GdSCA in the presence of Fe^{3+}. The corresponding DynaFit analysis indicated that a minimal 1:1 probe–iron association model provided the most interpretable description of the informative relaxometry datasets, while higher-order models introduced additional parameters that were less well constrained. The fitted results further supported a stronger apparent association of SCA with Fe^{3+} than with Fe^{2+} and a substantially stronger relaxometric response of SCA than Cat. Complementary UV–Vis measurements provided an independent indication of metal-dependent interaction through changes in the electronic absorption behaviour of the ligand environment, particularly upon addition of Fe^{3+}. Together, these results support the formation of an iron-associated species capable of altering the relaxation behaviour of the Gd probe, with the SCA platform providing the clearest overall response.Taken together with the

experimental observations, the results of this chapter demonstrate that iron-dependent modulation of relaxivity is observable under controlled aqueous conditions and is strongly dependent on ligand design. The SCA system provided the clearest evidence for an associated Gd–Fe species capable of altering relaxation behaviour beyond simple mixture effects, with Fe^{3+} producing a stronger response than Fe^{2+}. The Cat system also showed evidence of metal-dependent interaction in the spectroscopic measurements, but this interaction produced substantially weaker and less clearly resolved changes in Gd-centred relaxation. These findings identify SCA as the more promising platform for developing an iron-responsive MRI contrast mechanism.

Despite these findings, several important limitations remain. The relaxometry and UV–Vis experiments sampled different Fe concentration ranges and probe the interaction through different physical observables, while the simplified equilibrium models do not account explicitly for the full complexity of aqueous iron speciation or competing species. UV–Vis measurements may also be more susceptible to contributions from other absorbing species or impurities, particularly where small spectral changes are assessed at a fixed wavelength. Consequently, the magnitude and detectability of the observed responses may differ under more complex conditions.

Accordingly, this chapter establishes a chemical basis for iron-responsive relaxivity modulation and identifies the SCA platform as the stronger candidate for further development, but does not by itself demonstrate specific iron recognition or robust

imaging contrast in biological environments. The subsequent chapters therefore examine the behaviour of the probes under increasingly complex conditions, where cellular compatibility, competing biological components, sensitivity and whole-organism detectability become important determinants of their practical utility.

4. Testing contrast agents in vitro

4.1. General concept and cellular model

Following the characterisation of probe behaviour in aqueous solution as discussed in Chapter3, it is necessary to evaluate whether the observed iron-dependent relaxation effects can be translated into a biologically relevant environment. While the aqueous system provides a controlled framework for isolating probe–iron interactions, it does not capture key features of living systems, including compartmentalisation, restricted diffusion, and regulated iron handling. As such, the present chapter investigates probe behaviour at the cellular level, representing the simplest biological model in which these additional factors are introduced.

The primary objective of the in vitro experiments is therefore not simply to observe signal changes, but to determine whether MRI readouts obtained in a cellular system can be meaningfully interpreted in terms of probe behaviour and iron interaction. In particular, it is necessary to assess whether the deviations from additive relaxation behaviour identified in solution are preserved, modified, or obscured under biologically relevant conditions. This distinction is critical, as MRI signal reflects not only molecular properties but also spatial distribution and compartmentalisation.

Within this framework, three practical requirements must be addressed. First, a suitable concentration range must be established in which the probes can be applied without inducing significant cytotoxicity, ensuring that any observed effects arise from probe behaviour rather than cell damage. Secondly, an experimental system

must be defined in which probe localisation and retention can be controlled, allowing distinction between extracellular and cell-associated contributions to the MRI signal. Thirdly, the system must permit controlled variation of iron conditions, enabling comparison between baseline and iron-modulated states.

To achieve this, experiments were performed using cultured mammalian cells under standardised conditions. The cellular system introduces additional complexity relative to aqueous measurements, including intracellular compartmentalisation and regulated iron uptake, storage, and trafficking. These factors are expected to influence both the accessibility of iron to the probe and the spatial relationship between paramagnetic centres, and therefore may affect the observed relaxation behaviour.

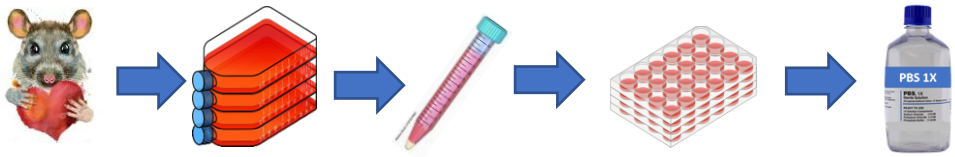


Figure 51 – in vitro experiment steps

In this project, the cardiomyocyte cell line, H9c2(2-1) was purchased from Elabscience Biotechnology Inc.® with a catalogue Number of EP-CL-0089.[187] The cell line was collected from Rattus norvegicus, Rat, at its embryo state, and the myoblast cells was collected from the heart/myocardium.[188]

All H9c2 cell lines were incubated in a tissue culture media of DMEM (10 % FBS + 1 % P/S) in humidified air (95 %) and CO_2(5 %) at 37 °C until reach an confluency of roughly 80 %. The tissue culture medium was renewed every 2 days. The cells are

subcultured weekly with a ratio of 1:3. The frozen cell sample was stored in 70% DMEM + 10% DMSO +20 % FBS + 1% P/S

Within this controlled cellular framework, subsequent sections examine the safety, applicability, and interpretability of the proposed contrast agents. Cytotoxicity studies define the operational concentration window, while MRI experiments evaluate whether probe-associated signal changes can be observed and related to underlying chemical interactions. Together, these experiments establish whether the probe systems retain functional relevance in a biological environment and provide a basis for progression to in vivo studies.

4.2. Cytotoxicity

4.2.1. Rationale of contrast agent toxicity in vitro

The evaluation of cytotoxicity represents a necessary step in the development of gadolinium-based contrast agents for biological applications. Although gadolinium(III) provides the paramagnetic properties required for MRI, the free Gd^{3+} ion is known to exhibit biological toxicity[83]. This makes cytotoxicity assessment a critical consideration for further development.

To address this, clinically used contrast agents employ strongly chelating ligands, most commonly macrocyclic systems such as DOTA or DO3A derivatives. These ligands confer high thermodynamic stability and kinetic inertness, significantly reducing the likelihood of gadolinium release under physiological conditions[189]. As a

result, Gd–DOTA-based complexes have been widely adopted in clinical imaging and are generally considered to exhibit favourable safety profiles.

However, the safety of a gadolinium-based system cannot be assumed solely from the presence of a stable chelating framework. [154] Toxicity may arise from multiple sources. One potential pathway is the partial release of gadolinium through de-chelation or trans-metalation processes, which has been associated with less stable contrast agents in clinical use.[157, 190] In addition, the molecular structure of the probe itself may contribute to cytotoxicity, for example through altered physicochemical properties such as increased lipophilicity, enhanced cellular uptake, or interactions with biological components. [182]

In the present work, the parent Gd–DO3A framework has been modified through the introduction of aromatic iron-binding moieties. While this modification is intended to enable interaction with iron, it may also influence biological behaviour relative to established clinical agents. Consequently, it is necessary to assess whether these structural changes introduce additional cytotoxic effects or alter the overall biological compatibility of the system.

Previous studies on related lanthanide-based systems have indicated that similar complexes can undergo cellular uptake without evident induction of cell death under specific experimental conditions.[182] However, such observations are system-specific and cannot be directly extrapolated to the present probe designs.

Therefore, cytotoxicity experiments were conducted to determine whether the

complexes are tolerated under controlled cellular conditions. This establishes an operational concentration range for subsequent in vitro MRI experiments and ensures that any observed signal changes can be attributed to probe behaviour rather than loss of cell viability.

4.2.2. Method of LDH cytotoxicity

The lactate dehydrogenase (LDH) cytotoxicity assay was employed as a rapid and scalable method for evaluating cell membrane integrity and, by extension, cytotoxicity.[191] This assay is based on the release of intracellular LDH into the extracellular medium upon loss of membrane integrity, which serves as an indicator of cell damage. The assay kit was bought from Cambridge Bioscience® as CytoSelect™ LDH Cytotoxicity Assay Kit (Cat. Number: CBA-241) [192]

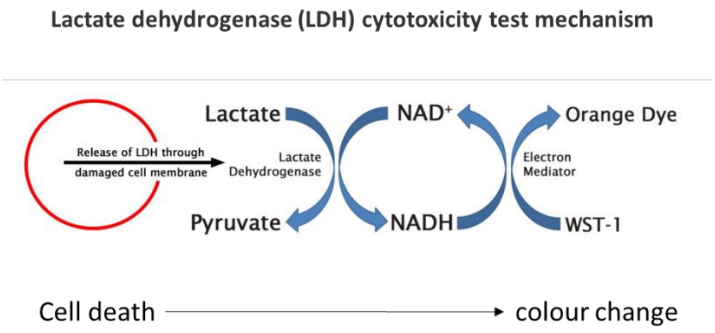


Figure 52 – LDH cytotoxicity assay mechanism[192]

As illustrated in Figure 52, the released LDH catalyses the conversion of lactate to pyruvate, accompanied by the reduction of NAD^+ to NADH. In a coupled enzymatic reaction, NADH subsequently reduces a tetrazolium salt (WST-1) to form a coloured formazan product. The accumulation of this chromophore can be monitored

spectrophotometrically, with absorbance measured at 450 nm. According to the Beer–Lambert law, the measured absorbance is proportional to the amount of LDH present in the medium and therefore reflects the extent of membrane damage.

In a standard experimental design, cells are cultured in 96-well plates and exposed to test compounds under controlled conditions. Untreated cells are used as the negative control, representing baseline LDH release, while complete cell lysis induced by Triton X-100 provides the positive control corresponding to maximal LDH release. The cytotoxic response is then quantified by normalising the absorbance of experimental samples to these controls, according to Equation 10.

$$\frac{OD_{\text{sample}} - OD_{\text{negative}}}{OD_{\text{positive}} - OD_{\text{negative}}} \times 100\% = \%\text{Relative Cytotoxicity}$$

Equation 29 – Calculation of relative cytotoxicity based on LDH release

This assay provides a convenient and high-throughput approach for cytotoxicity assessment, enabling comparison across multiple experimental conditions. However, its reliability depends on the assumption that background LDH activity and other potential sources of signal remain minimal under the experimental conditions.

4.2.3. Method development and validation of the LDH assay

The LDH assay was initially implemented following the standard protocol described in Section 4.2.2. However, under these conditions, the assay failed to provide meaningful differentiation between experimental groups. Specifically, both positive and negative controls exhibited similarly high absorbance values where more than

50% of the ranges suggested by their mean and standard deviation overlapped. This behaviour is inconsistent with the expected response, in which the negative control should represent minimal LDH release and the positive control should correspond to maximal signal.

To further investigate this issue, the assay was adapted to include time-resolved measurements, with absorbance monitored at regular intervals following addition of the LDH reagent. As shown in as Figure 53, the reaction exhibited a rapid and continuous increase in absorbance, reaching saturation at approximately 4000 a.u. within tens of minutes. Although the time-dependent progression of the reaction could be captured, substantial variability between replicates was observed, and the separation between experimental conditions remained minimal. These observations indicate that the assay response was dominated by signal saturation rather than reflecting genuine differences in cytotoxicity.

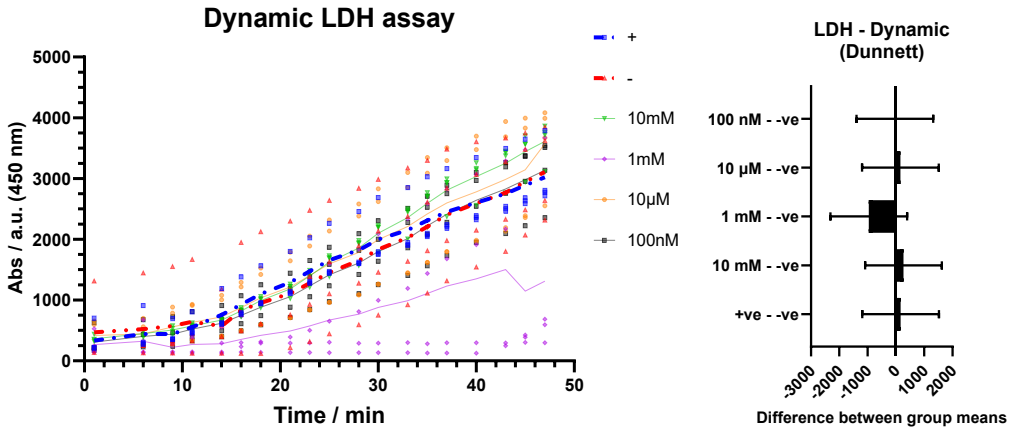


Figure 53 – Dynamic LDH assay of GdSCA.(Left) Time-dependent absorbance (450 nm) for GdSCA (100 nM–10 mM) with +ve and –ve controls.(Right) LDH release at 30 min (mean ± SD), but the assay failed to show difference between the negative and postive with this method.

Given that LDH release is intrinsically linked to cell membrane disruption, the presence of significant signal in the negative control suggested that the measured response was not solely derived from cell death. To test this, control experiments were performed in the absence of cells. Unexpectedly, measurable absorbance was still observed under these conditions, indicating that the LDH assay signal was influenced by components of the culture medium rather than originating exclusively from cellular LDH.

This observation prompted a systematic evaluation of the culture medium composition. The basal medium (DMEM) contains defined components such as glucose, amino acids, and inorganic salts,[193] none of which are expected to directly participate in the LDH-coupled reaction. In contrast, foetal bovine serum (FBS), typically present at 10% in standard culture conditions, is a biologically derived mixture containing proteins, enzymes, and other low-molecular-weight species. As FBS originates from blood, it may contain residual enzymatic activity, including LDH or related metabolites.

To evaluate the contribution of FBS, comparative experiments were conducted with and without serum, and in the presence or absence of cells (Figure 54). In the absence of FBS, the absorbance signal remained effectively constant over time, indicating minimal background activity. In contrast, conditions containing FBS exhibited a clear increase in absorbance, even in the absence of cells. These results demonstrate that FBS is the dominant source of background signal in this assay system, and that its presence compromises the ability of the LDH assay to resolve

cytotoxicity under standard conditions.

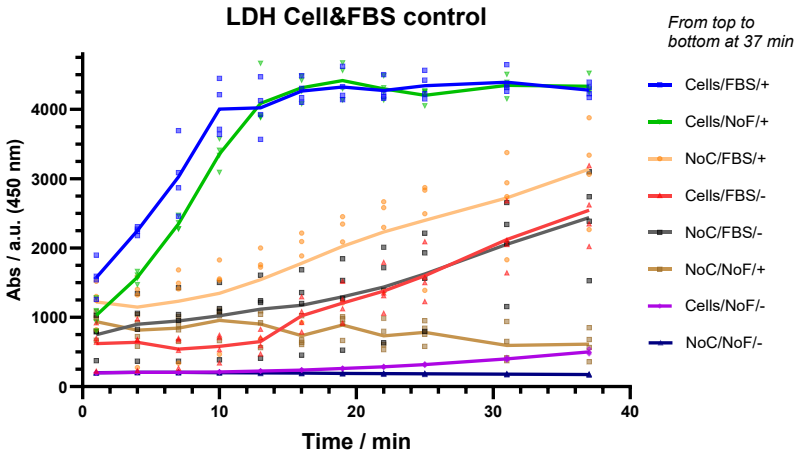


Figure 54 – LDH cytotoxicity assay with controls of cells and FBS ("Cells" represents the presence of cells; "NoC" represents the absence of cells; "FBS" represents the presence of the reagent FBS; "NoF" represents the absence of FBS; "+" means a positive controlled experiment; "-" means a negative controlled experimental.)

Based on these findings, the assay conditions were modified to minimise serum-derived interference while maintaining cell viability. The FBS concentration was reduced from 10% to 3% in subsequent experiments. Complete removal of FBS was avoided, as serum components are required to support normal cellular function and prolonged incubation in serum-free conditions may introduce non-specific cell stress. In addition, the duration of compound treatment and LDH reaction time were adjusted to ensure that measurements remained within the dynamic range of the assay.

Taken together, these results demonstrate that the standard LDH assay protocol is not directly applicable to this system due to serum-derived interference. Through systematic evaluation and modification of assay conditions, a protocol was

established that reduces background signal and enables meaningful comparison between experimental conditions. The final optimised protocol is described in Appendix 8.3.1.

4.2.1. LDH Cytotoxicity evaluation of GdSCA and GdCat

Under the optimised assay conditions, cytotoxicity of both GdSCA and GdCat was evaluated using time-resolved LDH measurements. Representative absorbance profiles are shown in Figure 55 and Figure 56, where all conditions exhibit a time-dependent increase in signal, eventually approaching saturation. This behaviour reflects the cumulative nature of the LDH-coupled reaction, with residual background contribution from the culture medium, particularly from FBS, as discussed in Section 4.2.3.

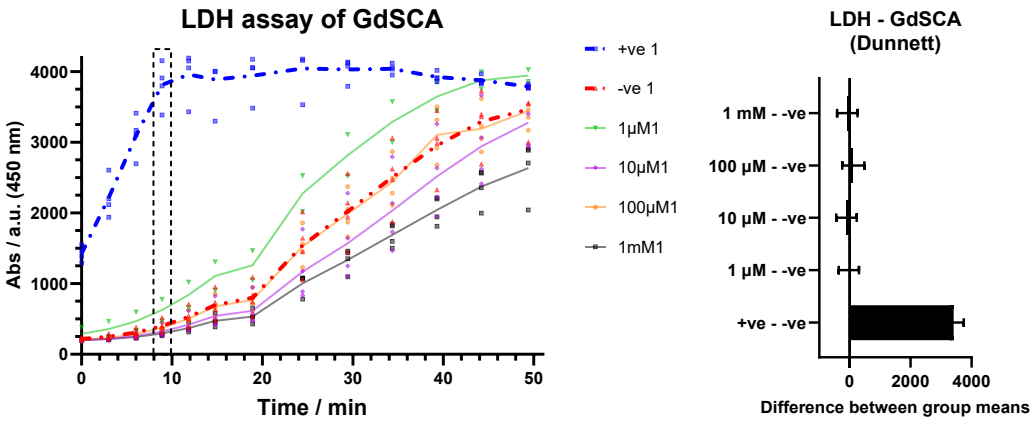


Figure 55 –LDH cytotoxicity assay of GdSCA.(Left) Time-dependent absorbance (450 nm) for GdSCA (1 µM–1 mM) with +ve and –ve controls.(Right) LDH release at 9 min (mean ± SD). One-way ANOVA (Dunnett vs control) showed no significant differences ($p > 0.05$).

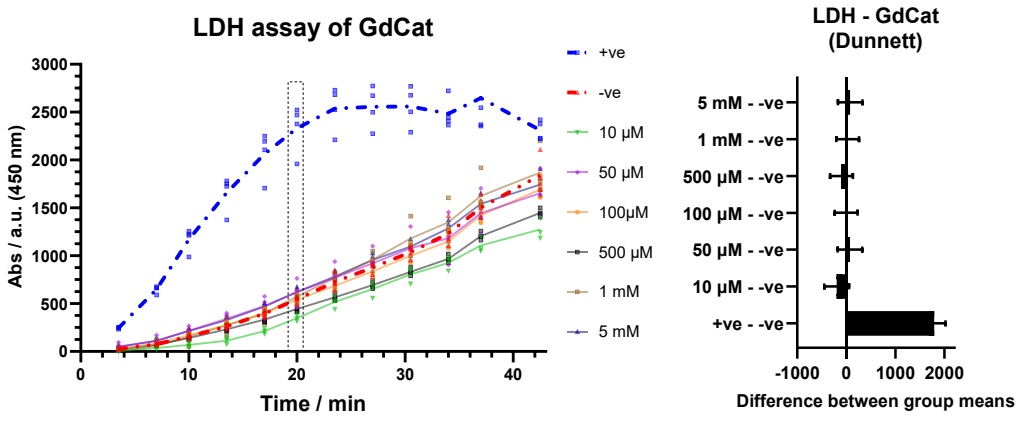


Figure 56 –LDH cytotoxicity assay of GdCat.(Left) Time-dependent absorbance (450 nm) for GdCat (10 µM–5 mM) with +ve and –ve controls.(Right) LDH release at 20 min (mean ± SD). One-way ANOVA (Dunnett vs control) showed no significant differences ($p > 0.05$).

Despite this overall trend, a clear distinction between the positive control and all other conditions is observed. The positive control shows a markedly elevated signal (mean ≈ 2332 a.u.), consistent with complete membrane disruption. In contrast, both GdSCA- and GdCat-treated samples display signal levels comparable to the negative control (mean ≈ 543.5 a.u.), with only minor variations across the tested concentration range. No systematic increase in signal intensity or reaction rate is observed with increasing concentration, indicating the absence of concentration-dependent cytotoxic effects.

For quantitative comparison, absorbance values at 9 min within the linear region of the assay were analysed using one-way ANOVA with Dunnett's multiple comparisons test against the negative control. In both cases, the positive control exhibited a highly significant increase in LDH release ($p < 0.0001$), confirming assay responsiveness. In contrast, no significant differences were observed for any concentration of GdSCA or GdCat relative to the control ($p > 0.05$ for all groups).

Taken together, these results indicate that neither probe induces detectable membrane damage in H9c2 cells under the experimental conditions employed. This establishes a working concentration range for subsequent in vitro MRI experiments, in which observed signal changes can be attributed to probe behaviour rather than loss of cell viability.

It should be noted that the assay conditions represent a compromise between minimising serum-derived interference and maintaining physiological relevance. The reduced FBS concentration and shortened treatment time may limit sensitivity to longer-term or subtle cytotoxic effects. However, within the scope of this study, the absence of detectable toxicity supports the feasibility of proceeding to cellular MRI evaluation.

4.3. MRI in vitro

4.3.1. Aim and concept

The aqueous studies described in Section 3.2 established that the GdSCA system, particularly in the presence of Fe^{3+}, exhibits deviations from additive relaxivity behaviour that are consistent with the formation of an associated Gd–Fe species.

The aim of the in vitro MRI experiments was to continue to establish a controlled cellular system for evaluating the iron-dependent behaviour of the gadolinium-based contrast agents developed in this work, namely GdSCA and GdCat. This model was intended to bridge the gap between aqueous relaxometry measurements and

in vivo imaging, where probe behaviour is influenced not only by coordination chemistry but also by cellular uptake, retention, and spatial distribution.

Within this framework, the primary experimental readout was the longitudinal relaxation time (T_1) obtained from MRI measurements of cell-containing samples. The measured signal therefore reflects the combined contributions of probe localisation, cellular association, and potential interaction with iron under different conditions.

The experimental design was developed to isolate these contributions in a stepwise manner. In particular, iron conditions were varied to span nominally iron-free, intermediate, and elevated levels, enabling assessment of whether the contrast agents exhibit differential behaviour across biologically relevant iron environments.[43, 194] In parallel, probe treatment conditions were controlled to distinguish between intracellularly associated and extracellular probe fractions.[42, 195]

It is noted that, in contrast to homogeneous solution measurements, the MRI signal in this system depends on the spatial distribution of cells within the sample and on the localisation of the probe relative to the detection region. As a result, the measured T_1 values represent local, sample-dependent quantities rather than bulk properties. The implications of this for experimental design and data interpretation are addressed in the following sections.

4.3.2. Method of MRI in vitro

To evaluate the performance of the contrast agents in a controlled cellular environment, in vitro MRI measurements were conducted using a phantom-style experimental configuration. All experiments were performed on a Bruker AVIII 400 system (9.4 T, 400 MHz for ^{1}H) at the Chemistry Research Laboratory, University of Oxford. This system provides a highly homogeneous superconducting magnetic field suitable for micro-imaging and relaxation measurements. [135]

Given the relatively small differences in iron concentration under investigation, sensitivity to spatial variation in the magnetic field was a critical consideration. Although spatial encoding in MRI is achieved through applied gradient fields, residual inhomogeneity in the static magnetic field (B_0), as well as susceptibility differences between samples, can introduce variability in measured relaxation times and signal intensity.[42, 138] For comparative measurements across multiple samples, it is therefore essential to minimise positional bias within the detection volume. [135]

To address this, samples were arranged in a concentric configuration within a cylindrical holder, such that each sample occupied an equivalent radial position relative to the magnet isocentre. This geometry ensures that all samples experience comparable magnetic field conditions, thereby reducing systematic variation arising from spatial effects and improving the reliability of relative comparisons.

For practical implementation, samples were loaded into 3 mm NMR tubes, allowing multiple conditions to be measured simultaneously within the 3 cm diameter

detection region of the instrument. A custom 12-position sample holder was designed to arrange the tubes at equal angular intervals on a common radius, with one position deliberately offset to serve as an orientation marker. Each experimental condition was measured in at least three independent biological replicates to account for variability inherent to cell-based systems.

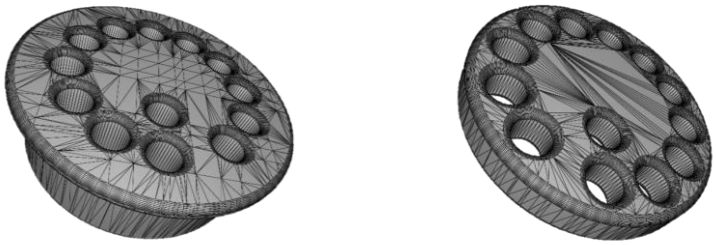


Figure 57 – Tube holders' blueprinting for 3D printing. The holder was designed with hole of marker position to label the orientation of the image and it involves two pieces to fix as cap (left) and bottom (right)

Accurate alignment of the sample tubes was found to be essential for obtaining consistent cross-sectional images. In particular, the tubes must remain parallel to one another and aligned with the imaging axis to avoid geometric distortion and artefacts such as partial-volume effects or signal overlap between adjacent samples. Initial attempts using manually drilled holders were unsuccessful due to poor control over tube orientation and deformation under wet conditions. Consequently, a custom holder was designed using 3D modelling (SolidWorks) and fabricated by 3D printing. The final design consisted of two aligned components that secure both the top and bottom of the tubes, ensuring stable positioning during MRI acquisition.

This configuration provides a reproducible and spatially controlled framework for simultaneous measurement of multiple samples, enabling systematic evaluation of

probe behaviour under different experimental conditions.

4.3.3. Setup design and development

To establish a reproducible and spatially controlled in vitro MRI system, several key aspects of experimental design were considered, including sample positioning, stabilisation of the imaging layer, and overall system sensitivity.

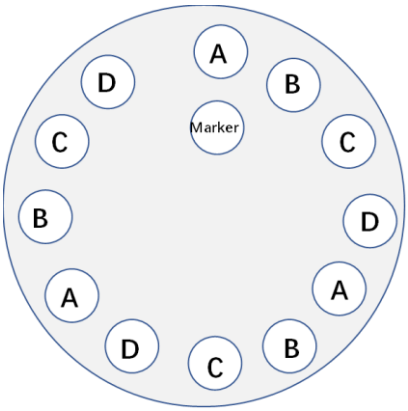


Figure 58 - Schematic of concentric tube arrangement for the tube holder of MRI in vitro

In high-field MRI measurements, spatial variation in the static magnetic field (B_0) and radiofrequency coil sensitivity can introduce systematic differences in signal intensity and apparent relaxation behaviour across the detection volume. To minimise such positional bias, all samples were arranged in a symmetric configuration, with each tube placed at an equivalent radial distance from the magnet isocentre. This concentric arrangement ensures that all conditions experience comparable magnetic field and detection sensitivity, thereby enabling meaningful relative comparison between samples.

To further improve spatial reproducibility, perfluorodecalin (PFD) was introduced as

an immiscible, high-density support phase. Due to its higher density relative to aqueous media, PFD forms a stable lower layer within the sample tube, allowing the aqueous phase containing cells and contrast agent to be positioned at a defined height within the imaging region. Importantly, PFD contains no detectable ^{1}H signal and does not contribute to MRI contrast, thereby providing an inert background that enables clear differentiation of the active sample layer. This configuration reduces variability associated with cell sedimentation and ensures consistent placement of the region of interest during imaging.

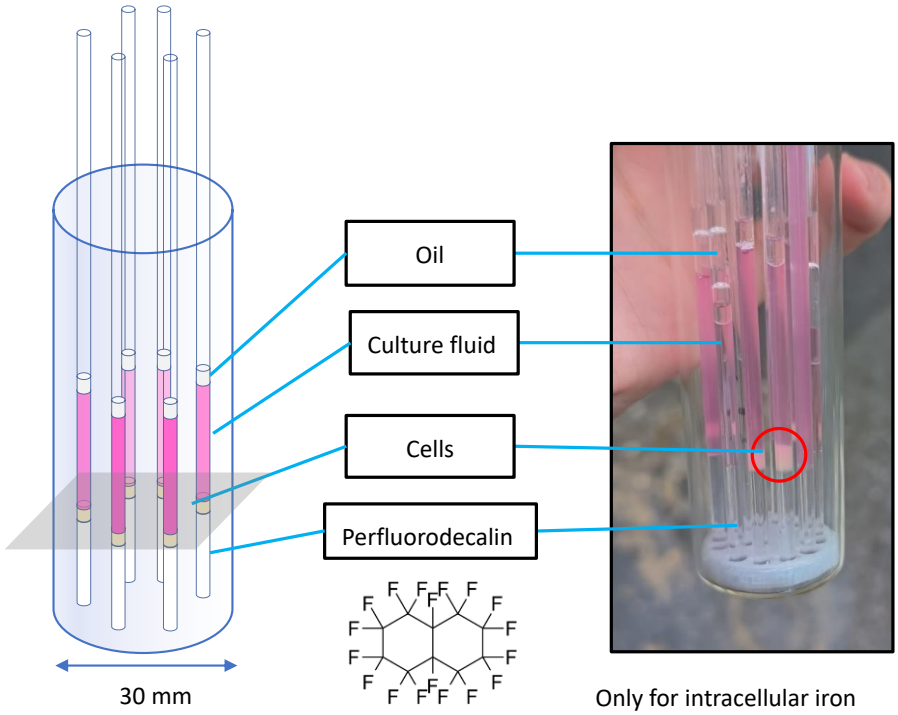


Figure 59 –MRI set up with perfluorodecalin

The operational sensitivity of the MRI system was assessed using aqueous solutions of the gadolinium-based contrast agent over a range of concentrations. These preliminary measurements indicate that observable signal contrast emerges only

above approximately 100 µM, while lower concentrations produce minimal detectable differences relative to background. This establishes a practical detection threshold for the system and defines the concentration regime in which subsequent experiments were conducted.

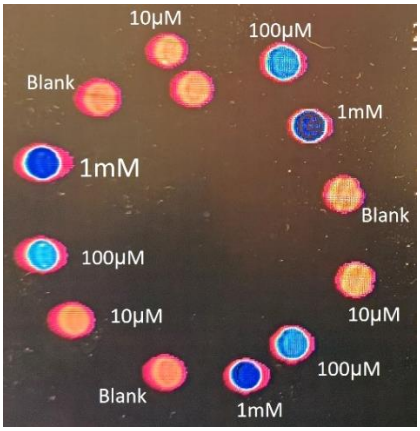


Figure 60 – Experiment of GdSCA concentration and sensitivity test in aquesous solution. The experiment estimated that the concentration of GdSCA requires a concentration of more than 100 $\mu M_{(aq)}$ equivalent to have enough signal intensity

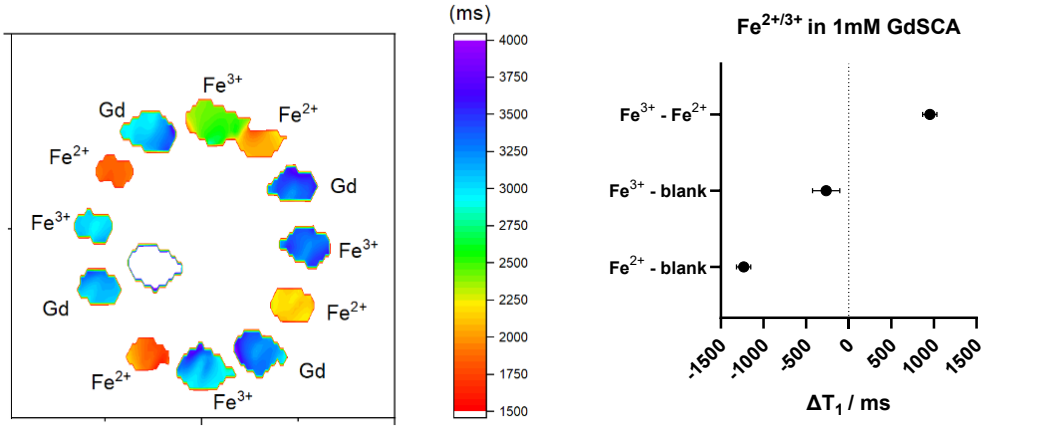
4.3.4. Iron-dependent MRI signal modulation

4.3.4.1. Probe-dependent response under ferrous and ferric conditions

Using the spatially controlled MRI system described in Section 4.3.3, the influence of iron speciation on MRI signal behaviour was evaluated for both GdSCA and GdCat systems under comparable in vitro conditions.

In the GdSCA system, a clear and reproducible trend was observed upon the introduction of iron. Both Fe^{2+} and Fe^{3+} led to a decrease in T_1 relative to the blank condition, corresponding to an enhancement of longitudinal relaxation. Notably, the effect was substantially more pronounced in the presence of Fe^{2+}. Quantitative

analysis of pixel-wise T_1 maps showed a reduction from 3240 ± 76 ms (GdSCA with no addition of other ions) to 3015 ± 212 ms (Fe^{3+}) and 2020 ± 69 ms (Fe^{2+}), indicating a strong enhancement of relaxation under Fe^{2+} conditions.



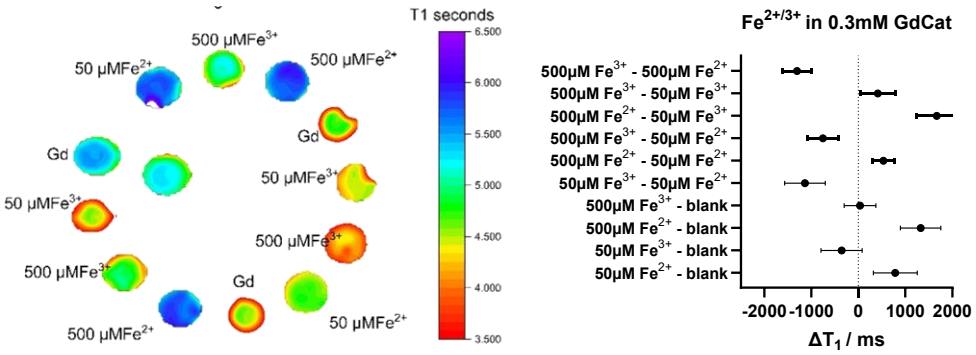
Gd:	Fe^{2+}:	Fe^{3+}:
1mM GdSCA	1mM GdSCA + 500 µM $FeSO_4$	1mM GdSCA + 500 µM Fe(iii) citrate

Figure 61 – H9c2 cell in vitro MRI T_1 mapping and quantitative analysis of 1mM GdSCA system under no addition, $FeSO_4$, and Fe(iii) citrate. (Left) Representative pixel-wise T_1 maps. (Right) Mean T_1 values extracted from samples (mean ± SD, n = 3), analysed by one-way ANOVA. (Bottom) conditions in each well

This behaviour contrasts with the trends observed in aqueous relaxometry (Section 3.2), where Fe^{3+} exhibited the dominant effect. The enhanced response under Fe^{2+} conditions in the present system may reflect additional factors in the cellular environment, such as differences in uptake, distribution, or accessibility of iron species. In particular, Fe^{2+} is generally considered to be more readily transported across cellular membranes compared to Fe^{3+}, which may lead to a higher effective intracellular concentration and thus a greater influence on relaxation behaviour.[120] However, this interpretation remains speculative and cannot be directly confirmed

within the present experimental framework.[24]

In contrast, the GdCat system exhibited substantial variation in T_1 values across different iron conditions, but without a consistent or interpretable trend. While statistical comparisons between conditions yielded significant differences, these variations did not follow a systematic dependence on either iron oxidation state or concentration. For example, both increases and decreases in T_1 were observed across Fe^{2+} and Fe^{3+} conditions, and no monotonic relationship was evident.



Gd:	50 µM Fe^{2+}:	500 µM Fe^{2+}:	50 µM Fe^{3+}:	500 µM Fe^{3+}:
0.3mM GdCat	0.3mM GdCat + 50 µM $FeSO_4$	0.3mM GdCat + 500 µM $FeSO_4$	0.3mM GdCat + 500 µM Fe(iii) citrate	0.3mM GdCat + 500 µM Fe(iii) citrate

Figure 62 - H9c2 cell in vitro MRI T_1 mapping and quantitative analysis of 0.3mM GdCat system under no addition, $FeSO_4$, and Fe(iii) citrate. (Left) Representative pixel-wise T_1 maps. (Right) Mean T_1 values extracted from samples (mean ± SD, n = 2 or 3), analysed by one-way ANOVA. (Bottom) conditions in each well

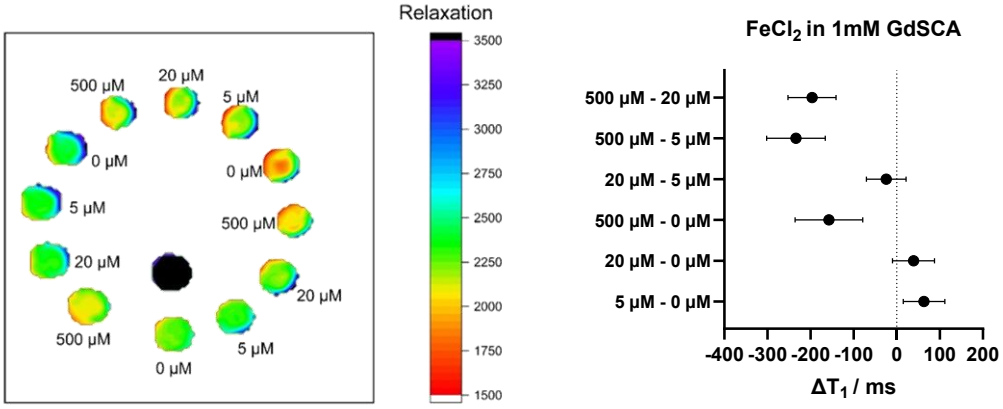
This lack of consistent behaviour suggests that, within the sensitivity limits of the present system, the GdCat probe does not exhibit a reproducible iron-dependent modulation of MRI signal. The observed variability is therefore more likely to reflect experimental or system-level factors rather than a defined interaction between the

probe and iron species.[64, 133]

Taken together, these results demonstrate that iron-dependent modulation of MRI signal is strongly probe-dependent under the present in vitro conditions. The GdSCA system exhibits a clear and interpretable response to iron speciation, whereas the GdCat system does not show a consistent trend despite apparent statistical variation.

4.3.4.2. Concentration-dependent response of GdSCA to ferrous ions

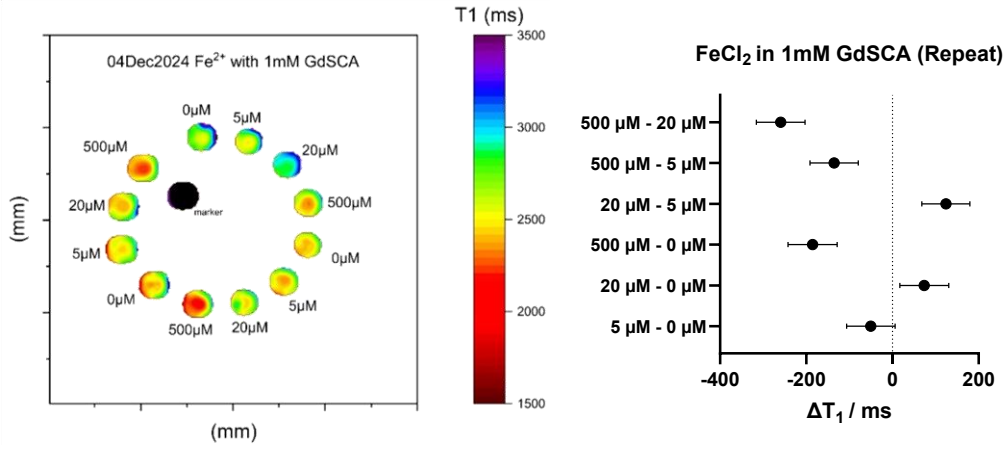
To further investigate the iron-dependent behaviour observed for the GdSCA system, a concentration series of $FeCl_2$ (0, 5, 20, and 500 µM) was examined in the presence of 1 mM GdSCA. Two independent experimental batches were performed to assess the reproducibility of the observed trends.



0 µM:	5 µM:	20 µM:	500 µM:
1mM GdSCA	1mM GdSCA + 5 µM $FeCl_2$	1mM GdSCA + 20 µM $FeCl_2$	1mM GdSCA + 500 µM $FeCl_2$

Figure 63 - H9c2 cell in vitro MRI T_1 mapping and quantitative analysis of the 1 mM GdSCA system with $FeCl_2$ at 0, 5, 20, and 500 µM (Batch 1).(Left) Representative pixel-wise T_1 maps.(Right) Mean T_1 values extracted from samples (mean ± SD, n = 3), analysed by one-way ANOVA. (Bottom) conditions in each well

Across both datasets, a consistent pattern was observed at higher iron concentrations. In particular, the 500 µM Fe^{2+} condition exhibited a clear reduction in T_1 relative to the lower concentration groups, corresponding to an increase in relaxation rate. This behaviour was reproducible between batches, despite differences in absolute T_1 values arising from experimental variation.



0 µM:	5 µM:	20 µM:	500 µM:
1mM GdSCA	1mM GdSCA + 5 µM $FeCl_2$	1mM GdSCA + 20 µM $FeCl_2$	1mM GdSCA + 500 µM $FeCl_2$

Figure 64 - T_1 mapping and quantitative analysis of the 1 mM GdSCA system with $FeCl_2$ at 0, 5, 20, and 500 µM (repeated work as Figure 63 but with another batch of GdSCA). (Left) Representative pixel-wise T_1 maps.(Right) Mean T_1 values extracted from samples (mean ± SD, n = 3), analysed by one-way ANOVA. (Bottom) conditions in each well

In contrast, no consistent or reproducible trend was observed within the lower concentration range (0–20 µM). While statistical comparisons based on pixel-level data indicated differences between certain conditions, these variations were not consistent in direction across independent experiments and remained within the variability of the system.

Quantitative analysis of pixel-wise T_1 maps confirmed that the 500 µM condition differed from the lower concentration groups in both experimental batches. However, differences between 0, 5, and 20 µM conditions were not consistently observed and did not define a clear concentration-dependent relationship within this range.

These results indicate that iron-dependent modulation of MRI signal in the GdSCA system exhibits a threshold-like behaviour, becoming detectable only at relatively high Fe^{2+} concentrations. Below this threshold, the contribution of iron to relaxation remains small relative to the dominant effect of gadolinium and falls within the sensitivity limits of the present experimental setup.

4.3.5. Analysis and conclusion

The results presented in this section demonstrate that iron-dependent modulation of MRI signal can be observed in vitro under controlled experimental conditions. In the GdSCA system, both Fe^{2+} and Fe^{3+} influence T_1, with a more pronounced effect observed for Fe^{2+}. In contrast, the GdCat system does not exhibit a consistent or interpretable trend despite apparent statistical differences between conditions.

The magnitude of the iron-dependent effect is strongly dependent on concentration, with a clear and reproducible response observed only at higher Fe^{2+} levels (500 µM). At lower concentrations, variations remain within the sensitivity limits of the system and do not show a consistent pattern.

Several limitations should be considered when interpreting these results. The observed signal behaviour is dominated by the gadolinium complex, with iron contributing a comparatively small effect. In addition, the experimental setup, while spatially controlled, is subject to inherent variability arising from imaging conditions and sample preparation. Finally, the complexity of the cellular environment may influence the behaviour of iron species, and the underlying mechanisms cannot be directly resolved in the present system.

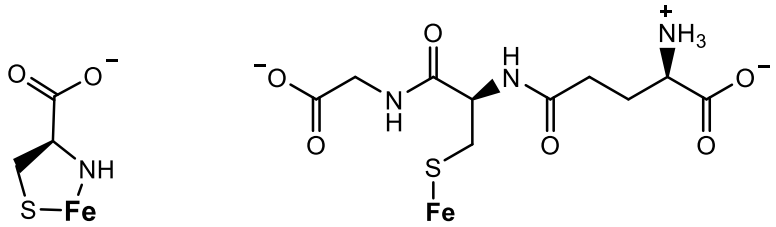


Figure 65 – Fe^{2+}-binding scheme with cysteine(left) and glutathione(right) on protein[196]

In addition, the cytosolic environment introduces chemical competition that is absent from the aqueous experiments described in Chapter 3. Intracellular labile iron does not exist as freely available Fe^{2+} or Fe^{3+}, but is dynamically buffered by endogenous ligands and proteins; glutathione, in particular, has been proposed as an important ligand for the cytosolic Fe^{2+} pool.[196] Iron entering the cytosol may also be redistributed to iron chaperones, ferritin, mitochondria and other iron-utilising pathways. Consequently, the concentration and oxidation state of iron added during incubation do not necessarily correspond to the iron species ultimately accessible to the SCA binding site at the time of MRI measurement. Conversely, interactions of GdSCA with intracellular macromolecules may alter molecular tumbling, water accessibility or local relaxation behaviour independently of iron binding.[197] These

competing processes provide additional sources of variation and may partly account for differences between the cellular MRI results and the simpler aqueous behaviour observed in Section 3.2.

These limitations must be taken into account when extending the interpretation of these findings to more complex biological systems, including in vivo imaging studies (Section 5.3).

Overall, these findings indicate that while iron-dependent MRI signal modulation is detectable in vitro, it remains limited in magnitude and dependent on both probe system and experimental conditions.

4.4. Summary and limitations of Chapter 0

This chapter has examined the behaviour of the candidate contrast agents in a cellular context, with the dual aim of establishing their biocompatibility and developing an experimental framework capable of probing iron-dependent MRI contrast at the cell level.

Cytotoxicity assessment demonstrated that both GdSCA and GdCAT are well tolerated under the investigated conditions, supporting their suitability for biological application. Method development for the LDH assay identified significant interference arising from serum components, which affected the reliability of conventional endpoint measurements. The adoption of dynamic time-resolved measurement and controlled serum conditions provided an improved and more

reproducible approach for assessing cell viability. These findings establish that the probes can be applied in vitro without inducing substantial cellular damage, while also highlighting the importance of assay optimisation in evaluating probe biocompatibility.

A central outcome of this chapter is the development of an in vitro MRI platform designed to bridge the gap between simplified aqueous measurements and in vivo imaging. Through a series of iterative experiments, key experimental parameters influencing signal detection were identified, including sample geometry, magnetic field positioning, and the spatial distribution of cells within the imaging volume. The introduction of perfluorodecalin as an inert support medium enabled reproducible localisation of the cell layer within the sensitive region of the coil, representing a critical improvement in experimental design. In addition, comparison between pre-loaded and add-late conditions demonstrated that intracellular association of the probe is a necessary requirement for detectable signal, with low intracellular Gd concentration identified as a limiting factor in early-stage experiments.

Despite these methodological advances, the detection of clear iron-dependent contrast at the cellular level remained limited. While variations in signal intensity were observed under different experimental conditions, these changes were not sufficiently robust or reproducible to support a definitive assignment of iron-specific response. The results suggest that a threshold level of intracellular probe concentration is required for detectable MRI contrast, and that under the present conditions this threshold is not consistently achieved. Consequently, the

contribution of any iron-dependent relaxivity modulation cannot be reliably distinguished from background signal and experimental variability.

Several important limitations arise from these findings. First, intracellular uptake of the probe is heterogeneous and difficult to control, leading to variability in effective Gd concentration between samples. Second, the cellular environment introduces additional complexity in iron speciation and compartmentalisation, which cannot be directly controlled or measured within the current experimental framework. Third, the magnitude of the expected iron-dependent relaxivity change is small relative to the inherent variability of the in vitro MRI system, limiting detection sensitivity. Finally, as in the in vivo case, the reliance on intensity-based MRI measurements further constrains the ability to resolve subtle differences in relaxation behaviour.

Within this context, the GdSCA system exhibited more consistent and interpretable behaviour across the developed platform, whereas the GdCAT system showed weaker and less reproducible responses. Accordingly, subsequent work focuses primarily on GdSCA as the lead candidate for further evaluation, with GdCAT retained as a comparative reference to provide insight into the influence of ligand structure on probe behaviour.

Taken together, this chapter establishes both the biological compatibility of the probe systems and a workable in vitro MRI methodology for studying contrast behaviour at the cellular level. While definitive evidence of iron-specific contrast could not be obtained under the present conditions, the results define an important intermediate stage in the overall experimental progression. In particular, they

demonstrate that the translation of iron-responsive relaxivity from controlled solution systems to cellular environments is constrained by probe uptake, signal magnitude, and biological complexity, thereby motivating the transition to in vivo studies.

5. Gd contrast agents in vivo

5.1. General concept for in vivo experiment

5.1.1. Ethical declaration

All in vivo experiments were conducted in accordance with the UK Animals (Scientific Procedures) Act 1986 and relevant institutional ethical guidelines governing the use of animals in research. Ethical approval for all procedures was obtained from the UK Home Office under Project Licence (PPL) PP9271002. All experimental procedures were performed by an individual holding a valid Personal Licence (PIL) I47249295. Documentation of the Personal Licence is provided in the Appendix.

All procedures were designed and carried out with consideration of animal welfare, with efforts made to minimise distress and reduce unnecessary variation. Experimental design, handling, and monitoring protocols were established in line with standard practice for small-animal imaging studies, ensuring consistency across all in vivo measurements.

5.1.2. Rationale for Animal Studies

In vivo studies provide an essential translational step between *in vitro* probe design and potential clinical use. While cell-based assays enable high-throughput screening and mechanistic insight, they cannot recapitulate the systemic complexity of iron metabolism—nor predict whole-organism responses to contrast agents. Key physiological parameters such as tissue perfusion, clearance kinetics, organ-specific

iron regulation, and immune responses can only be evaluated in vivo.

In the context of iron-responsive MRI probes discussed in the introduction chapter of this thesis, animal models are particularly important. Iron homeostasis involves dynamic interactions across multiple organs, notably the heart, liver, spleen, and kidneys. These regulatory pathways—and their impact on contrast agent distribution and signal—are inaccessible to isolated cell systems.

Therefore, in this chapter, the further extended in vivo study aims to evaluate both the biocompatibility and imaging efficacy of the Gd-based probe under physiologically relevant conditions. It provides functional data to support safety assessment, biodistribution analysis, and translational relevance—forming a critical bridge from bench validation to potential diagnostic use.

5.2. Toxicity in vivo

5.2.1. Assessment method and strategy

The in vivo toxicity study was designed as a preliminary tolerability assessment to determine whether the probe could be administered under the selected conditions without producing overt acute toxicity that would preclude subsequent MRI experiments. The purpose of this section was therefore not to establish a comprehensive toxicological profile, but to assess whether the probe was sufficiently well tolerated for exploratory in vivo imaging.

A total of six mice, including both male and female animals, were included in the

study and followed longitudinally after injection. In keeping with the feasibility-focused scope of this thesis, the assessment was based on repeatable non-terminal readouts collected over time in the same animals. These included urine reagent strip assessment, body-weight assessment, and serial health assessment based on general appearance and behaviour. [61]

Urine was assessed using SIEMENS Multistix® 10 SG reagent strips,[198] with results interpreted visually by comparison with the manufacturer colour chart. The strip contained ten indicators, providing a rapid multi-parameter overview of urinary and physiological status. Although this method is limited compared with serum biochemistry or histology, it was appropriate for an initial assessment within a small exploratory animal study. [61, 199]

Body weight was recorded throughout the study as a simple indicator of general tolerability. Clinical condition was assessed using a structured health assessment sheet covering movement, posture and grooming, and signs of dehydration. The full sheet is provided in Appendix 0. Together, these measures were used to identify any overt decline in well-being during the observation period. [61, 200]

Accordingly, the results presented below should be interpreted as evidence of preliminary in vivo tolerability within the context of an exploratory MRI feasibility study, rather than as a formal toxicology study.

5.2.2. Urine-based assessment

5.2.2.1. Inflammatory-related indicators (LEU, NIT, BLO)

Leukocytes (LEU), nitrite (NIT), and blood (BLO) were considered together as inflammatory-related urinary indicators because they are commonly used in routine urinalysis to flag possible urinary tract inflammation, bacterial infection, or overt bleeding or irritation. Although none of these parameters is diagnostic in isolation, their combined interpretation can provide a useful overview of whether a treatment-related abnormal urinary pattern is present. [199, 201, 202]

Urinary leukocytes indicate the presence of inflammatory cells in the urinary tract and may suggest local irritation or infection. In the present study, leukocyte readings remained negative across the assessed time points, with no significant difference observed between treatment and control groups. This did not indicate a treatment-associated inflammatory urinary response.

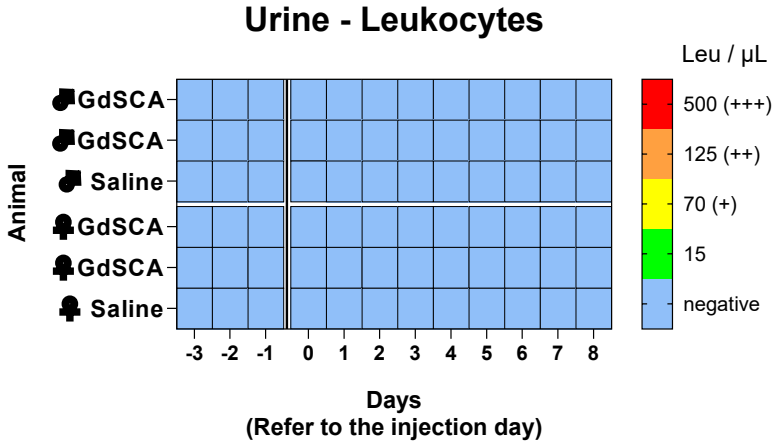


Figure 66 - Urine analysis results for leukocytes (both saline and GdSCA groups showed a negative results during the period of assessment)

Urinary nitrite is generally interpreted as an indirect marker of nitrate-reducing bacterial activity and is therefore often considered alongside leukocyte readings. In this study, nitrite remained negative throughout the observation period in both groups, again with no significant treatment-control difference. This finding did not support the presence of a probe-associated infective urinary pattern.

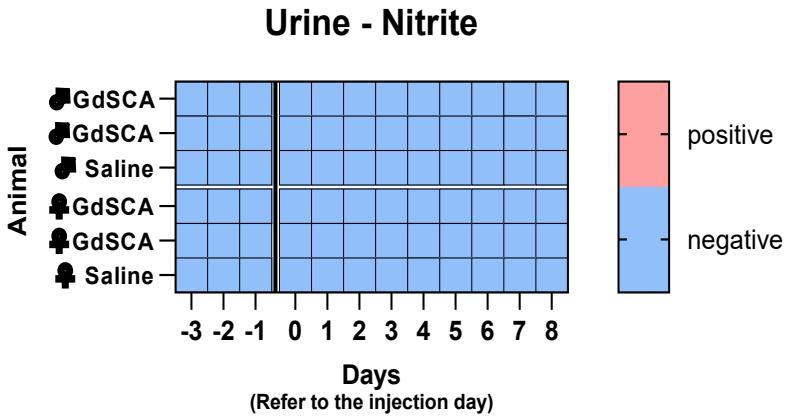


Figure 67 - Urine analysis results of nitrite(both saline and GdSCA groups showed a negative results during the period of assessment)

The blood parameter reflects the presence of erythrocytes, haemoglobin, or myoglobin in urine and may indicate haematuria or urinary tract injury when persistently abnormal. No consistent abnormal blood signal was observed in the present study, and no significant difference was detected between treatment and control groups. This did not suggest overt urinary bleeding or treatment-related irritation.

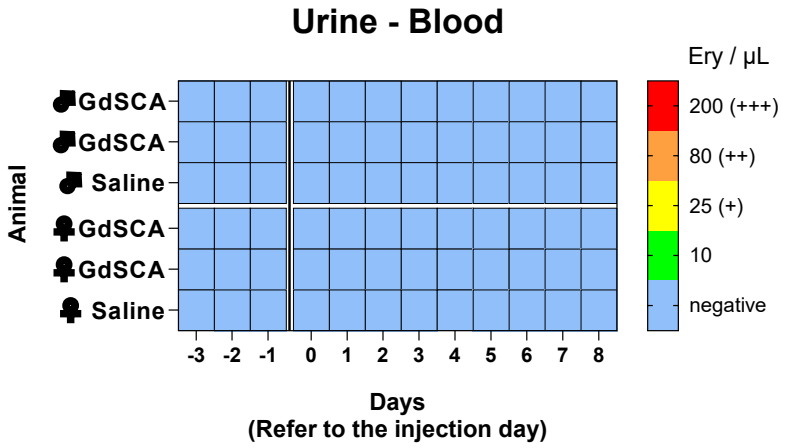


Figure 68 - Urine analysis results of blood (both saline and GdSCA groups showed a negative results during the period of assessment)

Taken together, the LEU, NIT, and BLO results did not show a consistent abnormal pattern in either group. In particular, no significant difference was observed between treatment and control animals across these inflammatory-related urinary indicators. Collectively, these findings did not suggest overt urinary tract inflammation, infection, or bleeding under the tested conditions.

No blood was detected in any of the urine samples collected from the six animals during the study period. Reagent strips remained uniformly negative on the blood pad across all timepoints and treatment groups. No discolouration or marginal colour change was noted, and results were visually clear and reproducible (Figure X).

This absence of haematuria or haemoglobinuria suggests that the intervention did not induce mechanical trauma, renal irritation, or systemic haemolysis. The negative findings were consistent between gadolinium-treated and control animals, and across both sexes. In the absence of blood, the reliability of other parameters—such as protein and leukocytes—is further reinforced, as potential artefacts from red cell

interference can be ruled out.

Taken together with the other negative indicators in this study, these results support the conclusion that the compound was well tolerated and did not elicit detectable tissue damage within the urinary system.

5.2.2.2. Renal-related indicators (PRO, pH, SG)

Protein (PRO), pH, and specific gravity (SG) were considered together as renal-related urinary indicators because they provide a simple overview of urinary protein leakage, urine acidity, and urine concentration. Although these parameters are not sufficient for formal renal assessment in isolation, their combined interpretation can help indicate whether a treatment-related abnormal urinary pattern is present. [199, 201, 202]

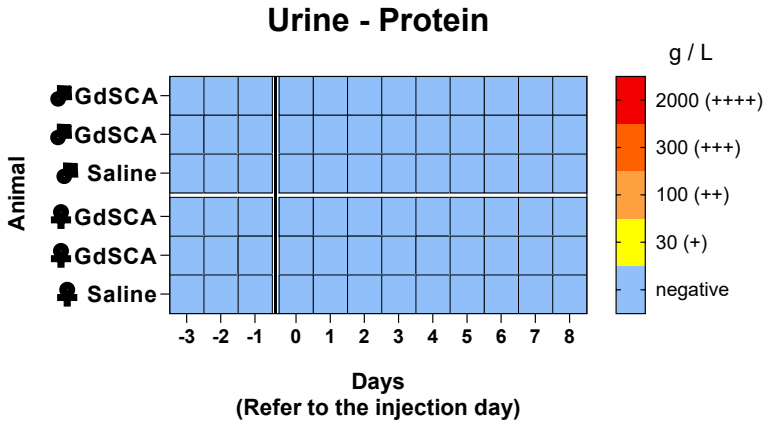


Figure 69 - Urine analysis results of protein (both saline and GdSCA groups showed a negative results during the period of assessment)

Urinary protein is commonly interpreted as an indicator of abnormal protein leakage and may suggest renal impairment when persistently elevated, although transient or trace findings can occur. In the present study, protein readings did not show a

consistent abnormal pattern, and no significant difference was observed between treatment and control groups. This did not suggest treatment-associated proteinuria under the tested conditions.

Urinary pH reflects the acidity or alkalinity of urine and can be influenced by physiology, diet, and metabolic state. In this study, pH values showed only limited variation and did not display a consistent treatment-related shift. No significant difference was observed between treatment and control groups. This did not indicate a meaningful disturbance in urinary acid-base characteristics within the scope of this experiment.

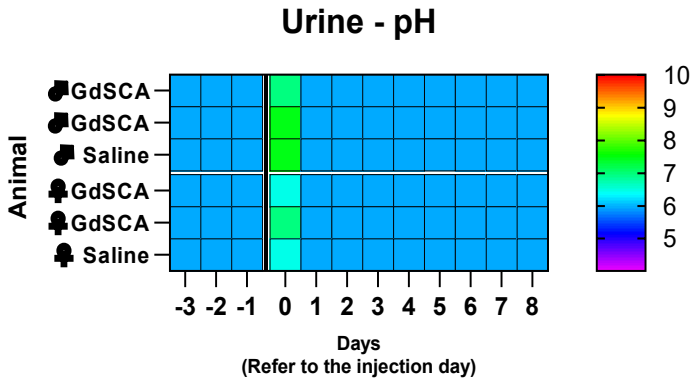


Figure 70 - Urine analysis results of pH (Though fluctation was observed, both saline and GdSCA groups were within the normal range, 4.6-8.0, during the period of assessment)

Urinary specific gravity provides a simple indication of urine concentration, which is and is often used to reflect hydration status and the kidney's concentrating function. In the present study, SG values remained within a broadly comparable range over the observation period, with no significant difference between treatment and control groups. This did not suggest a treatment-associated change in urine

concentration or an obvious impairment of renal concentrating ability.

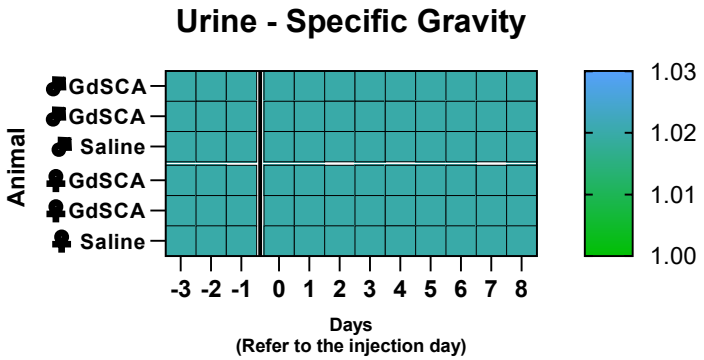


Figure 71 - Urine analysis results of Specific gravity (both saline and GdSCA groups showed no difference during the period of assessment)

Taken together, the PRO, pH, and SG results did not show a consistent abnormal pattern in either group. In particular, no significant difference was observed between treatment and control animals across these renal-related urinary indicators. Collectively, these findings did not suggest overt renal-associated urinary disturbance under the tested conditions.

5.2.2.3. Metabolic/hepatobiliary-related indicators (GLU, KET, BIL, URO)

Metabolic- and hepatobiliary-related urine indicators were considered together because glucose (GLU) and ketone (KET) are commonly interpreted in relation to metabolic state, whereas bilirubin (BIL) and urobilinogen (URO) are more often discussed in relation to hepatobiliary handling and haem metabolism. None of these parameters is fully diagnostic in isolation, but their combined interpretation can help determine whether a consistent treatment-related abnormal pattern is present.[199, 201, 202]

Urinary glucose is generally interpreted as a marker of glycosuria and may reflect altered glucose handling or hyperglycaemic stress when persistently abnormal, although isolated findings should be interpreted cautiously. In the present study, glucose readings did not show a consistent abnormal pattern over time, and no significant difference was observed between treatment and control groups. This did not suggest a treatment-associated disturbance in urinary glucose handling under the tested conditions.

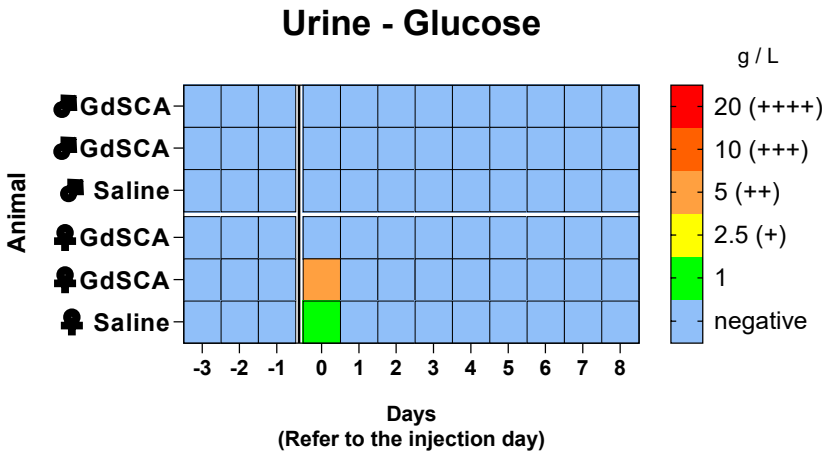


Figure 72 - Urine analysis results of Glucose (both of saline and GdSCA groups showed a negative results during the period of assessment but one exceptional high glucose in the urine)

Urinary ketones are usually associated with increased fatty acid catabolism and can be seen in states such as fasting, starvation, or diabetic ketoacidosis, but interpretation depends on context. In this study, ketone readings did not display a consistent abnormal trend, and no significant treatment-control difference was detected. This did not indicate a treatment-associated metabolic stress pattern based on urinary ketone excretion.

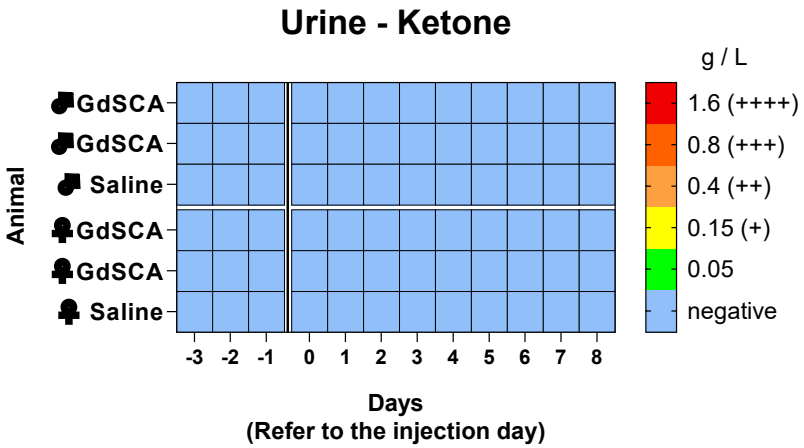


Figure 73 - Urine analysis results of ketone (both saline and GdSCA groups showed a negative results during the period of assessment)

Urinary bilirubin is commonly interpreted in relation to conjugated bilirubin excretion and may suggest hepatobiliary disturbance when persistently positive, although dipstick results require cautious interpretation. In the present study, bilirubin did not show a consistent abnormal signal, and no significant difference was observed between treatment and control groups. This did not support a treatment-associated bilirubinuria pattern.

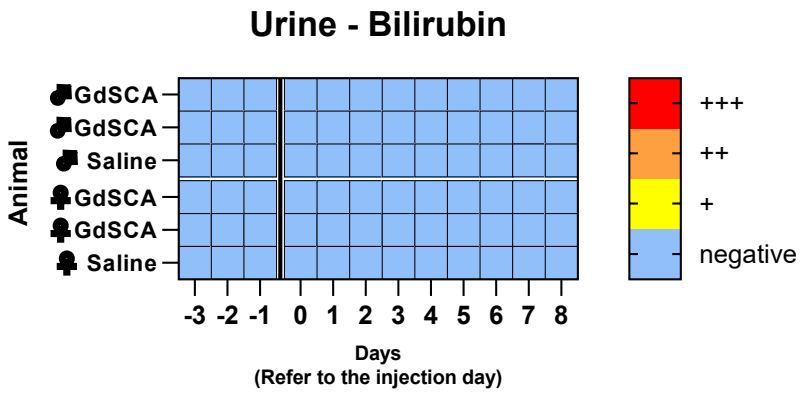


Figure 74 - Urine analysis results of bilirubin (both saline and GdSCA groups showed a negative results during the period of assessment)mg/µ

Urinary urobilinogen reflects downstream haem breakdown and enterohepatic

handling, and abnormal values may be associated with hepatic dysfunction or altered haem metabolism, although low-level urinary presence can be physiological. In this study, urobilinogen readings did not show a consistent abnormal pattern, and no significant difference was detected between treatment and control groups. This did not suggest a treatment-associated disturbance in urinary urobilinogen excretion.

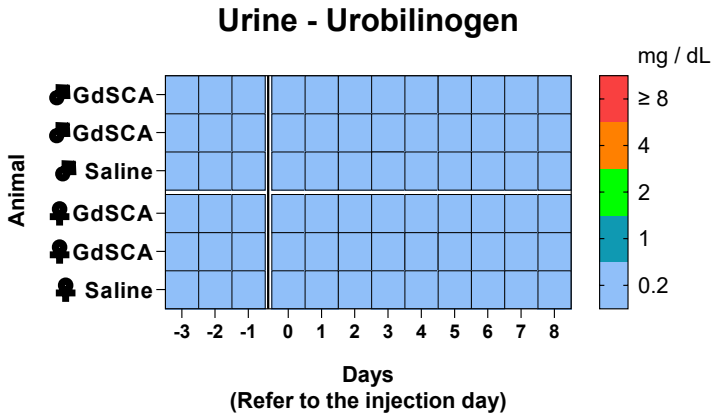


Figure 75 - Urine analysis results of blood (both saline and GdSCA groups were within the normal range during the period of assessment)

Taken together, the GLU, KET, BIL, and URO results did not show a consistent abnormal pattern in either group. In particular, no significant difference was observed between treatment and control animals across these metabolic- and hepatobiliary-related urinary indicators. Collectively, these findings did not suggest overt metabolic or hepatobiliary-associated urinary disturbance under the tested conditions.

5.2.3. Body-weight and clinical health assessment

Body weight was monitored throughout the study as a general indicator of physiological tolerability following injection. Relative body weight was calculated

with respect to the mean baseline value obtained from the three pre-injection measurements for each animal. Across all animals, a transient decrease in body weight was observed following injection, reaching a nadir at approximately 48 h. At this time point, the cumulative reduction in body weight ranged from 1.7% to 4.3% relative to baseline. Importantly, no animal exceeded a 5% loss of baseline body weight, and recovery towards baseline was observed from day 3–4 onwards.

Statistical analysis was performed using two-way repeated-measures ANOVA, with time and treatment as factors. A significant effect of time was observed ($p = 0.0010$), indicating a transient time-dependent change in body weight. In contrast, no significant effect of treatment was detected ($p = 0.9642$), indicating that animals in the GdSCA group did not exhibit additional weight loss compared to saline controls under the tested conditions. These results suggest that the observed body-weight change is consistent with a general post-procedural response rather than a treatment-specific effect.

Clinical condition was assessed using a structured health assessment sheet incorporating movement, posture and grooming, and signs of dehydration. Scores ranged from 0 to 15, with higher scores indicating poorer health status. Throughout the study, all animals consistently showed low scores, predominantly 0 and occasionally 1, with no sustained or progressive increase over time. No clear difference was observed between treatment and control groups.

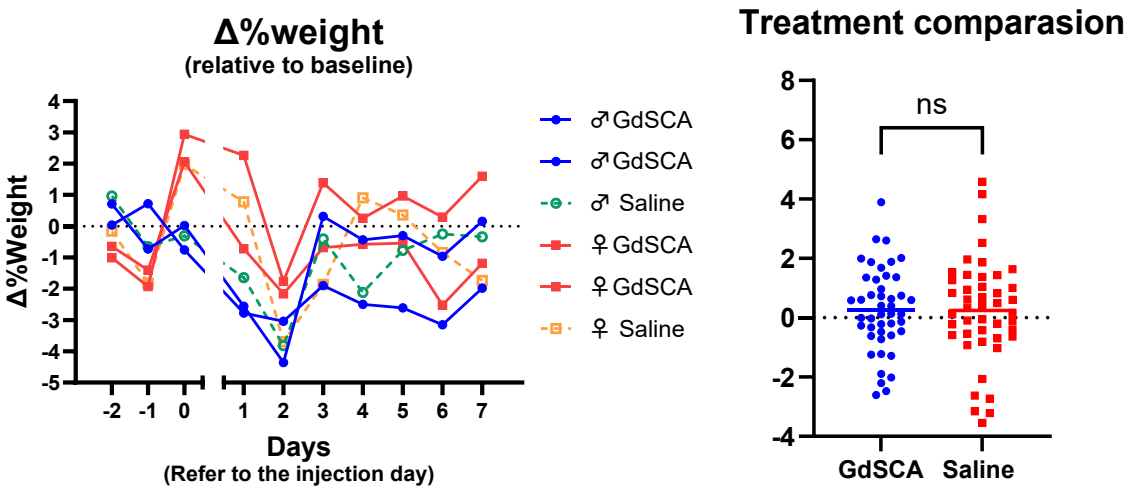


Figure 76 – Percentage weight change during the period of 3 days before and 7-days after the injection (left). The difference between two treatment methods was analysied by 2-way Anova, which has a p-value of 0.9642.

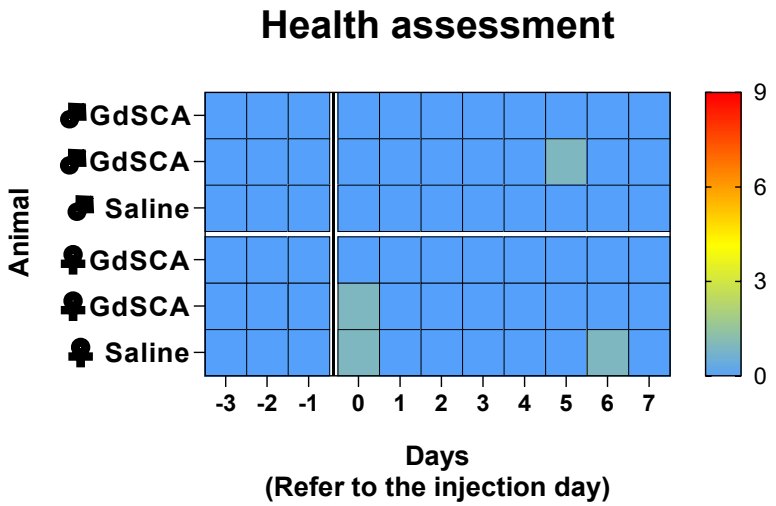


Figure 77 – Health assessment scores of mice. Scores ranged from 0 to 9, with higher scores indicating poorer health status, which would suggest further step-in cares if it is higher than 3

Overall, animals maintained normal appearance and behaviour throughout the experimental period, and no observable signs of systemic distress were detected. Minor reductions in activity were noted in some animals, which are considered more likely to be associated with repeated handling and sampling procedures rather than

treatment-related effects.

Taken together, body-weight changes and clinical health assessment did not indicate overt deterioration in general condition under the tested conditions, supporting the conclusion that the probe was well tolerated in this preliminary in vivo study.

5.2.4. Summary and limitations of in vivo toxicity assessment

Taken together, urine strip analysis, body-weight monitoring, and clinical health assessment did not reveal evidence of significant acute systemic toxicity under the tested conditions. Across all urinary indicators, no consistent abnormal pattern was observed, and no significant difference was detected between the GdSCA-treated and saline control groups. Body-weight analysis demonstrated a transient, time-dependent decrease following injection, with all animals remaining within 5% of baseline and subsequently recovering. In parallel, clinical health scores remained uniformly low, with no observable treatment-related deterioration in general condition. Collectively, these findings support that the probe was well tolerated in this preliminary in vivo setting.

However, several limitations of this assessment should be noted. The sample size was small and not powered for formal toxicological evaluation. Urine strip analysis was semi-quantitative and based on visual interpretation, and therefore provides only a coarse indication of physiological status. In addition, no serum biochemistry, histological analysis, or organ-specific endpoints were included, and the observation period was limited to short-term responses. Consequently, while the present results

do not indicate overt acute toxicity, they cannot exclude subtle, organ-specific, or longer-term effects.

Within the scope of this thesis, these data are therefore best interpreted as evidence of preliminary in vivo tolerability sufficient to support subsequent exploratory MRI experiments, rather than as a comprehensive safety evaluation.

5.3. In vivo MRI

5.3.1. Objective of In vivo MRI

This section uses in vivo MRI in mice to evaluate the imaging performance of the self-developed gadolinium-based small-molecule contrast agent GdSCA under controlled physiological and iron-loading conditions.[72] Liver signal intensity on T_1-weighted images, measured in predefined regions of interest (ROIs) under fixed acquisition parameters, is taken as the primary quantitative readout. The immediate objective is to confirm that GdSCA can generate robust and sustained enhancement of liver signal over a fixed series of post-injection time points in otherwise near-physiological animals. A further objective is to examine, in a descriptive manner, whether the temporal profile of this liver enhancement is altered when systemic iron handling is deliberately modified by pharmacological iron loading.

Iron overload is created in selected experiments by intravenous administration of ferric carboxymaltose (FCM). In this context, FCM is not evaluated as a contrast agent in its own right. Instead, it serves to increase LIP in tissues (baseline versus iron-

loaded) against which the behaviour of GdSCA can be compared while the underlying MRI protocol remains unchanged.[43] This design is intended to provide a first indication of whether GdSCA remains a usable liver T_1 agent in the presence of excess iron, and whether its liver time – intensity curve carries any detectable signature of altered iron status under the specific FCM conditions used here.[203]

Intravenous delivery via the tail vein was chosen as the route for both GdSCA and FCM in order to achieve rapid systemic distribution, a well-defined injection time, and a compact bolus profile compatible with dynamic imaging. A pre-placed tail-vein line with extension tubing permitted injections to be performed in-bore without disturbing the animal's position, which is essential for maintaining slice prescription and coil loading throughout the time course. In contrast, intraperitoneal or subcutaneous dosing would have introduced slower and more variable absorption kinetics, making it difficult to define a meaningful time zero or to relate changes in liver signal to a specific injection event.

Throughout all in vivo experiments, ECG monitoring was applied both for animal welfare and for basic motion control. Electrodes integrated into, or placed beneath, the thoracic region were used to track heart rate continuously and to confirm a stable depth of anaesthesia. Where supported by the system, the acquisition was synchronised to the cardiac cycle using ECG, so that data were collected at consistent phases of the heartbeat. This approach reduces ghosting and blurring related to cardiac motion around the liver, which is important when interpreting relatively modest percentage changes in liver signal over time. Residual respiratory motion

was not explicitly gated and is considered as a limitation when discussing the resulting liver time–intensity curves.

5.3.2. Basic experimental design for in vivo MRI

5.3.2.1. In vivo MRI experiment setup

All in vivo MRI experiments in this chapter were performed on a preclinical 7.0 T VARIAN small-animal system with a helium-filled superconducting magnet and horizontal bore. Proton detection was achieved with a 32 mm inner-diameter abdominal RF coil (“rapid32”, Rapid Biomedical), appropriate for mouse liver imaging. Scanner software, reconstruction settings, and receiver gain policy were kept constant across sessions to maintain comparability of intensity-based readouts. Before each experiment, central frequency calibration and B_0 shimming were performed over a liver-centred field of view.

Mice were positioned prone in a transverse orientation on a heated animal bed to maintain normothermia and provide stable support. External anatomical landmarks were used during setup to centre the liver near the magnet isocentre and to aid reproducible placement across animals. Anaesthesia was induced and maintained with isoflurane at approximately 2 % in oxygen delivered via a nose cone. A tail-vein line was established before the animal entered the magnet and extended with flexible tubing, so that intravenous injections could be performed in-bore without disturbing the animal’s position or coil loading. ECG electrodes integrated into, or placed beneath, the thoracic region of the bed were used for continuous monitoring

of heart rate and anaesthetic depth throughout all scans.

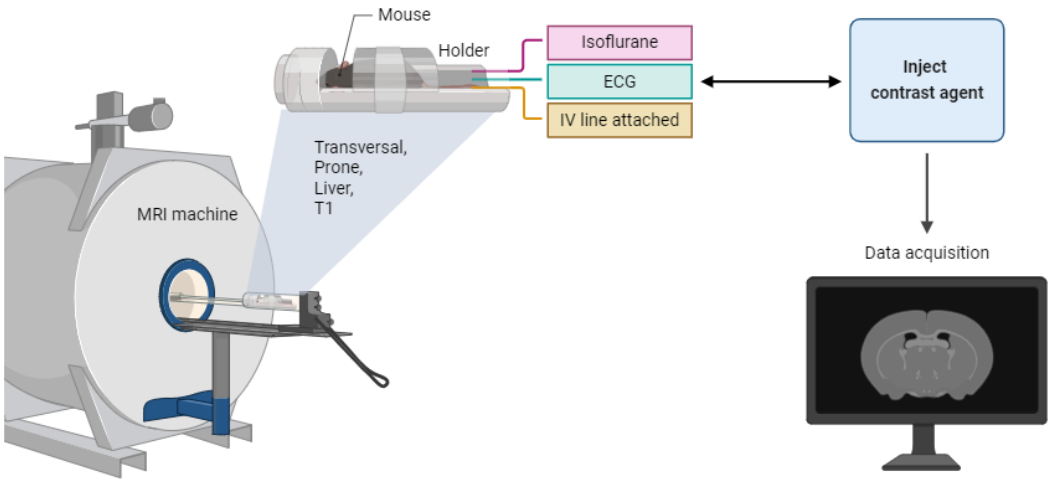


Figure 78 – in vivo MRI experiment setup

Liver imaging was carried out using a T_1-weighted spin-echo multi-slice (SEMS) sequence. Unless otherwise stated, sequence parameters were: repetition time (TR) 100 ms, echo time (TE) 10.93 ms, two signal averages, a 128 × 128 acquisition matrix, and an in-plane field of view of 35 mm × 35 mm. Five axial slices were prescribed at the hepatic level with a slice thickness of 1.5 mm and no inter-slice gap, providing coverage of the bulk of the liver in the cranio – caudal direction. At these settings, the per-frame acquisition time was approximately 25.6 s. Once planning images confirmed adequate hepatic coverage and acceptable shimming, the slice prescription and all sequence parameters were kept fixed for the remainder of the experiment. The external trigger option on the console was enabled to accept a physiological trigger from the monitoring unit, so that all dynamic frames were acquired under consistent physiological conditions.

For each imaging session, a single pre-contrast baseline data set was acquired first,

using the final slice prescription and sequence parameters. This baseline served both as the reference for subsequent intensity normalisation and as the template on which liver regions of interest were defined as explained in Appendix 8.3.7. Immediately after completing the baseline scan, the allocated contrast agent was injected intravenously through the pre-placed tail-vein line in-bore, and the time of injection was defined as t = 0. Dynamic image sets were then acquired every 5 min, starting from t = 0, for a total duration of 45 min. Each dynamic frame therefore represents one 5-min time point on a fixed time axis from 0 to 45 min after injection, with the pre-contrast baseline providing the t < 0 reference. This fixed acquisition schedule was applied identically in all experiments, so that differences in liver signal can be interpreted in terms of contrast agent and iron-loading status rather than variations in timing.

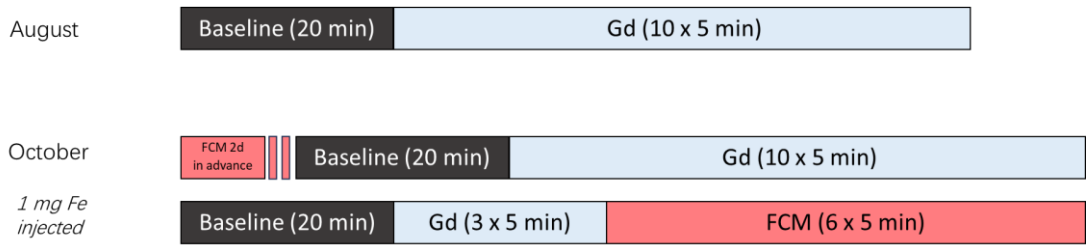


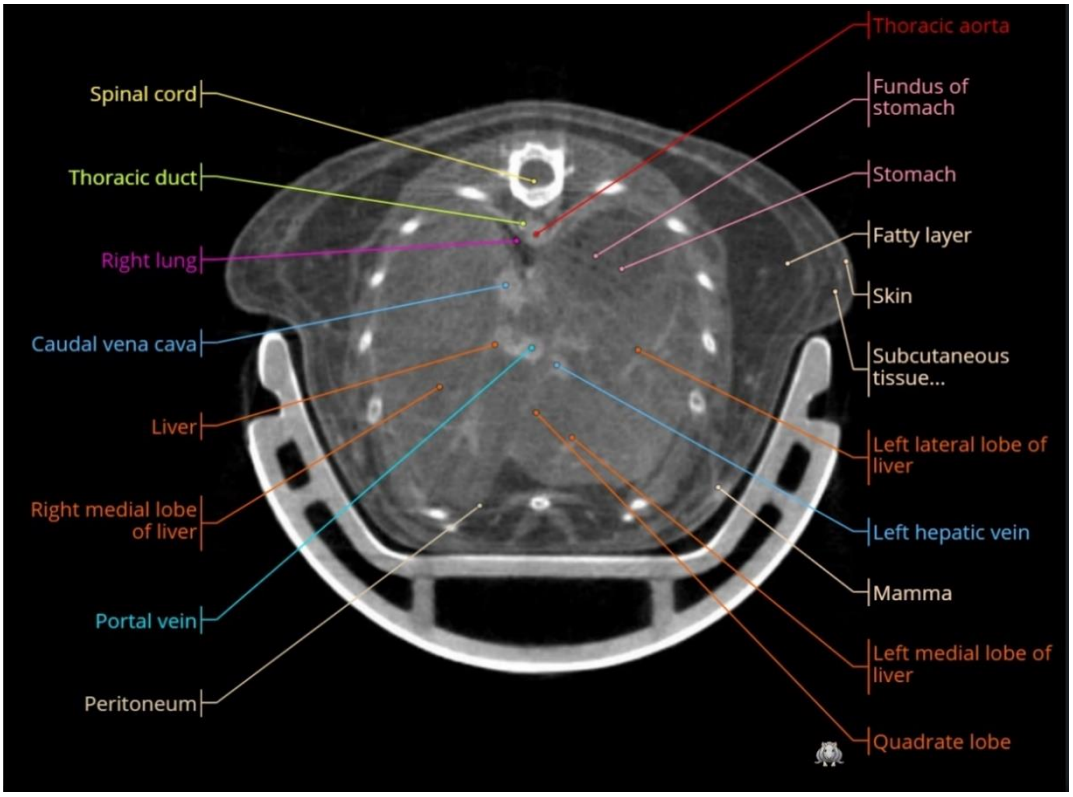
Figure 79 – Experimental plan for in vivo MRI

The stepwise setup and acquisition workflow, from animal preparation to completion of the dynamic series, is summarised in Figure 78.

5.3.2.2. Liver as target organ for in vivo MRI

The liver was selected as the primary target organ for in vivo assessment of GdSCA

because it is both anatomically dominant in the upper abdomen and closely linked to iron biology. In axial slices through the upper abdomen, the liver occupies most of the intra-abdominal cross-sectional area in a typical mouse, leaving only relatively small compartments for the body wall, stomach, vertebral column and major vessels. This relationship is illustrated by an external CT-based mouse anatomy atlas (IMAIOS Vet-Anatomy mouse model),[204] from which representative axial screenshots are reproduced in Figure 80. Three slices (158, 160, 163) were chosen, which has showed the mouse anatomy from the disappearance of the lungs to the domination of the liver to the presence of duodenum.



(contiunes on the next page)

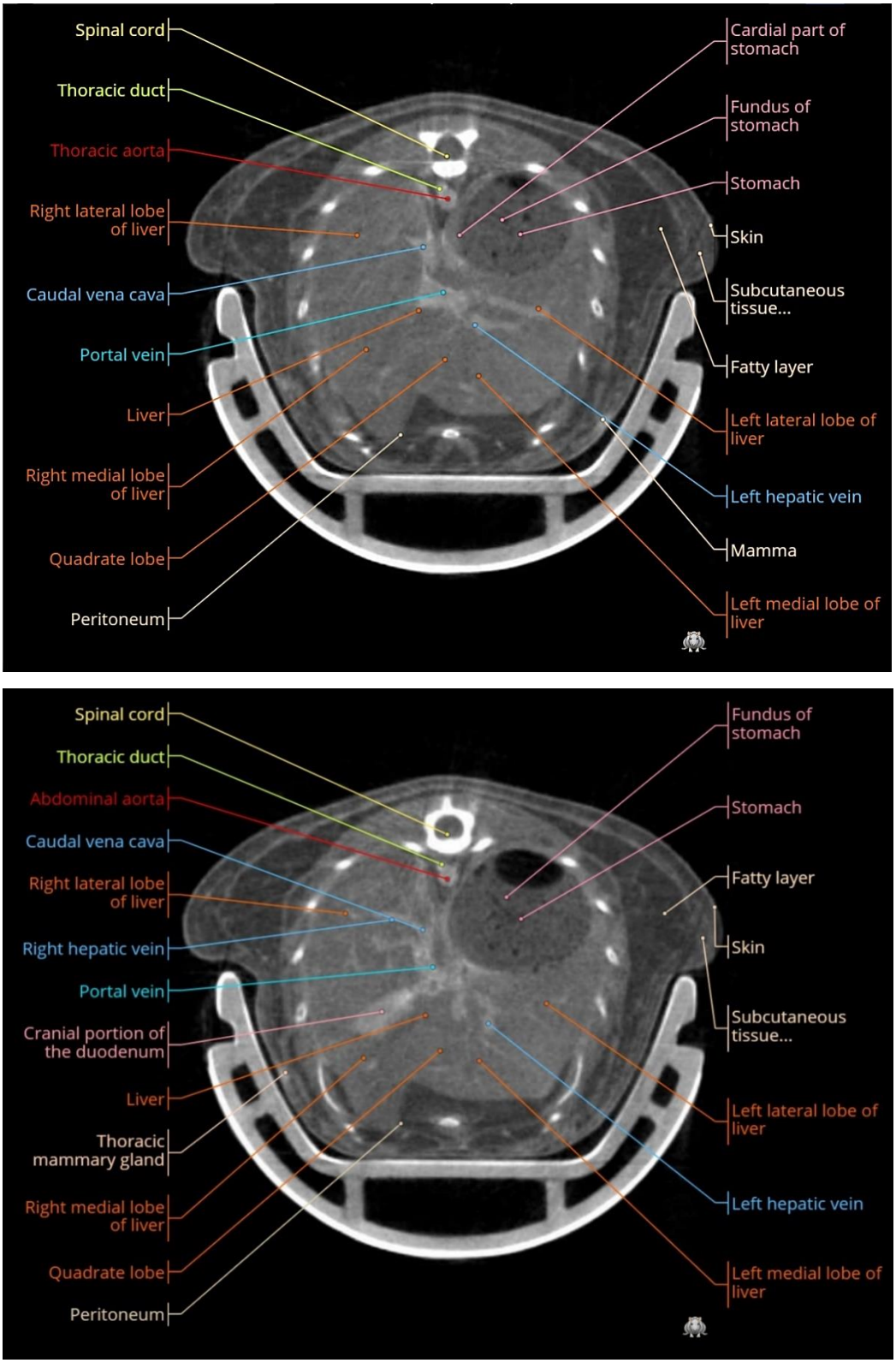


Figure 80 – Mouse's transversal illustration with liver from a CT scan 3D model of IMAIOS (Slice 158, 160, 163) [204]

On these images, the liver fills the majority of the parenchymal space, with only the skin, stomach, spine and large vessels such as the portal vein and inferior vena cava requiring explicit attention during slice planning and ROI placement. At the spatial resolution of the present MRI protocol, finer vascular and biliary structures are not individually resolved and were not treated separately. This geometry simplifies the definition of liver ROIs and maximises the proportion of each slice that samples hepatic parenchyma; the detailed ROI strategy is described in Section 5.3.2.4.

From a physiological perspective, the liver is a central regulator of systemic iron balance, particularly through hepcidin expression and ferritin-based iron storage.[26] Pharmacological iron loading with FCM is expected to alter hepatic iron content and trafficking, so any iron-responsive component of GdSCA's behaviour would plausibly manifest in liver signal. The combination of a large, relatively homogeneous parenchymal volume and direct involvement in iron homeostasis therefore makes the liver a practical and biologically relevant organ for intensity-based assessment under fixed T_1-weighted acquisition, and it was chosen as the primary readout in this study.

The spleen is a natural alternative candidate because of its role in erythrocyte turnover and iron recycling. However, in the mouse it is comparatively small, elongated and irregular in shape, and frequently lies in close proximity to the stomach and bowel gas on axial images. These features complicate both slice prescription and the placement of stable ROIs that can be copied reliably across time points, especially when only five slices are available in the dynamic protocol. In

addition, splenic signal on T_1-weighted images reflects a mixture of blood pool, stromal and lymphoid components, which would have required a dedicated analysis framework beyond the scope of this liver-focused work.

Bone marrow and lymphoid tissues are also involved in iron handling, but their distributed anatomy presents further challenges. Marrow spaces in the vertebrae and long bones are small and closely apposed to cortical bone, where susceptibility effects and partial-volume artefacts are prominent. Lymph nodes are small, variably located and often indistinguishable from surrounding soft tissue at the spatial resolution used here. For both compartments, robust and reproducible ROI-based analysis would have required higher resolution imaging, susceptibility-robust sequences, and a separate optimisation of slice placement, which were not feasible within the present experimental design.

Cardiac and vascular compartments, particularly the myocardium and ventricular blood pool, are important clinical targets for iron overload imaging.[139] In the current small-animal setup, however, these structures are strongly affected by cardiac motion and require dedicated ECG gating and sequence optimisation (for example cine or T_2*/T_1 mapping protocols) to yield interpretable quantitative readouts. Incorporating such cardiac-specific methods would have substantially increased methodological complexity and diverted the focus away from liver, without directly improving the interpretation of GdSCA' s hepatic behaviour.

The kidneys are another plausible imaging target, particularly for characterising the pharmacokinetics and renal clearance of gadolinium-based agents. Renal cortex and

medulla show rapid and pronounced T_1-weighted signal changes after contrast administration, and kidney enhancement is widely used as a marker of filtration and excretory function. In the context of iron overload, however, renal signal changes primarily report on contrast handling rather than iron storage, and are therefore less directly informative about iron-responsive aspects of GdSCA. Moreover, the mouse kidneys are smaller and more heterogeneous than the liver, with distinct cortical, medullary and pelvic compartments that are differentially affected by motion and partial-volume effects. A rigorous renal analysis would have required separate optimisation of slice placement, timing and ROI strategy tailored to renal function, which lay outside the scope of the present study.

Other abdominal organs, such as pancreas and bowel, were not considered as primary MRI targets because of their small size, complex and variable anatomy, and the strong influence of peristalsis and gas on image quality. In these regions it would be difficult to define stable parenchymal ROIs and to separate genuine tissue signal changes from artefacts under the current acquisition protocol.

Taken together, these considerations led to a deliberate decision to restrict quantitative analysis to the liver as the sole primary readout organ. This choice allows dynamic enhancement curves to be obtained with adequate spatial sampling and a straightforward ROI framework, while still providing a biologically relevant window onto iron loading and its potential interaction with GdSCA.

5.3.2.3. Route and dose for agent administration for in vivo MRI

For both GdSCA and ferric carboxymaltose (FCM), intravenous administration via the

tail vein was selected as the route of delivery. The dynamic *in vivo* MRI protocol used in this chapter relies on a well-defined injection time and a compact bolus profile, so that each dataset can be mapped onto a common time axis with a clear reference point at t = 0. Tail-vein IV injection provides rapid systemic distribution within seconds and allows the bolus to be delivered while the animal remains in the magnet, using a pre-placed line and extension tubing. In contrast, intraperitoneal or subcutaneous injection would introduce slower, route-dependent absorption kinetics and substantial inter-animal variability in onset time, making it difficult to interpret early changes in liver signal in terms of a defined post-injection interval. Oral dosing would be even less suitable, given the additional uncertainty from gastric emptying and first-pass metabolism. For these reasons, all contrast and iron-loading agents in this study were given as small-volume intravenous boluses via the tail vein.

Dose selection for GdSCA was guided by clinical practice for small-molecule gadolinium agents and by practical constraints on injection volume in mice. Clinically, agents such as Dotarem are supplied at 0.5 mol L^{-1} (0.5 mmol mL^{-1}) and are typically administered in volumes of around 10 mL, corresponding to a total of approximately 5 mmol Gd and an effective dose of about 0.07 – 0.10 mmol Gd kg^{-1} for a 50 – 70 kg adult.[205] Directly scaling this dose to a 25 g mouse would imply only a few microlitres of injection volume, which is technically difficult to deliver reproducibly in the tail vein. In the present work, a practical minimum injection volume of 100 µL was therefore adopted. On this basis, each mouse was targeted to receive 5 µmol of gadolinium, equivalent to roughly 0.20 mmol Gd kg^{-1} in a 25 g

animal. This dose remains within safety ranges based on prior in vivo toxicity results in Section 5.2, while providing a robust liver T_1 enhancement for ROI-based analysis. To deliver 5 µmol in 100 µL, a working concentration of 50 mM was required. GdSCA was thus prepared as a 50 mM solution, and clinical Dotarem (0.5 M stock) was diluted ten-fold to the same 50 mM working concentration, so that both agents delivered a matched nominal gadolinium dose under identical volume and injection conditions.

FCM dosing was determined from the perspective of creating a controlled iron overload rather than producing imaging contrast in its own right. The aim was to impose a reproducible iron load that was sufficient to perturb systemic and hepatic iron handling, yet below levels associated with acute toxicity in mice. Each animal therefore received 1 mg of elemental iron as FCM, corresponding to approximately 40 mg Fe kg^{-1} of human dose suggestion[205] in a 25 g mouse, which lies within commonly used iron-loading regimens in rodent models.[64] Practically, this was achieved by diluting the clinical FCM stock solution (50 mg Fe mL^{-1}) to 20 % of its original concentration, yielding a 10 mg Fe mL^{-1} working solution, and injecting 100 µL per mouse via the tail vein. Thus, both GdSCA (or Dotarem) and FCM were administered in the same 100 µL IV volume, simplifying the comparison between baseline and iron-loaded conditions and avoiding confounding effects from differences in bolus size or route of administration.[206]

5.3.2.4. ROI discussion

Liver signal was quantified using a region-of-interest approach implemented in ITK-

SNAP,[207] which allowed segmentation masks drawn on one image to be propagated to corresponding locations on other images within the same dynamic series. For each mouse, ROIs were defined on the pre-contrast baseline images and then rigidly copied to all subsequent time points, so that the same anatomical locations were sampled throughout the time course. Within each ROI, ITK-SNAP was used to extract the mean signal intensity and its standard deviation, providing a compact numerical summary for downstream analysis.

The ROI strategy itself evolved over the course of the project. Initially, the liver in each slice was segmented by freehand painting of what appeared to be the entire hepatic parenchyma on the baseline image. This whole-liver mask was attractive in principle because it maximised signal-to-noise and provided a single global value per slice. In practice, however, it proved difficult to control the inclusion of large intrahepatic vessels, portal tracts and neighbouring structures such as the stomach. The relative contributions of blood and hepatocytes within such a composite mask were hard to standardise between animals and time points, and small differences in how the boundary was drawn could translate into appreciable differences in the measured mean intensity. These issues motivated a move away from “paint-the-whole-liver” segmentation towards a more granular sampling scheme.

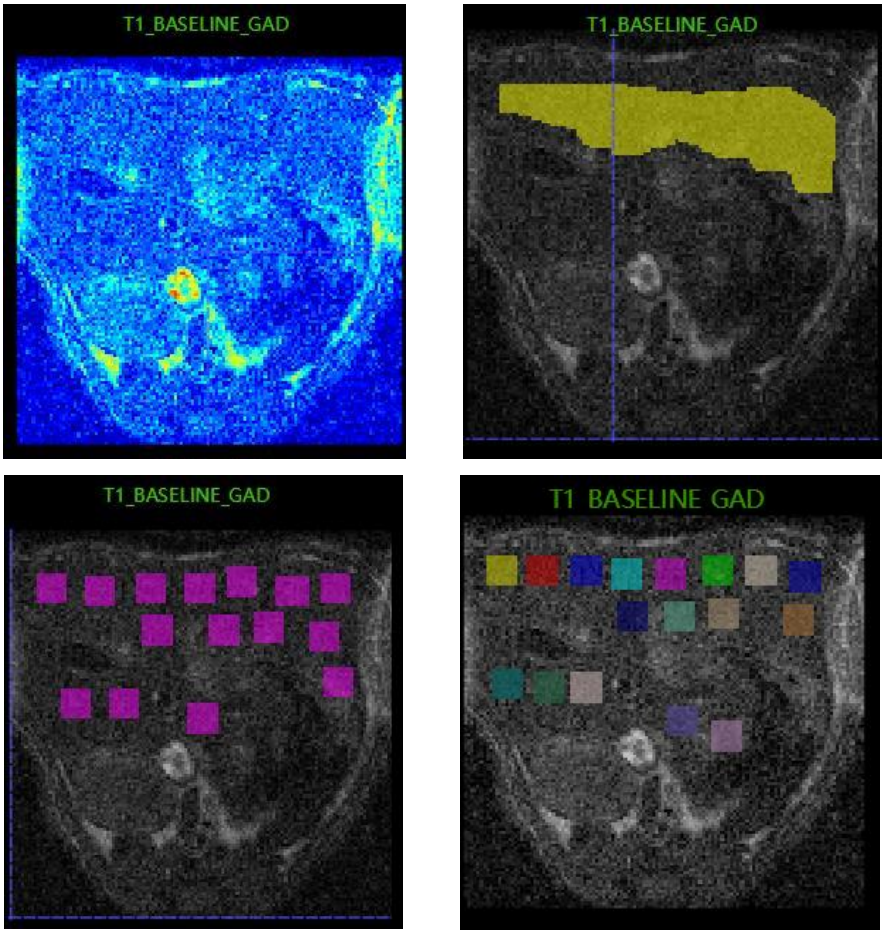


Figure 81 – Four types of view and ROI method. The top-left shall paint the image with false colour. The top-right shades the entire zone that might be the liver. The bottom-left shade area in diffinate squares and count the overall mean; the bottom-right shade the area in distinct squares that shall allow data extraction of each square seperately.

The second iteration of the method therefore used multiple square ROIs arranged as a grid over the liver. Rather than attempting to delineate the full liver contour, the field of view was overlaid with a lattice of regular squares, and those falling within visually homogeneous liver parenchyma were selected as ROIs. Squares overlapping obvious large vessels, bile ducts, stomach or the body wall were excluded manually. This approach reduced sensitivity to small changes in contour and allowed the spatial distribution of signal within the liver to be inspected, at the cost of replacing one large ROI with many smaller ones.

Subsequently, the size of the square ROIs was reduced further. Early grids still contained individual squares large enough to encompass both parenchyma and parts of vascular or periportal structures, so the grid spacing and ROI dimensions were refined to produce smaller, more localised samples. In the final protocol, each liver slice contained a set of relatively small square ROIs that sampled parenchyma at multiple positions while avoiding obvious non-parenchymal structures as far as possible. This progressive refinement from whole-liver masks to coarse, then finer, square ROIs is illustrated in Figure 81, together with example shading of the same image under each scheme. These comparisons highlight the trade-off between simplicity, robustness to drawing variability and sensitivity to local heterogeneity; the final small-square approach was adopted as the best compromise for the present study.

For each ROI and each time point, the mean intensity was exported from ITK-SNAP and assembled into a dataset for analysis in GraphPad Prism. To explore how the choice of normalisation affected interpretation, three related representations of the same underlying data were considered. First, “raw” intensities were examined, using the absolute signal values from the scanner. Secondly, baseline-subtracted intensities were calculated as

$$\Delta Signal_{(t)} = Signal_{(t)} - Signal_{(baseline)}$$

Equation 30 – Absolute signal change of in vivo MRI

So that each time point reflected the absolute increment above the pre-contrast value. Thirdly, relative changes were computed as

$$\Delta Signal\ \%_{(t)} = (\frac{Signal_{(t)}}{Signal_{(baseline)}} - 1) \times 100\%$$

Equation 31 – Relative signal change of in vivo MRI

Providing a dimensionless measure of enhancement that facilitated comparison between animals and experiments. For each representation, the distribution of ROI values at a given time point was summarized by the median and simple dispersion measures and plotted as time–intensity curves to assess overall trends and consistency between slices.

These analyses are presented in detail in the following experiment-specific sections (Sections 5.3.3 and 5.3.4), where the emphasis is on the shape and timing of the liver enhancement curves rather than on formal hypothesis testing. It should be noted that the ROI-based approach used here implicitly assumes that each anatomical slice occupies the same position at every time point, that the animal remains motionless under anaesthesia apart from physiological motion, and that the relative proportions of blood and hepatocytes within each ROI do not change dramatically over the course of the experiment. In reality, respiratory and cardiac motion, subtle shifts in posture, and dynamic changes in vascular filling can all introduce deviations from these assumptions. These factors are acknowledged as limitations when interpreting the numerical values of enhancement; the primary use of the ROI data in this chapter is to describe and compare broad temporal patterns of liver signal under different contrast and iron-loading conditions, rather than to derive absolute quantitative metrics.

5.3.3. Contrast performance of GdSCA for in vivo MRI

5.3.3.1. Design and dose for contrast performance of GdSCA for in vivo MRI

Experiment 1 was designed as an initial *in vivo* benchmark for the liver contrast performance of GdSCA under near-physiological iron conditions, using the licensed small-molecule agent Dotarem as a reference. The primary aim was to determine whether GdSCA, when administered as an intravenous bolus at a clinically relevant gadolinium dose, behaves in mice as a conventional extracellular T_1 agent in the liver. A secondary aim was to place the expected magnitude and time course of liver enhancement on the same approximate scale as a clinically used agent, without attempting to establish formal equivalence between the two.

To address these aims, two healthy male mice were allocated prospectively to receive either GdSCA or Dotarem. Both agents were administered as single intravenous boluses via the tail vein in-bore, using a pre-placed line and extension tubing as described in Section 5.3.2.3. The working concentration for each agent was 50 mM, so that a 100 µL bolus delivered 5 µmol of gadolinium per animal, corresponding to approximately 0.20 mmol Gd kg^{-1} in a 25 g mouse. This dose was chosen to be of the same order of magnitude as standard clinical dosing, while providing a robust liver T_1 signal change within the constraints of tail-vein injection volume and animal safety.

No ferric carboxymaltose (FCM) or other deliberate iron-loading intervention was used in this experiment. The intention was to characterise GdSCA under baseline

iron-handling conditions and to compare it qualitatively with Dotarem in an otherwise symmetric design. Both animals underwent identical preparation, anaesthesia and monitoring protocols, with prone positioning on a heated bed, isoflurane in oxygen delivered via a nose cone, and continuous ECG monitoring as outlined in Section 6.3.2.1. Slice prescription, sequence parameters and trigger settings were also kept identical between the two sessions, following the common *in vivo* MRI setup.

For each mouse, imaging followed the same dynamic protocol. A single pre-contrast baseline dataset was acquired first, using the final slice prescription and sequence parameters. The allocated contrast agent (GdSCA or Dotarem) was then injected intravenously in-bore through the tail-vein line, and this injection was defined as time zero (t = 0). Subsequent liver images were acquired every 5 min from t = 0 to t = 45 min, yielding 11 time points per slice (one baseline and ten post-contrast datasets). This fixed schedule was chosen to capture both the early enhancement phase and the later wash-out phase on a simple, reproducible time axis.

Liver signal was analysed using the ROI and data-processing strategy established in Section 6.3.2.X. Briefly, multiple small square ROIs were placed within visually homogeneous liver parenchyma on the baseline images and then propagated to all subsequent time points using ITK-SNAP, avoiding large vessels and non-hepatic structures. For each ROI and time point, mean signal values were exported for analysis in GraphPad Prism. In this experiment, the focus is on describing the temporal pattern of liver signal in the GdSCA session and on using the Dotarem

session as a qualitative reference under the same imaging conditions, rather than on performing formal statistical comparisons between agents.

5.3.3.2. The outcome of contrast in vivo

Representative *in vivo* T_1-weighted liver MRI images acquired following GdSCA administration and corresponding images with regions of interest (ROIs) overlaid are shown in Figure 84-Figure 88. All five axial slices are presented, including the pre-contrast baseline and serial post-contrast frames acquired every 5 min from 0 to 45 min, covering the full dynamic acquisition window. In each slice, multiple small square ROIs were placed within visually homogeneous liver parenchyma and deliberately positioned to avoid major vessels, arterial structures and non-hepatic tissues. All ROIs were defined on the baseline image and then rigidly propagated to all subsequent time points, such that the same anatomical locations were sampled throughout the time course. Under the conditions of anaesthesia and animal fixation used here, no obvious gross repositioning was observed during the dynamic acquisition, and ROI positions were therefore assumed to remain spatially consistent across time points for the purposes of analysis.

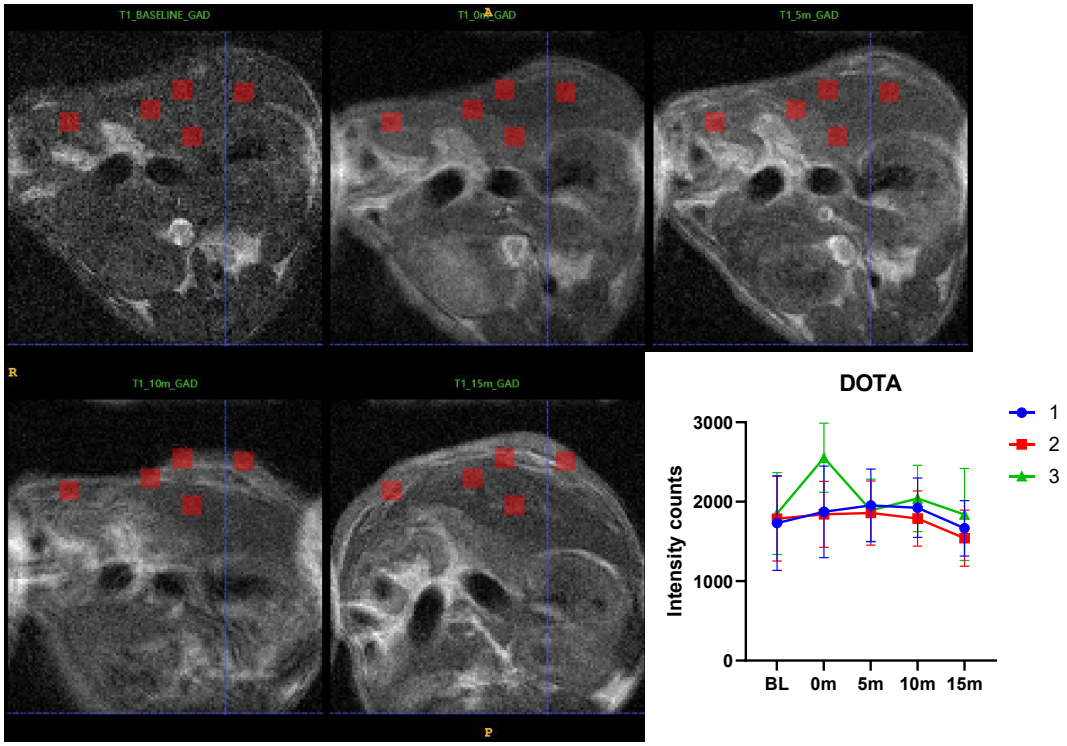


Figure 82 – The image slice #2 of MRI in vivo for the commercially available Dotarem and its intensity plot of 3 adjacent slices

For the Dotarem session, only baseline and early post-contrast frames are shown for qualitative reference in Figure 82. In this case, the animal exhibited ECG flatline at approximately 10 min after injection and died during acquisition, resulting in pronounced positional changes within the magnet. As a consequence, stable ROI placement could not be maintained in later frames for several slices, and this dataset was excluded from quantitative analysis. The Dotarem images presented here are therefore intended solely to document the comparator attempt and its limitations, rather than to support numerical comparison with GdSCA.[208, 209]

Quantitative changes in liver signal derived from the ROI analysis are summarised in Figure 83. Signal changes are reported relative to the pre-contrast baseline using the definitions described in Section 5.3.2. For clarity of presentation, the current figure

illustrates the data as mean ± SD across ROIs; in the final analysis, central tendency and dispersion were assessed using the median with 95% confidence intervals, which yielded trends consistent with those shown here. Following intravenous administration of GdSCA, all five slices exhibited clear increases in liver signal relative to baseline. The magnitude of enhancement varied between slices, indicating spatial heterogeneity at the slice level. In temporal terms, an early post-injection increase in signal was observed, followed by sustained elevation above baseline throughout the remainder of the 45 min acquisition window. Within this single-animal dataset, no clear monotonic time dependence or consistent peak time was apparent across slices, and the results are therefore presented descriptively without kinetic modelling or formal statistical testing.[131, 210]

To facilitate more detailed inspection while limiting the influence of slices with high vascular content or limited ROI sampling, two slices showing the maximum enhancement relative to baseline across the entire acquisition window were selected for focused analysis. This selection criterion was applied uniformly and reflects a methodological choice rather than post hoc optimisation. The corresponding slice-level distributions and time courses are shown in Figure 86 (Slice 3) and Figure 87 (Slice 4), where the dispersion of ROI values at each time point and their temporal evolution can be examined in greater detail. Across these representative slices, the enhancement patterns observed were consistent with the slice-averaged trends, with appreciable inter-ROI variability but a coherent overall increase in signal following GdSCA administration.

A partial Dotarem dataset was acquired as a clinical reference under nominally matched gadolinium dosing conditions; however, this session was interrupted by an ECG flatline event at approximately 10 min after injection, followed by animal death and substantial positional changes within the magnet. As illustrated in Figure 82, only baseline and a limited number of early post-contrast frames could be obtained before acquisition was terminated. In the later frames, stable slice positioning and ROI placement could not be maintained for several slices, precluding reliable quantitative analysis. Consequently, the Dotarem dataset is presented solely for qualitative context and is excluded from all numerical comparisons.

Notably, within the period during which the animal remained alive, the Dotarem images did not show liver signal enhancement of comparable visual magnitude to that observed in the GdSCA session, despite the fact that the injected Dotarem concentration was not lower than that used for GdSCA. This observation should not be interpreted as a direct performance comparison between agents. Instead, it is more plausibly attributed to the rapid deterioration of physiological status, altered perfusion, and positional instability associated with the terminal event, as well as to uncertainties related to dilution, effective delivered concentration, and small-animal handling of a clinical formulation.[64, 72, 208] For these reasons, no quantitative or inferential conclusions are drawn from the Dotarem session.

Taken together, the results of this experiment demonstrate that intravenous administration of GdSCA produces a clear and readily detectable increase in liver signal on T_1-weighted *in vivo* MRI under baseline conditions. Although variability

between slices and ROIs was observed, the presence of robust enhancement relative to baseline was consistent across the dataset. These findings establish the baseline *in vivo* contrast behaviour of GdSCA and provide the foundation for subsequent experiments in which systemic iron handling is deliberately perturbed.

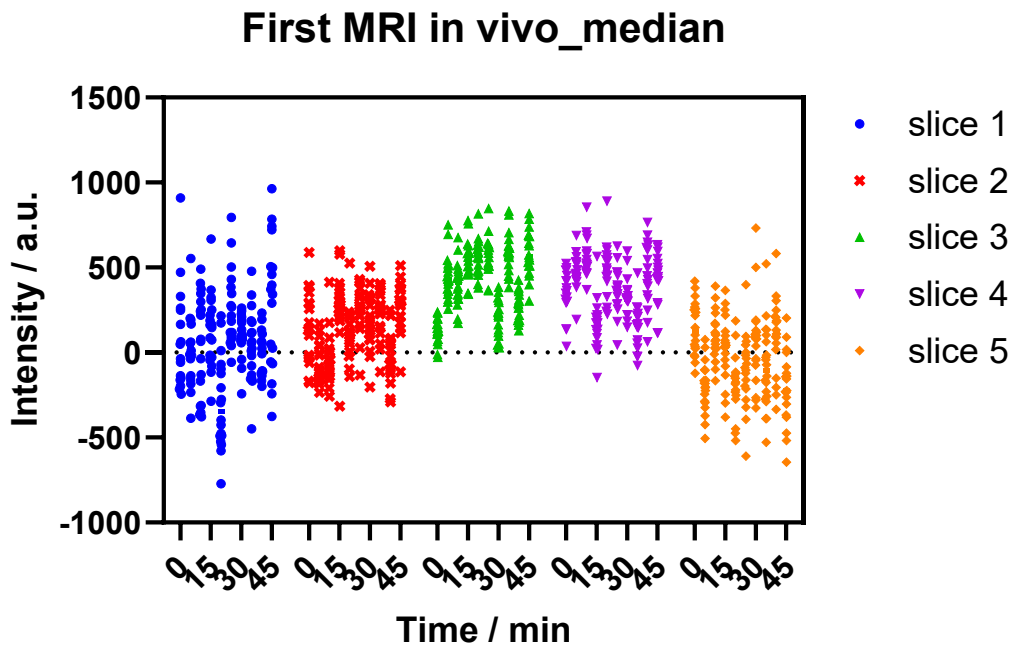


Figure 83 – Signal intensity of the MRI in vivo of GdSCA performance against time. Each dot respresent the signal intensity of an ROI square of the slices shown in Figure 84-Figure 88, which showed a increase of contrast from slice 3 and 4

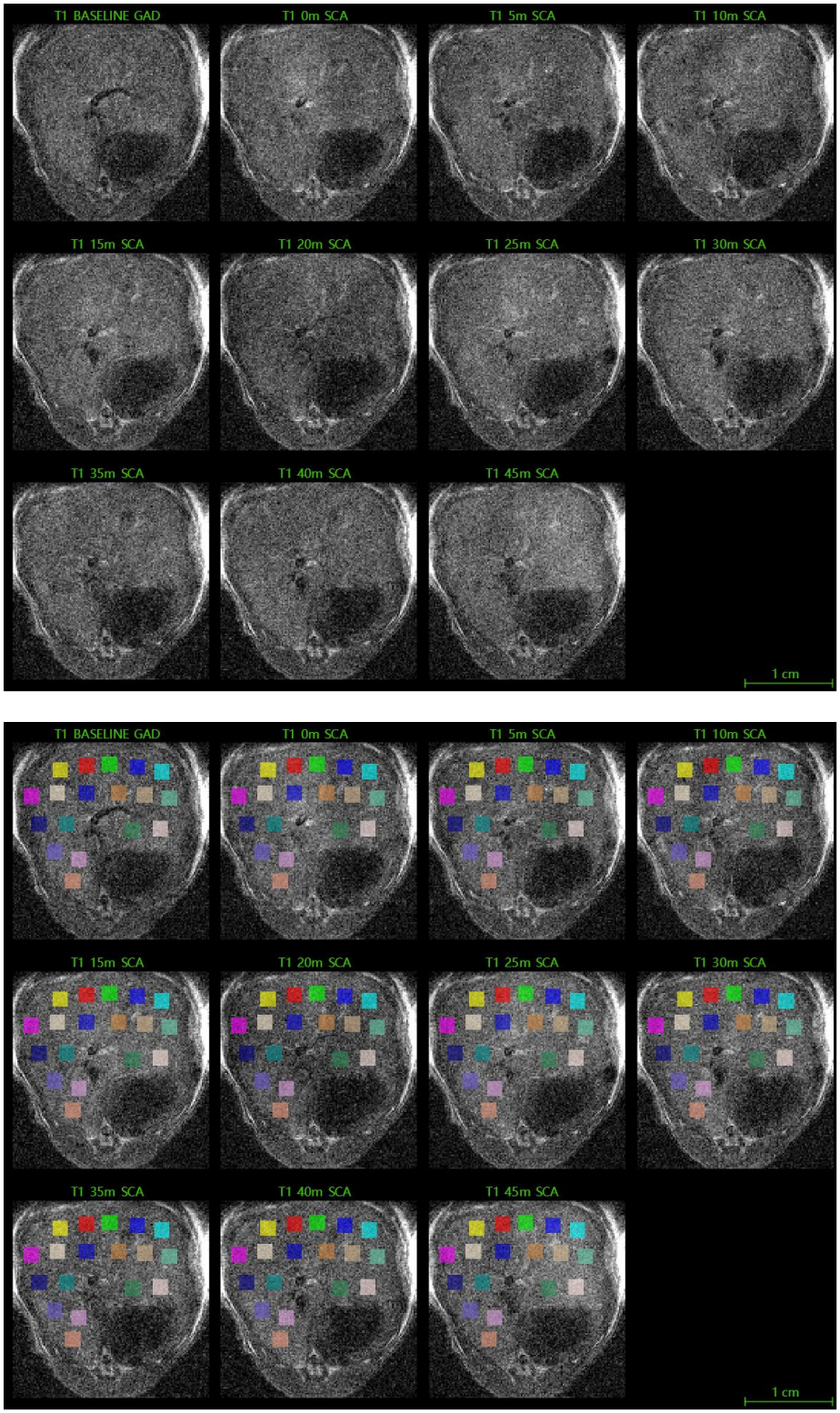


Figure 84 –In vivo T1-weighted liver in vivo MRI of a mouse for GdSCA (slice 1): (A) Baseline and serial acquisitions every 5 min from 0–45 min; (B) The same series with ROI overlaid for subsequent quantitative analysis.

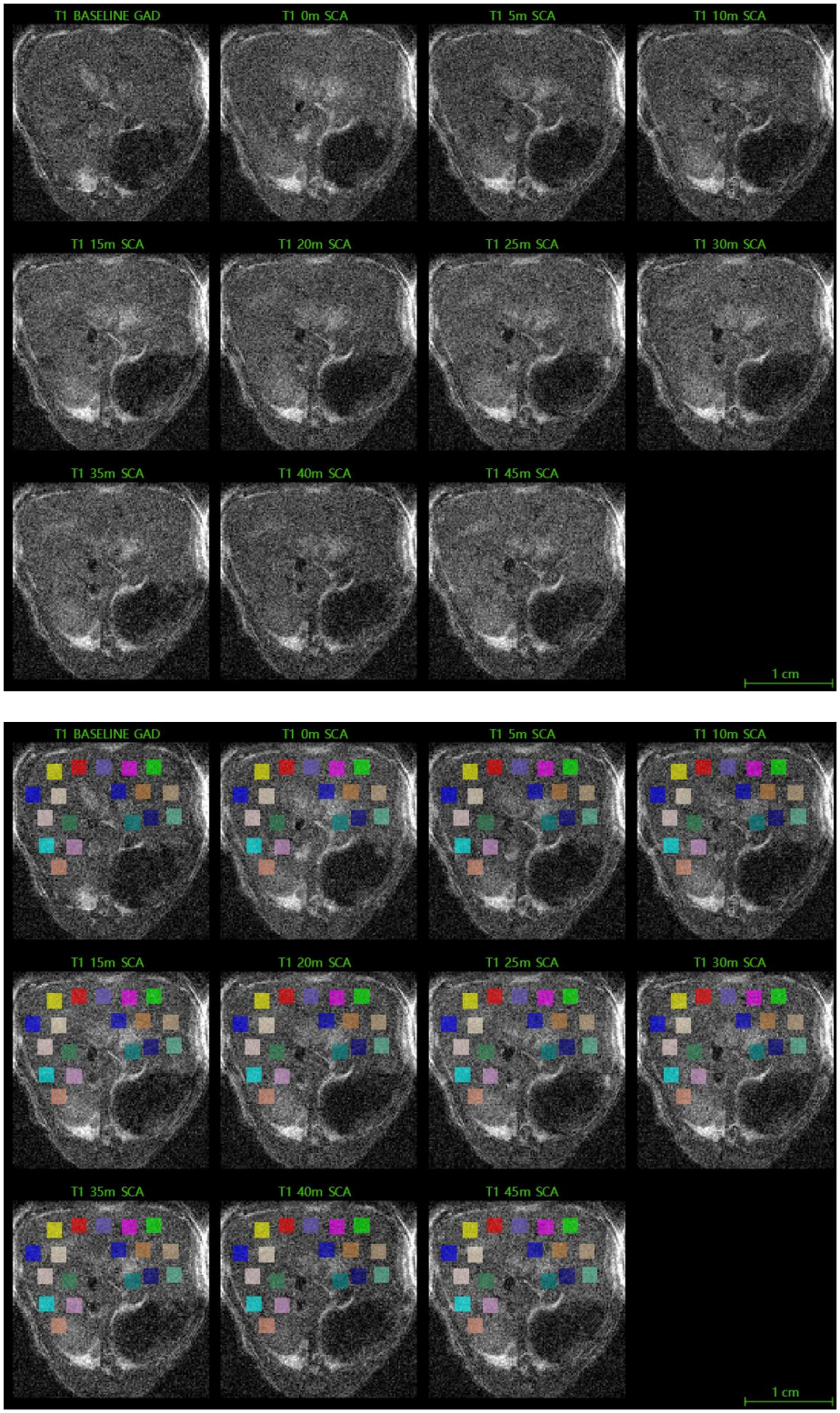


Figure 85 –In vivo T1-weighted liver in vivo MRI of a mouse for GdSCA (slice 2): (A) Baseline and serial acquisitions every 5 min from 0–45 min; (B) The same series with ROI overlaid for subsequent quantitative analysis.

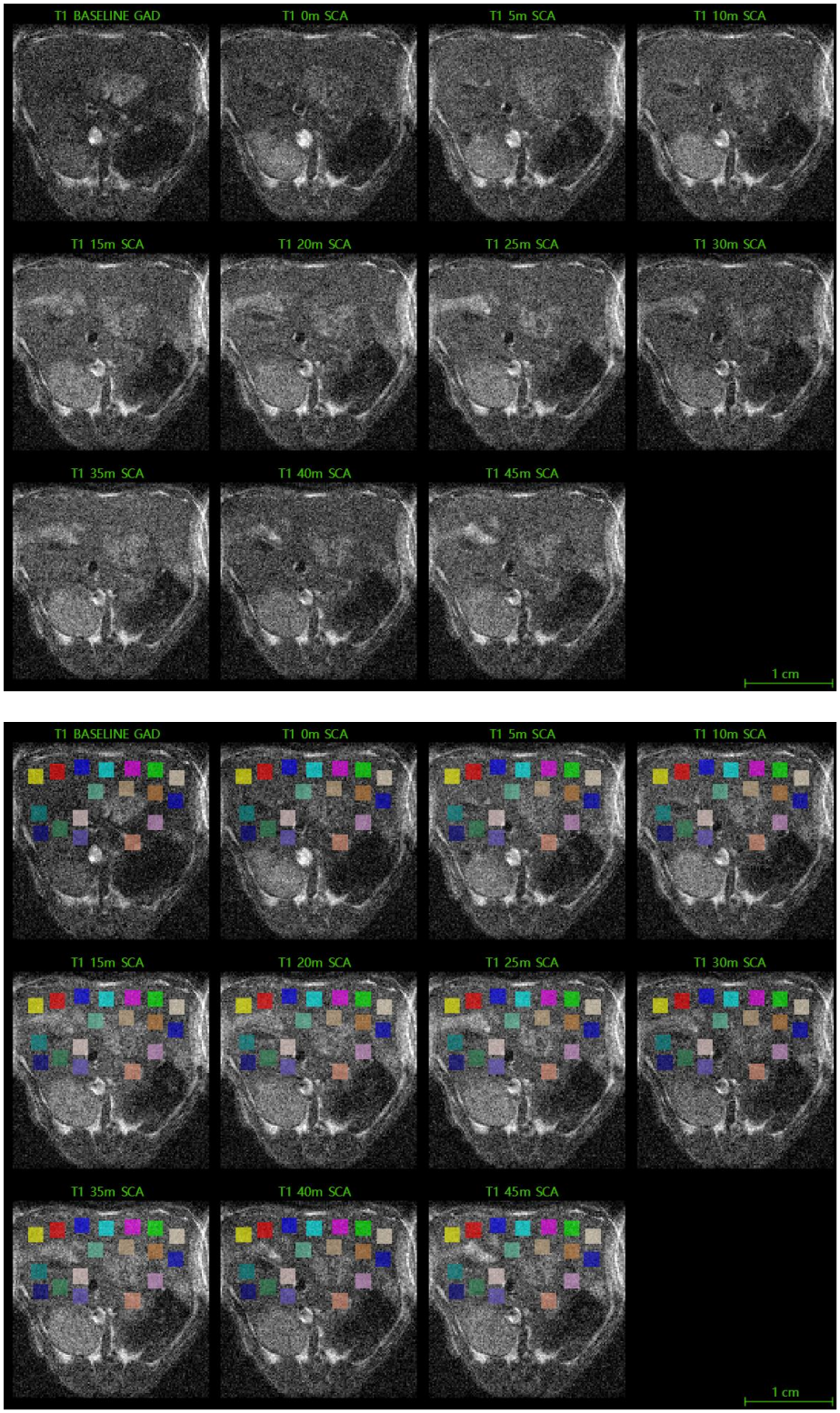


Figure 86 –In vivo T1-weighted liver in vivo MRI of a mouse for GdSCA (slice 3): (A) Baseline and serial acquisitions every 5 min from 0–45 min; (B) The same series with ROI overlaid for subsequent quantitative analysis.

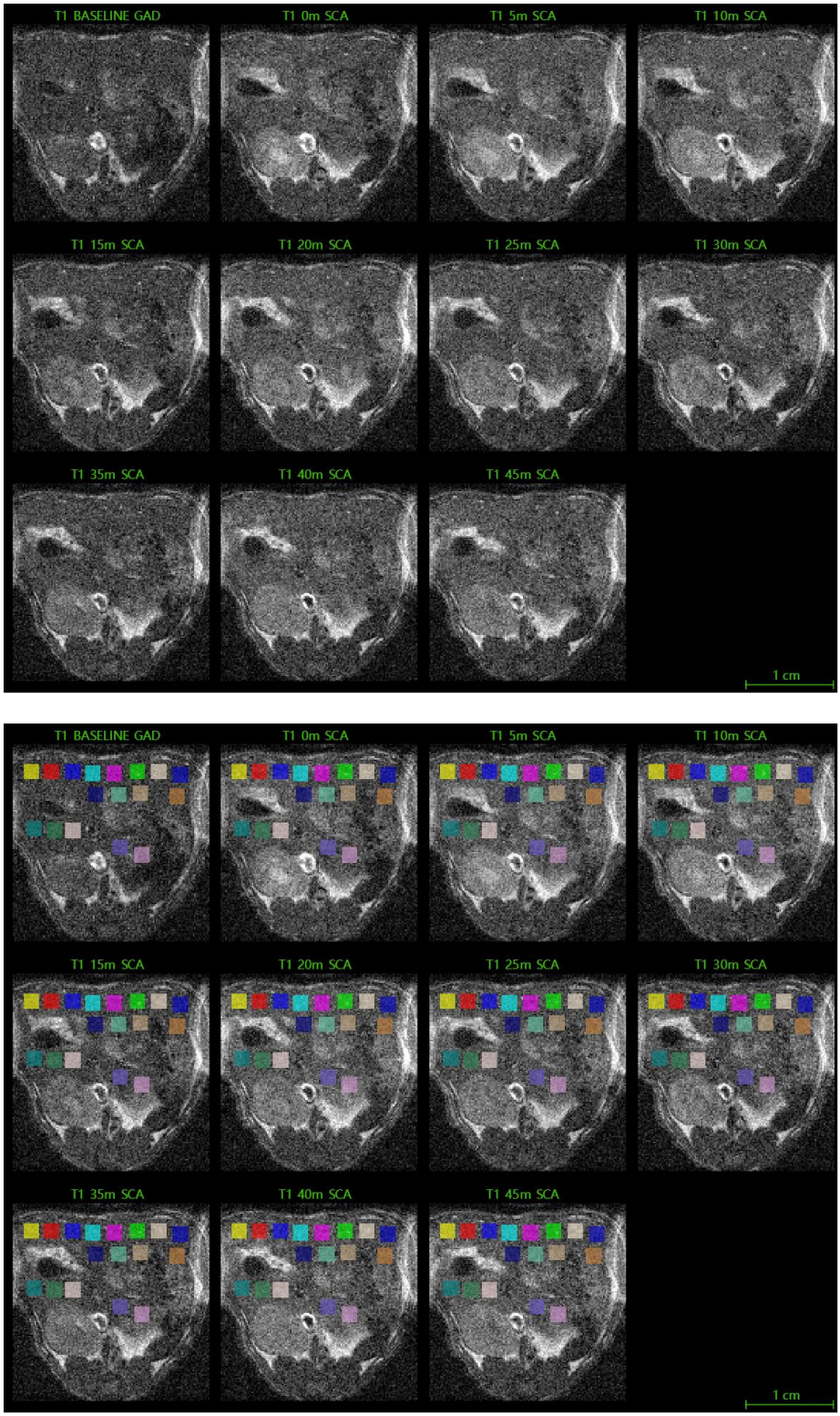


Figure 87 –In vivo T1-weighted liver in vivo MRI of a mouse for GdSCA (slice 4): (A) Baseline and serial acquisitions every 5 min from 0–45 min; (B) The same series with ROI overlaid for subsequent quantitative analysis.

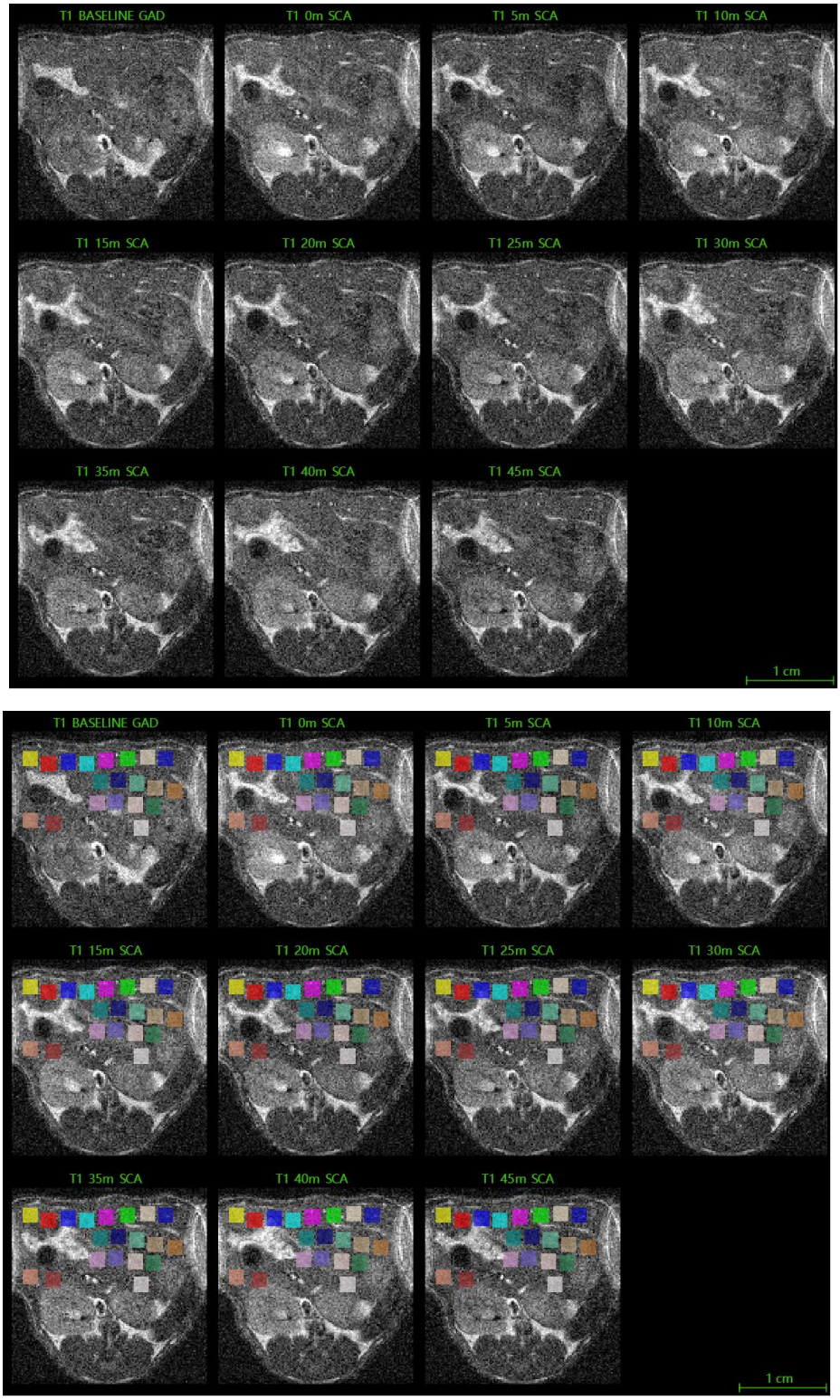


Figure 88 –In vivo T1-weighted liver in vivo MRI of a mouse for GdSCA (slice 5): (A) Baseline and serial acquisitions every 5 min from 0–45 min; (B) The same series with ROI overlaid for subsequent quantitative analysis.

5.3.4. In vivo MRI with GdSCA under altered iron handling with FCM

5.3.4.1. Design of FCM controlled experiment

Following the baseline in vivo evaluation described in Section 6.3.3, an additional MRI experiment was conducted to examine whether modifying systemic iron handling could influence the liver enhancement behaviour of GdSCA. Ferric carboxymaltose (FCM) was used as a pharmacological intervention to alter iron status, while all other aspects of the imaging protocol, contrast dose, and ROI analysis strategy were kept identical to those described previously.

Two mice were studied under different FCM administration schedules. In one case, FCM was administered intravenously two days before the MRI session, such that GdSCA was injected into a physiological background expected to reflect a pre-existing iron-loaded state. In the other case, baseline imaging and GdSCA injection were performed first, followed by intravenous administration of an equivalent dose of FCM 15 min later during the dynamic acquisition. In both cases, FCM was injected outside the magnet, after which the animals were repositioned and scanning was resumed using the same slice prescription and acquisition settings.

For both animals, MRI acquisition followed the same dynamic schedule as in Section 6.3.3, consisting of a single pre-contrast baseline dataset followed by liver imaging every 5 min from t = 0 to t = 45 min after GdSCA injection. Physiological monitoring indicated stable vital signs throughout the imaging sessions, and both animals

completed the full acquisition. A schematic overview of the two FCM administration schedules relative to the MRI timeline is shown in Figure 79.

5.3.4.2. FCM MRI in vivo results

Quantitative liver signal changes for the two FCM-modulated conditions are summarised in the figures below. Signal changes are reported relative to the pre-contrast baseline using the same ROI-based approach and summary statistics as described in Section 6.3.3. For consistency with the baseline experiment, two slices from each animal showing the maximum enhancement relative to baseline across the entire acquisition window were selected for detailed presentation.

In the condition where FCM was administered two days before MRI (FCM → GdSCA), intravenous GdSCA injection resulted in clearly detectable liver signal enhancement across the analysed slices. The overall magnitude of enhancement and its temporal evolution were broadly comparable to those observed in the baseline experiment, although differences in absolute signal change were evident between slices and time points. Signal remained elevated relative to baseline throughout the 45-min acquisition window.

In the condition where FCM was administered 15 min after GdSCA injection (GdSCA → FCM), liver enhancement following GdSCA administration was again readily observed. Subsequent signal behaviour after FCM administration differed in detail from the pre-loaded condition, with the enhancement curves not fully overlapping between the two iron-handling schedules. Directional differences in magnitude and temporal profile were apparent in some slices and time intervals.

Across both FCM-modulated conditions, substantial variability was present at multiple levels, including between slices and among ROIs within individual slices. The distributions of ROI values overlapped across conditions and time points, and no statistically significant separation between the two iron-loading schedules could be established within this limited dataset. Representative MRI images with ROI overlays for these experiments are provided for qualitative reference.

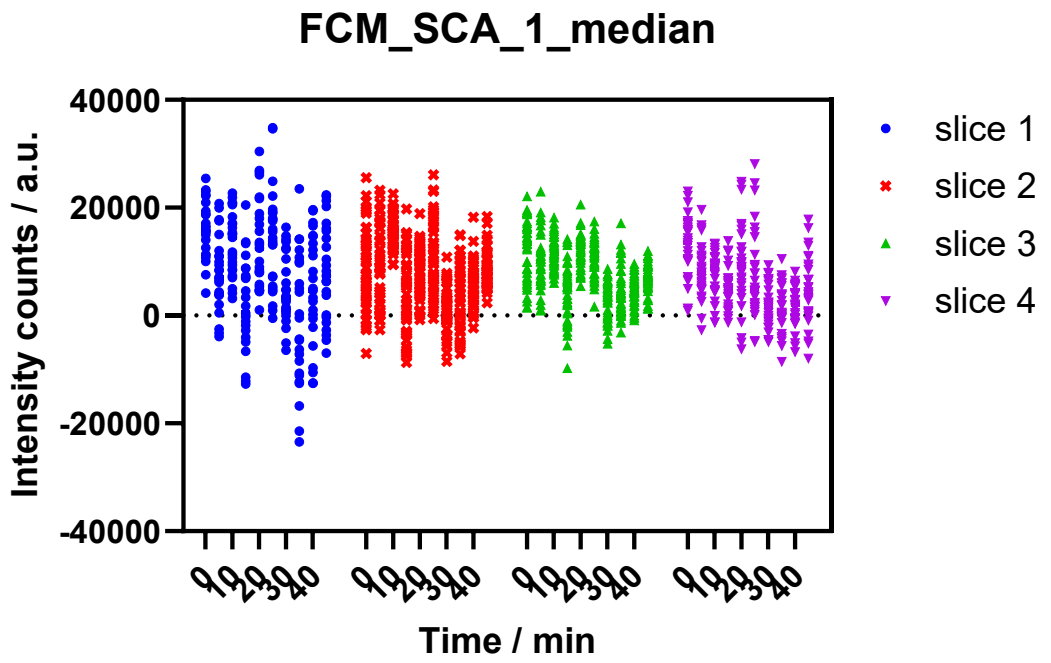


Figure 89– Signal intensity of the MRI in vivo of GdSCA performance with 2-day-pre-injected FCM against time. Each dot respresent the signal intensity of an ROI square of the slices shown in Figure 90-Figure 94

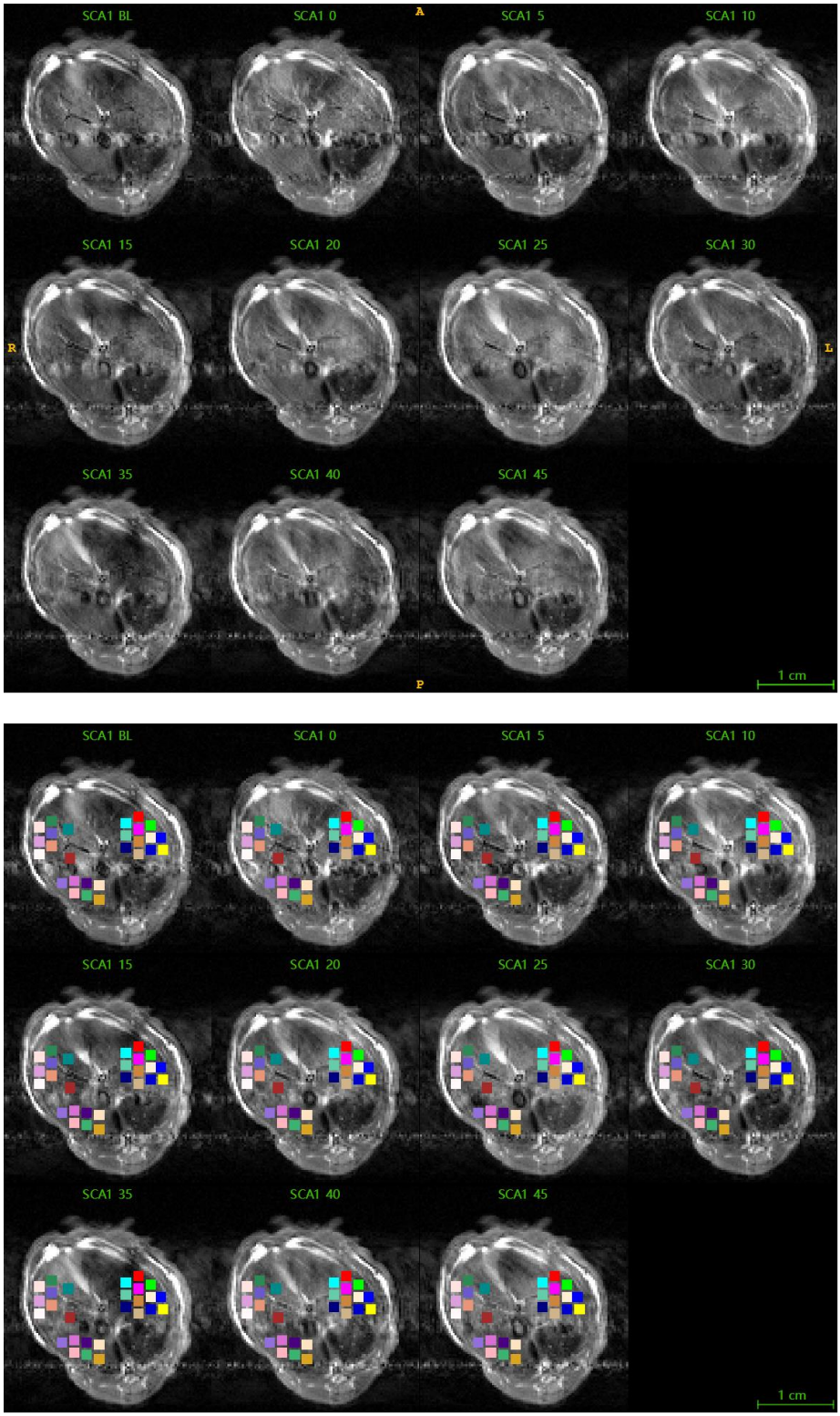


Figure 90 –In vivo T1-weighted liver in vivo MRI of a mouse for GdSCA with 2day-pre-injected FCM (slice 1): (A) Baseline and serial acquisitions every 5 min from 0–45 min; (B) The same series with ROI overlaid for subsequent quantitative analysis.

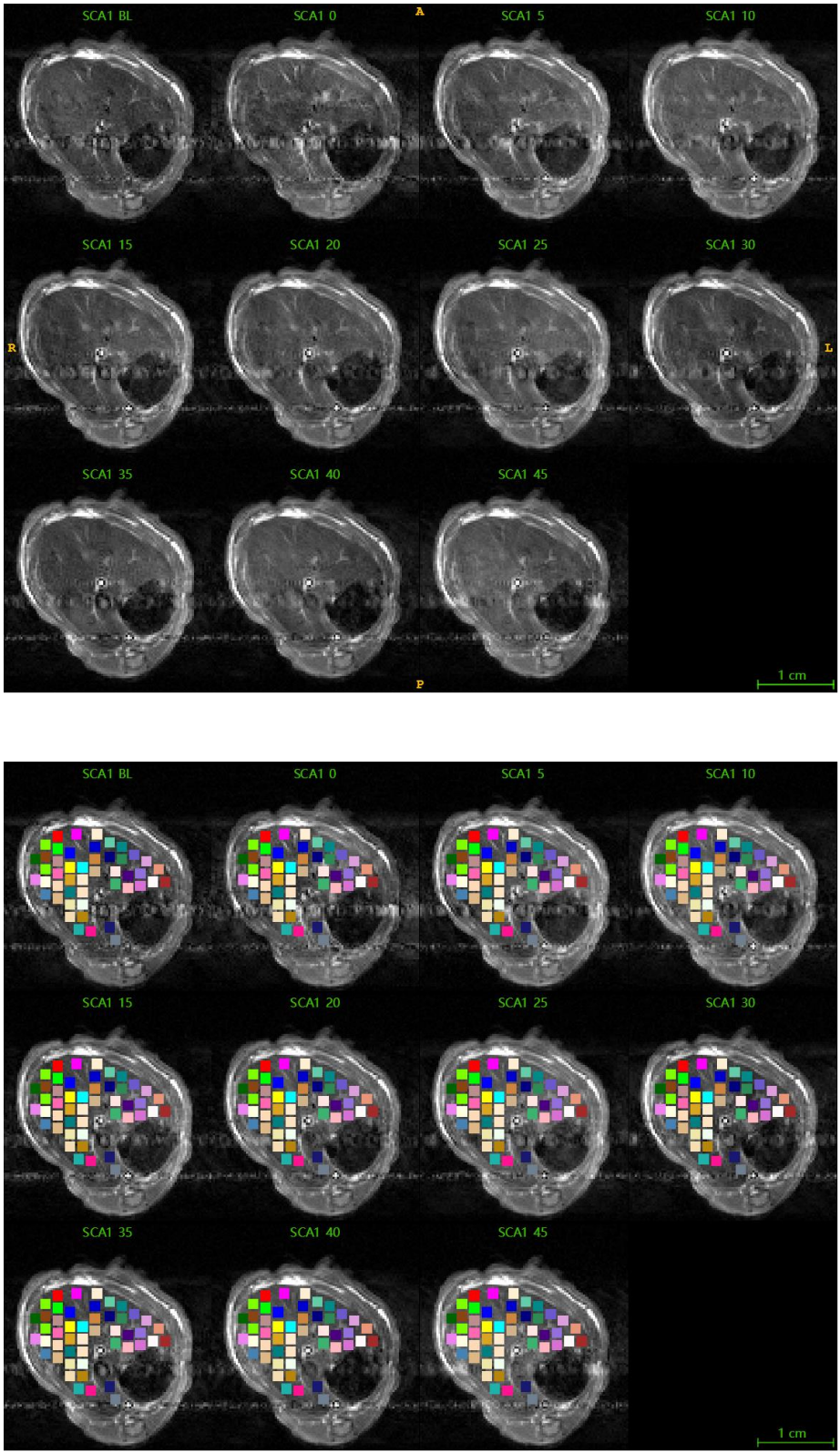


Figure 91 –In vivo T1-weighted liver in vivo MRI of a mouse for GdSCA with 2day-pre-injected FCM (slice 2): (A) Baseline and serial acquisitions every 5 min from 0–45 min; (B) The same series with ROI overlaid for subsequent quantitative analysis.

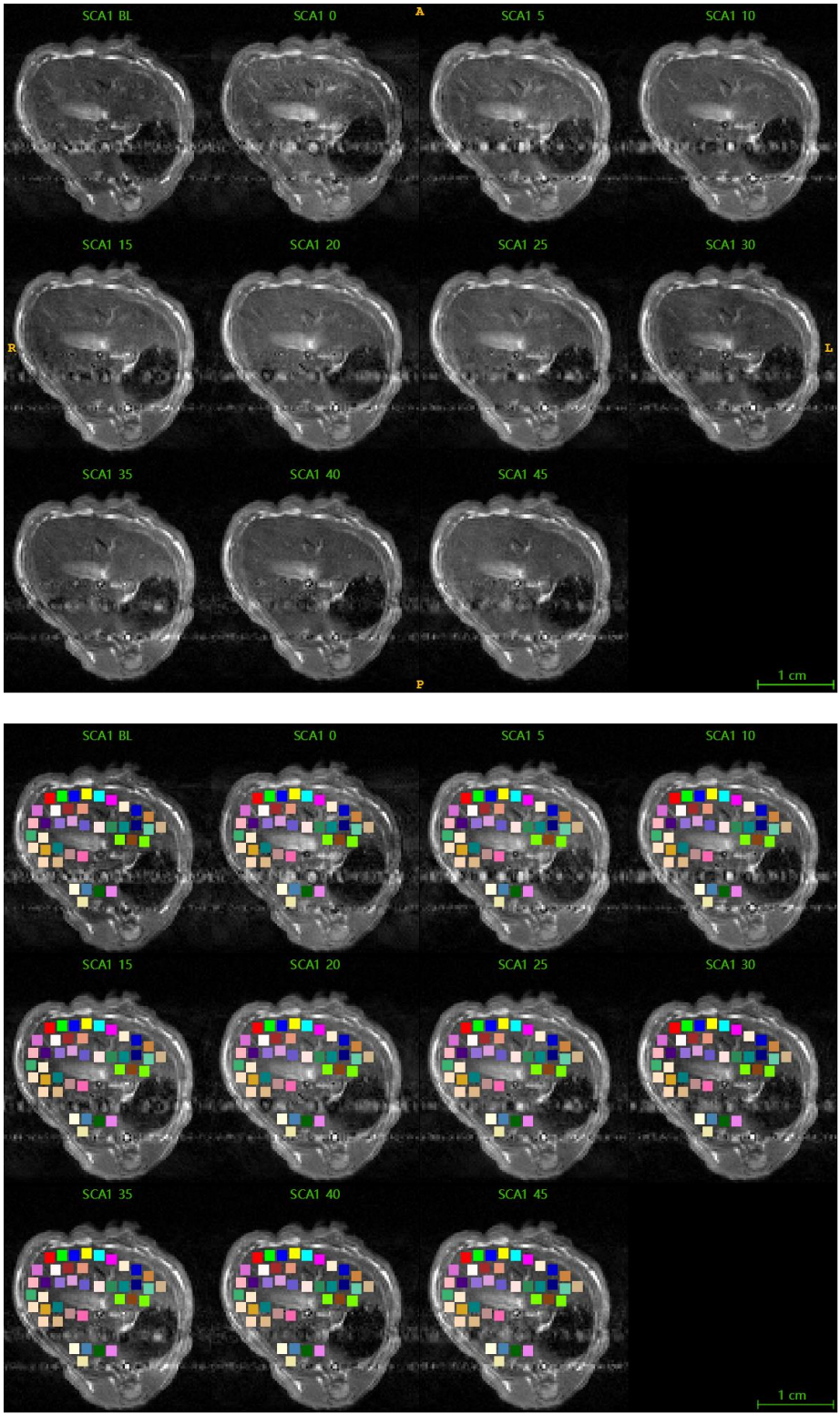


Figure 92 –In vivo T1-weighted liver in vivo MRI of a mouse for GdSCA with 2day-pre-injected FCM (slice 3): (A) Baseline and serial acquisitions every 5 min from 0–45 min; (B) The same series with ROI overlaid for subsequent quantitative analysis.

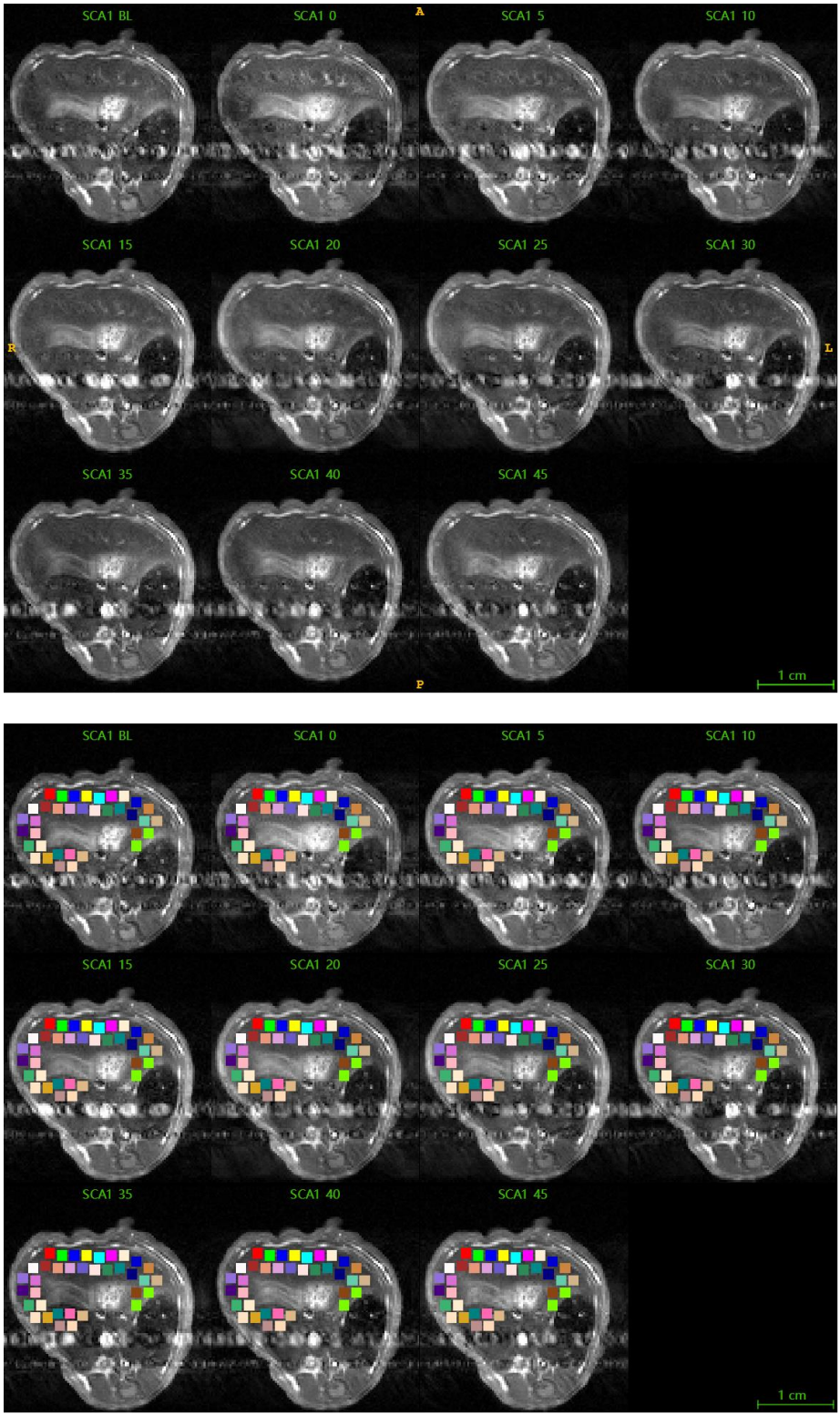


Figure 93 –In vivo T1-weighted liver in vivo MRI of a mouse for GdSCA with 2day-pre-injected FCM (slice 4): (A) Baseline and serial acquisitions every 5 min from 0–45 min; (B) The same series with ROI overlaid for subsequent quantitative analysis.

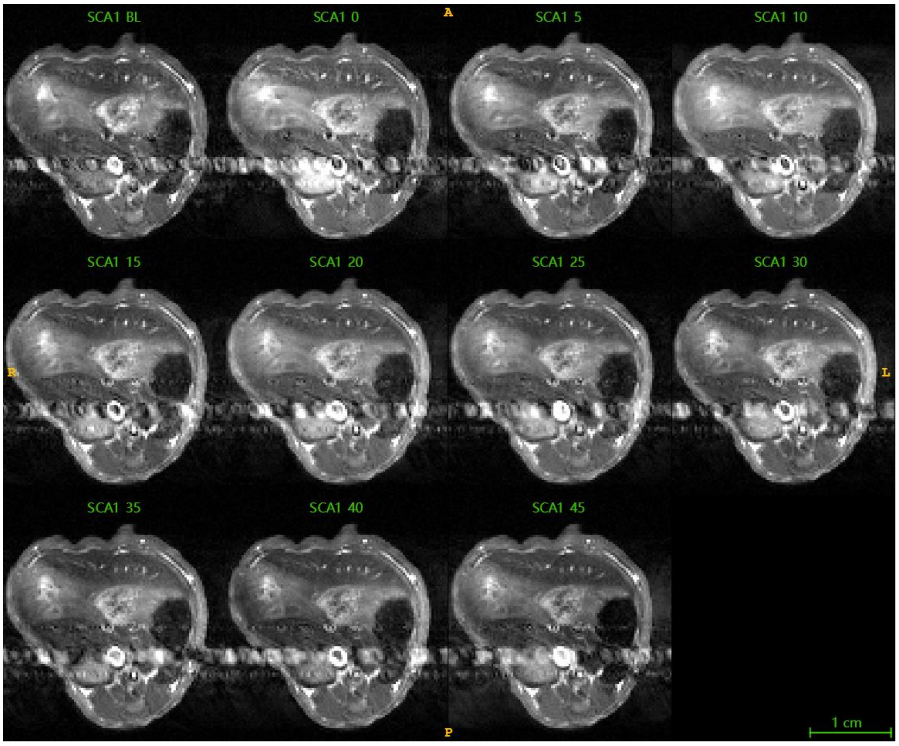


Figure 94 –In vivo T1-weighted liver in vivo MRI of a mouse for GdSCA with 2day-pre-injected FCM (slice 5): (A) Baseline and serial acquisitions every 5 min from 0–45 min. (the recognizable liver area was limited and this slice was not adopted for further ROI statistics)

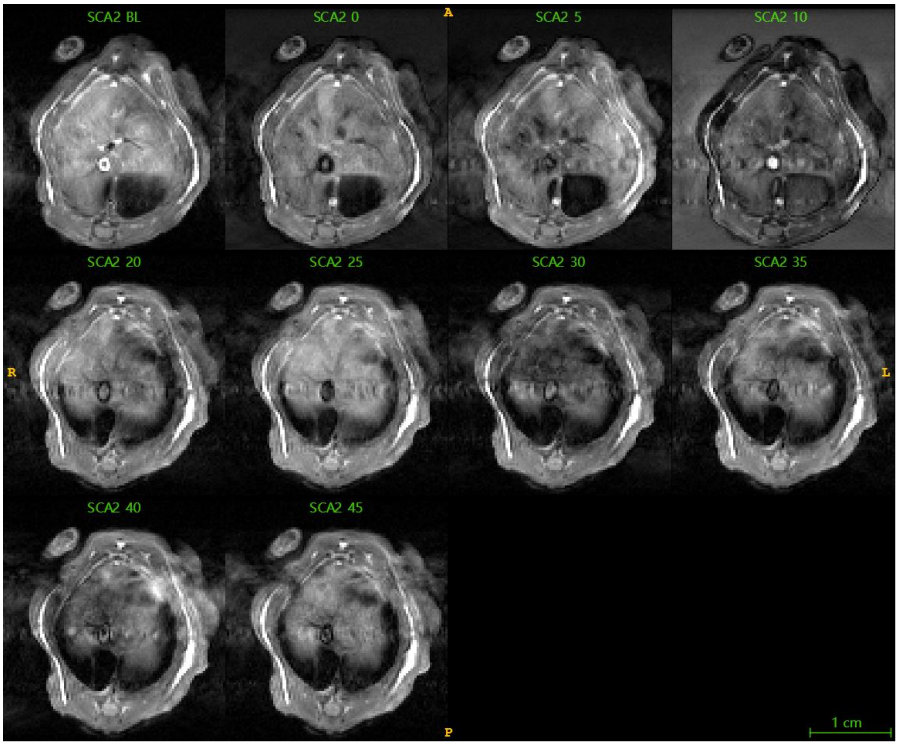


Figure 95 –In vivo T1-weighted liver in vivo MRI of a mouse for GdSCA with 10min-post-injected FCM (slice 1): (A) Baseline and serial acquisitions every 5 min from 0–45 min; (the recognizable liver area was limited and this slice was not adopted for further ROI statistics)

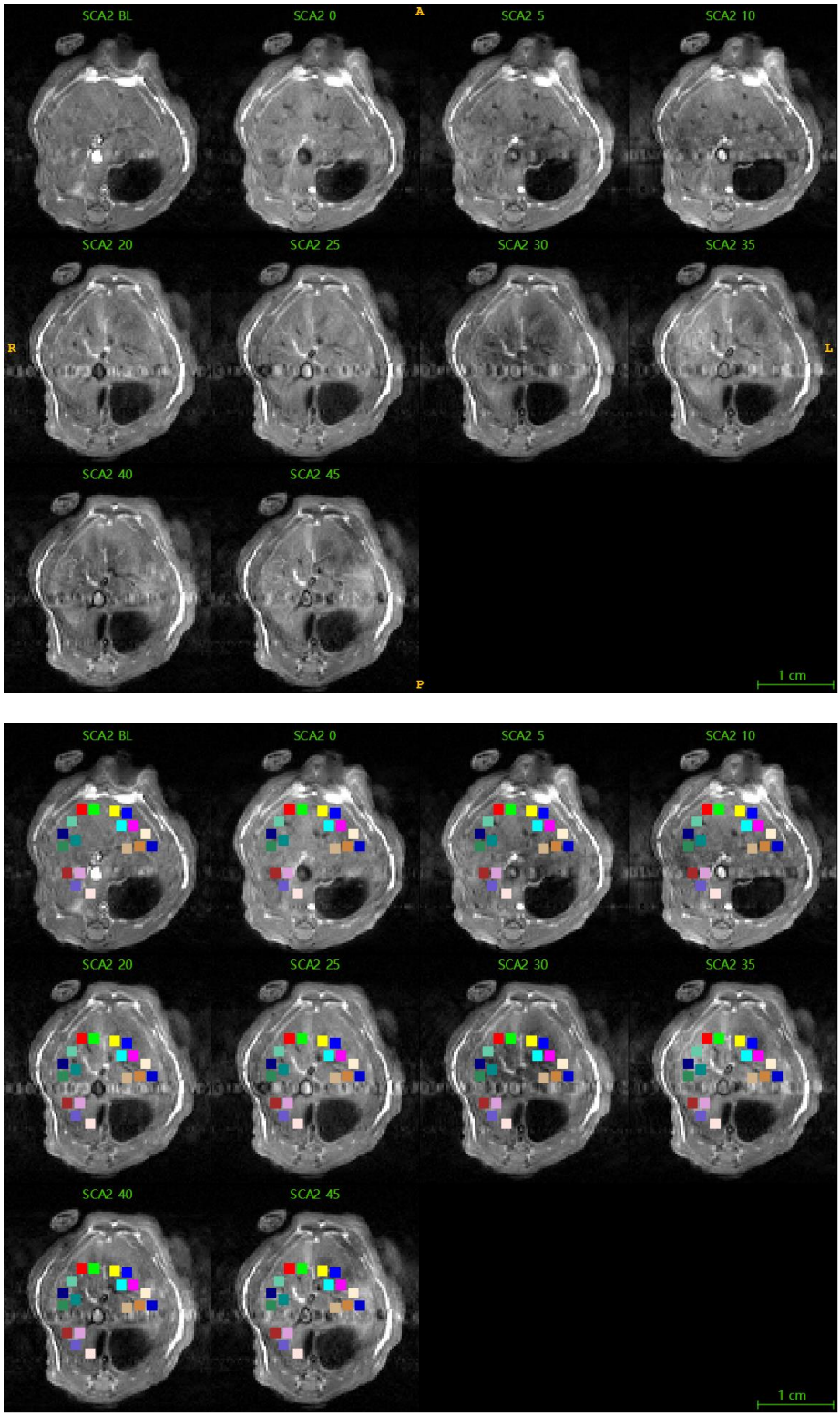


Figure 96 –In vivo T1-weighted liver in vivo MRI of a mouse for GdSCA with 10min-post-injected FCM (slice 2): (A) Baseline and serial acquisitions every 5 min from 0–45 min; (B) The same series with ROI overlaid for subsequent quantitative analysis.

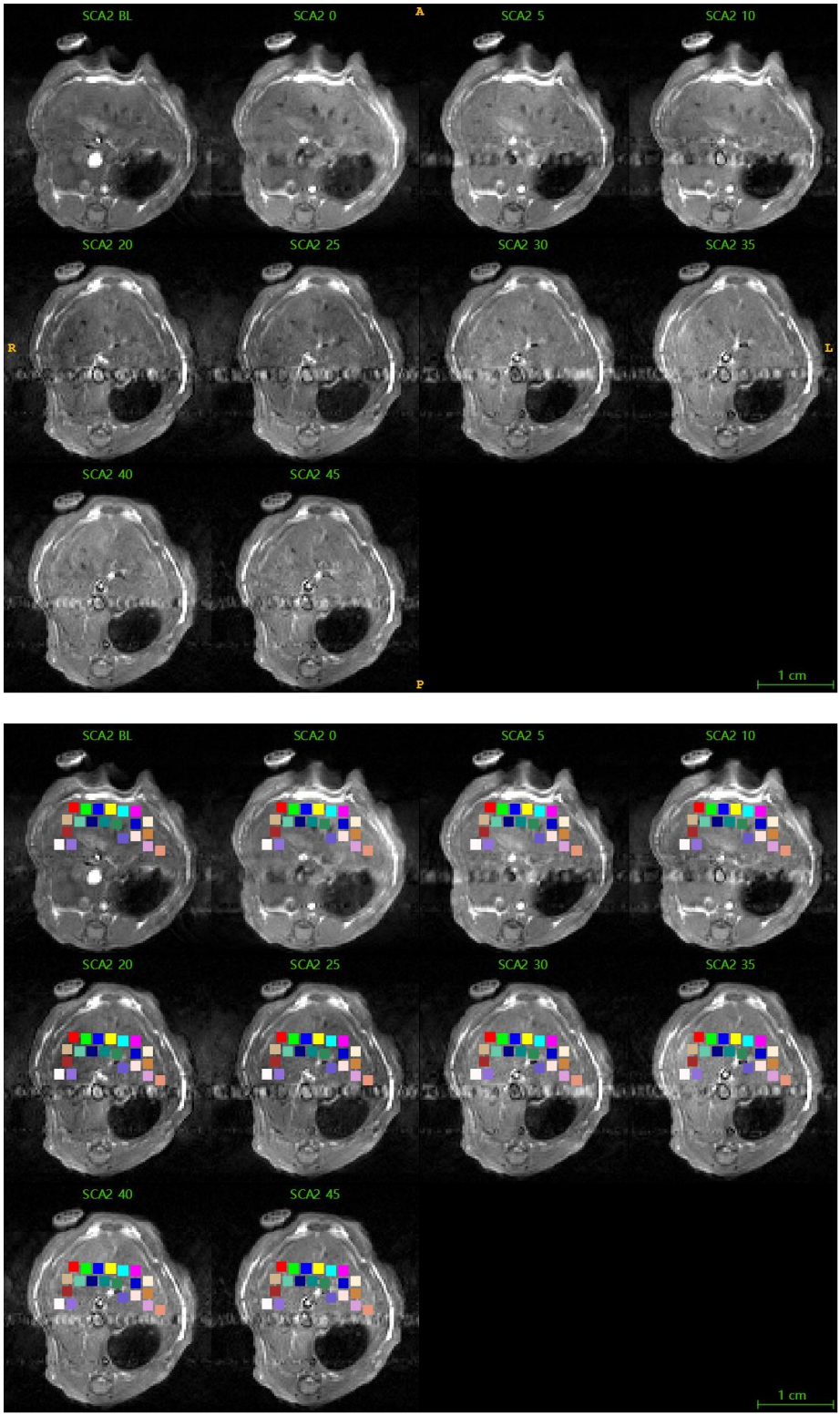


Figure 97 –In vivo T1-weighted liver in vivo MRI of a mouse for GdSCA with 10min-post-injected FCM (slice 3): (A) Baseline and serial acquisitions every 5 min from 0–45 min; (B) The same series with ROI overlaid for subsequent quantitative analysis.

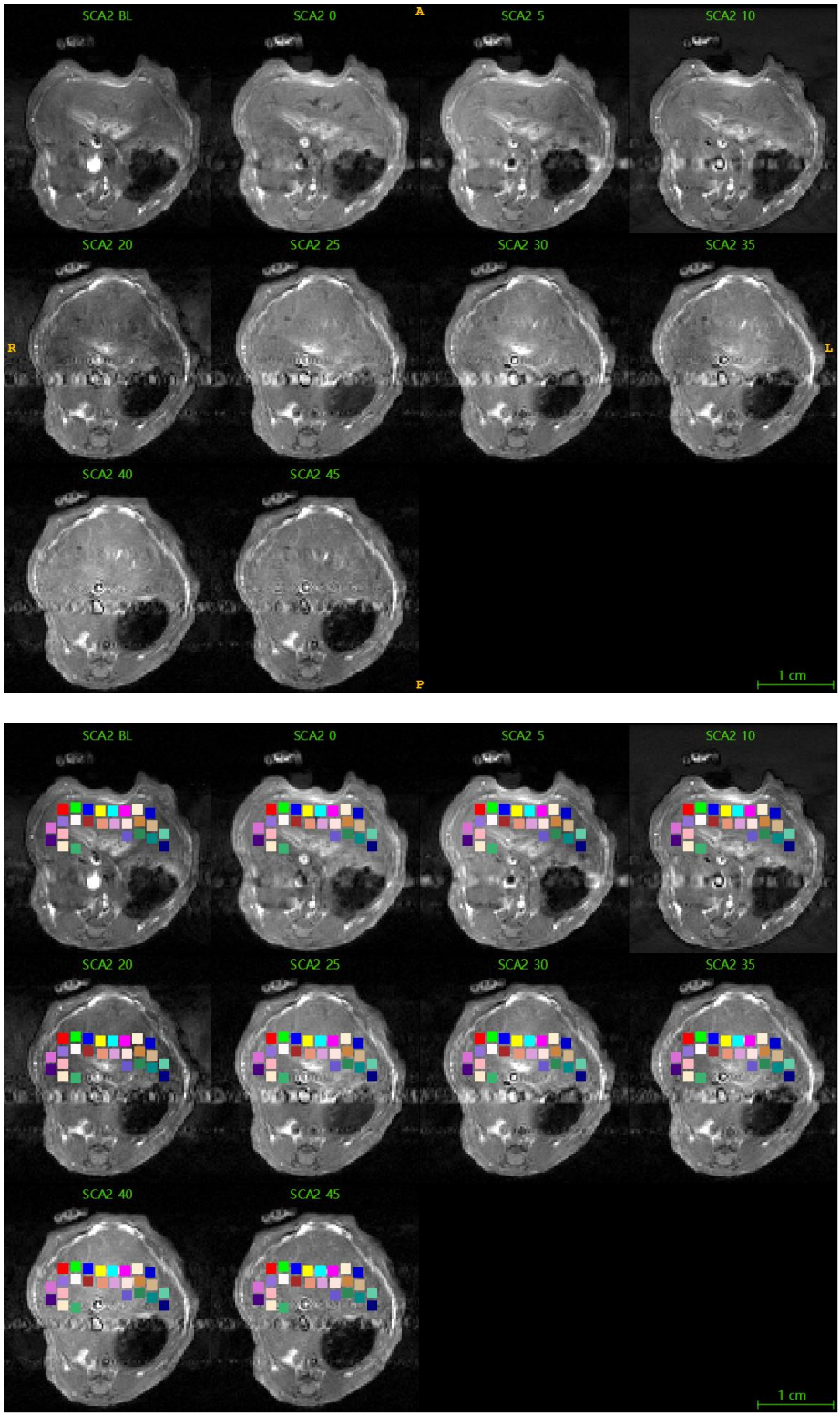


Figure 98 –In vivo T1-weighted liver in vivo MRI of a mouse for GdSCA with 10min-post-injected FCM (slice 4): (A) Baseline and serial acquisitions every 5 min from 0–45 min; (B) The same series with ROI overlaid for subsequent quantitative analysis.

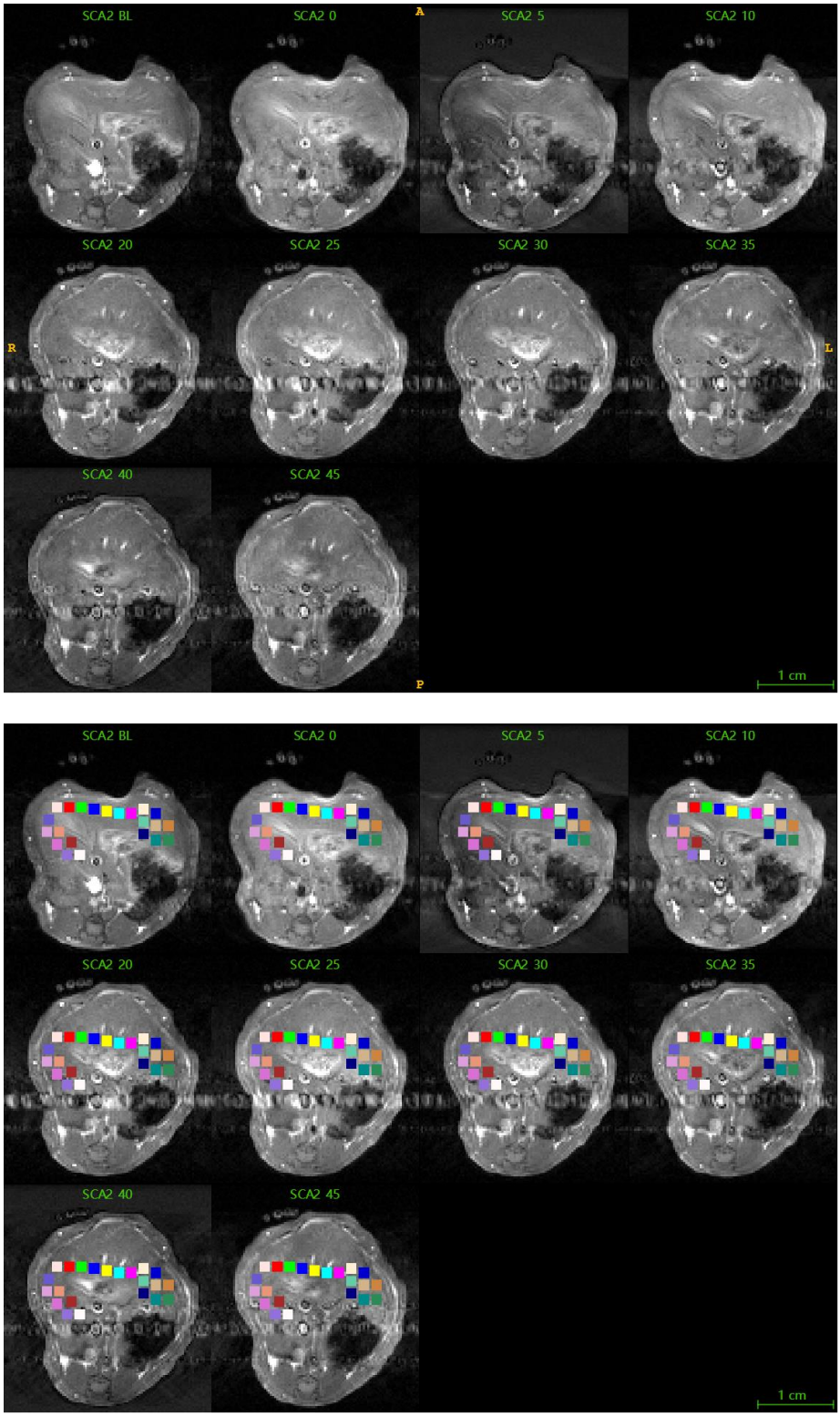


Figure 99 –In vivo T1-weighted liver in vivo MRI of a mouse for GdSCA with 10min-post-injected FCM (slice 5): (A) Baseline and serial acquisitions every 5 min from 0–45 min; (B) The same series with ROI overlaid for subsequent quantitative analysis.

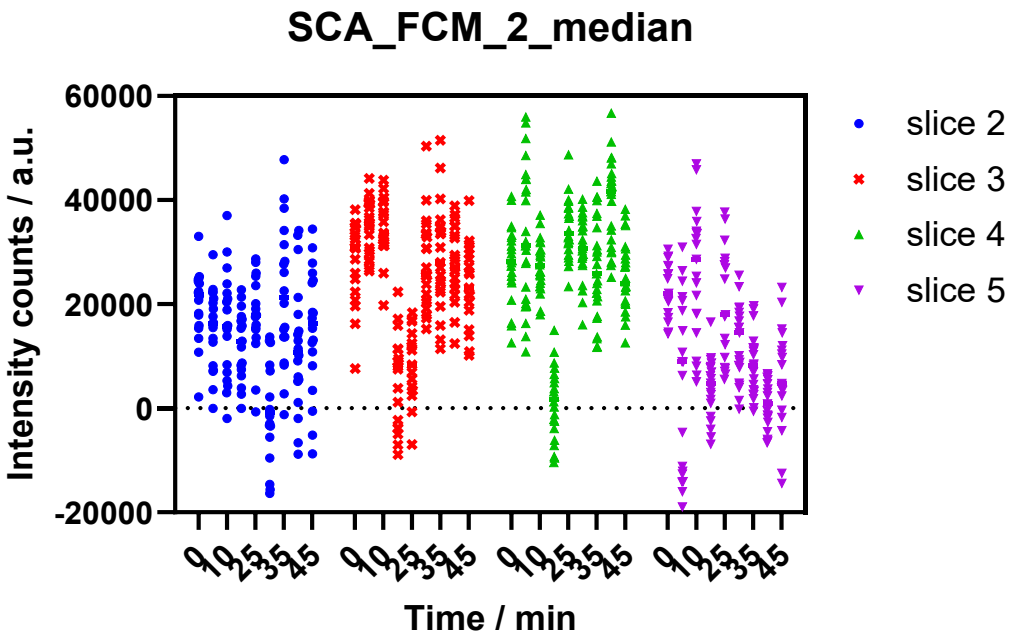


Figure 100– Signal intensity of the MRI in vivo of GdSCA performance with 15-min-post injected FCM-after the injection of GdSCA against time. Each dot respresent the signal intensity of an ROI square of the slices shown in Figure 95 - Figure 99

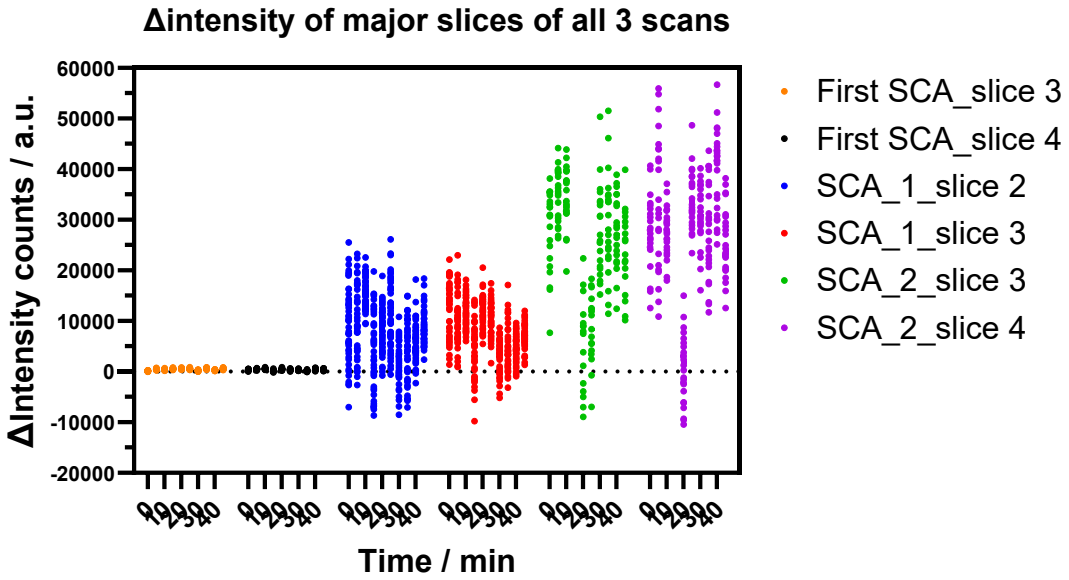


Figure 101 – the absolute difference of intensity of two representable slices each of all three scanning results shown in Figure 83, Figure 89, and Figure 100.

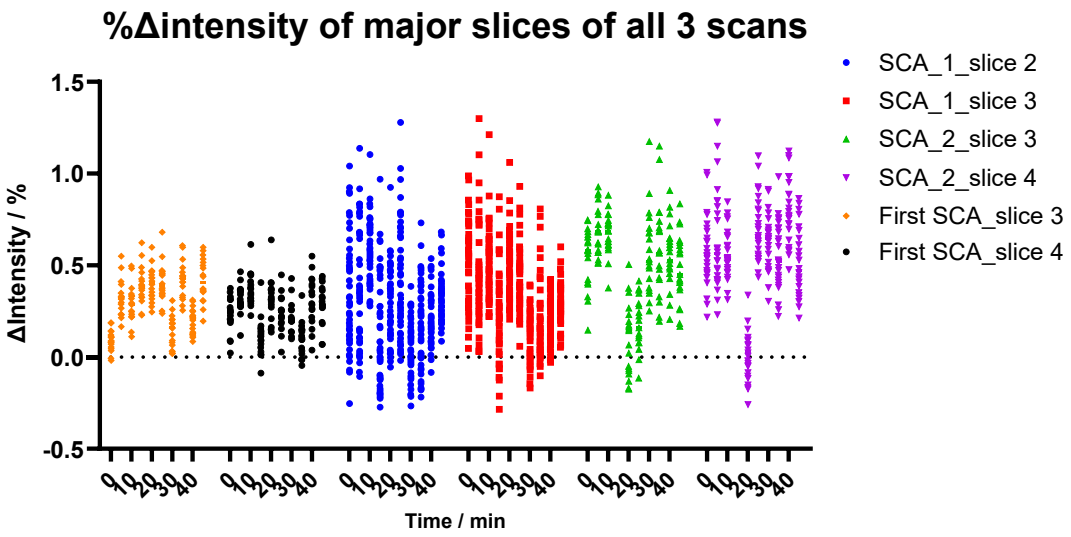


Figure 102 - the percentage difference of intensity of two representable slices each of all three scanning results sho wn in Figure 83, Figure 89, and Figure 100.

5.3.4.3. Discussion

The results obtained under FCM-modulated conditions indicate that altering systemic iron handling can be accompanied by observable differences in the liver enhancement behaviour of GdSCA in vivo. In both iron-loading schedules, GdSCA continued to produce readily detectable liver signal enhancement relative to baseline, confirming that its basic contrast behaviour is preserved under these conditions. At the same time, the enhancement curves obtained with pre-existing iron loading and with acute iron perturbation during imaging were not identical, suggesting that the timing of iron administration may influence the observed signal behaviour.

However, these differences must be interpreted with caution. The magnitude of variability observed between slices, between ROIs within a slice, and between animals was substantial, and the distributions of signal changes overlapped

extensively across conditions. Within the scope of the present dataset, these sources of experimental variability preclude the establishment of statistically significant or mechanistically definitive differences between the two iron-loading schedules. The data therefore support, at most, a qualitative sensitivity of GdSCA enhancement to changes in iron-handling context, rather than a demonstrable or quantifiable iron-specific response.

Several factors may contribute to this limited interpretability. From an experimental standpoint, the analysis relies on intensity-based measurements from fixed-parameter T_1-weighted images, which are inherently sensitive to physiological variability, residual motion, and local haemodynamic effects. From a molecular perspective, the intrinsic specificity and affinity of GdSCA for iron-related species under in vivo conditions may be insufficient to resolve subtle iron-dependent effects against this background variability. Moreover, systemic iron status was not independently quantified in this experiment (for example by blood iron indices or elemental analysis), further limiting the strength of any mechanistic inference.[1, 5]

Taken together, the FCM-modulated experiments suggest that GdSCA behaviour in vivo is compatible with, but does not establish sensitivity to iron-related physiological changes. These findings should therefore be viewed as exploratory rather than confirmatory. A more comprehensive assessment of iron responsiveness would require improved molecular discrimination, tighter control of experimental variability, and independent validation of iron status. Broader interpretation of iron-related effects, and their implications for the design and application of GdSCA, is

deferred to the overall discussion and summary of this chapter.

5.4. Summary and limitations of Chapter 5

This chapter has examined the in vivo performance of the GdSCA system, with the aim of establishing its biocompatibility, evaluating its baseline MRI contrast behaviour, and exploring the extent to which its signal may be influenced by iron-related physiological conditions.

In terms of tolerability, GdSCA was found to be well tolerated under the experimental conditions employed. Transient changes in selected physiological parameters were observed within the first 24 hours following administration, including a temporary increase in glucose levels and minor variation in urinary pH; however, these remained within acceptable ranges and did not persist. Body weight exhibited a modest reduction during the initial post-injection period, remaining below 5% of baseline, and subsequently returned to pre-administration levels. No significant differences were observed between treated and control groups across behavioural indicators, including movement, posture, grooming, and signs of dehydration. All animals recovered to baseline condition and survived beyond one week. Taken together, these observations indicate the absence of sustained or clinically meaningful adverse effects, supporting the use of GdSCA for in vivo imaging at the investigated dose.

Under baseline imaging conditions, GdSCA produced clear and reproducible enhancement of liver signal on T_1-weighted MRI following intravenous

administration. The magnitude and temporal evolution of signal enhancement were consistent with the expected behaviour of a small-molecule extracellular gadolinium contrast agent, confirming that the probe is functionally effective in vivo. This establishes a necessary foundation for evaluating any additional responsiveness arising from interaction with endogenous species.

When systemic iron handling was perturbed using ferric carboxymaltose, differences in liver enhancement behaviour were observed between experimental conditions. However, these differences were not sufficiently robust or consistent to support a definitive assignment to iron-specific interactions. Substantial variability was present across animals, imaging slices, and regions of interest, with overlapping signal distributions between conditions. As a result, the observed contrast behaviour remains consistent with that of a conventional extracellular agent, with any iron-dependent contribution not reliably distinguishable within the present experimental framework.

These findings highlight several important limitations. First, the reliance on intensity-based MRI measurements restricts sensitivity to subtle changes in relaxivity and does not permit direct quantification of T_1 or separation of contributing relaxation mechanisms. Second, the absence of independent measurement of systemic or tissue iron levels limits the ability to correlate imaging observations with underlying iron status. Third, biological variability, including differences in probe distribution, perfusion, and iron compartmentalisation, introduces additional uncertainty that may obscure small iron-dependent effects. Finally, although earlier aqueous and

controlled in vitro experiments indicate that iron-dependent modulation of relaxivity can occur under favourable conditions, the magnitude of this effect appears insufficient to overcome the complexity and noise inherent to the in vivo environment under the conditions tested.

Taken together, this chapter demonstrates that GdSCA is a biocompatible and functional liver contrast agent in vivo, but provides only exploratory evidence for iron-dependent modulation of its MRI signal. The results therefore support a staged interpretation of the overall project, in which iron-responsive behaviour is established under controlled conditions but remains unresolved in vivo. These limitations define key directions for future work, including improved probe design to enhance sensitivity, the incorporation of quantitative imaging approaches, and the integration of complementary measurements to more directly assess iron status in biological systems.

6. Conclusion

The aim of this thesis was to examine whether a gadolinium-based molecular MRI contrast agent, modified with a pendent iron-binding group, could generate iron-dependent changes in longitudinal relaxation and thereby provide a basis for imaging iron-related biology beyond the limits of conventional susceptibility-based approaches. This question was approached through a staged experimental framework, beginning with molecular design and simplified aqueous systems, and extending progressively into cellular and in vivo models. In this respect, the work was not intended merely to produce a new ligand scaffold, but to test a broader mechanistic proposition: that controlled proximity between Gd^{3+} and a second paramagnetic iron centre could introduce an additional relaxation contribution beyond the linear sum of the isolated species.

A central outcome of the thesis is that this mechanistic proposition is chemically feasible, but only under specific structural and experimental conditions. The species-resolved framework developed in the design chapter established an important conceptual distinction between simple additive behaviour and true interaction-dependent relaxivity enhancement. Within that framework, the mere formation of a probe–iron species is not, in itself, sufficient to generate a measurable MRI response. A detectable enhancement requires both appreciable formation of an associated species and a relaxation contribution from that species that exceeds the behaviour expected from independent paramagnetic centres. This distinction proved essential for interpreting the subsequent relaxometry data and for

separating chemically meaningful responsiveness from trivial superposition.

The aqueous studies provided the clearest support for iron-responsive relaxivity modulation. Both GdSCA and GdCat displayed intrinsic longitudinal relaxivity in water, but their behaviour in the presence of iron differed markedly. In the SCA system, especially with Fe^{3+}, the observed increase in R_1 exceeded that expected from simple additive contributions, most clearly at lower ferric concentrations. This behaviour was consistent with the emergence of a non-zero interaction term, as anticipated in the species-based framework, and provided the strongest direct evidence in the thesis that molecular design can convert probe–iron association into an additional relaxation pathway. A smaller but still measurable enhancement was also observed for Fe^{2+} in the SCA system, indicating that iron responsiveness was not restricted to a single oxidation state, although its magnitude was substantially lower than in the ferric case. By contrast, the Cat platform remained closer to additive behaviour across the concentration range studied. Although some iron-dependent change was observed, particularly with Fe^{3+}, the response was weaker and the extent of deviation from additive behaviour was insufficient to support equally robust mechanistic interpretation. Taken together, these results identify the SCA platform as the stronger scaffold and indicate that the effectiveness of iron-responsive MRI probe design depends critically on the detailed nature of the appended binding motif rather than on the simple presence of an O,O donor arm.

The DynaFit modelling further clarified what could, and could not, be concluded from the aqueous relaxometry. For the SCA–Fe^{3+} system, the experimental data could be

reproduced satisfactorily by a minimal 1:1 association model, and the response coefficient associated with the Gd–Fe species was consistently better constrained than the corresponding equilibrium constant. This is an important point. The modelling supports the existence of an additional relaxometry contribution associated with probe–iron interaction, but it does not provide a definitive thermodynamic characterisation of that interaction. The fitted equilibrium constants remained strongly correlated with the response parameters, and more complex models did not improve identifiability or explanatory power. In the SCA–Fe^{2+} system, the same general model could still reproduce the observed trend, but the smaller deviation from additive behaviour meant that parameter uncertainty became much greater. For the Cat system, no tested model yielded a stable, well-constrained interpretation. These outcomes reinforce a broader mechanistic conclusion: under the present conditions, the observable MRI response is governed more strongly by the effective relaxivity of the associated species than by binding affinity alone. In other words, coordination can contribute to MRI contrast only when it produces a sufficiently strong perturbation of the relaxation properties of the system.

The UV–Vis studies provided an independent line of evidence that was consistent with this aqueous interpretation, although not identical in emphasis. Both probe families exhibited iron-selective spectral perturbation in water, with a clear preference for Fe^{3+} over Fe^{2+} and negligible response to Ca^{2+} and Zn^{2+}. For EuSCA, ferric iron induced pronounced non-linear perturbation and suppression of the higher-wavelength feature, while ferrous iron produced a weaker and more gradual

response. TbCat likewise showed its strongest spectral reorganisation in the presence of Fe^{3+}, with far less substantial changes for Fe^{2+} and minimal effects for Ca^{2+} and Zn^{2+}. These data support the view that both probe systems are chemically responsive to iron, and that Fe^{3+} is generally the more perturbing ion in aqueous coordination terms. At the same time, the fact that UV–Vis selectivity alone did not translate directly into equivalent relaxometry performance reinforces the point that probe design must be judged not simply by iron binding, but by the extent to which binding generates a measurable effect on MRI-relevant relaxation parameters.

The key question, however, was not only whether iron-dependent modulation could be established in simplified aqueous systems, but whether any part of that behaviour would remain detectable in more complex biological environments. The in vitro studies addressed this question at two levels: first by defining workable concentration ranges and experimental conditions, and secondly by examining MRI behaviour in cell-associated samples under altered iron loading conditions. These cellular experiments revealed an important shift in the apparent oxidation-state preference of the system. Whereas the aqueous relaxometry data pointed most clearly to the SCA–Fe^{3+} interaction, the cellular MRI experiments produced stronger signal enhancement under Fe^{2+} loading than under Fe^{3+} loading. This difference should not be treated as a contradiction. Rather, it reflects the fact that the two sets of experiments probe different regimes. The aqueous studies isolate coordination-dependent relaxivity under controlled conditions, while the cellular MRI measurements were performed on washed, centrifuged cell samples following

removal of the incubation medium. Under those conditions, the final T_1 readout is expected to depend more strongly on intracellular accessibility, retention, and compartmentation of iron-related species than on bulk-solution binding behaviour alone. A plausible interpretation is therefore that Fe^{3+}, although more effective in producing a measurable aqueous relaxometry perturbation with GdSCA, contributed less to the final cell-associated signal because ferric species remaining predominantly in the incubation medium were largely removed during washing. By contrast, Fe^{2+} loading may have generated a larger intracellularly retained pool capable of influencing the measured MRI response. On this basis, the cell experiments are best interpreted as evidence that the dominant iron-dependent response of the probe is strongly context-dependent and shaped by biological handling of iron as well as by intrinsic coordination chemistry.

The in vivo studies extended this progression one step further. The most secure conclusion from these experiments is that GdSCA functions as a liver-enhancing small-molecule MRI contrast agent in vivo. Under the baseline imaging protocol, intravenous administration produced clear liver enhancement, establishing that the scaffold remains operational in a whole-animal setting and that the probe reaches the relevant tissue compartment in sufficient quantity to generate observable contrast. This is not a trivial result, because many chemically responsive systems fail to retain measurable performance outside simplified conditions. The subsequent ferric carboxymaltose experiments were designed to examine whether altered systemic iron handling might modify the enhancement profile of GdSCA. Observable

differences between the two FCM schedules were indeed seen, and these findings are therefore compatible with some degree of iron-related sensitivity. However, the dataset remained limited, and variability between slices, ROIs, and animals was substantial. The overlap in signal distributions means that these experiments cannot yet support a definitive claim of iron-specific imaging in vivo. The appropriate conclusion is therefore that biological translation was demonstrated at the level of feasibility, but not yet at the level of rigorous mechanistic proof.

Taken together, the results of this thesis support three broad conclusions. First, iron-responsive relaxivity modulation in a Gd-based molecular probe is chemically feasible. Secondly, the observed response depends strongly on molecular design, with the SCA scaffold providing the most convincing evidence for interaction-dependent relaxation enhancement, whereas the Cat scaffold remains comparatively weak under the conditions examined. Thirdly, the dominant manifestation of iron responsiveness is system-dependent. In aqueous relaxometry, the strongest and most interpretable response is obtained for Fe^{3+}, whereas in the washed-cell MRI model the stronger enhancement is observed under Fe^{2+} loading. This divergence indicates that the experimentally observed MRI signal is not controlled by coordination chemistry alone, but by the combination of iron speciation, accessibility, retention, and the physical environment in which the readout is made. In that sense, the thesis does not end with a single simple ranking of Fe^{2+} against Fe^{3+}. Instead, it shows that the meaning of “iron responsiveness” changes as the system moves from idealised solution chemistry into biological space.

At the same time, the work also makes clear where the present evidence remains limited. The strongest mechanistic support still comes from the aqueous studies, not from the cellular or in vivo experiments. The fitted model parameters, particularly those associated with equilibrium binding, remain semi-quantitative because the observable signal couples association and relaxation contributions in a way that does not permit full independent resolution. The intracellular iron pool influencing the cellular MRI signal was not independently quantified or speciated, and the washed-cell design, while experimentally useful, necessarily compresses multiple biological processes into a single final readout. Likewise, the in vivo experiments remained constrained by biological variability and by the use of signal-intensity-based measurements rather than fully quantitative T_1 mapping coupled to independent biochemical iron analysis. These limitations do not invalidate the conclusions of the thesis, but they define the level at which those conclusions should be stated.

For future development, the most rational path is not to pursue all probe designs equally, but to concentrate on the SCA scaffold, which consistently gave the clearest evidence for interaction-dependent relaxivity. Within that framework, the most important next step is to define the Gd–Fe associated species more directly, whether through improved equilibrium analysis, complementary spectroscopic methods, or structural surrogates that better constrain stoichiometry and local geometry. At the cellular level, orthogonal measurements of intracellular iron loading and retention would be needed to distinguish more clearly between chemical binding effects and differences in biological handling of iron. At the in vivo level, more quantitative MRI

protocols, combined with independent confirmation of tissue iron status, will be required before any strong claim of iron-specific imaging can be justified. Nevertheless, the present work has established a coherent design rationale, identified the more promising molecular platform, and defined the conditions under which progress is most likely to be made. It therefore provides a substantive foundation for the further development of MRI probes directed not simply at total iron burden, but at iron-related biology in a more functionally relevant sense.

7. Experimental procedure

7.1. General Concept and Synthetic Plan

Two ligand platforms based on a DO3A scaffold were investigated in this work, incorporating either a salicylate-derived arm (SCA) or a catechol-derived arm (CAT). The SCA system was adapted from a reported synthetic approach with minor modifications from the work of Yao, K. et al.. [182], while the CAT system was developed in this work from this using a modified alkylation strategy.

Both ligand families were synthesised from a common cyclen precursor via formation of a protected triester intermediate, enabling controlled functionalisation of the macrocycle. For the SCA system, the salicylate-derived precursor was first functionalised to introduce a reactive bromoacetyl group prior to coupling. In contrast, the CAT system employed a pre-functionalised catechol-derived precursor, allowing direct coupling to the triester.

Subsequent deprotection of the tert-butyl ester groups afforded the corresponding DO3A-based ligands, which were then complexed with lanthanide ions under aqueous conditions with controlled pH adjustment to ensure complete metal incorporation.

An overview of the synthetic routes from cyclen to the final lanthanide complexes is shown in Figure 103 and Figure 104. Individual synthetic steps, reaction conditions, and purification procedures are described in detail in the following sections.

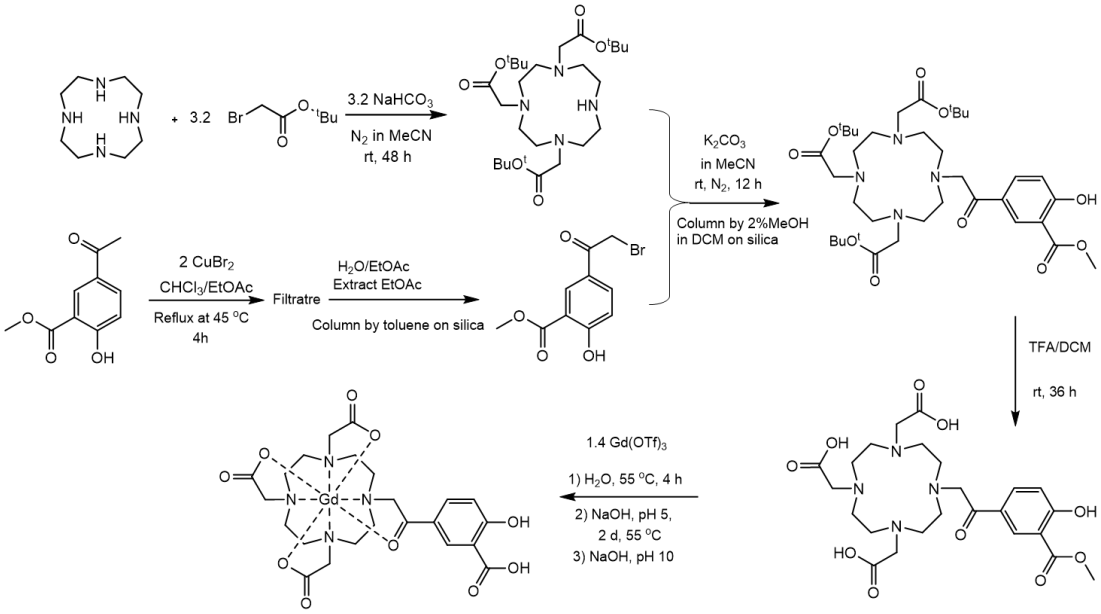


Figure 103 – Synthetic plan of GdSCA

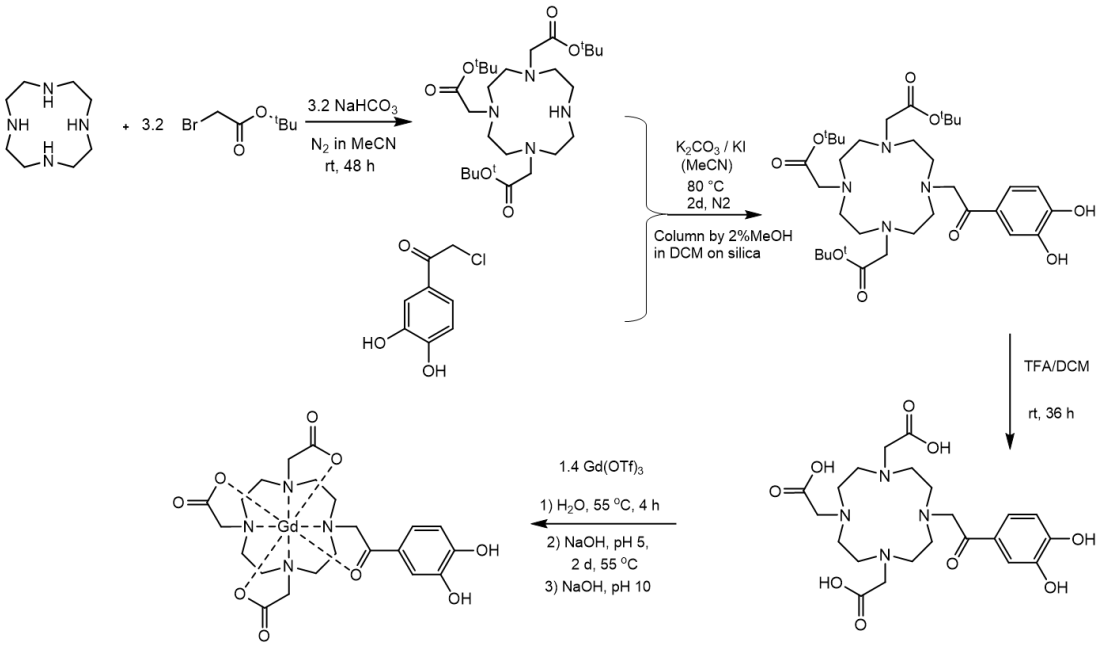


Figure 104 – Synthetic plan of GdCat

NB: For lanthanide complexes, purification was performed either by dialysis or by semi-preparative HPLC depending on the stage of the work. In later experiments, semi-preparative HPLC purification was employed following filtration to obtain reproducible product purity.

7.2. General methods

Reagents and solvents were purchased from commercial suppliers including Sigma-Aldrich (UK), Alfa Aesar, and Fluorochem, and were used. Miliq water (18 MΩ) was prepared from an Elix® Essential water purification system. Unless otherwise stated, all reactions were carried out open to air at atmospheric pressure. Silica gel for column chromatography was carried out using Merck silica gel (40–63 µm under positive pressure of nitrogen gas.

NMR spectra were recorded on Bruker AVIII HD Nanobay 400 MHz spectrometers equipped with a 5 mm z-gradient multinuclear BBFO probe and operated using TopSpin software (version 3, Bruker BioSpin).

Chemical shifts (δ) are reported in parts per million (ppm) and referenced to residual solvent peaks according to literature values[211]. Signal multiplicities are denoted as s (singlet), br s (broad singlet), d (doublet), t (triplet), q (quartet), m (multiplet), or combinations thereof. The number of protons is indicated as nH. Coupling constants (J) are reported in Hz to the nearest 0.1 Hz, with identical coupling constants averaged where appropriate. Spectral assignments were supported by two-dimensional NMR techniques including COSY, HSQC, and HMBC where required. Data processing was carried out using MestReNova software.

Mass spectrometry measurements (general) were performed using electrospray ionisation (ESI) on time-of-flight (TOF) instruments. High-resolution LC-MS analysis was carried out using a Waters RDa bench-top TOF system coupled to an Acquity LC system. Additional mass spectrometric measurements were obtained using a Waters LCT Premier XE orthogonal acceleration TOF system, operated in direct infusion mode where appropriate. Data were processed using MestReNova software.

LC-MS (for final product) was performed using an Agilent 1260 Infinity II system coupled to a G6125B mass spectrometer with electrospray ionisation. Separations were carried out using a Poroshell 120 SB-C18 column (50 × 2.1 mm, 2.7 µm) at 40 °C

with a flow rate of 0.4 mL min^{-1}. Detection wavelengths included 220, 254, 280, 365, and 450 nm. Data were processed using Chromera software (version 3.4.4) and MestReNova.

Analytical **HPLC** was carried out on an Agilent 1260 Infinity II system equipped with a diode array detector. Samples were filtered through PTFE (0.2 µm) filters prior to injection. Separations were performed using Poroshell 120 EC-C18 reverse-phase columns (4 µm, 4.6 × 150 mm or 4.6 × 100 mm) at 40 °C, with a constant flow rate of 1 mL min^{-1}. Elution employed gradient mixtures of solvent A (H_2O with 0.1% formic acid) and solvent B (MeCN with 0.1% formic acid). Compound purity was assessed using UV/Vis detection at multiple wavelengths.

Semi-preparative HPLC purification was performed using an Agilent 1260 Infinity II system equipped with a preparative pump, fraction collector, and UV detection. Separations were carried out using a C18 preparative column (50 × 21.2 mm), with flow rates and solvent systems as specified. Injection volumes typically ranged from 100 µL to 750 µL depending on sample concentration and repeated for bulk purification

UV–Vis absorption spectra were recorded on a Jasco V-770 spectrophotometer using quartz cuvettes with a 10 mm path length. Measurements were performed at 25 °C and analysed using Spectra Manager and Origin software.

Centrifugation was used for purification and phase separation where required, using a Beckman Coulter Allegra X-12R centrifuge at 3750 rpm for 5 min at 4 °C.

Dialysis was carried out for selected lanthanide complexes using regenerated cellulose membrane tubing (MWCO 500Da). Samples dissolved in MiliQ water were transferred into dialysis tubing and stirred in large volumes of deionised water with periodic solvent exchange over extended periods.

7.3. Purity control

Purification became progressively more challenging along the synthetic route as the polarity and coordination properties of the compounds changed as shown in Figure 103 and Figure 103Figure 104. In particular, removal of the tert-butyl ester protecting groups generated the highly polar polycarboxylate DO3A-based ligands, for which conventional normal-phase chromatographic purification became considerably less practical. Following lanthanide complexation, assessment of the final complexes was further complicated by their highly polar and ionic character. For the Gd^{3+} complexes in particular, strong paramagnetic effects substantially limit the use of conventional NMR spectroscopy for straightforward purity assessment. Mass spectrometry was useful for confirming the presence of the expected molecular species, but was not treated as a quantitative measure of chemical purity because signal intensities depend on the ionisation and detection efficiencies of the individual species.

For these reasons, the protected functionalised ligand was treated as the principal purification checkpoint in the synthetic workflow. At this stage, the SCA or CAT binding group had already been incorporated into the triester scaffold, while retention of the tert-butyl ester groups maintained sufficient compatibility with silica chromatography to allow effective separation of organic impurities. Particular emphasis was therefore placed on chromatographic purification and NMR assessment at this stage. Following deprotection, the ligand was assessed again, principally by NMR spectroscopy, before lanthanide complexation. The final lanthanide complexes were subsequently subjected to dialysis or, in later

preparations, HPLC purification to remove residual reagents, salts and other potential impurities that could no longer be assessed as readily using the analytical methods applicable to the organic ligand precursors.

7.3.1. Purification of ligand precursors

The protected functionalised ligands represented the principal purification stage of the synthetic workflow. Following attachment of the SCA or CAT pendant group, the products were purified by normal-phase silica column chromatography using DCM/MeOH mixtures. Despite retention of the tert-butyl protecting groups, the phenolic and carboxylic functionalities of the pendant groups retained substantial polarity and interacted strongly with the silica stationary phase, resulting in broad elution bands and pronounced tailing. In addition, the protonated and deprotonated forms of these acidic functionalities have different effective polarities and silica affinities and can therefore exhibit different retention behaviour and apparent (R_f) values. Et_3N was included as a basic mobile-phase modifier to favour the deprotonated forms and reduce heterogeneity arising from different protonation states, while also suppressing strong interactions with acidic silanol sites on the silica surface. This gave more consistent chromatographic behaviour and facilitated separation. Where necessary, column chromatography was repeated two or three times until satisfactory separation was achieved.

^{1}H NMR spectroscopy was used as the principal method for assessing the purity of the isolated organic intermediates. The major resonances were assigned to the

proposed structure and their relative integrations compared with the expected proton ratios. Particular attention was paid to the aromatic region, where the three aromatic protons of the SCA or CAT pendant group provided a sensitive diagnostic pattern. Additional resonances or shoulders that could not be accounted for by the expected coupling pattern were considered indicative of residual organic species and prompted further purification. Material was carried forward when the significant resonances could be satisfactorily assigned, the relative integrations were consistent with the proposed structure, and no appreciable unexplained features were observed in the diagnostic aromatic region.

A larger quantity of the SCA precursor was required for the subsequent preparation of GdSCA for cellular and in vivo studies. Direct proportional scale-up of a single reaction was found to give poorer isolated yield and purity and to make chromatographic purification substantially more difficult. The protected precursor was therefore prepared as four parallel smaller-scale batches under the established reaction conditions. Each batch was purified and assessed independently by ^{1}H NMR spectroscopy using the criteria described above, and the satisfactory batches were combined only after this assessment. The resulting common precursor pool provided sufficient material for the subsequent synthesis while reducing variation in the starting material used to prepare GdSCA for the biological experiments.

Following deprotection, the ligand was assessed again by ^{1}H NMR spectroscopy before lanthanide complexation. Complete removal of the tert-butyl protecting groups was confirmed by disappearance of their characteristic resonances, while

assignment, relative integration and the diagnostic aromatic region were reassessed for significant unexplained features. This provided a second NMR-based checkpoint after the major change in polarity associated with deprotection. Mass spectrometry was used as complementary confirmation of the expected molecular species where applicable.

7.3.2. Purification and Assessment of Complexes

Following lanthanide complexation, conventional assessment of purity became more limited, particularly for the paramagnetic Gd^{3+} complexes. Final purification therefore relied principally on dialysis in the earlier preparations and HPLC in the later stages of the project as mentioned in Section 7.2.

Dialysis using a 500 Da molecular-weight cut-off membrane was initially employed as a practical method for removing low-molecular-weight salts, residual reagents and other small species from the water-soluble lanthanide complexes. Its principal advantage was the efficient removal of these components without requiring further manipulation of the highly polar product. However, dialysis provides separation predominantly according to molecular size and does not readily distinguish the desired complex from structurally related or other potential impurities that are also retained by the membrane. Furthermore, unlike a chromatographic method, the dialysis process itself provides no direct analytical measure of the homogeneity of the retained material.

During the initial biological evaluation of dialysis-purified material, an unexpected

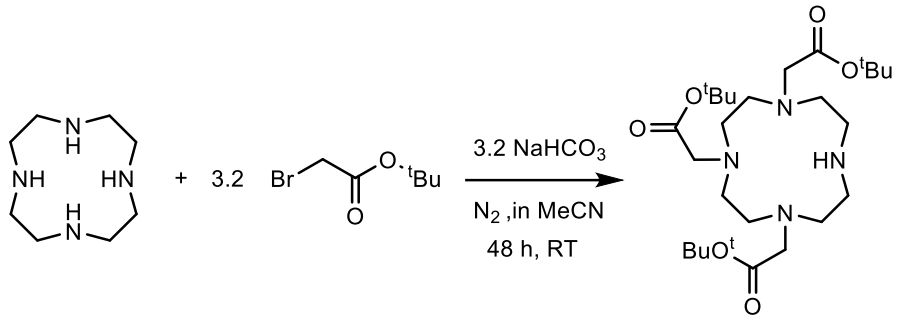
adverse response raised additional concern over whether dialysis alone provided sufficiently stringent purification for subsequent in vivo use. The origin of this observation could not be established, and no causal relationship with compound purity was demonstrated. Nevertheless, the possibility that a biologically relevant impurity had been retained could not be excluded. A more stringent final purification procedure was therefore adopted as a precaution for subsequent preparations.

Semi-preparative reverse-phase HPLC was subsequently used to isolate the desired lanthanide complex chromatographically, allowing separation from potential impurities of similar molecular size that could not necessarily be removed by dialysis. The collected product was then assessed by analytical HPLC, for which a single detectable chromatographic peak was observed under the conditions employed. Mass spectrometry provided complementary confirmation of the expected molecular species. Together, these measurements provided substantially stronger evidence for the identity and chromatographic homogeneity of the final material and were considered sufficient for its subsequent physicochemical and biological use.

7.4. Chemical Synthetics

7.4.1. Triester synthesis

The synthetic method of triester was adopted from work by A. Dadabhoy et al..[212]



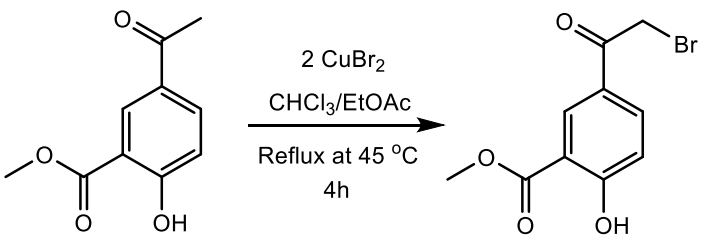
Scheme 1 – Triester synthesis

Cyclen (8.000 g, 46.4 mmol) and $NaHCO_3$ (3.2 equiv. 12.502 g, 149 mmol) was dissolved in MeCN (250 ml) and cooled to 0 °C. A solution of tert-butyl bromoacetate (29.010, 149 mmol) in MeCN (20 mL) was added dropwise to the mixture over a period of 1 hr. The reaction mixture was left to reach room tempreture under N_2. After 48 hrs, the filterate was collected and dried *in vacuo* to form a off-white solid as the crude product. Purification was performed twice by washing and string in toluene (300 mL) for 24 hrs then filtered to collect the residue and dried to give a white solid as the product (12.43 g, 24.2 mmol, 52%). R_f = 0.73 (DCM: methanol = 1:1).

^{1}H NMR (400 MHz, $CDCl_3$) δ 10.00 (s, 1H, N-H), 3.41 – 2.76 (m, 22H, ring-H), 2.02 – 1.76 (m, 6H), 1.44 (d, *J* = 2.4 Hz, 27H, ^{t}Bu).

7.4.2. BrSCA synthesis (bromination)

The synthetic method of triester was adopted from work by K. Yao et al..[182]



Scheme 2 – SCA bromination

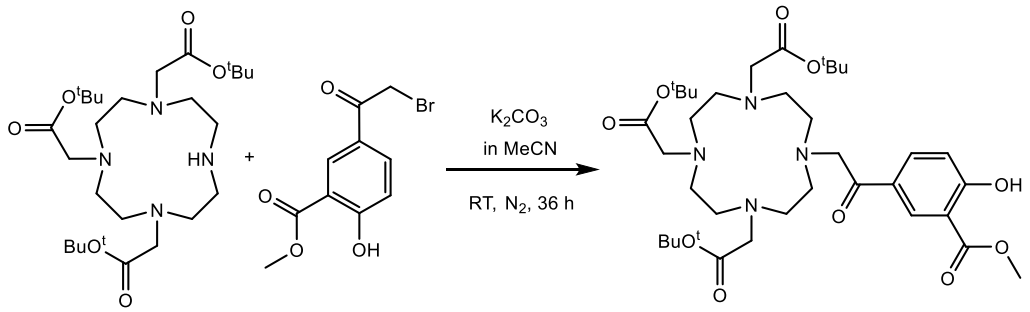
Methyl 5-acetyl-2-hydroxybenzoate (3.000 g, 15.4 mmol) was dissolved in a mixture

of $CHCl_3$ / EtOAc (150 mL, 1:1, 100). $CuBr_2$ (6.90 g, 30.8 mmol) was added to the mixture. The mixture was heated via reflux at 45 °C for 4 hrs and then left it to cool to room temperature. The solvent of the mixture was removed *in vacuo* and to give a greenish grey power as the 1st-crude product. The solid was dissolved in a mixture of H_2O / EtOAc (200 mL, 1:1) and collect the organic layer. The aqueous layer was washed with EtOAc (3 X 30 ml) and combined all of the organic layers and dried by $MgSO_4$. The solvent was removed *in vacuo* to give the 2nd-crude product as a bright yellow solid, which was further purified by column on silica by toluene to give a cream-coloured powder as the final product (1.92 g, 7.0 mmol, 45%)

^{1}H NMR (400 MHz, $CDCl_3$) δ 11.44 (s, 1H,PhO-**H**), 8.62 (s, 1H, Ph-H), 8.21 (d, *J* = 8.8 Hz, 1H, Ph-H), 7.17 (d, *J* = 8.8 Hz, 1H, Ph-H), 4.50 (s, 2H, CO-C**H**$_2$-Br), 4.11 (s, 3H, -OC**H**$_3$).

7.4.3. Triester-SCA synthesis (TriSCA; alkylation)

The synthetic method of triester was adopted from work by K. Yao et al..[182]



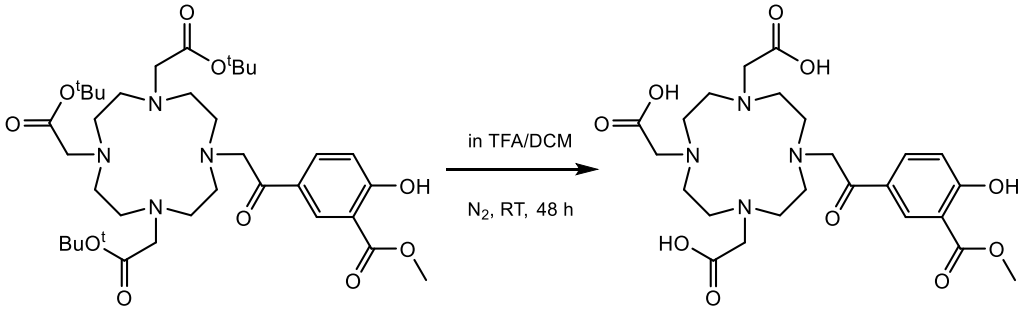
Scheme 3 - SCA-triester by alkylation

BrSCA (3.00 g, 11.0 mmol), triester (5.65 g, 11.0 mmol) were dissolved in MeCN(100 mL). K_2CO_3 (3.04 g, 22.0 mmol) was added to solution and reacted under N_2 at room tempureture for 36 hrs. The filtrate of the reaction mixture was collected and the solvent was removed *in vacuo* to form a yellow power as the crude product, which was further purified by column chromatography on silica with DCM/MeOH/Et_3N (97:2:1 to 89:10:1) twice to get a pale-yellow power (2.83 g, 4.01 mmol)

^{1}H NMR (400 MHz, $CDCl_3$) δ 8.31 (s, 1H, Ph-H), 7.91 (d, *J* = 9.0 Hz, 1H, Ph-H), 6.93 (d, *J* = 8.8 Hz, 1H, Ph-H), 3.90 (s, 3H, COOMe), 3.53 – 1.76 (m, 24H, cyclen), 1.34 (s, 9H), 1.16 (s, 18H).

7.4.4. DO3A-SCA by deprotection

The synthetic method of triester was adopted from work by K. Yao et al..[182]



Scheme 4 - DO3A-SCA by deprotection

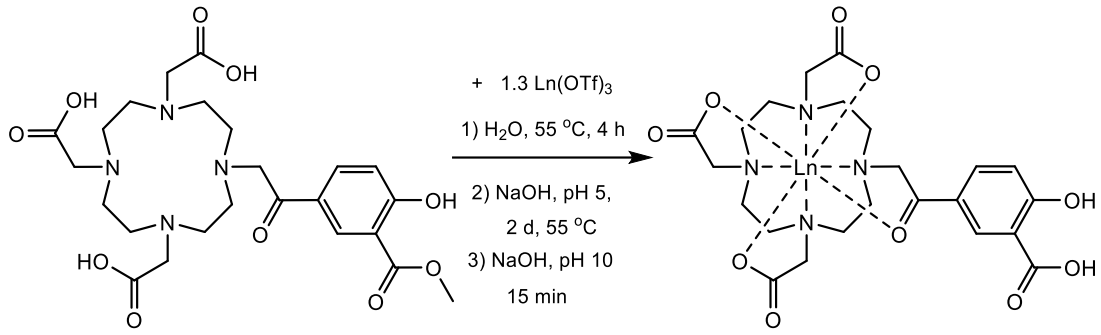
TriSCA (0.85 g, 1.12 mmol) was dissolved in DCM (9 ml). TFA (9 ml) was added dropwise. The solution was stirred at room temperature for 2 d. The solvent was removed in vacuo. The resulting solid dissolved in MeOH (3 ml) and dried in vacuo. The crude product was dissolved in a minimal amount of MeOH and diethyl ether was added to triturate the product as a white powder, DO3A-SCA (0.42 g, 0.78 mmol, 66 %).

^{1}H NMR (400 MHz, D_2O) δ 8.38 (s, 1H, Ph-H), 8.00 (d, *J* = 8.4 Hz, 1H, Ph-H), 7.01 (d, *J* = 8.8 Hz, 1H, Ph-H), 3.91 (s, 3H, O-Me), 3.76 (brs, 8H, ^{t}Bu), 3.27 (brs, 16H, ^{t}Bu).

LC-MS (MeOH): m/z cal. for [M]- 538.2, found m/z 538.3 [M]-.

7.4.5. LnSCA complexation

The synthetic method of triester was adopted from work by K. Yao et al..[182]

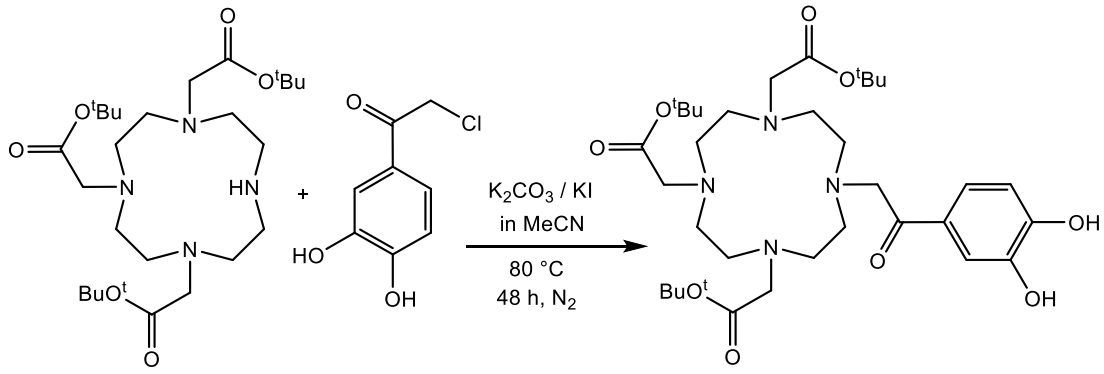


Scheme 5 - Ln-DO3A-SCA complexation; Ln = Gd, Eu, Tb

DO3A-SCA (0.50 g, 0.95 mmol) and $Gd(OTf)_3$ (0.70 g, 1.1 mmol) were dissolved in H2O (8 ml). The solution was heated to 55 °C for 4 h. 1 M NaOH was added to the solution dropwise to adjust the pH to 5, and the solution was continued to react at 55 °C for 2 d. The pH of the solution was adjusted to 10 by dropwise addition of 1 M NaOH. By centrifugation, the precipitate was separated and the supernatant was collected and filtered by a syringe filter. The solvent was removed *in vacuo* to obtain the crude product. The solid was dissolved in H2O (high purity, 4 ml) and purified by 500-1000 u dialysis for 2 d. The solvent was removed by a freeze dryer to obtain the final product (0.33 g, 0.49 mmol, 49 %).

LC-MS (H_2O; Ln = Gd): m/z cal. for [M]- 679.1, found m/z 679.0 [M]-. UV-vis (H_2O; Ln = Gd): λ_{max} = 311 nm. UV-vis (H_2O; Ln = Eu): λ_{max} =216.6, 350.1 nm.

7.4.6. TriCat by SN2



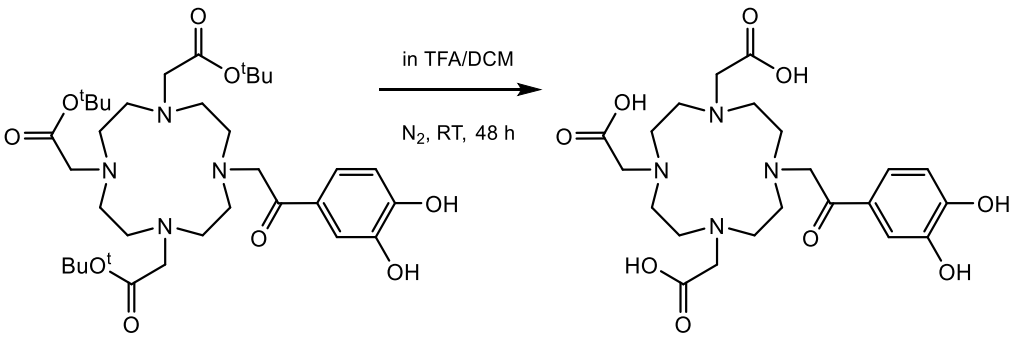
Scheme 6 - CAT-triester by SN2

Cl-dihydroxyphenyl (0.300 g, 1.61 mmol) and triester (0.95g, 1.85 mmol) were dissolved in MeCN (35 ml). K_2CO3 (2 eq.) was added to the solution. The solution was reacted under N_2 at room temperature. After 48 h, the filtrate was collected and the solvent was removed in vacuo. The crude product was purified on silica by column (DCM : MeOH = 97:3 to 90 : 10). The product was collected as a brown oil (0.239 g, 0.359 mmol, 22 %).

^{1}H NMR (400 MHz, $CDCl_3$) δ 7.80 (s, 1H, Ph-H), 7.34 (dd, *J* = 8.3, 2.0 Hz, 1H, Ph-H), 7.09 (d, *J* = 8.4 Hz, 1H, Ph-H), 3.63 – 2.73 (m, 16H, cyclen), 2.69 – 2.10 (m, 8H), 1.46 (brs, 27H, ^{t}Bu).

LC-MS (MeOH): m/z cal. for [M+H]+ 665.4, found m/z 665.3 $[M+H]^+$, 687.3 $[M+Na]^+$. R_f = 0.21 (DCM: methanol = 9:1); UV-vis (H_2O): λ_{max} = 277 nm.

7.4.7. DO3A-CAT by deprotection

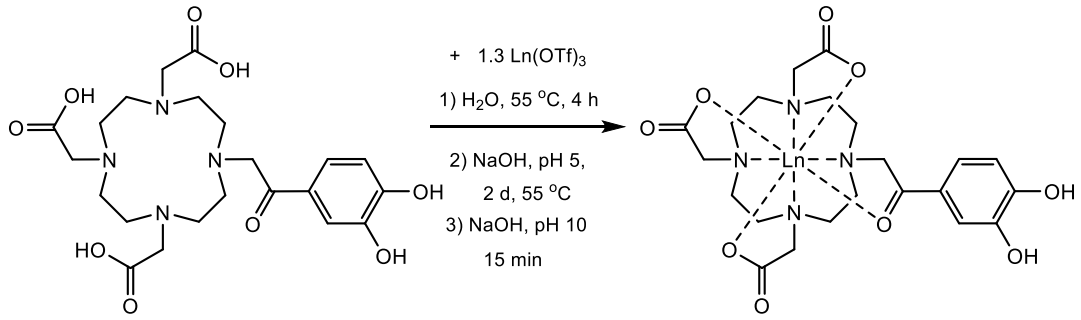


Scheme 7 - DO3A-CAT by deprotection

TriCat (0.85 g, 1.12 mmol) was dissolved in DCM (9 ml). TFA (9 ml) was added dropwise. The solution was stirred at room temperature for 2 d. The solvent was removed in vacuo. The resulting solid dissolved in MeOH (3 ml) and dried in vacuo. The crude product was dissolved in a minimal amount of MeOH and diethyl ether was added to triturate the product as a white powder, DO3A-Cat (0.42 g, 0.78 mmol, 66 %).

^{1}H NMR (400 MHz, D_2O) δ 8.38 (s, 1H, Ph-H), 8.00 (d, *J* = 8.4 Hz, 1H, Ph-H), 7.01 (d, *J* = 8.8 Hz, 1H, Ph-H), 4.06 – 2.76 (m, 36H, cyclen). LC-MS (MeOH): m/z cal. for [M]- 538.2, found m/z 538.3 [M]-.

7.4.8. LnCAT complexation



Scheme 8 - Ln-DO3A-CAT complexation; Ln = Gd, Eu, Tb

DO3A-Cat (0.1 g, 0.20 mmol) and $Gd(OTf)_3$ (0.15 g, 2.4mmol) were dissolved in H_2O (8 ml). The solution was heated to 55 °C for 4 h. 1 M NaOH was added to the solution dropwise to adjust the pH to 5 and the solution was continued to react at 55 °C for 2 d. The pH of the solution was adjusted to 10 by dropwise addition of 1 M NaOH. After 2 min, the pH of the solution was neutralized to 7 by dropwise addition of 1M $HCl_{(aq)}$. By centrifugation, the precipitate was separated and the supernatant was collected and filtered by a syringe filter. The solvent was removed *in vacuo* to obtain the crude product. The solid was purified by semi-preparative HPLC as described in section 7.2 and the solvent was removed by a freeze dryer to obtain the final product (0.061 g, 0.09 mmol. 45 %)

LC-MS (H_2O; Ln = Gd): m/z cal. for [M]- 651.1, found m/z 651.2 [M]-. UV-vis (H_2O; Ln = Tb): λ_{max} = 206.6, 237.4, 259.4, 372.6 nm.

8. Appendix

8.1. Declaration of the use of AI

This declaration aims to clarify the scope and context of artificial intelligence (AI) tool usage during the preparation of this doctoral thesis. It is provided in the spirit of transparency and academic responsibility.

At certain stages of the writing process—mainly in the later phases—AI-assisted tools were used in a limited capacity to support language-related tasks such as grammar correction, sentence restructuring, and stylistic adjustments. All such usage was undertaken with full authorial oversight.

The core scientific content of this thesis, including the development of ideas, experimental design, data analysis, and academic argumentation, was conceived and completed solely by the author. Where AI suggestions were consulted, they were subject to critical review and revision to ensure alignment with the author's own judgment and writing style.

Full responsibility for the originality, accuracy, and integrity of the thesis rests with the author. AI tools, when used, served a restricted editorial function and were never involved in shaping the research content or intellectual contributions. All usage adhered to institutional guidance on the ethical application of AI in academic contexts.

This declaration is made to ensure clarity for examiners and readers, and to affirm the author's commitment to the integrity of the research process in an era of evolving technologies.

Home Office

PERSONAL LICENCE

Zepeng Cao

A personal licence on its own does not authorise you to perform regulated procedures on protected animals. You apply regulated procedures of the category or categories specified below to animals of the species or groups specified below at places specified in authorised project licences subject to the restrictions and provisions contained in the Act and the conditions and restrictions below.

You are required to keep a record of all regulated procedures that you have carried out, and to make this record available to the Home Office upon request. If you cease to work at the establishment given as the primary availability on your licence, or it ceases to be the place where you wish your licence to be primarily available, you must notify the Home Office.

This licence shall be in force until it is revoked by the Home Office and shall be subject to periodic review.

Primary establishment

Medical and Scientific Departments of the University of Oxford

University Offices Wellington Square Oxford OX1 2JD

Handling Instructions: Contains personal sensitive information, subject to confidentiality requirements under the Data Protection Act. This should only be circulated in accordance with ASPA Guidance. All government information may be subject to an FOI request and subsequent assessment.

Animal types

- Mice

Procedures

Categories

- **A.** Minor / minimally invasive procedures not requiring sedation, analgesia or general anaesthesia.
- **B.** Minor / minimally invasive procedures involving sedation, analgesia or brief general anaesthesia. Plus surgical procedures conducted under brief non-recovery general anaesthesia
- **C.** Surgical procedures involving general anaesthesia. Plus - administration and maintenance of balanced or prolonged general anaesthesia.

Additional conditions

None

Handling Instructions: Contains personal sensitive information, subject to confidentiality requirements under the Data Protection Act. This should only be circulated in accordance with ASPA Guidance. All government information may be subject to an FOI request and subsequent assessment.

Standard conditions

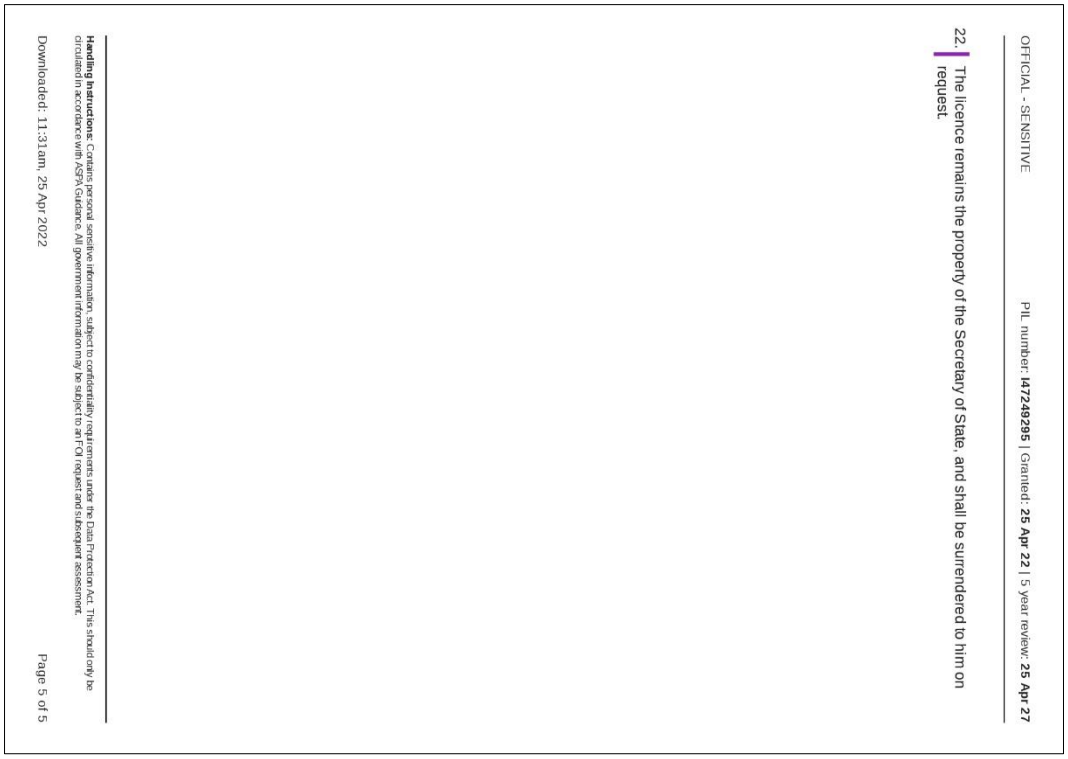
1. In exercising his or her responsibilities, the licence holder shall act at all times in a manner that is consistent with the principles of replacement, reduction and refinement.
2. The licence holder is entrusted with primary responsibility for the welfare of the animals on which he or she has performed regulated procedures; the licence holder must ensure that animals are properly monitored and cared for.
3. The licence holder must not apply a regulated procedure to an animal if the procedure may cause the animal severe pain, suffering or distress that is likely to be long-lasting and cannot be ameliorated.
4. The licence holder must not apply a regulated procedure to an animal unless the holder has taken precautions to prevent or reduce to the minimum consistent with the purposes of the procedure any pain, suffering, distress or discomfort that may be caused to the animal.
5. Where the licence holder is applying a regulated procedure to an animal the holder must ensure that any unnecessary pain, suffering, distress or lasting harm that is being caused to the animal is stopped.
6. Where the licence holder is applying or has applied a regulated procedure which is causing the animal severe pain, suffering or distress the holder must take steps to ameliorate that pain, suffering or distress.
7. The licence holder shall ensure that where the holder applies a regulated procedure death as the end-point of the procedure is avoided as far as possible and is replaced by an early and humane endpoint.
8. In all circumstances where an animal which is being, or has been, subjected to a regulated procedure is in severe pain, suffering or distress which is likely to be long-lasting and cannot be ameliorated, the licence holder must ensure that the animal is immediately killed in accordance with section 15A.
9. The licence holder may apply a regulated procedure without the use of general or local anaesthesia only if the holder is satisfied that— (a) the procedure will not inflict serious injuries capable of causing severe pain; and (b) the use of general or local anaesthesia would be more traumatic to the animal than the procedure itself or would frustrate the purposes of the procedure.
10. When anaesthesia (whether general or local) is used, it shall be of sufficient depth to prevent the animal from being aware of pain arising during the procedure.
11. If the licence holder applies a regulated procedure to an animal with the use of general or local anaesthesia the holder must, unless it would frustrate the purpose of the procedure, use such

Handling Instructions: Contains personal sensitive information, subject to confidentiality requirements under the Data Protection Act. This should only be circulated in accordance with ASPA Guidance. All government information may be subject to an FOI request and subsequent assessment.

analgesics or other pain-relieving methods as may be necessary to reduce any pain that the animal may experience once the anaesthesia wears off.

12. The licence holder must use analgesia or another appropriate method to ensure that the pain, suffering and distress caused by regulated procedures are kept to a minimum.
13. It is the responsibility of the personal licence holder to notify the project licence holder as soon as possible when it appears either that the severity limit of any procedure listed in the project licence or that the constraints upon adverse effects described in the project licence have been or are likely to be exceeded.
14. The licence holder shall ensure that suitable arrangements exist for the care and welfare of animals during any period when the personal licence holder is not in attendance.
15. The licence holder shall ensure that, whenever necessary, veterinary advice and treatment are obtained for the animals in his or her care.
16. The licence holder shall ensure that all cages, pens or other enclosures are clearly labelled. The labelling must be such as to enable Inspectors, named veterinary surgeons and named animal care and welfare officers to identify the number of the project licence authorising the procedures, the project licence protocol in which the animals are being used, the date the protocol was started, and the responsible personal licence holder.
17. In order to ensure that regulated procedures are performed competently, the licence holder shall not apply regulated procedures unless given the appropriate level of supervision by the project licence holder or an experienced personal licence holder deputed by him/her for such time as may be needed to achieve competence.
18. The licence holder is authorised to delegate to assistants, who do not themselves possess the requisite personal licence authority but are under his or her control, the delegable tasks which form an integral part of the regulated procedures the licence holder is authorised to perform by this licence. The tasks must not require technical knowledge or skill, and delegation shall be in accordance with any relevant guidance published by the Secretary of State under section 21.
19. The licence holder must take all reasonable steps to ensure appropriate personal and project licence authorities exist before performing regulated procedures. The licence holder must be aware of the nature of the authorities given by this licence and the project licence, and of the conditions of issue attached to the licences.
20. The licence holder shall maintain a record of all animals on which procedures have been carried out, including details of supervision and declarations of competence by the project licence holder as appropriate. This record shall be retained for at least five years and shall, on request, be submitted to the Secretary of State or made available to an Inspector.
21. The licence holder must give any necessary assistance to inspectors carrying out visits by virtue of section 18(2A)(b) ; and to experts of the European Commission carrying out duties under Article 35 of the Animals Directive.

Handling Instructions: Contains personal sensitive information, subject to confidentiality requirements under the Data Protection Act. This should only be circulated in accordance with ASPA Guidance. All government information may be subject to an FOI request and subsequent assessment.



8.3. Experimental Protocols

8.3.1. DynaFit script template example

```
Model Discrimination
[task]
     task = fit
     data = equilibria
     model = 1:1 ?
[mechanism]
  Gd + Fe <===> GdFe    :    K1    assoc
[constants]
     K1 = 10000 ?
[concentrations]
     Gd = 0.000418 ?
[responses]
      intensive
[data]
     variable Fe
set 1| response Gd = 10800 ?? , GdFe = 26200 ??
[output]
     directory C:\Users\DynaFit_Data\
;_____________________________________
[set:1]
0     4.83
0.001     9.85
; (insert your data here in SI units)
;_____________________________________
```

```
[task]
    task = fit
    data = equilibria
    ?model = 2:1 ?
[mechanism]
    Gd + Fe <===> GdFe    :       K1        assoc
    GdFe + Gd <===> GdFeGd       :       K2        assoc
[constants]
    K1 = 58000 ??
    K2 = 14000 ??
[concentrations]
    Gd = 0.001 ?
[responses]
     intensive
[data]
    variable Fe
set 1| response Gd = 9410 ??        , GdFe = 24200    ??   , GdFeGd = 27500 ??
;_____________________________________
[task]
    task = fit
    data = equilibria
    ?model = 3:1 ?
[mechanism]
    Gd + Fe <===> GdFe          :          K1        assoc
    GdFe + Gd <===> GdFeGd          :          K2        assoc
    GdFeGd + Gd <===> GdFeGdGd          :          K3        assoc
[constants]
    K1 = 58000 ??
    K2 = 14000 ??
    K3 = 10000 ??
[concentrations]
    Gd = 0.001 ?
[responses]
     intensive
[data]
    variable Fe
set 1| response Gd = 9410 ??  , GdFe = 24200    ??   , GdFeGd = 27500 ??       ,
GdFeGdGd = 2.12e7 ??
;_____________________________________
[task]
    task = fit
    data = equilibria
    ?model = 1:1 ?
[mechanism]
    Gd + Fe + Gd <===> FeGdGd     :     K4        assoc
[constants]
    K4 = 10000    ??
[concentrations]
    Gd = 0.001 ?
[responses]
     intensive
[data]
    variable Fe
set 1| response Gd = 9410 ??        , FeGdGd = 24200 ??
;_____________________________________
[task]
    task = fit
    data = equilibria
    ?model = 1:2 ?
[mechanism]
    Gd + Fe <===> GdFe          :          K1        assoc
```

```
    GdFe + Fe <===> GdFeFe          :          K5          assoc
[constants]
    K1 = 58000 ??
    K5 = 14000 ??
[concentrations]
    Gd = 0.001 ?
[responses]
     intensive
[data]
    variable Fe
set 1| response Gd = 9410 ??        , GdFe = 24200    ??   , GdFeFe = 27500 ??
;_____________________________________
[task]
    task = fit
    data = equilibria
    ?model = 1:1 ??
[mechanism]
    Gd + Fe + Fe <===> GdFeFe          :          K6          assoc

[constants]
    K6 = 14000 ??
[concentrations]
    Gd = 0.001 ?
[responses]
     intensive
[data]
    variable Fe
set 1| response Gd = 9410 ??        , GdFeFe = 27500 ??
;_____________________________________
[end]
```

8.3.2. DynaFit results Table

Table 7 – DynaFit analysis of the T1 relaxmetry results of GdSCA and GdCat

Complex	Cation	Model	$\log K_{bc}$	$\log K_{\Delta bc}$	%Δ
GdSCA	Fe^{3+}	1:1	$\log K_1 = 4.00$	2.89	7.7
		2:1	$\log K_1 = 4.14$ $\log K_2 = 3.22$	3.40 2.60	17.8 24.1
		3:1	$\log K_1 = 8.18$ $\log K_2 = 8.00$ $\log K_3 = 5.49$	8.52 8.30 6.15	> 100 > 100 > 100
		1:1:1	$\log K_1 = 7.12$	6.15	10.3
GdSCA	Fe^{2+}	1:1	$\log K_1 = 2.65$	1.00	2.3
		2:1	$\log K_1 = 0.66$ $\log K_2 = 9.40$	0.32 9.11	45.3 53.0
		3:1	$\log K_1 = 0.85$ $\log K_2 = 7.05$ $\log K_3 = 1.30$	0.26 6.42 0.26	25.2 23.2 9.2
		1:1:1	$\log K_1 = 8.16$	6.53	2.3
GdCat	Fe^{3+}	1:1	$\log K_1 = 1.41$	−0.30	2.0
		2:1	$\log K_1 = -1.93$	−2.72	16.1

			$\log K_2$ = 8.41	7.61	15.9
		3:1	$\log K_1$ = 0.65 $\log K_2$ = 7.69 $\log K_3$ = 3.90	0.32 7.32 3.51	42.6 42.0 40.0
		1:1:1	$\log K_1$ = 7.11	6.68	> 100
GdCat	Fe^{2+}	1:1	$\log K_1$ = −10.20	−11.85	2.3
		2:1	$\log K_1$ = −0.87 $\log K_2$ = 5.89	−1.85 4.63	10.6 5.5
		3:1	$\log K_1$ = −0.15 $\log K_2$ = 0.51 $\log K_3$ = 6.26	0.04 4.18 10.93	> 100 >> 100 >> 100
		1:1:1	$\log K_1$ = 7.64	20.88	>> 100

Table 8 – DynaFit analysis of the UV-Vis results of EuSCA and TbCat

Complex	Cation	Model	$\log(K_{bc})$	log(Std. Error)	CV / %
EuSCA	Fe^{3+}	1:1	$\log K_1$ = 17.23	16.15	8.5
		2:1	$\log K_1$ = 6.27 $\log K_2$ = -1.95	5.86 -2.54	38.9 25.8
	Fe^{2+}	1:1	$\log K_1$ = 6.09	5.43	22.0
		2:1	$\log K_1$ = 6.26 $\log K_2$ = -12.29	7.26 7.26	> 100 >> 100
	Ca^{2+}	1:1	$\log K_1$ = 13.86	12.61	5.7
		2:1	$\log K_1$ = 11.16 $\log K_2$ = -16.96	7.20 7.20	0 >> 100
	Zn^{2+}	1:1	$\log K_1$ = 13.86	12.83	9.4
		2:1	$\log K_1$ = 11.16 $\log K_2$ = -16.96	7.64 7.64	0 >> 100
TbCat	Fe^{3+}	1:1	$\log K_1$ = 5.45	4.58	13.4
		2:1	$\log K_1$ = 11.04 $\log K_2$ = -3.06	15.32 -4.21	>> 100 7.0
	Fe^{2+}	1:1	$\log K_1$ = 15.74	20.11	>> 100
		2:1	$\log K_1$ = 11.63 $\log K_2$ = -7.82	6.81 6.81	0 >> 100
	Ca^{2+}	1:1	$\log K_1$ = 13.84	23.38	>> 100
		2:1	$\log K_1$ = 11.16 $\log K_2$ = -15.02	6.68 6.68	0 >> 100
	Zn^{2+}	1:1	$\log K_1$ = 16.32	14.59	1.9
		2:1	$\log K_1$ = 11.18 $\log K_2$ = 12.23	10.04 11.11	7.4 7.4

8.3.4. Final protocol for LDH assay

The LDH cytotoxicity uses normal (10 % FBS) tissue culture DMEM medium for incubation and deficient (3 % FBS) tissue culture DMEM medium for treatment and measurement. For each condition, the experiment prefer to have at least 4 replicates. The positive (+) is for a positive control that uses Triton-X to kill all the cell where the negative (-) is for a negative control that uses sterile milli-Q water to keep all the cells alive. The experiment requires to dissolve the Gdcontrast agent in deficient (3 % FBS) tissue culture DMEM medium with required concentration and filtered by 0.22 µm filter to keep the medium sterile. Then it would be diluted to other required concentration. All the Gd-containing medium requires 1 mL during sample preparation.

	1	2	3	4	5	6	7	8	9	10	11	12
A	+				1µM				100µM			
B	+				1µM				100µM			
C	+				1µM				100µM			
D	+				1µM				100µM			
E	-				10µM				1mM			
F	-				10µM				1mM			
G	-				10µM				1mM			
H	-				10µM				1mM			

Figure 105 – LDH cytotoxicity's plate design where the columns of the odd numbers are for incubation and treatement while the columns of even numbers are for measurement on plate reader.

Procedure

Pre	1. Gd contrast agent agent (1.0 mM, 1.5 mL) was prepared in 3%-FBS-DMEM 2. The medium above was filtered through 0.22 µM filter for sterilization

	3. 100µL of the medium was transferred to an Eppendorf tube for a 10% dilution to get 1mM 4. 10µL of the medium above was transferred to an Eppendorf tube for a 1% dilution to get 10µM 5. 10µL of the medium above was transferred to an Eppendorf tube for a 1% dilution to get 100nM
Flask	6. A flask of healthy cells was used for the experiment when it reaches 1 million cells (ideally no more than 70% confluency) 7. The medium was removed and the flask was washed by PBS (2 × 5 mL) 8. the trypsin (1 mL) was added to the flask 9. The flask was put into the incubator (2 min) and tapped. 10. When 90% of the cells are floating, medium (10 mL) was added to the flask to neutralize the trypsin. 11. The medium was filtered through a 70 µm filter to create a single cells suspension 12. The cells in the medium were counted. 13. The suspension was centrifuged (1000 rpm, 4 min) and remove the supernatant 14. The cells pellet was resuspended in medium to make a solution as 0.5 million /mL
Plate	15. Cells (150 µL each) were added to column 1/5/9 of a 96-well plate. 16. The 96-well plate was left in the incubator to let the cells to attach overnight. 17. The medium was removed. 18. The wells were washed by 3% FBS-DMEM (50 µL × 2 for each well) 19. 3% FBS-DMEM (May contain GdSCA, 150 µL) was added wells with corresponding the concentration of complex, 20. The plate was incubated (5 h) to let the cells to interact with the complex. 21. The poison, Triton X-100 (15 µL) was added to A1-D4 for positive control 22. Sterile water (15 µL) was added to the rest for negative and standard control 23. The plate was left in incubator (45 min). 24. While waiting, the plate reader was preheated (≥ 10 min) at 37 °C, and set the wavelength at 450 nm. 25. Medium (90 µL) was transferred to adjacent well (1/5/9 to 2/6/10) 26. LDH reagent (10 µL) was added to 2/6/10 with a multichannel pipette and start from the lower concentrations. 27. The plate was read instantly. 28. After the first reading, change the setting to 2.5 min incubation before reading.

	29. Keep recording the data until the positive control saturated. 30. Change the setting to 4.5 min incubation before reading. 31. Keep recording until the data shows a clear trend. 32. Plot the data on GraphPad Prism and find the largest gap of OD between the average positive and negative control. 33. Work out % relative cytotoxicity

$$\frac{OD_{experimental\ sample(450\ nm)} - OD_{negative\ control(450\ nm)}}{OD_{positive\ control(450\ nm)} - OD_{negative\ control(450\ nm)}} \times 100\ \%$$

$$= \%\ \text{Relative Cytotoxicity}$$

8.3.5. Protocol of MRI in Vitro

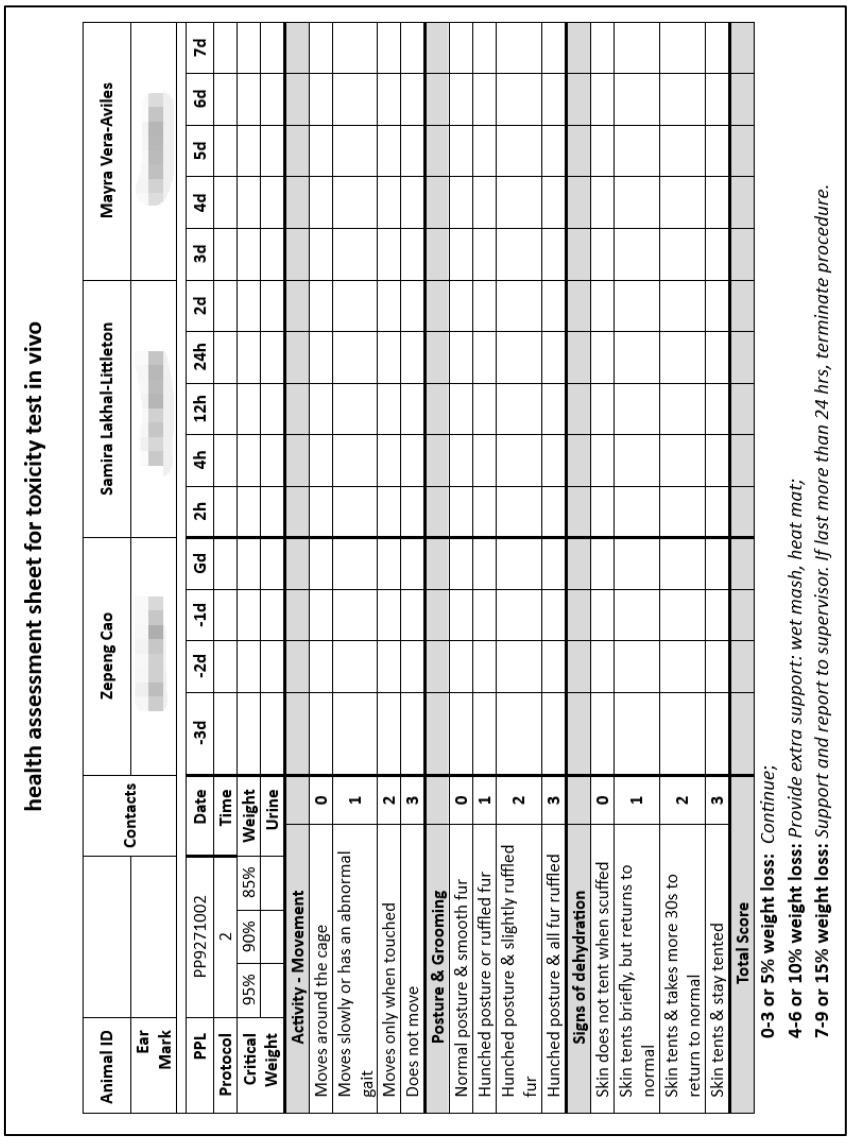
A total of 12 samples can be run at the same time. A Standard 3 mm NMR tube's volume is around 200 µL. I will prepare 0.8mL Gd-containing cell sample for each condition and add 100 µL Perfluorodecalin and 100 µL to each tube.

Table 9 – Schedule for cell MRI experiement

Pre	10mM of GdSCA was prepared in medium. 100µL of Perfluorodecalin was added to the bottom of the 3mm tubes and adjust them to the same height
Flask Day 1 9am	3 large-sized flasks of H9c2 cells was used for the experiment The cells trypsinised to have a cell suspension. The cell suspension were combined redispensed in 10mL of medium and centrifuged to remove the trypsin residue. The cells were splitted into 3 medium-sized flasks. The flasks were left for 6 hrs for cells to settle down.
Flask Day 1 6 pm	The flasks were washed with PBS The flasks were treated with Fe The flask were incubated over-half-night.
Flask Day 2 4am,	The flasks were washed by PBS (2 × 10 mL) GdSCA/Fe containing medium was added to the flasks The flask was incubated for 2 hrs.
Flask Day 2 7am,	The medium was removed and washed by PBS (2 × 10 mL) The cells were trypsinised and collected (5 min). The cells were centrifudged and remove the medium to get rid of the trypsin residue The cells were redispensed in 1ml of fresh medium The cells were loaded into the NMR tubes Transfered a 0.1mL sample to Perfluorodecalin pre-loaded NMR and sealed with mineral oil The top of the tubes were wrapped but not sealed with parafilm to fix the position of the tubes. The tube holder was tapped gently to let the cells deposit.
Tube holder Day 2 9:30 am	The tube holder was sent to CLR for testings. The run takes roughly 5 hrs.
Tube holder Day 2 3 pm	The raw data was collected and the process for T1 calculation.

8.3.6. Urine analysis protocol

1. Confirm the temperature as the room temperature
2. Remove frozen samples from －80° C and allow to thaw completely at room temperature.
3. Shake gentally to ensure homogenization.
4. Take MULTISTIX® 10 SG strips and place them in a petri dish and immediately reseal the bottle to avoid humidity exposure.
5. Label the strips
6. For each urine sample, start timing and pipette 2 µL to each test pads.
7. Use a timer to read each parameter at its specified time (per Siemens instructions, typically 30 seconds).
8. Compare pad colours to the reference chart on the bottle and record each result.



health assessment sheet for toxicity test in vivo

Animal ID		Contacts	Zepeng Cao					Samira Lakhal-Littleton						Mayra Vera-Aviles						
Ear Mark			-3d	-2d	-1d	Gd	2h	4h	12h	24h	2d	3d	4d	5d	6d	7d				
PPL	PP9271002	Date																		
Protocol	2	Time																		
Critical Weight	95% 90% 85%	Weight																		
		Urine																		
Activity - Movement																				
Moves around the cage	0																			
Moves slowly or has an abnormal gait	1																			
Moves only when touched	2																			
Does not move	3																			
Posture & Grooming																				
Normal posture & smooth fur	0																			
Hunched posture or ruffled fur	1																			
Hunched posture & slightly ruffled fur	2																			
Hunched posture & all fur ruffled	3																			
Signs of dehydration																				
Skin does not tent when scuffed	0																			
Skin tents briefly, but returns to normal	1																			
Skin tents & takes more 30s to return to normal	2																			
Skin tents & stay tented	3																			
Total Score																				

0-3 or 5% weight loss: *Continue;*
4-6 or 10% weight loss: *Provide extra support: wet mash, heat mat;*
7-9 or 15% weight loss: *Support and report to supervisor. If last more than 24 hrs, terminate procedure.*

8.3.7. Protocol of MRI In vivo

Before the MRI test

1) A stock of 0.4mL of 0.5 µmol/mL (50 mM, 13.58 mg) of GdSCA is prepared with sterilised water and filtered by 0.22 µm filter.
2) The night before the experiment, one of mice was injected with Iron supplement for overload
3) Mice are weighted and recorded for mass
4) 1 mL of 10% FCM is prepare through 1 in 4 dilutions of FCM with sterilised saline

The day of MRI in vivo

1) The MRI machine is settled
2) Have ECG ready/respiration sensor
3) The dose of Gd contrast agent was calculated based on the mass.
4) The mice is anaesthetised
5) Apply eye gel
6) IV line is injected into the tail
7) Transfer the mice into the MRI Chamber and get anaesthetised
8) Insert rectal probe
9) Push the mouse into the coil with IV line left outside.
10) Scan the mouse and locate the liver with a baseline and record time
11) Inject Gd slowly

12A) Scanning Gd (3 x 5 minutes) and record the time

13A) Inject iron

14A) Scan Iron (8 x 5 minutes) and record the time

12B) Scanning Gd (10 x 5 minutes) and record the time

15) The MRI data is analysed by ITK-SNAP and calculate the ROI
16) The numbers are analysed by GraphPad Prism

Reference

1. A. Yiannikourides and G. O. Latunde-Dada, *Medicines (Basel)*, 2019, **6**, 85.
2. S. Lakhal-Littleton and J. G. F. Cleland, *Nat Rev Cardiol*, 2024, **21**, 463-486.
3. N. Abbaspour, R. Hurrell and R. Kelishadi, *J Res Med Sci*, 2014, **19**, 164-174.
4. N. I. o. H. O. o. D. Supplements, Iron Fact Sheet for Health Professionals, 2026).
5. M. U. Muckenthaler, S. Rivella, M. W. Hentze and B. Galy, *Cell*, 2017, **168**, 344-361.
6. B. Galy, M. Conrad and M. Muckenthaler, *Nat Rev Mol Cell Biol*, 2024, **25**, 133-155.
7. Z. I. Cabantchik, *Front Pharmacol*, 2014, **5**, 45.
8. A. Katsarou and K. Pantopoulos, *Mol Aspects Med*, 2020, **75**, 100866.
9. N. I. o. H. O. o. D. Supplements, Iron: Fact Sheet for Health Professionals, 2026).
10. R. Hurrell and I. Egli, *Am J Clin Nutr*, 2010, **91**, 1461S-1467S.
11. J. L. Bresson, B. Burlingame, T. Dean, S. Fairweather-Tait, M. Heinonen, K. I. Hirsch-Ernst, I. Mangelsdorf, H. McArdle, A. Naska, M. Neuhäuser-Berthold, G. Nowicka, K. Pentieva, Y. Sanz, A. Siani, A. Sjödin, M. Stern, D. Tomé, D. Turck, H. Van Loveren, M. Vinceti, P. Willatts and E. P. D. P. Nutr, *Efsa J*, 2015, **13**.
12. K. Skoczen, Hemoglobin + Myoglobin Bohr Effect).
13. C. E. Housecroft and A. G. Sharpe, *Journal*, 2018, 1 online resource (1,297 pages).
14. R. Di Lorenzo, E. Marzetti, H. J. Coelho-Junior, R. Calvani, V. Pesce, F. Landi, C. Leeuwenburgh and A. Picca, *Cells-Basel*, 2025, **14**.
15. Y. X. Li, Q. Ran, Q. H. Duan, J. L. Jin, Y. J. Wang, L. Yu, C. J. Wang, Z. Y. Zhu, X. Chen, L. J. Weng, Z. Li, J. Wang, Q. Wu, H. Wang, H. L. Tian, S. H. Song, Z. Z. Shan, Q. W. Zhai, H. L. Qin, S. L. Chen, L. Fang, H. Y. Yin, H. Zhou, X. J. Jiang and P. Wang, *Nature*, 2024, **626**.
16. K. Haas, Chapter 5: Biological Molecules: Transferrin).
17. J. Nunez, A. Mollar, M. Vera-Aviles, S. Kabir, A. Shah, P. Polzella, M. Desborough, I. Cardells, G. Minana, I. Del Canto, V. Ferreira, S. Piechnik, A. Maceira and S. Lakhal-Littleton, *Eur J Heart Fail*, 2025, **27**, 2352-2356.
18. J. G. F. Cleland, P. Pellicori and S. Lakhal-Littleton, *JACC Heart Fail*, 2024, **12**, 549-551.
19. E. C. Theil, in *Encyclopedia of Metalloproteins*, eds. R. H. Kretsinger, V. N. Uversky and E. A. Permyakov, Springer New York, New York, NY, 2013, DOI: 10.1007/978-1-4614-1533-6_348, ch. Chapter 348, pp. 996-1006.
20. K. Gkouvatsos, G. Papanikolaou and K. Pantopoulos, *Bba-Gen Subjects*, 2012, **1820**, 188-202.
21. H. Kawabata, *Free Radical Bio Med*, 2019, **133**, 46-54.
22. A. S. Zhang and C. A. Enns, *J Biol Chem*, 2009, **284**, 711-715.
23. J. Barra, I. Crosbourne, C. L. Roberge, R. Bossardi-Ramos, J. S. A. Warren, K. Matteson, L. Wang, F. Jourd'heuil, S. M. Borisov, E. Bresnahan, J. J. Bravo-Cordero, R. I. Dmitriev, D. Jourd'heuil, A. P. Adam, J. M. Lamar, D. T. Corr and M. M. Barroso, *Oncogene*, 2024, **43**, 650-667.
24. R. R. Crichton, *Journal*, 2016, 1 online resource (576 pages).
25. A. T. McKie, D. Barrow, G. O. Latunde-Dada, A. Rolfs, G. Sager, E. Mudaly, M. Mudaly, C. Richardson, D. Barlow, A. Bomford, T. J. Peters, K. B. Raja, S. Shirali, M. A. Hediger, F. Farzaneh and R. J. Simpson, *Science*, 2001, **291**, 1755-1759.
26. P. Aisen, C. Enns and M. Wessling-Resnick, *Int J Biochem Cell B*, 2001, **33**, 940-959.

27. C. C. Winterbourn, *Toxicol Lett*, 1995, **82-83**, 969-974.
28. M. Kruszewski, *Mutat Res-Fund Mol M*, 2003, **531**, 81-92.
29. N. P. Talbot, M. Downs, J. Cane, S. Yen, G. Mohammad, A. Gates, J. Snowball, M. Laskawiec-Szkonter, M. Dobson, S. Lakhal-Littleton, J. S. Johnson, N. M. Rahman, S. Gerry, S. J. Chapman and W. G. Flight, *Eur Respir J*, 2025, **66**.
30. Y. Kohgo, Y. Torimoto and J. Kato, *Int J Hematol*, 2002, **76**, 213-218.
31. T. Ganz and E. Nemeth, *Cold Spring Harb Perspect Med*, 2012, **2**, a011668.
32. G. J. Anderson and D. M. Frazer, *Am J Clin Nutr*, 2017, **106**, 1559S-1566S.
33. L. M. Sorokin, E. H. Morgan and G. C. Yeoh, *J Biol Chem*, 1988, **263**, 14128-14133.
34. A. Mollar, C. Garcia-Conejo, E. Revuelta-Lopez, I. Cardells, R. Lopez, I. Del Canto, R. de la Espriella, M. P. Lopez-Lereu, J. V. Monmeneu, A. Maceira, S. Lakhal-Littleton, L. Almenar, A. Cases, M. Peiro, A. Bayes-Genis and J. Nunez, *Sci Rep*, 2026, **16**, 5044.
35. C. E. Herbison, K. Thorstensen, A. C. Chua, R. M. Graham, P. Leedman, J. K. Olynyk and D. Trinder, *Am J Physiol Cell Physiol*, 2009, **297**, C1567-1575.
36. R. R. Crichton, *Journal*, 2008, 1 online resource (383 p.
37. M. C. R. Symons and J. M. C. U. Gutteridge, *Free radicals and iron : chemistry, biology, and medicine*, Oxford University Press, Oxford, 1998.
38. C. Camaschella, A. Nai and L. Silvestri, *Haematologica*, 2020, **105**, 260-272.
39. S. Lakhal-Littleton, M. Wolna, Y. J. Chung, H. C. Christian, L. C. Heather, M. Brescia, V. Ball, R. Diaz, A. Santos, D. Biggs, K. Clarke, B. Davies and P. A. Robbins, *Elife*, 2016, **5**.
40. H. Drakesmith and A. M. Prentice, *Science*, 2012, **338**, 768-772.
41. A. D. Sheftel, A. B. Mason and P. Ponka, *Biochim Biophys Acta*, 2012, **1820**, 161-187.
42. D. J. Taatjes and J. Roth, *Journal*, 2013, DOI: 10.1007/978-1-62703-056-4, 1 online resource (XVII, 550 p. 150 illus., 553 illus. in color.
43. M. Vera-Aviles, S. N. Kabir, A. Shah, P. Polzella, D. Y. Lim, P. Buckley, C. Ball, D. Swinkels, H. Matlung, C. Blans, P. Holdship, J. Nugent, E. Anderson, M. Desborough, S. Piechnik, V. Ferreira and S. Lakhal-Littleton, *Eur Heart J*, 2024, **45**, 4497-4508.
44. J. Emerit, C. Beaumont and F. Trivin, *Biomed Pharmacother*, 2001, **55**, 333-339.
45. P. Ponka, M. Tenenbein and J. W. Eaton, *Handbook on the Toxicology of Metals, Vol I & Ii, 4th Edition*, 2015, DOI: 10.1016/B978-0-444-59453-2.00041-X, 879-902.
46. A. T. Aron, M. C. Heffern, Z. R. Lonergan, M. N. Vander Wal, B. R. Blank, B. Spangler, Y. Zhang, H. M. Park, A. Stahl, A. R. Renslo, E. P. Skaar and C. J. Chang, *Proc Natl Acad Sci U S A*, 2017, **114**, 12669-12674.
47. W. J. Chen, G. P. Kung and J. P. Gnana-Prakasam, *Antioxidants-Basel*, 2022, **11**.
48. D. D. Zhang, *Nat Cell Biol*, 2024, **26**, 1386-1393.
49. S. Lakhal-Littleton, *Free Radic Biol Med*, 2019, **133**, 234-237.
50. B. H. Baumann, W. Shu, Y. Song, J. Sterling, Z. Kozmik, S. Lakhal-Littleton and J. L. Dunaief, *Am J Pathol*, 2019, **189**, 1814-1830.
51. A. Mizumoto, *WHO global anaemia estimates Key findings, 2025* Switzerland, 2025.
52. N. Vilaplana-Lopera, J. Kim, G. Nam, I. D. C. Tullis, S. Paillas, J. L. Ruan, P. J. Lee, Y. Jiang, S. Park, T. Hou, A. Nasir, E. Charlesworth, E. Walker, A. Abu-Halawa, M. A. Hill, C. Choi, I. J. Lee, Y. Jeong, S. Lakhal-Littleton, C. K. Then, S. C. Shen, A. J. Giaccia, K. Petersson and E. J. Moon, *Cell Death Dis*, 2025, **16**, 668.

53. S. von Haehling, E. A. Jankowska, D. J. van Veldhuisen, P. Ponikowski and S. D. Anker, *Nat Rev Cardiol*, 2015, **12**, 659-669.
54. A. J. Schwartz, J. W. Goyert, S. Solanki, S. A. Kerk, B. Chen, C. Castillo, P. P. Hsu, B. T. Do, R. Singhal, M. K. Dame, H. J. Lee, J. R. Spence, S. Lakhal-Littleton, M. G. Vander Heiden, C. A. Lyssiotis, X. Xue and Y. M. Shah, *Nat Metab*, 2021, **3**, 969-982.
55. Y. J. Chung, P. Swietach, M. K. Curtis, V. Ball, P. A. Robbins and S. Lakhal-Littleton, *Front Cardiovasc Med*, 2020, **7**, 616920.
56. A. E. Armitage, P. J. Lim, J. N. Frost, S. R. Pasricha, E. J. Soilleux, E. Evans, A. Morovat, A. Santos, R. Diaz, D. Biggs, B. Davies, U. Gileadi, P. A. Robbins, S. Lakhal-Littleton and H. Drakesmith, *J Innate Immun*, 2016, **8**, 517-528.
57. P. Brissot, A. Pietrangelo, P. C. Adams, B. de Graaff, C. E. McLaren and O. Loreal, *Nat Rev Dis Primers*, 2018, **4**, 18016.
58. G. Mohammad, A. Matakidou, P. A. Robbins and S. Lakhal-Littleton, *Kidney Int*, 2021, **100**, 559-569.
59. Y. Y. Zhao, M. J. Yang and X. X. Liang, *J Transl Med*, 2024, **22**.
60. S. Lakhal-Littleton, M. Wolna, C. A. Carr, J. J. Miller, H. C. Christian, V. Ball, A. Santos, R. Diaz, D. Biggs, R. Stillion, P. Holdship, F. Larner, D. J. Tyler, K. Clarke, B. Davies and P. A. Robbins, *Proc Natl Acad Sci U S A*, 2015, **112**, 3164-3169.
61. I. Campos-Luna, A. Miller, A. Beard and M. Leach, *Sci Rep*, 2019, **9**, 10249.
62. S. Lynch, C. M. Pfeiffer, M. K. Georgieff, G. Brittenham, S. Fairweather-Tait, R. F. Hurrell, H. J. McArdle and D. J. Raiten, *J Nutr*, 2018, **148**, 1001S-1067S.
63. S. Cherubin, T. Peoples, J. Gillard, S. Lakhal-Littleton, J. Kurinczuk and M. Nair, *J Epidemiol Commun H*, 2020, **74**, A25-A25.
64. J. Wahsner, E. M. Gale, A. Rodríguez-Rodríguez and P. Caravan, *Chem Rev*, 2019, **119**, 957-1057.
65. E. L. Que and C. J. Chang, *Chem Soc Rev*, 2010, **39**, 51-60.
66. R. D. Caterina, R. De Caterina, J. A. Martínez Hernández and M. Kohlmeier, *Journal*, 2020, 1 online resource (588 pages).
67. S. Cherubin, T. Peoples, J. Gillard, S. Lakhal-Littleton, J. J. Kurinczuk and M. Nair, *Open Heart*, 2020, **7**.
68. E. D. Weinberg, *Drug Metab Rev*, 1990, **22**, 531-579.
69. J. L. Major and T. J. Meade, *Accounts Chem Res*, 2009, **42**, 893-903.
70. S. Epsztejn, O. Kakhlon, H. Glickstein, W. Breuer and I. Cabantchik, *Anal Biochem*, 1997, **248**, 31-40.
71. J. C. Wood, *Hematol Oncol Clin North Am*, 2014, **28**, 747-764, vii.
72. I. Elliott and G. C. U. Skerritt, *Handbook of small animal MRI*, Wiley-Blackwell, Oxford, 2010.
73. Y. J. Chung, A. Luo, K. C. Park, A. A. Loonat, S. Lakhal-Littleton, P. A. Robbins and P. Swietach, *Jci Insight*, 2019, **4**.
74. The most abundant 90 natural elements, https://www.euchems.eu/euchems-periodic-table/).
75. PERIODIC TABLE OF ELEMENTS).
76. H. C. Aspinall, *Journal*, 2023, DOI: 10.1093/hesc/9780198825180.001.0001, 1 online resource (vii, 135 pages).
77. S. A. Cotton, *Lanthanide and actinide chemistry*, Wiley, Hoboken, New Jersey, Second edition. edn., 2024.

78. J. C. G. Bünzli, *Chem Rev*, 2010, **110**, 2729-2755.
79. R. D. Shannon, *Acta Crystallogr A*, 1976, **32**, 751-767.
80. G. R. Choppin and D. R. Peterman, *Coordin Chem Rev*, 1998, **174**, 283-299.
81. J. Ribas Gispert, *Coordination chemistry*, Wiley-VCH, Weinheim, 2008.
82. B. Weber, *Journal*, 2021, DOI: 10.1007/978-3-662-66441-4, 1 online resource (273 pages).
83. P. Caravan, J. J. Ellison, T. J. McMurry and R. B. Lauffer, *Chem Rev*, 1999, **99**, 2293-2352.
84. H. Nakazawa and J. Koe, *Journal*, 2021, 1 online resource.
85. S. Gündüz, S. Vibhute, R. Botár, F. K. Kálmán, I. Tóth, G. Tircsó, M. Regueiro-Figueroa, D. Esteban-Gómez, C. Platas-Iglesias and G. Angelovski, *Inorganic Chemistry*, 2018, **57**, 5973-5986.
86. A. D. Sherry and Y. K. Wu, *Curr Opin Chem Biol*, 2013, **17**, 167-174.
87. S. Faulkner and O. A. Blackburn, *Chemistry of Molecular Imaging*, 2015, 179-197.
88. S. Kaur-Ghumaan, *Journal*, 2021, 1 online resource (452 pages).
89. N. C. Martinez-Gomez, H. N. Vu and E. Skovran, *Inorg Chem*, 2016, **55**, 10083-10089.
90. D. Parker, J. D. Fradgley and K. L. Wong, *Chem Soc Rev*, 2021, **50**, 8193-8213.
91. S. V. Eliseeva and J. C. G. Bünzli, *Chem Soc Rev*, 2010, **39**, 189-227.
92. A. J. Amoroso and S. J. Pope, *Chem Soc Rev*, 2015, **44**, 4723-4742.
93. B. R. Judd, *Phys Rev*, 1962, **127**, 750-&.
94. S. Faulkner, S. J. A. Pope and B. P. Burton-Pye, *Appl Spectrosc Rev*, 2005, **40**, 1-31.
95. S. Faulkner, A. Beeby, M. C. Carrié, A. Dadabhoy, A. M. Kenwright and P. G. Sammes, *Inorg Chem Commun*, 2001, **4**, 187-190.
96. M. Latva, H. Takalo, V. M. Mukkala, C. Matachescu, J. C. RodriguezUbis and J. Kankare, *J Lumin*, 1997, **75**, 149-169.
97. W. D. Horrocks and D. R. Sudnick, *Accounts Chem Res*, 1981, **14**, 384-392.
98. A. Beeby, I. M. Clarkson, R. S. Dickins, S. Faulkner, D. Parker, L. Royle, A. S. de Sousa, J. A. G. Williams and M. Woods, *J Chem Soc Perk T 2*, 1999, DOI: DOI 10.1039/a808692c, 493-503.
99. D. Parker, *Chem Soc Rev*, 2004, **33**, 156-165.
100. N. Kaltsoyannis and P. R. Scott, *Journal*, 2023, DOI: 10.1093/hesc/9780198504672.001.0001, 1 online resource (85 pages).
101. L. Banci, M. Piccioli and A. Scozzafava, *Coordin Chem Rev*, 1992, **120**, 1-28.
102. A. Abragam, *The principles of nuclear magnetism*, Clarendon Press, Oxford, First paperback edition. edn., 1985.
103. P. W. Atkins, J. De Paula and J. U. Keeler, *Atkins' physical chemistry*, Oxford University Press, Oxford ; New York, Twelfth edition. edn., 2023.
104. J.-C. G. Bünzli and S. V. Eliseeva, in *Lanthanide Luminescence*, 2010, vol. 7, ch. Chapter 3, pp. 1-45.
105. P. B. Jin, Q. C. Luo and Y. Z. Zheng, *Accounts Chem Res*, 2026, **59**, 221-233.
106. L. R. B. Wilson, M. Coletta, M. Evangelisti, S. Piligkos, S. J. Dalgarno and E. K. Brechin, *Dalton T*, 2022, **51**, 4560-4560.
107. E. M. Haacke, Y. B. Xu, Y. C. N. Cheng and J. R. Reichenbach, *Magnetic Resonance in Medicine*, 2004, **52**, 612-618.
108. M. A. Halcrow, *Chem Soc Rev*, 2008, **37**, 278-289.
109. I. Solomon, *Phys Rev*, 1955, **99**, 559-565.
110. N. Bloembergen, *J Chem Phys*, 1957, **27**, 572-573.

111. N. Bloembergen and L. O. Morgan, *J Chem Phys*, 1961, **34**, 842-&.
112. A. E. Merbach, L. Helm and É. U. Tóth, *The chemistry of contrast agents in medical magnetic resonance imaging*, Wiley, Chichester, Second edition. edn., 2013.
113. E. M. Haacke and J. r. R. U. Reichenbach, *Susceptibility weighted imaging in MRI : basic concepts and clinical applications*, Wiley-Blackwell, Hoboken, N.J., 2011.
114. P. Verwilst, S. Park, B. Yoon and J. S. Kim, *Chem Soc Rev*, 2015, **44**, 1791-1806.
115. S. Aime, M. Botta and E. Terreno, *Adv Inorg Chem*, 2005, **57**, 173-237.
116. M. Botta and L. Tei, *Eur J Inorg Chem*, 2012, DOI: 10.1002/ejic.201101305, 1945-1960.
117. M. W. Hentze, M. U. Muckenthaler and N. C. Andrews, *Cell*, 2004, **117**, 285-297.
118. M. W. Hentze, M. U. Muckenthaler, B. Galy and C. Camaschella, *Cell*, 2010, **142**, 24-38.
119. D. F. Shriver, M. T. Weller, T. Overton, J. Rourke and F. A. U. Armstrong, *Inorganic chemistry*, W. H. Freeman and Company, New York, N.Y., Sixth edition. / edn., 2014.
120. E. Terreno, D. Delli Castelli, A. Viale and S. Aime, *Chem Rev*, 2010, **110**, 3019-3042.
121. T. Zhou, G. Winkelmann, Z. Y. Dai and R. C. Hider, *J Pharm Pharmacol*, 2011, **63**, 893-903.
122. B. P. Hay, D. A. Dixon, R. Vargas, J. Garza and K. N. Raymond, *Inorganic Chemistry*, 2001, **40**, 3922-3935.
123. T. R. Ward, A. Lutz, S. P. Parel, J. Ensling, P. Gütlich, P. Buglyó and C. Orvig, *Inorganic Chemistry*, 1999, **38**, 5007-5017.
124. M. Aplincourt, C. Gerard, R. P. Hugel, J. C. Pierrard, J. Rimbault, A. Bertrandie, B. Magny and P. J. Siret, *Polyhedron*, 1992, **11**, 1161-1168.
125. E. Mentasti and E. Pelizzetti, *J Chem Soc Dalton*, 1973, DOI: DOI 10.1039/dt9730002605, 2605-2608.
126. M. V. Park, *J Chem Soc A*, 1966, DOI: DOI 10.1039/j19660000816, 816-&.
127. R. J. Abergel, J. A. Warner, D. K. Shuh and K. N. Raymond, *Journal of the American Chemical Society*, 2006, **128**, 8920-8931.
128. J. A. Iggo, K. V. Luzyanin and J. A. Iggo, *Journal*, 2023, DOI: 10.1093/hesc/9780198794851.001.0001, 1 online resource (xiii, 122 pages).
129. M. H. Levitt, *Journal*, 2008, 1 online resource (724 pages).
130. P. J. Hore, J. A. Jones and S. Wimperis, *Journal*, 2023, DOI: 10.1093/hesc/9780198703426.001.0001, 1 online resource (xii, 120 pages).
131. R. W. Brown, E. M. Haacke, M. R. Thompson, R. Venkatesan and N. U. Cheng, *Magnetic resonance imaging : physical principles and sequence design*, Wiley-Blackwell, Hoboken, New Jersey, Second edition. edn., 2014.
132. D. W. McRobbie, E. A. Moore, M. J. Graves and M. R. U. Prince, *MRI from picture to proton*, Cambridge University Press, Cambridge ; New York, Third edition. edn., 2017.
133. P. Caravan, *Chem Soc Rev*, 2006, **35**, 512-523.
134. S. Laurent, *Journal*, 2016, 1 online resource (125 pages).
135. H. H. Chen, R. D. Boykin, G. D. Clarke, J. H. Gao and J. W. Roby, 3rd, *Med Phys*, 2006, **33**, 4299-4306.
136. R. Bowtell, *Nature*, 2008, **453**, 993-994.
137. W. S. Price, *Concept Magn Reson A*, 2009, **34a**, 60-61.
138. Y.-C. N. C. Robert W. Brown, E. Mark Haacke, Michael R. Thompson, Ramesh Venkatesan *Magnetic Resonance Imaging: Physical Principles and Sequence Design, 2nd Edition*, Wiley

Blackwell, 2nd edn., 2014.
139. L. J. Anderson, S. Holden, B. Davis, E. Prescott, C. C. Charrier, N. H. Bunce, D. N. Firmin, B. Wonke, J. Porter, J. M. Walker and D. J. Pennell, *Eur Heart J*, 2001, **22**, 2171-2179.
140. R. Pohmann, O. Speck and K. Scheffler, *Magn Reson Med*, 2016, **75**, 801-809.
141. L. M. De León-Rodríguez, A. F. Martins, M. C. Pinho, N. M. Rofsky and A. D. Sherry, *Journal of Magnetic Resonance Imaging*, 2015, **42**, 545-565.
142. A. Deagostino, N. Protti, D. Alberti, P. Boggio, S. Bortolussi, S. Altieri and S. G. Crich, *Future Med Chem*, 2016, **8**, 899-917.
143. C. T. Yang and K. H. Chuang, *Medchemcomm*, 2012, **3**, 552-565.
144. E. C. Constable, *Journal*, 2023, DOI: 10.1093/hesc/9780198556923.001.0001, 1 online resource.
145. S. P. Lin and J. J. Brown, *Journal of Magnetic Resonance Imaging*, 2007, **25**, 884-899.
146. A. Sigel and H. Sigel, *Journal*, 2000, 1 online resource (816 pages).
147. J. S. McDonald and R. J. McDonald, *Magn Reson Imaging C*, 2020, **28**, 497-+.
148. J. H. Duyn, *Neuroimage*, 2012, **62**, 1241-1248.
149. G. Zabow, S. J. Dodd and A. P. Koretsky, *Nature*, 2015, **520**, 73-U157.
150. P. Khalighinejad, D. Parrott and A. D. Sherry, *Pharmaceuticals-Base*, 2020, **13**.
151. M. Wyskocka-Gajda, L. Przypis, M. Olesiejuk, T. Krawczyk, A. Kuznik, K. Nawara, M. Minoshima, F. Sugihara, K. Kikuchi and N. Kuznik, *Eur J Med Chem*, 2021, **211**.
152. E. L. Que and C. J. Chang, *Journal of the American Chemical Society*, 2006, **128**, 15942-15943.
153. G. M. Brittenham, G. Moir-Meyer, K. M. Abuga, A. Datta-Mitra, C. Cerami, R. Green, S. R. Pasricha and S. H. Atkinson, *J Nutr*, 2023, **153 Suppl 1**, S7-S28.
154. V. Gulani, F. Calamante, F. G. Shellock, E. Kanal, S. B. Reeder and I. S. M. R. Med, *Lancet Neurol*, 2017, **16**, 564-570.
155. H. S. Thomsen, *Radiol Clin North Am*, 2009, **47**, 827-831, vi.
156. I. Bertini, C. Luchinat and G. Parigi, *Prog Nucl Mag Res Sp*, 2002, **40**, 249-273.
157. T. Kanda, K. Ishii, H. Kawaguchi, K. Kitajima and D. Takenaka, *Radiology*, 2014, **270**, 834-841.
158. J. Hoffmann, A. Henning, I. A. Giapitzakis, K. Scheffler, G. Shajan, R. Pohmann and N. I. Avdievich, *Nmr Biomed*, 2016, **29**, 1131-1144.
159. E. L. Que and C. J. Chang, *Abstr Pap Am Chem S*, 2010, **240**.
160. A. C. Esqueda, J. A. Lopez, G. Andreu-de-Riquer, J. C. Alvarado-Monzon, J. Ratnakar, A. J. Lubag, A. D. Sherry and L. M. De Leon-Rodriguez, *J Am Chem Soc*, 2009, **131**, 11387-11391.
161. A. Y. Louie, M. M. Huber, E. T. Ahrens, U. Rothbacher, R. Moats, R. E. Jacobs, S. E. Fraser and T. J. Meade, *Nat Biotechnol*, 2000, **18**, 321-325.
162. W. S. Warren, S. Ahn, M. Mescher, M. Garwood, K. Ugurbil, W. Richter, R. R. Rizi, J. Hopkins and J. S. Leigh, *Science*, 1998, **281**, 247-251.
163. L. Schröder, T. J. Lowery, C. Hilty, D. E. Wemmer and A. Pines, *Science*, 2006, **314**, 446-449.
164. F. A. Gallagher, M. I. Kettunen, S. E. Day, D. E. Hu, J. H. Ardenkjær-Larsen, R. in't Zandt, P. R. Jensen, M. Karlsson, K. Golman, M. H. Lerche and K. M. Brindle, *Nature*, 2008, **453**, 940-U973.
165. C. A. Chang, L. C. Francesconi, M. F. Malley, K. Kumar, J. Z. Gougoutas, M. F. Tweedle, D. W. Lee and L. J. Wilson, *Inorganic Chemistry*, 2002, **32**, 3501-3508.
166. S. K. Piechnik, P. Polzella, A. Shah, M. Vera-Aviles, S. N. Kabir, M. Desborough, V. M. Ferreira and S. Lakhal-Littleton, *Br J Haematol*, 2025, **206**, 349-352.

167. R. Maurice, C. de Graaf and N. Guihéry, *Phys Chem Chem Phys*, 2013, **15**, 18784-18804.
168. S. Lakhal-Littleton and C. Peyssonnaux, *Adv Exp Med Biol*, 2025, **1480**, 89-102.
169. I. P. Pozdnyakov, V. F. Plyusnin, V. P. Grivin and E. Oliveros, *J Photoch Photobio A*, 2015, **307**, 9-15.
170. S. Aime, M. Botta, M. Fasano and E. Terreno, *Spectrochim Acta A*, 1993, **49**, 1315-1322.
171. A. N. Pham and T. D. Waite, *J Phys Chem A*, 2008, **112**, 5395-5405.
172. J. M. Berg, *Journal*, 2023, 1 online resource.
173. A. Leone and J. F. B. Mercer, *Copper transport and its disorders : molecular and cellular aspects*, Plenum, New York ; London, 1998.
174. S. El-Andaloussi, Y. Lee, S. Lakhal-Littleton, J. Li, Y. Seow, C. Gardiner, L. Alvarez-Erviti, I. L. Sargent and M. J. Wood, *Nat Protoc*, 2012, **7**, 2112-2126.
175. P. Kuzmic, Getting Started with DynaFit Software Version 4.0).
176. C. F. Baes and R. E. Mesmer, *Am J Sci*, 1981, **281**, 935-962.
177. W. Stumm and J. J. Morgan, *Journal*, 2012, 1 online resource (1042 pages).
178. C. X. Zhu, H. Daigle and B. Y. Zhang, *J Petrol Sci Eng*, 2018, **161**, 121-127.
179. Z. Baranyai, F. Carniato, A. Nucera, D. Horváth, L. Tei, C. Platas-Iglesias and M. Botta, *Chem Sci*, 2021, **12**, 11138-11145.
180. T. Ohno, J. D. Kubicki and A. Amirbahman, *Soil Sci Soc Am J*, 2022, **86**, 181-194.
181. L. T. Tsai, C. C. Wang, C. Y. Liu, C. K. Chiang and S. H. Liu, *Life Sci*, 2025, **380**.
182. K. Yao, G. Karunanithy, A. Howarth, P. Holdship, A. L. Thompson, K. E. Christensen, A. J. Baldwin, S. Faulkner and N. J. Farrer, *Dalton Trans*, 2021, **50**, 8761-8767.
183. S. Suresh, S. Gunasekaran and S. Srinivasan, *Spectrochim Acta A*, 2014, **132**, 130-141.
184. K. Yao, Doctor of Philosophy in Inorganic Chemistry, University of Oxford, 2021.
185. S. Goia, G. W. Richings, M. A. P. Turner, J. M. Woolley, J. J. Tully, S. J. Cobb, A. Burriss, B. Robinson, J. V. Macpherson and V. G. Stavros, *Chemphotochem*, 2024, **8**.
186. P. Wang, G. P. A. Yap and C. G. Riordan, *Chem Commun*, 2014, **50**, 5871-5873.
187. *Journal*.
188. D. J. Shah, R. M. Judd and R. J. Kim, *Nat Clin Pract Cardiovasc Med*, 2005, **2**, 597-605; quiz 606.
189. S. Aime and P. Caravan, *J Magn Reson Imaging*, 2009, **30**, 1259-1267.
190. T. Grobner, *Nephrol Dial Transpl*, 2006, **21**, 1745-1745.
191. F. K. Chan, K. Moriwaki and M. J. De Rosa, *Methods Mol Biol*, 2013, **979**, 65-70.
192. Product Manual CytoSelect™ LDH Cytotoxicity Assay Kit, 2025).
193. Gibco™ DMEM, high glucose).
194. E. L. Mackenzie, K. Iwasaki and Y. Tsuji, *Antioxid Redox Sign*, 2008, **10**, 997-1030.
195. M. Hoehn, D. Wiedermann, C. Justicia, P. Ramos-Cabrer, K. Kruttwig, T. Farr and U. Himmelreich, *J Physiol*, 2007, **584**, 25-30.
196. R. C. Hider and X. L. Kong, *Biometals*, 2011, **24**, 1179-1187.
197. P. Caravan, *Accounts Chem Res*, 2009, **42**, 851-862.
198. Multistix® 10 SG Reagent Strips).
199. J. A. Simerville, W. C. Maxted and J. J. Pahira, *Am Fam Physician*, 2005, **71**, 1153-1162.
200. T. Burkholder, C. Foltz, E. Karlsson, C. G. Linton and J. M. Smith, *Curr Protoc Mouse Biol*, 2012, **2**, 145-165.
201. A. St John, J. C. Boyd, A. J. Lowes and C. P. Price, *Am J Clin Pathol*, 2006, **126**, 428-436.

202. N. Hitzeman, M. P. H. Greer D Md and E. Carpio, *Am Fam Physician*, 2022, **106**, 27-35B.
203. B. E. Van Beers, C. M. Pastor and H. K. Hussain, *J Hepatol*, 2012, **57**, 421-429.
204. M. Antoine MICHEAU, Denis HOA, MD, Labeled cross-sectional anatomy of the mouse on micro-CT, DOI: doi.org/10.37019/vet-anatomy/564757).
205. Contrast Agent for MRI Dotarem® (Gadoteric acid - Gadoterate meglumine)).
206. C. Camaschella, *N Engl J Med*, 2015, **373**, 485-486.
207. ITK-SNAP demo).
208. *Small Animal Imaging: Basics and Practical Guide*, 2011, DOI: 10.1007/978-3-642-12945-2, 1-597.
209. T. F. Massoud and S. S. Gambhir, *Gene Dev*, 2003, **17**, 545-580.
210. P. U. Tofts, *Quantitative MRI of the brain : measuring changes caused by disease*, Wiley, Chichester, 2003.
211. G. R. Fulmer, A. J. M. Miller, N. H. Sherden, H. E. Gottlieb, A. Nudelman, B. M. Stoltz, J. E. Bercaw and K. I. Goldberg, *Organometallics*, 2010, **29**, 2176-2179.
212. A. Dadabhoy, S. Faulkner and P. G. Sammes, *J Chem Soc Perk T 2*, 2002, DOI: 10.1039/b104541p, 348-357.